UNIVERSITÀ
DEGLI STUDI
DI PADOVA

Sede Amministrativa: Università degli Studi di Padova

Dipartimento di Tecnica e Gestione dei Sistemi Industriali

SCUOLA DI DOTTORATO DI RICERCA IN INGEGNERIA MECCATRONICA E DELL'INNOVAZIONE MECCANICA DEL PRODOTTO

CICLO XXVI

Innovative Estimation and Control Techniques in Electric Drives for Mechatronic Applications

Direttore della scuola: Ch.mo Prof. Alessandro Persona

Supervisore: Ch.mo Prof. Mauro Zigliotto

Dottorando: Matteo Carraro

INNOVATIVE ESTIMATION AND CONTROL TECHNIQUES IN ELECTRIC DRIVES FOR MECHATRONIC APPLICATIONS

Matteo Carraro, 2013

Submitted in fulfilment of the requirements for the Degree of Doctor of Philosophy in "Mechatronics and Product Innovation Engineering"

This dissertation was typeset adopting the typographical `classicthesis` style, available for both LaTeX and LyX at: http://code.google.com/p/classicthesis/.

– A mio nonno Mario –

ABSTRACT

The research presented in this thesis involves different aspects related to advanced control methodologies and self-commissioning identification algorithms in modern electrical drives. The theoretical study and the validation of the results obtained were performed in the three years of Ph.D. at the Electric Drives Laboratory in the Department of Management and Engineering of the University of Padova, (VI) Italy. The research topics were mainly three, all related to the implementation and development of advanced controls for electric drives, aimed at a more efficient use of the electric machines in the modern mechatronic applications. The demand of electric drives capable of guarantee high-performance and flexible enough to update in real time the parameters involved in the control algorithm are the motivation of the present research, as well as the meshing or replacement of standard or obsolete control techniques with modern ones, able to fully exploit the new hardware resources. In order to contextualizes and motivate the choice of the present research in the world scenario, a comprehensive bibliographic framework can be found in the introduction of each chapter of the thesis.
The part one of the thesis presents two new control architectures for Permanent Magnet Synchronous Motors, that is a type of electric machine notoriously appreciated by both academia and industry for its flexibility of use and controllability. To this aim, in Chap.2 is proposed a non-linear control algorithm for the automatic search of the Maximum Torque Per Ampere (MTPA) operating condition for Permanent Magnet Synchronous Motors with anisotropic structure, to be integrated in a conventional Field Oriented Control scheme. The exhaustive convergence and stability analysis performed in order to derive a new and original tuning method of the controller (proven by numerous experimental evidences) is definitely one of the distinguishing features in this research topic.
In parallel to the first topic, for the same type of motor has been investigated and developed (first analytically and then by simulation) a speed and current Direct Predictive Control with Hierarchical decisional structure. Unlike the traditional control techniques, the proposed Direct Predictive Control with modified hierarchical control structure has a faster dynamic and the capability to impose different operating conditions aimed at the energy efficiency optimisation. The on-line execution of the algorithm required for the experimental validation, has become possible thanks to the adoption of a control platform based on FPGA logic (Chap.3). In fact, the processing speed provided by these devices, released from the execution of sequential instructions (typical of the architecture of the microprocessors), ensures an execution time of the algorithm contained in a few μs.
The part two of the thesis (i. e. Chap.5) presents an innovative technique of parameter identification for induction motors, capable of estimating the parameters of the equivalent inverse-Γ electric circuit completely at standstill. As known, the saturations in the parameters of the magnetic circuit of the induction motor and the relative non-linearities, deteriorate the performance of the standard sensored or sensorless vectorial controls. The studied self-commissioning procedure addresses and solves many problems related to the estimate of the non-linearity of the parameters, and then it can be considered as an evolution of the classical identification techniques in the literature. The practical feasibility, doubly validated by numerous experimental tests and by many finite element simulations on three different induction motors, concludes the chapter and proves definitely the method.

SOMMARIO

La ricerca presentata in questa tesi coinvolge molteplici aspetti che si legano alle più recenti metodologie di controllo studiate per azionamenti elettrici di ultima generazione. Lo studio teorico e la validazione in ambito sperimentale sono il frutto del lavoro svolto nel triennio di dottorato presso il laboratorio di azionamenti elettrici del Dipartimento di Tecnica e Gestione dei Sistemi Industriali dell'Università degli Studi di Padova. I temi di ricerca trattati sono principalmente tre, tutti legati alla realizzazione e allo sviluppo di algoritmi di controllo innovativi, capaci di incrementare l'efficienza e le prestazioni delle macchine elettriche di ultima generazione per applicazioni meccatroniche. Azionamenti elettrici in grado di garantire elevate prestazioni ma sufficientemente flessibili da aggiornare in tempo reale i diversi parametri coinvolti nel algoritmo di controllo sono il filo conduttore e la motivazione della presente ricerca, così come la sostituzione di logiche di controllo standard o obsolete con nuove architetture di controllo capaci di sfruttare le più recenti innovazioni hardware. Al fine di contestualizzare e motivare la ricerca condotta nel panorama mondiale, nell'introduzione di ciascun capitolo è inserito un esaustivo inquadramento bibliograficoinerente inerente il problema affrontato.
La prima parte della tesi presenta due nuove architetture di controllo per motori sincroni a magnete permanente, tipologia di macchina elettrica notoriamente apprezzata dal mondo accademico e industriale sia per la sua flessibilità d'uso che per la sua facile controllabilità. In tal senso, nel Capitolo2 è descritto e formalizzato un controllo non lineare per motori sincroni a magnete permanente anisotropi, inseribile in schemi di controllo convenzionali ad orientamento di campo per ottenere la condizione di funzionamento a massima coppia su corrente (MTPA). L'esaustiva analisi di convergenza e stabilità condotta al fine di ottenere un nuovo ed originale metodo per la sintonizzazione del regolatore (comprovato da numerose evidenze sperimentali) è sicuramente una delle caratteristiche distintive per questo ramo della ricerca.
Per la stessa tipologia di motore è stato poi sviluppato un controllo predittivo a stati finiti con struttura decisionale gerarchica. A differenza delle tecniche di controllo tradizionali, la soluzione studiata garantisce una dinamica veloce e la possibilità di imporre condizioni operative diverse, volte all'ottimizzazione e all'incremento dell'efficienza energetica. L'esecuzione on-line di tale algoritmo per le verifiche sperimentali si è resa fattibile grazie all'adozione di una piattaforma di controllo basata su logica FPGA (Capitolo3), in quanto la velocità di calcolo offerta da tali dispositivi, svincolata dall'esecuzione sequenziale delle istruzioni tipica dei microprocessori, garantisce tempi di esecuzione dell'algoritmo contenuti a pochi μs.
Nella seconda parte della tesi (Capitolo5) è presentata un innovativa tecnica di identificazione parametrica per motori asincroni, capace di stimare i parametri del circuito equivalente a Γ-inverso del motore asincrono, a rotore fermo. Come noto, le saturazioni del circuito magnetico della macchina e le non linearità ad esso associate deteriorano le performances nei normali controlli vettoriali sensored e soprattutto sensorless. Il metodo di identificazione parametrica studiato affronta e risolve molti problemi connessi alla stima delle non linearità dei parametri, configurandosi a tutti gli effetti come un evoluzione delle classiche tecniche di identificazione presenti in letteratura. La fattibilità pratica del metodo, validata con innumerevoli prove sperimentali e simulazioni agli elementi finiti su tre diversi motori ad induzione, conclude il capitolo e prova in modo definitivo la realizzabilità del metodo.

ACKNOWLEDGMENTS

In these years of study many people have been fundamental for me, but the first one that I want deeply thanking is undoubtedly my supervisor, the Prof. Mauro Zigliotto. I would like to express him my most sincere gratitude, because he has been a guide that with patience has gave me skill and a solid scientific research method. Definitely an example to follow for me.
A second special thanks go to Dr. Riccardo Antonello for his support, his friendship and for the infinite availability shown in these years.
My deep gratitude is also to all my italian close friends and to all the guys who I've met at the Department of Technical and Management in Vicenza: Alessandro Costabeber, Omar Daud, Davide Cattin, Fabio Tinazzi, Roberto Loco, Roberto Ricci and many others with whom I shared a lot of my time in the Mechatronics laboratory.
I would also like to thank the Dr. Luca Peretti, Giovanni Zanuso and all the members of the Electrical Machines and Motion Control group of the the ABB Corporate Research Center of Västerås, that so kindly welcomed me when I was a visiting student there.
Finally, I would like to express my deepest gratitude to my parents, to my sister Silvia and to my girlfriend, whose love and support have been fundamentally for me.

— Vicenza, January 2014

Matteo Carraro

This research has been supported by
FSU (Fondazione Studi Universitari) of Vicenza.
I would like to express my sincere gratitude to the Foundation
for having sponsored my Doctoral Course throughout these three years

CONTENTS

LIST OF TABLES

PWM Pulse Width Modulation

PMSM Permanent Magnet Synchronous Motor

PMSM-SPM Surface mounted PM motor

PMSM-IPM Interior PM motor

PMASRM Permanent Magnet-Assisted Synchronous Reluctance Motors

MTPA Maximum Torque Per Ampere

ESC Extremum Seeking Control

EMF Electromotive Force

BEMF Back Electromotive Force

IM Induction Motor

FEA Finite Element Analysis

FCP Fast Control Prototyping

FOC Field-Oriented Control

DTC Direct Torque Control

PPC Pulse-width Predictive Control

DPC Direct Predictive Control

MPC Model Predictive Control

HDPC Hierarchical Direct Predictive Control

DFT Discrete Fourier Transform

FFT Fast Fourier Transform

CFTOC Constrained Finite Time Optimal Control

SVM Space Vector Modulation

LUT Look Up Table

DOB Disturbance Observer

VSI Voltage Source Inverter

TF Transfer Function

FPGA Field Programmable Gate Array

VHDL VHSIC Hardware Description Language

GUI Graphical User Interface

FSM Finite State Machine

IGBT Insulated Gate Bipolar Transistor

FIFO First In First Out data buffer

LPF Low Pass Filter

HPF High Pass Filter

DT Dead Time

IIR Infinite Impulse Response

FIR Finite Impulsive Response

OLS Ordinary Least Squares

$\alpha\beta$: Fixed stator reference frame

dq: Rotating reference frame

u_{su}, u_{sv}, u_{sw}: Stator voltages in the uvw reference frame

u_α, u_β: Stator voltages in the $\alpha\beta$ reference frame

U_α, U_β: Stator voltages in the $\alpha\beta$ reference frame at steady state

u_d, u_q: Stator voltages in the rotating reference frame

U_d, U_q: Stator voltages in the rotating reference frame at steady state

i_d, i_q: Stator currents in the rotating reference frame

I_d, I_q: Stator currents in the rotating reference frame at steady state

λ_d, λ_q: Flux linkages in the rotating reference frame

Λ_{mg}: Flux generated by the permanent magnets

L_d: d-axis stator inductance

L_q: q-axis stator inductance

R_s: Stator resistance (when symmetric for all phases)

$\chi = L_q/L_d - 1$: Inductances ratio

p: Pole pairs

P_N: Nominal power

ω_N: Nominal mechanical speed

τ_N: Nominal torque

τ_L: Load torque

I_N: Nominal motor current

ω_{me}: Electromechanical speed

Ω_{me}: Electromechanical speed at steady state

ω_m: Mechanical speed

Ω_m: Mechanical speed at steady state

ϑ_{me}: Electromechanical position

ϑ_m: Mechanical position

f_{sw}: Switching frequency of the VSI

T_c: Sampling period (i. e. $\frac{1}{f_{sw}}$)

$|i|$, ϑ: Current vector magnitude and phase

$K_{P,\omega}$, $K_{I,\omega}$: Speed PI regulator proportional and integral gains

x_I: Speed PI regulator integrator state

e_ω, i^*: Speed PI regulator input (speed error) and output

$(\cdot)_0$: Steady state value at P_0

$\Delta(\cdot)$: Small variations with respect to P_0

ω_{AC}: MTPA tracker perturbation frequency

A: MTPA tracker perturbation amplitude

τ_{HPF}, τ_{LPF}: Time constants of MTPA tracker HP / LP filters

k_p, γ: MTPA tracker proportional and integral gains

Δi, $\Delta\vartheta$: Current vector magnitude and phase perturbations

ε, ε_f: Mixer unfiltered and filtered outputs of the MTPA controller

β: Current vector angle with respect to q–axis

$W(s)$: Phase–to–current perturbation transfer function of the MTPA controller

k_{HF}, φ_{HF}: Mag / phase of MTPA controller HP filter at ω_{AC}

T_e: Algorithm Execution time

kT_c, $(k+1)T_c$ ... $(k+j)T_c$: Generic sampling instant

s_u, s_v, s_w: State configuration of uvw phase legs of the VSI

N_{pd}: Length of the Prediction Horizon

N_s: Number of voltage state vectors

U_{DC}: DC-link bus voltage

$\boldsymbol{u}_{s0}$....$\boldsymbol{u}_{sN_s}$: Voltage vector configuration for each of the N_s state vectors

$\boldsymbol{T}_{uvw/dq}$: Park's matrix transformation

$\boldsymbol{T}_{uvw/\alpha\beta}$: Clarke's matrix transformation

N_{TC}: Number of periods considered to calculates the commutations

$N_{cu,i}$ $N_{cv,i}$ $N_{cw,i}$: Number of commutations of uvw phase legs of the power converter

R_r: Rotor resistance

L_s: Stator inductance

L_r: Rotor inductance

L_m: Mutual inductance between stator and rotor

R_{sr}: Rotor resistance referred to the stator of the inverse-Γ equivalent circuit

L_t: Transient inductance

L_φ: Magnetising inductance

$\boldsymbol{u}_s$: Stator voltage

$\boldsymbol{i}_s$: Stator current

$\boldsymbol{i}_r$: Rotor current

$\boldsymbol{\lambda}_s$: Stator flux linkage

$\boldsymbol{\lambda}_r$: Rotor flux linkage

$\boldsymbol{\lambda}_\varphi$: Magnetizing flux linkage

R_0: Equivalent iron losses

Part I

EFFICIENT CONTROL ALGORITHMS FOR PMSM ELECTRIC DRIVES

PREFACE AND CONTEXTUALIZATION

The fundamental purpose of the research in the field of electrical drives for isotropic or anisotropic permanent magnet synchronous motor is to thoroughly study new control techniques capable to improve the overall efficiency and the performances of the modern electrical drives. Electric drives with an high dynamic are required but an optimum use of the overall system is an essential aspect in the new AC drives generations, always more widespread in many fields, e. g. in robotics applications, wind or hydro energy generation and automotive industry [1].
The recent environmental and energy efficiency laws have pushed a renewed interest into a more efficient utilisation of electrical motors, that can be reached only by means of modern control techniques. This first part of the dissertation collects different control strategy to obtain more feasible and energy-efficient drives for PMSM.
The aim of the research is to the create of a more efficient control architectures capable to overcome the canonical industrial control algorithm and able to take advantage of the high efficiency of the modern PMSM. All the topics presented and discussed are framed within those issues, and in detail:

- Chap.1 presents the basic equations and the equivalent model of the anisotropic synchronous machine used for the development of the control algorithms discussed in this part of the thesis. From the classical voltage balance equations, a non-linear model that takes into account the saturation effects which involves currents and flux linkages and the non-linear magnetic relationship is obtained by performing a FEA of the machine for the whole current range of the motor, and the comparison between the canonical linear representations of the machine and the non-linear modelization is discussed and presented.

- Chap.2 deals with the theoretical study, the simulation and the experimental implementation of an on-line perturbation-based method that retrieves automatically the MTPA operating point. As known, the MTPA operation guarantees a specific torque with the minimum current magnitude, and this leads to a copper losses minimization and an increased overall system efficiency. The proposed method is based on the non-linear ESC techniques, where a small perturbation is forced in the control chain and the informations on the operating working point are retrieved by considering the induced disturbance on the measurements. By evaluating the changes in current reference magnitude produced by the speed regulator, a variation in the phase reference vector of the modified FOC scheme is performed and the MTPA trajectory is guarantee. The main feature and the innovative contribution of this research is related to the convergence analysis of the control algorithm and the possibility to tune the integral gain of the PI controller by using the convergence time estimation retrieved by the complete Lyapunov stability analysis. Moreover, a series of simulations and experimental validations are presented and discussed considering two different PMSM-IPM motors, in order to validate the proposed solution also from an industrial point of view. It is worth noting that this topic of research and the related improvements in terms of energy efficiency and energy consumption is strictly correlated with the architecture described in Chap.3. Moreover, some features and innovative aspects of this control technique could be applied without too many modifications to other motor types and, with some adjustments in different fields of the research (e. g. in the photovoltaic MPP tracking controller based on the ripple correlation techniques [2]).

- Chap.3 deals with the theoretical study, the simulation and the experimental implementation of a finite state predictive control for PMSM machines. This control algorithm overcomes the standard FOC or Direct Torque Control (DTC) cascade control schemes by adopting an on-line solution that tests and selects the optimal voltage configuration by successive refinements of the applicable set, based on a hierarchical decision structure. The algorithm guarantees an extremely fast dynamic, while the use of a finite set of voltages greatly enhances the robustness against parameter variations. Moreover, in the decisional structure can be easily integrated many control objects in order to achieve interesting performance in terms of efficiency (as the MTPA condition of Chap.2, achievable without taking into account complicated adaptive controllers) or by minimizing the number of commutations of the VSI. The studied control operates either with anisotropic or isotropic motors (although in this latter case the MTPA condition is reduced to the standard FOC), although one of the main contributes of the research resides into the capability to operate with industrial AC drive configurations. An alternative implementation on a Field Programmable Gate Array (FPGA) platform, instead of the canonical microprocessor platform, has been used for the experimental validation of the algorithm, since the large number of computations requires an hardware capable to manages in real time all the operations. It is worth noting that the use of this new technology is always more merged with standard microprocessors in the modern drive control boards, since frequently the computational resources of complex control algorithms, as the proposed predictive control, have an high computational requirement for an on-line implementation. Part of this research has been developed during my brief permanence at the ABB Corporate Research Center in Sweden.

1 THE PERMANENT MAGNET SYNCHRONOUS MOTOR

1.1 INTRODUCTION

The inverter-fed synchronous motors are widely used in many Mechatronic drive systems (e. g. in robotic arms, where an high torque and a small moment of inertia is a prerequisite in a small motor size).
If the PMSM synchronous machine is supplied by a current controlled voltage-source Pulse Width Modulation (PWM) inverter, the stator reference currents are generated by the reference speed (or reference electromagnetic torque) PI controllers, while the inner PI currents regulators provides the couple of voltage references to the VSI.
In general, the PMSM is formed by a rotor containing the permanent magnets and a stator with a distributed winding, and there are two main advantages in using the permanent magnets to create the magnetic flux of the machine, rather than use the field coil operating principle, where the current flows into the rotor composed by an armature of wired coils to generates the flux linkage (e. g. the DC motors).
Firstly, the occupation area of the PMs for the magnetization is small, leading to several degrees of freedom in the geometry design of the rotor. Secondly, the absence of an excited rotor circuit avoids magnetization losses, leading to an increased high energy and power density.
The stator winding of the PMSM exhibit the same geometry of that used in the well known and robust induction motors, and it is obtained by using a compacted stack of ferromagnetic laminations. An air gap g separates the rotor and the stator windings, and it is necessary for the correct operating of the motor.
There are basically three types of PMSM machines (depending on the rotor typologies, according to the positioning of the magnets into the rotor), but the motors with radial magnetized PMs can be distinguished in two main classes:

- PMSM-SPM: the polar magnets are located on the surface of the rotor with alternating polarity and the motor behaves as a smooth-air-gap machine, since in this motor the direct and quadrature axis synchronous inductances are equal with only magnet torque produced. A cross section is represented in Fig.1.1a.

- PMSM-IPM: in these machines, the permanent magnets are generally buried (radially or axially) into the rotor. Shape and dimensions of the magnets depends by the specific design of the motor, but several flux barriers can be inserted in the rotor structure, since the deviation of the magnetic flux linkage operated by these barriers reduce the effects of the cogging torque. More in general, an increased number of barriers leads to an increment of the the anisotropy of the motor [3]. The conventional materials used for the construction of the permanent magnets, as NdFeB or SmCo alloys, have a magnetic permeability comparable to that of air (i. e. almost unitary), which is much lesser of the iron. Therefore, when the magnets are placed within the rotor, the spatial distribution of the magnetic permeability is no longer uniform, although it varies within the rotor: in brief the rotor exhibits a magnetic "anisotropy". For the purposes of this thesis, the meaning of "anisotropic" motors will be equivalent of that of "Interior Permanent Magnet" motors, due of the same magnetic properties. With respect to the position of the PMs in the rotor, several machine geometries and topologies can be obtained (also by modifying the dimensions and the shapes of both the PMS and

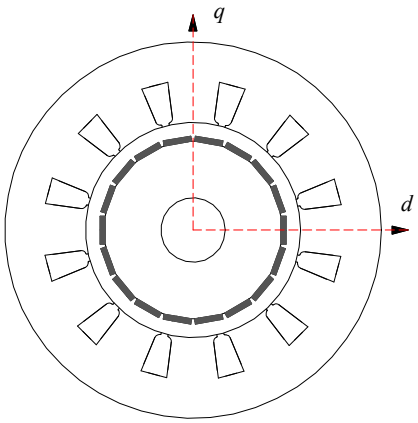

(a) *Sketch of a 2 poles PMSM-SPM motor with surface mounted PMs.*

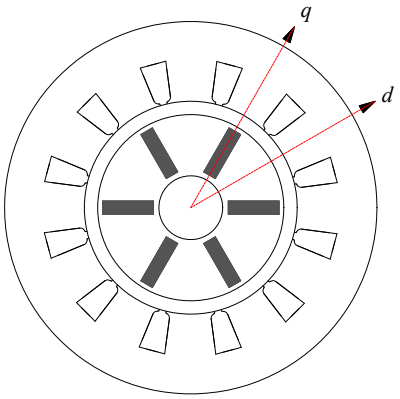

(b) *Sketch of a 6 poles PMSM-IPM motor with tangential arrangement of the magnets (IPMTAN).*

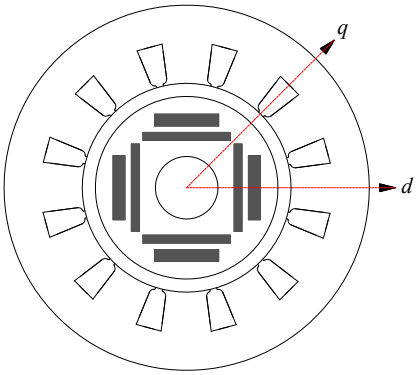

(c) *Sketch of a 4 poles PMASRM motor.*

Fig. 1.1: Examples of rotor configurations for PMSM machines.

the flux barriers), as shown in Fig. 1.1. The sketch in Fig. 1.1b is relative to a motor with tangential arrangement, while Fig. 1.1c refers to a motor PMASRM (a reluctance motor assisted by permanent magnets). In both the figures, are also reported the magnetic axis, that depends by the pole pairs of the machines.

Since the mathematical model of a PMSM-SPM can be derived by the more general model of a PMSM-IPM, for all the rest of the discussion, only the PMSM-IPM will be considered.

1.2 STRUCTURE AND OPERATING PRINCIPLE

The electromechanical conversion implemented by the PMSM-IPM follows the double principle of electrodynamic systems and systems reluctance, and the torque generated by them appears to be the sum of these two components.
Using the general equations of the three-phase voltage balance as starting point [4]:

$$\begin{cases} u_u(t) = R_s i_u(t) + \dfrac{d\lambda_u(t)}{dt} \\ u_v(t) = R_s i_v(t) + \dfrac{d\lambda_v(t)}{dt} \\ u_w(t) = R_s i_w(t) + \dfrac{d\lambda_w(t)}{dt} \end{cases} \tag{1.1}$$

the distribution of the stator windings and the shaping of the magnets lead to sinusoidal concatenated fluxe linkages (as in the case of the isotropic machine) $\lambda_{u,mg}(t)$, $\lambda_{v,mg}(t)$, $\lambda_{w,mg}(t)$. Assuming that no saturation affects the magnetic circuits, then the flux linkage of each phase is the sum of the flux linkage given by the permanent magnet and the flux linkage due to the phase currents.

$$\begin{cases} \lambda_u(t) = \lambda_{u,mg}(t) + \lambda_{u,i}(t) \\ \lambda_v(t) = \lambda_{v,mg}(t) + \lambda_{v,i}(t) \\ \lambda_w(t) = \lambda_{w,mg}(t) + \lambda_{w,i}(t) \end{cases} \tag{1.2}$$

By arbitrarily choosing the electrical angle ϑ_{me}[1] (which is considered the angle between phase u and the flux linkage produced by the permanent magnet) as a reference coordinate, as shown in Fig.1.2, the distribution of the stator windings allows us to consider $\lambda_{u,mg}(t)$, $\lambda_{v,mg}(t)$ and $\lambda_{w,mg}(t)$ as sinusoidal flux linkages.

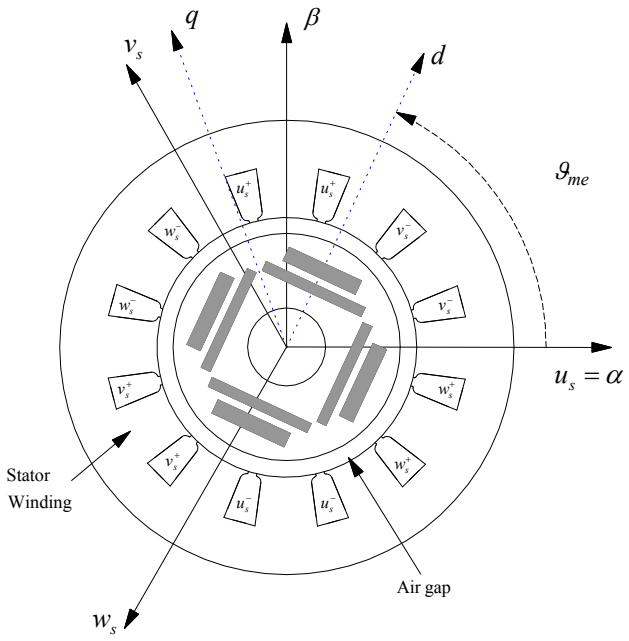

Fig. 1.2: Section of a PMASRM with $p = 2$ pole pairs and $Q_s = 12$ stator slots. In figure are indicated the stator axes and the equivalent dq reference frame.

In particular:

$$\begin{cases} \lambda_{u,mg}(t) = \Lambda_{mg} \cos(\vartheta_{me}) \\ \lambda_{v,mg}(t) = \Lambda_{mg} \cos\left(\vartheta_{me} - \dfrac{2\pi}{3}\right) \\ \lambda_{w,mg}(t) = \Lambda_{mg} \cos\left(\vartheta_{me} - \dfrac{4\pi}{3}\right) \end{cases} \tag{1.3}$$

1 The electric angle ϑ_{me} is related to the mechanical positon ϑ_m by the relationship $\vartheta_{me} = p\vartheta_m$, where p = number of polar pairs.

For the sake of simplicity, the time dependency will be omitted from now on. Λ_{mg} represents the maximum flux concatenated with each phase as a result of the permanent magnet. The three equations of (1.3) are devoid of the omopolar component, and so they can be associated to the spatial vector:

$$\mathbf{\Lambda}^{s}_{mg} = \Lambda_{mg} e^{j\vartheta_{me}} \tag{1.4}$$

The suffix "s" indicates the stationary reference frame with the $\alpha\beta$ represented in Fig.1.2. The $\lambda_{uvw,i}(t)$ terms of the (1.2) are the fluxes due to the interaction between the currents ad stator inductances. They are expressed as:

$$\begin{cases} \lambda_{u,i} = L_u i_u + M_{uv} i_v + M_{wu} i_w \\ \lambda_{v,i} = L_v i_v + M_{uv} i_u + M_{vw} i_w \\ \lambda_{w,i} = L_w i_w + M_{wu} i_u + M_{vw} i_v \end{cases} \tag{1.5}$$

where L_u, L_v ans L_w are the mutual-inductances between the windings of the stator phases and the others. Since the permanent magnets have magnetic permeability similar to that of air (this constitutes a virtual increase of the air gap g), the reluctance along the axis of the magnetic field (defined as the d-axis) is greater than the reluctance along the q-axis.
In particular, the auto and mutual inductances can be regarded as their dependence on the position of the rotor and thus also indirectly by time. The anisotropic auto inductances L_u, L_v ans L_w are further expressed as:

$$\begin{cases} L_u = L_\sigma + L_0 - L_2 \cos\left(2\vartheta_{me}\right) \\ L_v = L_\sigma + L_0 - L_2 \cos\left(2\vartheta_{me} - \dfrac{4\pi}{3}\right) \\ L_w = L_\sigma + L_0 - L_2 \cos\left(2\vartheta_{me} - \dfrac{2\pi}{3}\right) \end{cases} \tag{1.6}$$

L_0 is related to the anisotropy of the structure, while L_σ represents the leakage inductance, due to the stator flux which closes in the air without affecting the rotor.
By defining the inductances along the d and q axes as $\mathcal{R}_{\int d}$ and $\mathcal{R}_{\int q}$, and assuming that N represents the real number of coils per phase, the analytic expression of L_0 and L_2 is:

$$\begin{aligned} L_0 &= N^2 \frac{1/\mathcal{R}_{\int d} + 1/\mathcal{R}_{\int q}}{2} \\ L_2 &= N^2 \frac{1/\mathcal{R}_{\int d} - 1/\mathcal{R}_{\int q}}{2} \end{aligned} \tag{1.7}$$

The mutual inductances M_{uv}, M_{vw} ans M_{wu} in (1.5) can be expressed as:

$$\begin{cases} M_{uv} = -\dfrac{1}{2} L_0 - L_2 \cos\left(2\vartheta_{me} - \dfrac{2\pi}{3}\right) \\ M_{vw} = -\dfrac{1}{2} L_0 - L_2 \cos\left(2\vartheta_{me}\right) \\ M_{uw} = -\dfrac{1}{2} L_0 - L_2 \cos\left(2\vartheta_{me} - \dfrac{4\pi}{3}\right) \end{cases} \tag{1.8}$$

where L_0 and L_2 as the same ddefined in (1.7). Substituting the equations (1.3) -(1.8) in the (1.1), the extended formulation of the voltage balances is obtained[2].
In compact spatial vector form:

$$\boldsymbol{u}_{uvw} = \boldsymbol{R}_s \boldsymbol{i}_{uvw} + \frac{d\left(\boldsymbol{L}_{uvw}\boldsymbol{i}_{uvw}\right)}{dt} + \boldsymbol{e}_{uvw} \tag{1.10}$$

where voltages, currents and Back Electromotive Force (BEMF) of (1.9) are represented as:

$$\boldsymbol{u}_{uvw} = \begin{pmatrix} u_u \\ u_v \\ u_w \end{pmatrix}; \qquad \boldsymbol{i}_{uvw} = \begin{pmatrix} i_u \\ i_v \\ i_w \end{pmatrix}; \qquad \boldsymbol{e}_{uvw} = \begin{pmatrix} e_u \\ e_v \\ e_w \end{pmatrix} \tag{1.11}$$

where the three BEMF e_u, e_v, e_w, generated by the movement of the permanent magnet with respect to the stator can be written as:

$$\begin{cases} e_u = \dfrac{d\lambda_{u,mg}}{dt} = -\Lambda_{mg}\omega_{me}\sin\left(\vartheta_{me}\right) = -\Lambda_{mg}\omega_{me}\cos\left(\vartheta_{me} - \dfrac{\pi}{2}\right) \\ e_v = \dfrac{d\lambda_{v,mg}}{dt} = -\Lambda_{mg}\omega_{me}\cos\left(\vartheta_{me} - \dfrac{\pi}{2} - \dfrac{2\pi}{3}\right) \\ e_w = \dfrac{d\lambda_{w,mg}}{dt} = -\Lambda_{mg}\omega_{me}\cos\left(\vartheta_{me} - \dfrac{\pi}{2} - \dfrac{4\pi}{3}\right) \end{cases} \tag{1.12}$$

with ω_{me} expressed in [rad.el./s]. The resistance and the matrix of the inductances ($\boldsymbol{R}_s$ and $\boldsymbol{L}_{uvw}$) are defined as follows:

$$\boldsymbol{R}_s = \begin{bmatrix} R_s & 0 & 0 \\ 0 & R_s & 0 \\ 0 & 0 & R_s \end{bmatrix}; \qquad \boldsymbol{L}_{uvw} = \begin{bmatrix} L_u & M_{uv} & M_{wu} \\ M_{uv} & L_v & M_{vw} \\ M_{wu} & M_{vw} & L_w \end{bmatrix} \tag{1.13}$$

With the previous compact notation it is easy to express (1.10) in the rotary reference frame dq (as represented in Fig.1.2, synchronous to the magnetic field generated by the PMs of the rotor).
Using the canonical coordinate transformation matrix $T_{uvw/dq0}$ (Park's Transformation) the coordinates changes from the stationary three phase system (uvw) to the ($dq0$) reference frame[3].

2

$$\begin{aligned} u_u &= R_s i_u + L_a\frac{di_u}{dt} + M_{uv}\frac{di_v}{dt} + M_{uw}\frac{di_w}{dt} + \frac{dL_a}{dt}i_u + \frac{dM_{uv}}{dt}i_v + \frac{dM_{uw}}{dt}i_w + e_u \\ u_v &= R_s i_v + M_{uv}\frac{di_u}{dt} + L_b\frac{di_v}{dt} + M_{vw}\frac{di_w}{dt} + \frac{dM_{uv}}{dt}i_u + \frac{dL_b}{dt}i_v + \frac{dM_{vw}}{dt}i_w + e_v \\ u_w &= R_s i_w + M_{uw}\frac{di_u}{dt} + M_{vw}\frac{di_v}{dt} + L_c\frac{di_w}{dt} + \frac{dM_{uw}}{dt}i_u + \frac{dM_{vw}}{dt}i_v + \frac{dL_c}{dt}i_w + e_w \end{aligned} \tag{1.9}$$

3 The transformation is not conservative for the power. It follows that a correction factor of 2/3 has to be considered in (1.14).

$$\boldsymbol{T}_{uvw/dq0} = \frac{2}{3}\begin{bmatrix} \cos(\vartheta_{me}) & \cos\left(\vartheta_{me} - \frac{2\pi}{3}\right) & \cos\left(\vartheta_{me} + \frac{2\pi}{3}\right) \\ \sin(\vartheta_{me}) & \sin\left(\vartheta_{me} - \frac{2\pi}{3}\right) & \sin\left(\vartheta_{me} + \frac{2\pi}{3}\right) \\ 1/2 & 1/2 & 1/2 \end{bmatrix} \tag{1.14}$$

Applying the (1.14) to the (1.10) return:

$$\boldsymbol{u}_{dq0} = \boldsymbol{R}_s \boldsymbol{i}_{dq0} + \boldsymbol{L}_{dq0}\frac{d\boldsymbol{i}_{dq0}}{dt} + \boldsymbol{T}_{uvw/dq0}\frac{d\boldsymbol{T}^{-1}_{uvw/dq0}}{dt}\boldsymbol{L}_{dq0}\boldsymbol{i}_{dq0} + \boldsymbol{e}_{dq0} \tag{1.15}$$

where

$$\boldsymbol{u}_{dq0} = \begin{pmatrix} u_d \\ u_q \\ u_0 \end{pmatrix}; \qquad \boldsymbol{i}_{dq0} = \begin{pmatrix} i_d \\ i_q \\ i_0 \end{pmatrix}; \qquad \boldsymbol{e}_{dq0} = \begin{pmatrix} e_d \\ e_q \\ e_0 \end{pmatrix} \tag{1.16}$$

the matrix of the resistances is independent of the reference system, while the matrix $\boldsymbol{L}_{dq0}$ is defined as:

$$\boldsymbol{L}_{dq0} = \begin{bmatrix} L_d & 0 & 0 \\ 0 & L_q & 0 \\ 0 & 0 & L_0 \end{bmatrix} \tag{1.17}$$

The result is obtained using the trigonometric Werner identity, which transforms the products of two angles of the trigonometric functions of trigonometric sums and differences[4].
Due to the particular choice of the reference system, not even the matrix of $\boldsymbol{L}_{dq0}$ inductances changes; it remains constant as the new system is synchronous to the rotor and the parameters lose their dependence on its position, and then by time.
The terms of mutual coupling among the axes $dq0$ are mutually orthogonal, and the L_d, L_q and L_0 auto inductances are called direct synchronous inductance, quadrature axis synchronous inductance and zero sequence inductance. The relationship with the terms L_0, L_2 and L_σ is:

$$\begin{aligned} L_d &= L_\sigma + \frac{3}{2}(L_0 - L_2) \\ L_q &= L_\sigma + \frac{3}{2}(L_0 + L_2) \\ L_0 &= L_\sigma \end{aligned} \tag{1.18}$$

4

$$\begin{aligned} \sin(j)\sin(k) &= 1/2\,[\cos(j-k) - \cos(j+k)] \\ \sin(j)\cos(k) &= 1/2\,[\sin(j+k) + \sin(j-k)] \\ \cos(j)\cos(k) &= 1/2\,[\cos(j+k) + \cos(j-k)] \end{aligned}$$

As already mentioned, the reluctance of the magnetic circuit relative to the d is greater than that for the q axis. From (1.7) it follows that L_0 and L_2 are both positive, with $L_0 > L_2$; and this is verified by (1.18) ($L_q > L_d$).
The L_q/L_d is then called the "saliency ratio ξ" and in a PMSM-IPM it can be higher (up to 5). Note that, in the case of an isotropic rotor, the term L_2 is missing, leading to $L_d = L_q = L = L_\sigma + (3/2)L_0 = L_{ss} + |M_{ss}|$; and then the isotropic behaviour of the motor would be seen as a special case of an anisotropic machine, with a unitary salience ratio. By expanding the matricial equations (1.15) in each of the $dq0$ component it follows that:

$$\begin{cases} u_d = R_s i_d + L_d \dfrac{di_d}{dt} - \omega_{me} L_q i_q \\ u_q = R_s i_q + L_q \dfrac{di_q}{dt} + \omega_{me} L_d i_d + \omega_{me} \Lambda_{mg} \\ u_0 = R_s i_0 + L_0 \dfrac{di_0}{dt} \end{cases} \tag{1.19}$$

To derive the right torque expression, a general power balance can be applied to (1.19). Multiplying both members of (1.19) for $i_d dt$, $i_q dt$, $i_0 dt$ and summing each of the three equations term by term, the result is:

$$\begin{aligned} \left(u_d i_d + u_q i_q + u_0 i_0\right) dt = R_s \left(i_d^2 + i_q^2 + i_0^2\right) dt + L_d i_d di_d + L_q i_q di_q \cdots \\ \cdots + L_0 i_0 di_0 + \omega_{me} \left(\Lambda_{mg} i_q + \left(L_d - L_q\right) i_d i_q\right) dt \end{aligned} \tag{1.20}$$

The left-hand side of (1.20) represents the electric power supplied to the motor in dt.
On the right-hand side $R_s \left(i_d^2 + i_q^2 + i_0^2\right) dt$ represents the energy converted to heat by the resistances on the windings.
$L_d i_d di_d + L_q i_q di_q + L_0 i_0 di_0$ is the energy stored in the magnetic field, related to the synchronous inductances. $\omega_{me} \left(\Lambda_{mg} i_q + \left(L_d - L_q\right) i_d i_q\right) dt$, under the hypothesis of a conservative system, represents the mechanical energy developed by the machine.
This term represents the electromechanical power and is equal to the product between the torque developed by the machine τ and the electromechanical speed $\omega_{me} = p\omega_m$.
Since the transformation (1.14) is not invariant for the synchronous power, it must be decreased by a factor 2/3. The final expression of the electromagnetic torque results:

$$\tau = \frac{3}{2} p \Lambda_{mg} i_q + \frac{3}{2} p \left(L_d - L_q\right) i_d i_q \tag{1.21}$$

The (1.21) combines the electromagnetic torque (related to the flux-linkage by the permanent magnets) and the torque produced by the reluctance terms (linked anisotropy of the rotor).
The mechanical torque balance finally completes the model:

$$\tau = \tau_L + B\omega_m + J \frac{d\omega_m}{dt} \tag{1.22}$$

Combining (1.19), (1.21) and (1.22) it is possible to draw up the block diagram reported in Fig. 1.3.
It represents the linear dynamics of a PMSM-IPM, and has been widely used in many chapters of this thesis in relation to the controls of PMSM-IPM and PMSM-SPM machines.

Unfortunately, although this scheme is easy to derive and implement, it has some limitations. These are related to the linear approximation of the inductances, which cannot, in many cases, be considered linear.
To overcome the former, a more detailed model has been derived, but in general, if few parameters relative to the machine are known, as is usual, the scheme in Fig. 1.3 can be considered as the starting point to simulate the electromechanical dynamic of the machine.

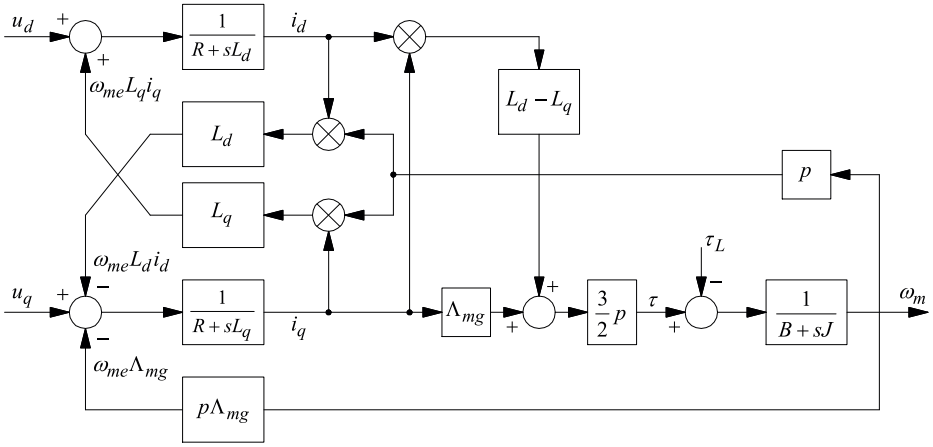

Fig. 1.3: Linear block diagram for a PMSM-IPM machines.

1.3 MODEL OF THE PMSM-IPM WITH MAGNETIC SATURATION

In the previous paragraph some simplifications are taken into account to obtain the final linear model of the PMSM-IPM machine. The real dynamic of a PMSM motor is complex and involves non-linear effects related to the iron magnetic saturation and the mutual interaction between the currents that have not been considered in the previous paragraph.
Depending on the particular type of applications and by the specific requirement of the control action, in the following chapters will not only be considered the linear equations of the motor, but also their non-linear expression. Although the linear model of the motor has general validity, in particular to mathematically derive the equations of the control algorithms, the non-linear modelization of the machine is necessary to obtain an accurate simulation model.
Efficient PMSM control schemes in fact, typically rely on a precise knowledge of the machine mechanical and electrical characteristics. This is especially true for all modern sensorless drives, where a mathematical model of the machine is used to estimate the rotor position/velocity required for the motor control: obviously, any parameter mismatch between the model and the real device yields an estimation error that may worsen the control performances.
As mentioned above, a real machine is affected by iron saturation (the effect increases with high currents) and the flux linkage-current relations for the d and q axis cannot be expressed through linear equations and constant inductances. Moreover the saturation effects produces an interaction between the d- and q-axis, and the relationship depends on the "cross saturation effect".
To derive a complete block diagram for a PMSM-IPM machine useful in a simulation environment and that takes into account the non-linearity related to saturation of the

magnetic circuits (not included in Fig.1.3), the general voltage balance is reconsidered as:

$$\boldsymbol{u}_{uvw} = R_s \boldsymbol{i}_{uvw} + \frac{d\boldsymbol{\lambda}_{uvw,i}}{dt} + \frac{d\boldsymbol{\lambda}_{uvw,mg}}{dt} \tag{1.23}$$

To transform the (1.23) in the $dq0$ reference frame, is sufficient to multiply the (1.23) by the (1.14), obtaining:

$$\boldsymbol{T}_{uvw/dq0}\boldsymbol{u}_{uvw} = R_s\, T_{uvw/dq0}\boldsymbol{i}_{uvw} + \boldsymbol{T}_{uvw/dq0}\frac{d\boldsymbol{\lambda}_{uvw,i}}{dt} + \boldsymbol{T}_{uvw/dq0}\,\frac{d\boldsymbol{\lambda}_{uvw,mg}}{dt} \tag{1.24}$$

Defining also

$$\underbrace{\begin{pmatrix}\lambda_d\\ \lambda_q\\ \lambda_0\end{pmatrix}}_{\lambda_{dq0}} = \boldsymbol{T}_{uvw/dq0}\underbrace{\begin{pmatrix}\lambda_{u,i}\\ \lambda_{v,i}\\ \lambda_{w,i}\end{pmatrix}}_{\lambda_{uvw,i}} + \boldsymbol{T}_{uvw/dq0}\underbrace{\begin{pmatrix}\lambda_{u,mg}\\ \lambda_{v,mg}\\ \lambda_{w,mg}\end{pmatrix}}_{\lambda_{uvw,mg}} \tag{1.25}$$

and decomposing the vectorial equation into the three $dq0$ components, the general voltage balance for the PMSM-IPM machine in the dq reference frame can be written as:

$$\begin{cases} u_d = R_s i_d + \dfrac{d\lambda_d(i_d,i_q)}{dt} - \omega_{me}\lambda_q(i_d,i_q) \\ u_q = R_s i_q + \dfrac{d\lambda_q(i_d,i_q)}{dt} + \omega_{me}\lambda_d(i_d,i_q) \\ u_0 = R_s i_0 + \dfrac{d\lambda_0(i_d,i_q)}{dt} \end{cases} \tag{1.26}$$

and the electromagnetic torque equation:

$$\tau = \frac{3}{2}p\left(\lambda_d(i_d,i_q)i_q - \lambda_q(i_d,i_q)i_d\right) \tag{1.27}$$

The main problem in this description is related to the knowledge of two relationship

$$\begin{aligned} \lambda_d &= f_1(i_d,i_q) \\ \lambda_q &= f_2(i_d,i_q) \end{aligned} \tag{1.28}$$

To find the couple of functions (1.28) without direct measurement in the real machine, a possible alternative is to develop a finite element analysis, if the geometry and the materials used for the construction of the electric machine are known with sufficient precision. For the purposes of this research, an open-source simulation software called *Femm33* [5] has been adopted to perform the analysis of the machine and to calculate the flux linkages relationships as a function of the stator currents.
Although this software limits the magnetic analysis of the machine of only two dimensions[5], the results achieved can be considered reasonably correctly [6] and the machine stack length can be considered as the total length of the simulated system.

5 If necessary the three-dimensional secondary effects as the skewing or the rotor resistance variation can be computed separately and added after the computation of the field solution.

A first batch of simulations is always performed at "no–load", with the d and q-axis currents at zero in order to tune the simulations parameters (e. g. the PM flux linkage which is directly compared with that measured) and correct the geometrical parameters or the materials characteristics.
Since the flux linkage is linked by each stator winding and it varies with the rotor position, the FEA simulations are carried out by assuming a planar symmetry and the magnetic field distribution in each polar section of the machine can be considered equally distributed with a stator windings distribution defined with accuracy by means of the star of slots [7]. The star of slots can be represented as a matrix of $m \times Q_s$ elements (m indicates the number of phases and Q_s the number of stator slots), and the numerical value of each element in the matrix indicates the amount of phase conductors which fill each of the Q_s stator slots.
Disregarding any other theoretical and practical details for implementation and development of the FEA analysis, by keeping the rotor locked in position $\vartheta_{me} = 0\,\text{rad.el}$ and by varying the amplitude of the currents i_d and i_q from a predetermined minimum value to a maximum one, the results are collected in Fig. 1.4.

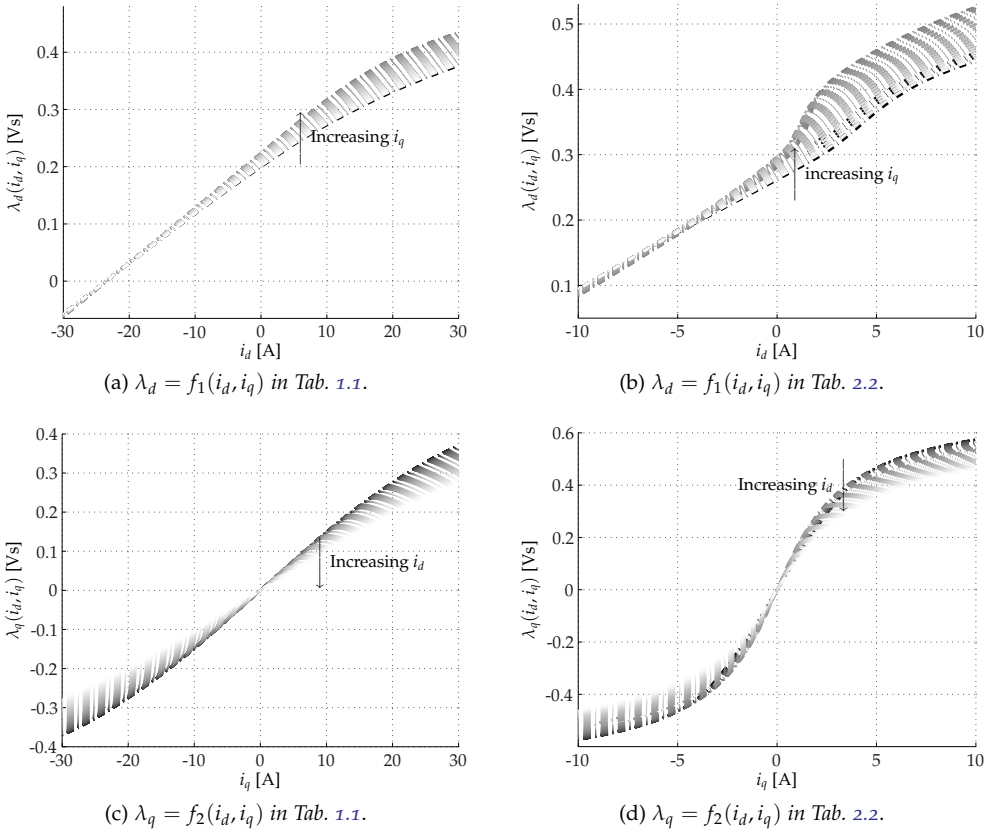

(a) $\lambda_d = f_1(i_d, i_q)$ *in Tab. 1.1.*

(b) $\lambda_d = f_1(i_d, i_q)$ *in Tab. 2.2.*

(c) $\lambda_q = f_2(i_d, i_q)$ *in Tab. 1.1.*

(d) $\lambda_q = f_2(i_d, i_q)$ *in Tab. 2.2.*

Fig. 1.4: Instantaneous flux distribution of the two PMSM-IPM machines (Tab. 1.1 and Tab. 2.2) at no-load, and the curve beam $\lambda_d = f_1(i_d, i_q)$ and $\lambda_q = f_2(i_d, i_q)$ obtained with the FEA simulations.

The figure represents the pair of non-linear functions (1.28) relating to the motor of Fig. 1.1b and Fig.1.1c The couple of functions f_1 ed f_2 calculated with the FEA analysis can be used to return to the (1.19) using (1.26) and (1.27) by simply imposing the linear flux-current relationship.

Using (1.26) and (1.27) the dynamic model of the IPM motor is complete. In fact, using these relations, all the phenomena related to magnetic saturation and the mutual interactions between the two axes are considered.
The flux linkages of Fig. 1.4 cannot be used directly in the form of a look-up table in any simulation environment (such as the Simulink platform) to implements the model described by (1.26) and (1.27). The structure of the FEA simulation, in fact, allows us to impose a specific current distribution in the windings and to read the related flux linkages (calculated on a basis of the potential vector), but not vice versa.
However, there are several methods to reverse the non linear curves of Fig. 1.4. Since the relationships $\lambda_d = f_1(i_d, i_q)$ and $\lambda_q = f_2(i_d, i_q)$ are monotone increasing, they can be reversed and defined as two auxiliary functions $i_d = f_3(\lambda_d, \lambda_q)$ and $i_q = f_4(\lambda_d, \lambda_q)$. The analytic calculation of f_3 and f_4 can be done only numerically and the information contained in the functions $i_d = f_3(\lambda_d, i_q)$ and $i_q = f_4(i_d, \lambda_q)$ can be used in a feedback scheme that is simulated off-line, based on the model in Fig. 1.6 [4].
In detail, a simple integral controller $1/s$ and a gain regulate the steady-state speed convergence of the error. The result is that the output sizes of the blocks storing f_1 and f_2 as Look Up Table (LUT) are the references set void of any steady state error. The outputs of the regulators represent the currents $i_d = f_3(\lambda_d, \lambda_q)$ and $i_q = f_4(\lambda_d, \lambda_q)$ that are necessary to obtain the reference fluxes.

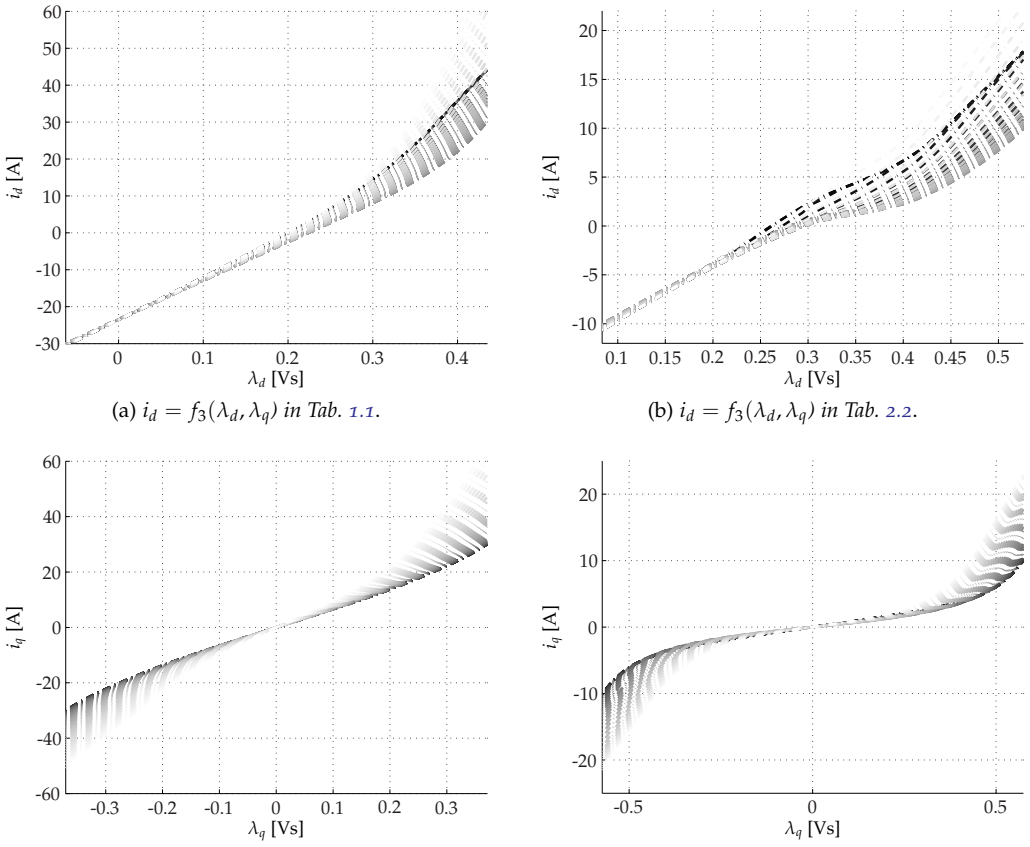

(a) $i_d = f_3(\lambda_d, \lambda_q)$ *in Tab. 1.1.*

(b) $i_d = f_3(\lambda_d, \lambda_q)$ *in Tab. 2.2.*

(c) $i_q = f_4(\lambda_d, \lambda_q)$ *in Tab. 1.1.*

(d) $i_q = f_4(\lambda_d, \lambda_q)$ *in Tab. 2.2.*

Fig. 1.5: Current $i_d = f_3(\lambda_d, \lambda_q)$ and $i_q = f_4(\lambda_d, \lambda_q)$ of the machine in Tab. 1.1 and Tab. 2.2.

Varying the reference fluxes λ_d^* and λ_q^* from their minimum value $\lambda_{d,min-max}$ to the maximum value $\lambda_{q,min-max}$ (that can be found in Fig. 1.4), and saving the couple of currents i_d and i_q for every set of references fluxes, the functions f_3 and f_4 are obtained.

Waiting for a minimum time for the end of the transient, the results are shown in Fig. 1.6. For the complete mapping of the new pair of functions, a double nested "*for*" loop between all the fluxes in the range $\lambda_{d,min}$ - $\lambda_{d,max}$ and $\lambda_{q,min}$ - $\lambda_{q,max}$ is created. Fig. 1.5 shows the functions f_3 and f_4, used in the IPM model with magnetic saturation shown in Fig. 1.7.

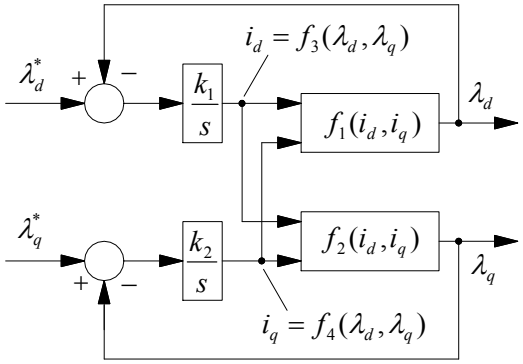

Fig. 1.6: Scheme for the off-line inversionof the functions $\lambda_d = f_1(i_d, i_q)$ and $\lambda_q = f_2(i_d, i_q)$

From the curves of Fig. 1.4, it is possible to deduce the exact value of the apparent inductance L_d and L_q, by measuring the slope of the curves in their linear section, expressed as the ratio between the increase of the flux compared to the increase of current. Both the procedures illustrated in Sec. 1.2 and in Sec. 1.3 requires the perfect knowledge of the main parameters (linear or non-linear) of the machine, in order to obtain a robust model to be used in simulation environment.
In particular, the method illustrated in Sec. 1.3 has some limitations, as the necessity for an accurate FEA to obtain the flux curves $\lambda_d = f_1(i_d, i_q)$ and $\lambda_q = f_2(i_d, i_q)$, and in general the dimensional and project data of the machine are not available. This means that, to obtain a detailed model of the machine, also considering cross-saturation, a self-commissioning procedure must be performed in the absence of information.

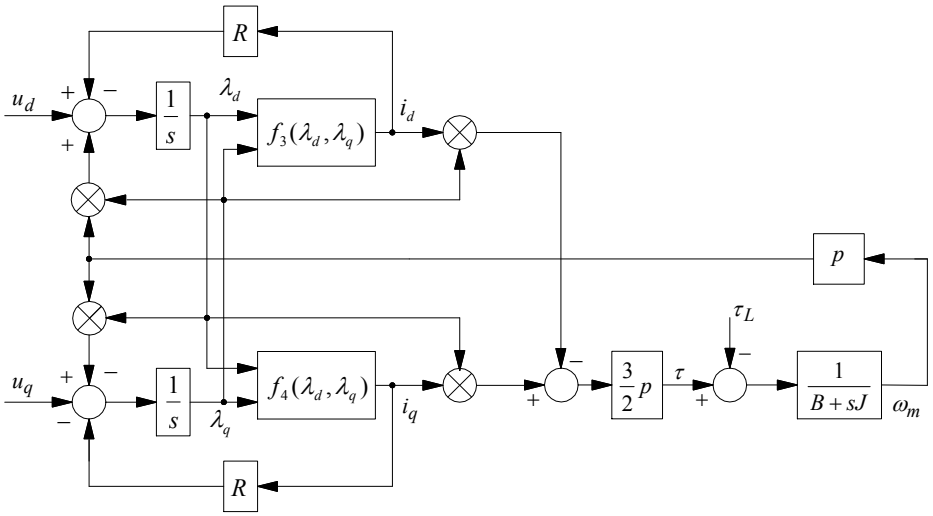

Fig. 1.7: Block diagram of the PMSM-IPM motor based on the equations 1.26 and 1.27

In the electrical model of the machine, both for the model derived in Sec. 1.2 and Sec. 1.3, parameters such as the resistance R_s and the permanent magnet flux Λ_{mg} can be measured with low cost equipment, and they change quite slowly during motor operation, since they are mostly affected by temperature increase.

Nowadays, the commissioning procedures are necessary for the estimation of the flux linkages $\lambda_d = f_1(i_d, i_q)$ and $\lambda_q = f_2(i_d, i_q)$ (or in the simplest case of linear relationship to estimate L_d and L_q), and in general for the identification of the mechanical parameters B_m and J_m [8].

Tab. 1.1: PMSM syncronous motor $PMSM_1$ parameters

Parameter	**Value**
Nominal ph-ph voltage U_N	345 Veff
Rated current I_N	10 Aeff
Pole pairs p	3
PM flux linkage Λ_{mg}	0.234 Vs
Rotor inertia J_m	0.0038 kgm^2
Viscous friction B_m	0.05 Nms

Unfortunately, most of the conventional parameter estimation methods available in literature are unable to provide a reasonable description of the non-linear behaviour of these quantities, and typically they only focus on the estimation of the linearised characteristics around a certain working point.
Even though such flux linkage is in general a non-linear function of the motor currents, also the knowledge of the linear inductance of (1.19) plays an important role in many electric drive control schemes, such as in axes cross-decoupling or sensorless control schemes [9].
Since these self-commissioning techniques come at the price of more complex drives required to operate the motor properly, usually the inductances have been roughly estimated by means of simple experiments, such as the DC current decay measurement method [10], [11], which require low cost equipment, but this simple approach does not satisfy the increasing demand for drive performances, which, in turn, require full knowledge of the machine parameters [12]. Unfortunately, this estimation method does not provide information about important phenomena as saturations or cross-coupling effects, which strongly affect this type of motors.

2 THE MTPA STRATEGY FOR PMSM-IPM DRIVES

2.1 INTRODUCTION AND LITERATURE REVIEW

An increasingly important line of research in modern electric drives for PMSM-IPM concerns the improvement of torque generation efficiency, which substantially implies the minimization of the overall motor losses through either the implementation of specific design and construction expedients [13], or the adoption of sophisticated control techniques [14] [15] [16]. Regarding the latter option [17], only the iron and copper losses can be actually minimized, being the mechanical loss dependent on the motor speed and not controllable [18]. Especially at lower speeds, when iron losses become negligible compared to copper losses [18], the optimal operating conditions can be identified with those yielding minimum copper losses, which indeed coincide with the so-called MTPA condition [19]. It is important to underline that an on-line procedure for the minimization of the overall motor losses would be desirable, but the studied control technique can be adopted only for the minimization of the copper losses, since only the armature currents are monitored by the on-line optimizing procedure. The method discussed and presented in this research not implement an on-line procedure for the minimization of the overall (controllable) motor losses and the main feature and the main contribute is represented by the better formalization of the tuning procedure for a standard MTPA controller based on sinusoidal signal injection.
Considering a FOC scheme for PMSM-SPM [20], in this case the MTPA condition is easily achieved by imposing a null d-axis current. On the contrary, for PM synchronous motors with magnetic anisotropy, the situation becomes more complicated, since the MTPA condition has to be achieved by finding the correct balance between the two mechanisms underlying the generation of the motor torque, namely those exploiting the electrodynamics and the variable reluctance principles [21]. In literature there are many solutions that compute the conditions for MTPA operations in an off-line fashion, by relying on a sufficiently accurate mathematical model of the motor, and then use such information on-line to attain maximum efficiency (in the MTPA sense). A drawback to this approach is obviously its lack of robustness, being impossible to track off-line any parameter variation or other discrepancy between the mathematical model used for the off-line computations and the actual motor dynamics.
To overcome the robustness issue, a possible solution consists of updating the pre-computed MTPA condition on-line, by using an estimate of the motor parameters retrieved with an on-line parameter estimation procedure, as done in [22]. Unfortunately, this method has several drawbacks, such as the increased computational burden [23, 24] or the need to make restrictive assumptions, such as allowing the replacement of the actual voltage measures with their reference [25], or having an available map of the motor inductance non-linearities [26].
An alternative approach to the aforementioned off-line procedure consists of finding the condition for MTPA operations on-line, without relying on any pre-computed information or mathematical model of the system dynamics. For this purpose, the most appropriate control techniques have proved to be based on the working principle of the ESC [27]. A marked improvement is represented by the solution first proposed in [28], and then taken up by several other authors [29], [30] or [31] (where the MTPA has been successfully implemented also in direct torque control (DTC) of synchronous motor drives).

The innovative approach still foresees the perturbation of the system around the steady state working point, but the MTPA condition is detected without any reference to the system model, as in [32], where it is accomplished by monitoring the speed controller demand (i. e. the amplitude of the current reference).
The method illustrated in [28] was refined in [33] and [34], where the injection of a high frequency sinusoidal perturbation of the phase angle and a novel demodulation algorithm, followed by a PI regulator, takes the place of the straightforward action on the current phase. In some ways, all these works are based on the extremum-seeking theory [27], which has proven to be both robust and effective in many different application domains [35], [34]. Equally being model free, they suffer anyway of clear limitations to what can be achieved, since they can be considered as gradient based optimization techniques. They rely on an appropriate exploration of the process to be optimized to provide the user with an approximate gradient, and hence the means to locate a so-called *extremum*. This method is surely a good solution, due to the inherent simplicity and low computational requirements, but the implementation issues are manifold, and the analysis of stability and convergence properties, not discussed in the previous cited papers, is a challenging task, that requires averaging and time-scale separation techniques [36, 37]. Nevertheless, they are surely the best candidates in industrial applications, due to their inherent simplicity and low computational requirements.
Even if the principle of operation is well outlined in literature, there is still a lack of implementation details, as well as a comprehensive analysis of convergence and stability. These aspects turn out to be of key importance in emancipating from empirical tuning, and their study represents, as mentioned before, the main scope and the main contribute of the present research, where a complete mathematical analysis of the control architecture is presented and a complete experimental and simulative validation by considering two different motors.
In detail, Sec. 2.2 presents an overview of the MTPA control architecture, in order to explain in Sec. 2.4 the study of the convergence and stability analysis of the overall control algorithm togheter with a complete sensitivity and parametric analysis. Sec. 2.6.2 collects some design hints to be considered for the effective implementation of the control algorithm, as the simple and effective MTPA search enable mechanism. This last issue avoids the typical malfunctioning of the real implementation [32] caused by the impact of external factors.
The concepts and the main insights, along with their simulation, are presented in Sec. 2.6, while Sec. 2.7 reports a complete and commented set of experimental results obtained by using two different PMSM-IPM motors. Finally, Sec. 2.8 draws some conclusive considerations.

2.2 MTPA BASICS

The permanent magnet synchronous motors with anisotropic structure, as mentioned in the previous chapter, have the fundamental characteristic of generating torque through the principle of electrodynamic generation (due to the permanent magnet) and through the principle of reluctance, due to the difference between the inductances on the axes d and q. This second feature represents a further degree of freedom than the torque generated by an isotropic machine, where the term of the reluctance torque is lacking for constructive reasons. A careful choice of the contribution of reluctance torque allows, in principle, a better exploitation of the IPM motor from the point of view of energy efficiency, by ensuring a compact design and small size but having at the same time a large torque to inertia ratio (i. e. an high acceleration).
Unfortunately, the optimal performances ensured by the high power to weight ratio described above cannot be reached by considering the canonical condition used into the

FOC ($i_d = 0$), since it not ensures the lower module of current for a given torque demand. For this reason, the general equations (1.19) of the PMSM-IPM expressed in the dq rotating frame synchronous to the rotor combined with the electromagnetic and the load torque equations (1.21) must be reconsidered, in order to get some interesting results about the MTPA operating condition. The loci at minimum current vector amplitude (that ensures the optimal torque) can be obtained by replacing the current $i_q = \pm\sqrt{|i|^2 - i_d^2}$ into the (1.21), obtaining:

$$\tau = \frac{3}{2} p \operatorname{sgn}(i_q) \left[\Lambda_{mg} \sqrt{|i|^2 - i_d^2} + (L_d - L_q)\, i_d \sqrt{|i|^2 - i_d^2} \right] \tag{2.1}$$

From (2.1) it is evident that there are several combinations of the direct/quadrature currents i_{dq} capable of satisfying the torque demand τ_0. However, the MTPA operating condition is achieved only for the combination that yields the minimum current magnitude $|i(i_d, i_q)| \triangleq \sqrt{i_d^2 + i_q^2}$, i. e. the combination that solves the following constrained optimization problem:

$$\min_{i_d, i_q} |i(i_d, i_q)| \qquad \text{subject to} \qquad \tau(i_d, i_q) = \tau_0 \tag{2.2}$$

To find the maximum of torque as a function of the current i_d, it is sufficient to derive the (2.1) and placing it equal to zero[1], obtaining:

$$\begin{aligned} \frac{\partial \tau}{\partial i_d} &= \frac{3p}{2} sgn(i_q) \left[\Lambda_{mg} \frac{-i_d}{\sqrt{|i|^2 - i_d^2}} + (L_d - L_q) \frac{|i|^2 - 2i_d^2}{\sqrt{|i|^2 - i_d^2}} \right] \\ &= -(L_d - L_q)\, i_d^2 - \Lambda_{mg} i_d + (L_d - L_q) \left(|i|^2 - i_d^2 \right) \\ &= -2(L_d - L_q)\, i_d^2 - \Lambda_{mg} i_d + (L_d - L_q)\, |i|^2 \\ &= 2(L_q - L_d)\, i_d^2 - \Lambda_{mg} i_d - (L_q - L_d)\, |i|^2 = 0 \end{aligned} \tag{2.4}$$

If follows that, the current i_d that maximize the torque is:

$$i_d = \frac{\Lambda_{mg} \pm \sqrt{\Lambda_{mg}^2 + 8 (L_q - L_d)^2 |i|^2}}{4 (L_q - L_d)} \tag{2.5}$$

The positive solution of the (2.5) is usually discarded because it would generate an opposite contribution to that of i_q (usually $L_d < L_q$). Therefore, the pair of currents i_d, i_q able to maximize the torque for a given current (or, equivalently, to minimize the the current amplitude for a specific torque) are equal to:

$$\begin{aligned} i_d &= \frac{\Lambda_{mg} - \sqrt{\Lambda_{mg}^2 + 8 (L_q - L_d)^2 |i|^2}}{4 (L_q - L_d)} \\ i_q &= \sqrt{|i|^2 - i_d^2} \end{aligned} \tag{2.6}$$

1 As it comes from the *Implicit Function* theorem, this is equivalent to differentiate the torque (1.21) with respect to the i_d component only:

$$\frac{\partial \tau}{\partial |i|} = \frac{\partial \tau}{\partial i_d} \left(\frac{\partial |i|}{\partial i_d} \right)^{-1} \tag{2.3}$$

The theoretic MTPA curve for a generic machine is shown in Fig.2.1, but although useful for the understanding of the problem, the (2.6) is practically unfeasible. The use of these curves in determining the MTPA point, in fact, is limited by the knowledge of the inductances L_d and L_q.
As described in Sec. 1.3 the inductances are affected by the saturation of the magnetic circuit due to the effects of cross-coupling for the partial share of the magnetic circuits of the two orthogonal axes. The use of (2.6), therefore, would require a complete mapping of the inductors for the entire range of current i_d and i_q, including the phenomenon of cross-coupling. As a valid alternative, a signal-injection based scheme has been proposed by [34], reconsidered here with some adjustments, to perform the mathematical analysis of the next paragraphs.

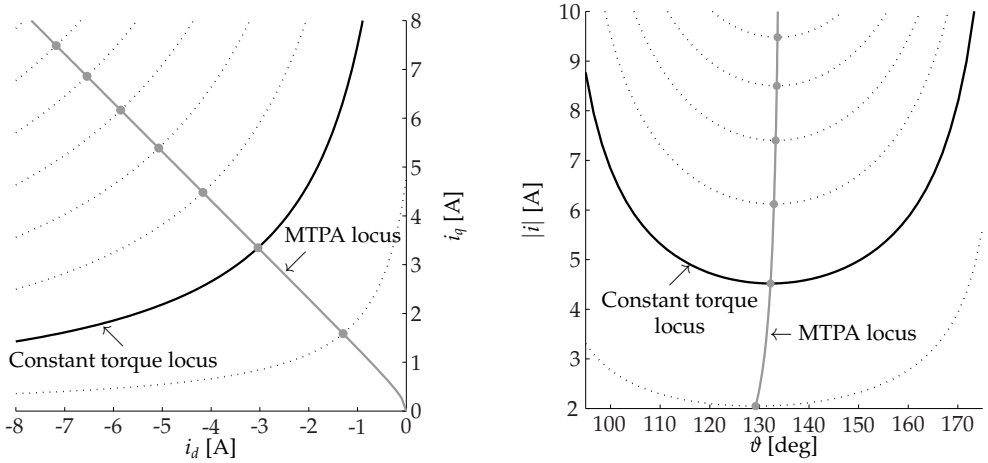

(a) *MTPA loci in Cartesian coordinates*

(b) *MTPA loci in Polar coordinates*

Fig. 2.1: Theoretical MTPA curve in the dq plane (cartesian coordinates) and in polar coordinates.

2.3 THE PROPOSED MTPA CONTROL

The proposed solution for the automatic seeking of the MTPA working point is represented by the control scheme of Fig.2.2. The general FOC scheme [20] of a PMSM is very simple, and it is composed by only two equal tuned current control loops that receive the current reference from an external speed control loop and generate the voltage references for the PWM block. The PI current controllers operate in the dq rotating rotor reference frame, aligned with the PM rotor flux linkage, shifted of the angular position ϑ_{me} with respect of the u-phase of the motor.
The external speed control loop generates the correct current reference amplitude by zeroing the speed error. In the FOC, any non-linear effect related to magnetic saturations in the motor is neglected during the normal operations, and then, model of the motor adopted for the tuning of the PI controllers is that of Sec. 1.2.
The studied solution differers to a standard FOC control scheme only for the block that generates the current references ("MTPA detector" in Fig.2.2), that is the base of the MTPA algorithm. Basically, the idea is to consider a sinusoidal perturbation signal

$$\Delta\vartheta(t) = A\sin(\omega_{AC}t)\,, \qquad A > 0 \qquad \text{(small)} \tag{2.7}$$

superimposed to the phase of the reference current vector. The effect of this perturbation is propagated on the current amplitude reference i^* issued by the speed regulator, which presents a high frequency component $\Delta i(t)$.
The couple of variables $\Delta\vartheta(t)$, $\Delta i(t)$ serves as input to a demodulator composed by the chain of two High Pass Filter (HPF), a multiplier block and a low pass filter. It can be easily demonstrated [28] that the low-frequency component ε_f of the demodulated signal changes its sign around the MTPA point, where also the amplitude of ε_f approaches zero.
The zeroing of ε_f is equivalent to reach the MTPA condition, and this accomplished by the PI_{MTPA} regulator in Fig.2.2. It is worth noting that the choice of its parameters heavily influences the convergence time and, possibly, even the stability of the whole system.
For this reason, a manual/empirical tuning is thus not advisable, as it could lead to unpredictable results. Moreover, due to the system's non-linearity, it is not certain that the system will work properly in every load condition.
Although the behaviour of the controller can be explained in different ways, the easiest way to understand the control actions is to simulate the control (refers to Sec. 2.6 for the simulation implementation details) by opening the tracking control loop and forcing a phase sweep of β from $\pi/2$ rad to π rad, as reported in Fig.2.3a. The two signals, before and after the point of MTPA, are respectively in phase and in anti-phase, and they cover the entire torque region. In detail:

- in the MTPA working point, the current phase reference $\angle i^*$ generated by the "MTPA detector" increases and decreases very little indeed, since any disturbance forces the PI current controller to increase and decrease slightly the reference of the current i^*;
- in working points with a phase $\angle i^*$ higher than the MTPA point, an increase of phase leads to a upper torque curve, and the control speed reacts with a reduction of amplitude of the the vector i^*. Therefore, the phase noise $d(t)$ and the amplitude i^* are in anti-phase;
- in working points with a phase lower than the MTPA working point, an increase of phase leads to a lower torque curve, and the control speed reacts increasing in the amplitude of the vector i^*. This situation leads to a phase noise $d(t)$ and an amplitude i^* in phase.

The amplitude component of the current vector at the disturbance frequency is obtained via a HPF; the same used to filter the disturbance $d(t)$ (as shown in Fig.2.2) with a time constant equal of $\tau_{HPF} = \dfrac{1}{2\pi\, f_{AC}}$. The multiplication of the two filtered signals in Fig.2.3a returns the following expression:

$$\begin{aligned}\varepsilon = d(t)i^*(t) &= AI_{hf}\sin(\omega_{AC}t)\sin(\omega_{AC}t + \frac{k+1}{2}\pi) \\ &= \frac{kAI_{hf}}{2}[1-\cos(2\omega_{AC}t)]\end{aligned} \tag{2.8}$$

where the constant $k = 1$ if the two signals are in phase, while $k = -1$ if the two signals are in anti-phase. The low frequency component of ε at the frequency $kAI_{hf}/2$ is extracted by using a 1^{th} order low pass filter, characterized by a cut-off frequency positioned a decade before the injection disturbance's frequency ($\tau_{LPF} = 10/(2\pi f_{AC})$). Fig.2.3b shows graphically the product of the two signals, and the filtered low-frequency content.

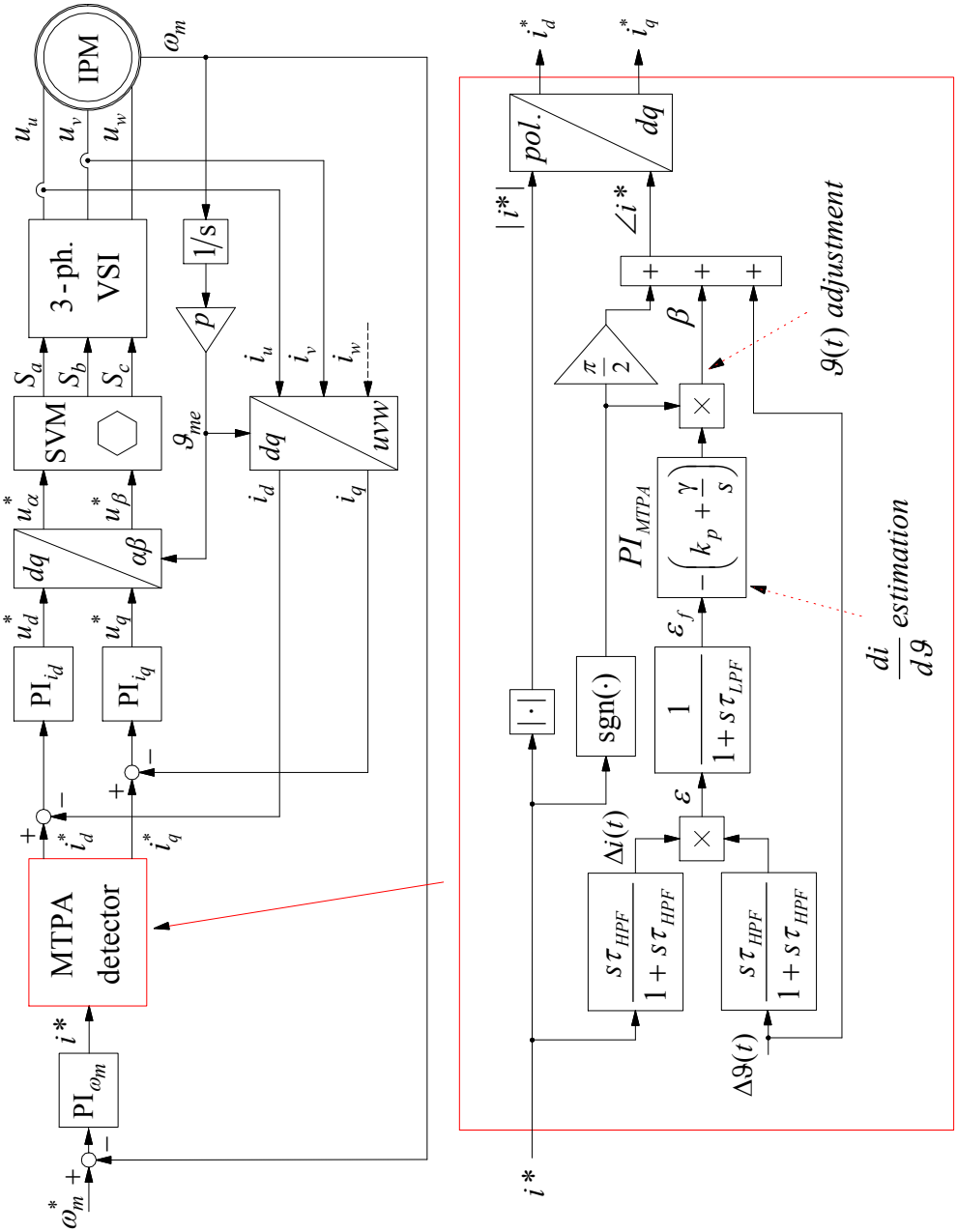

Fig. 2.2: Modified FOC scheme for PMSM-IPM drives for the MTPA detector algorithm and the detailed of the proposed solution.

From the same figure is also evident that for a correct operation in feedback, the sign of ε_f in (2.8) must be reversed, as shown in Fig.2.2, in order to ensures a correct operating of PI_{MTPA}.
The angular compensation β is added to the disturbance $d(t)$ and to the initial phase angle $\pi/2$ rad in order to create the entire phase compensation to pass from the polar coordinate system to the equivalent system in the rotating dq reference frame.
Since the system operates with a phase equal to $\beta_{MTPA} + \pi/2$ in the MTPA working point and a phase perturbation induced by the signal $d(t) = A\sin(\omega_{AC}t)$ leads to amplitude variation in the currents references i_d and i_q is approximately equal to zero, before and after the correct β_{MTPA} compensation the disturbance $d(t) = A\sin(\omega_{AC}t)$ causes a marked variation in the currents.
Furthermore, the continuous presence of $d(t)$ in the composition of the overall phase of the current reference is required, since it serves to maintain the drive in MTPA operation even after a new transient (i. e. induced by a sudden load torque).

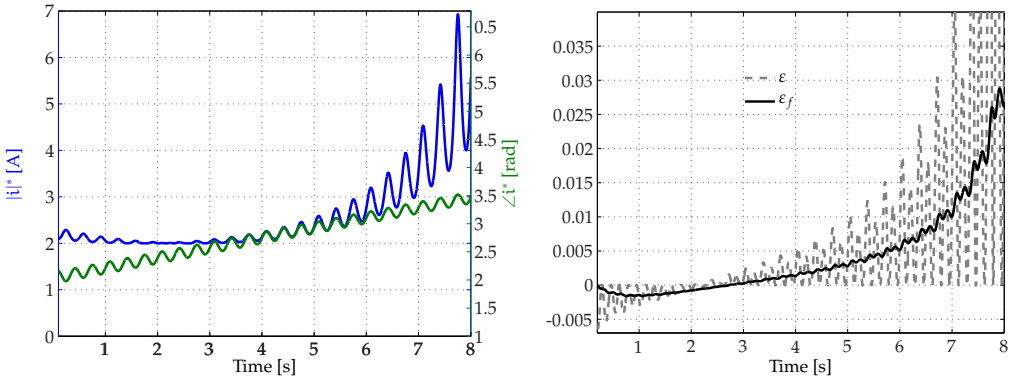

(a) *Module and phase with forced displacement from $\pi/2$ to π rad.*

(b) *Mixer product (ε), with highlighted the average component extracted with the low pass filter (ε_f).*

Fig. 2.3: Signal modulation and demodulation sequence for the automatic regulator MTPA, forced by a ramp variation of the phase.

The description of the control architecture performed up to now does not takes into account some formal aspects and of interesting properties of the algorithm, that can be studied by reconsidering the optimization problem of (2.2) in polar coordinates.
By defining as $|i|$ and $\vartheta \triangleq \angle i$ the magnitude and phase of the current vector in the dq plane, and by replacing the couple of variables i_d and i_q in (2.2) with their equivalent polar notation

$$i_d = |i|\cos\vartheta, \qquad i_q = |i|\sin\vartheta \tag{2.9}$$

the following optimization problem represents the MTPA definition in polar coordinates.

$$\min_{\vartheta} \ |i(\vartheta)| \qquad \text{subject to} \qquad \tau\left(|i(\vartheta)|, \vartheta\right) = \tau_0 \tag{2.10}$$

where:

$$\tau(|i(\vartheta)|, \vartheta) = \frac{3}{2}p\Lambda_{mg}|i(\vartheta)|\sin\vartheta - \frac{3}{4}p\,\chi L_d|i(\vartheta)|^2\sin 2\vartheta \tag{2.11}$$

and $\chi \triangleq L_q/L_d - 1$[2]. Moreover, Fig.2.1 shows that the objective function $|i(\vartheta)|$ to be minimized in (2.11) is a convex function with a (global and unique) minimum.
Therefore, a simple automatic minimum search procedure would consist of increasing the phase ϑ whenever the slope $d|i(\vartheta)|/d\vartheta$ of the objective function, evaluated locally around the current value of ϑ, is negative, and vice versa in case of a positive slope[3].
The slope can be estimated by observing the variation $\Delta|i(\vartheta)| \approx (d|i(\vartheta)|/d\vartheta)\,\Delta\vartheta$, which is the objective function to minimize when a small perturbation $\Delta\vartheta$ is applied to the current value of ϑ.
Fig.2.4 shows a sketch of the operating principle described above. In particular, by considering the sinusoidal perturbation of (2.7), the slope information can be easily recovered from the perturbed current magnitude, that rewritten in polar coordinates returns:

$$|i(\vartheta + \Delta\vartheta)| \approx |i(\vartheta)| + A\frac{d|i(\vartheta)|}{d\vartheta}\sin(\omega_{AC}t) \tag{2.13}$$

By exploiting the simple analogue processing operations described above adopting the high-pass filtering to remove the DC-component of $|i(\vartheta)|$, and an AM-demodulation to determine the amplitude of the remaining sinusoidal variation $\Delta|i(\vartheta)|$, the proportional output ε_f of the AM-demodulator is used to adjust the value of the phase reference $\angle i^*$ according to the proportional-integral (PI) control law: when ε_f approaches zero, the MTPA operating point is attained.
It is worth noticing that although a pure integral law would suffice to steer the system toward the MTPA operating condition, a proportional component usually speeds up the system response.
The choice of the PI regulator parameters heavily influences the stability and convergence time of the whole system. Either manual or empirical tuning is not advisable, as it could lead to unpredictable results.
Moreover, due to the system non-linearity, there is no confidence that the system will properly work in all loading conditions. For these reasons, a more formal analysis of the proposed MTPA tracking controller is required.

2.4 STABILITY AND CONVERGENCE ANALYSIS

The working principle of the proposed MTPA detector can be studied by considering a control strategy that has been already studied in the automatic control literature, namely the ESC strategy.
Detailed analyses of the local and (semi)global (practical) stability of the method have been recently proposed, and the interested reader is invited to refer to [36] for formal stability proofs of the control scheme.
This section reports a simplified convergence analysis of the overall control architecture described in Sec. 2.3, aimed more to provide some hints about the choice of the design

2 The MTPA expression can be alternatively reformulated by solving the (2.11) substituting $\vartheta = atan2\left(-\frac{i_d}{i_q}\right)$ and $|i| = \sqrt{i_d^2 + i_q^2}$. After some easy simplifications, the MTPA condition can be rewritten as [34]:

$$i_d + (L_d - L_q)\,\frac{\left(i_d^2 - i_q^2\right)}{\Lambda_{mg}} = 0 \tag{2.12}$$

The function (2.12) presents two different solutions, but the positive ones ($i_d > 0$) must be avoided. At the end, the condition $2\frac{(L_d - L_q)}{\Lambda_{mg}} i_d + 1 < 0$ must be considered together the (2.12).

3 This is a sufficient condition, being the objective function convex and so, the condition $d|i|/d\vartheta = 0$ is reached for the existence of a local minimum.

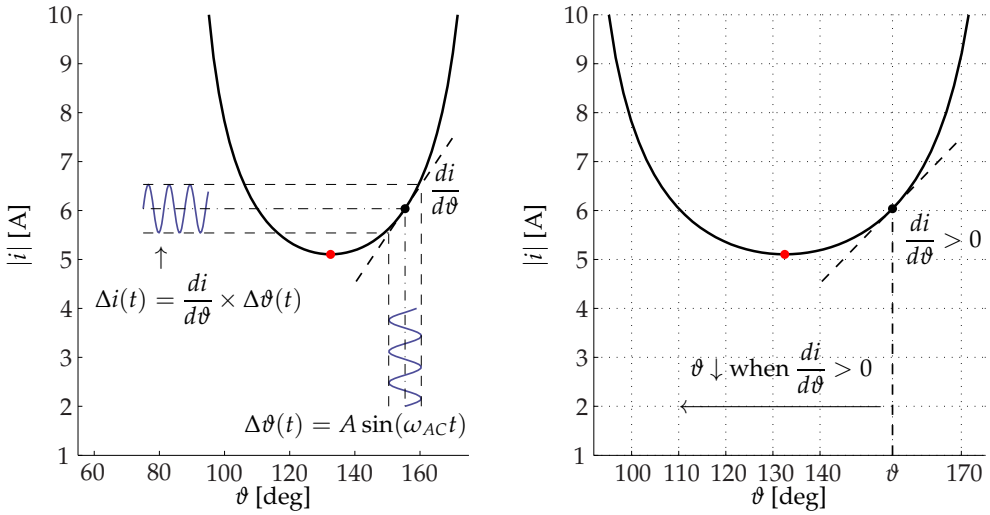

(a) *Sinusoidal current perturbation* (b) *Local gradient variation*

Fig. 2.4: Effects of the ESC perturbation technique expressed in dq plane, applied of the MTPA loci. Effect of the perturbation and equivalent local gradient movement.

parameters of the MTPA detector, rather than formally proving the capability of the proposed scheme to attain the MTPA operating point.

2.4.1 *Model linearization*

Stability and convergence (to the MTPA working point) properties of the proposed MTPA detector can be analysed using the same methods applied to standard perturbation-based extremum seeking controllers, such as those proposed in [36] (for local stability around the extremum point) and [38] (for semi-global practical stability).

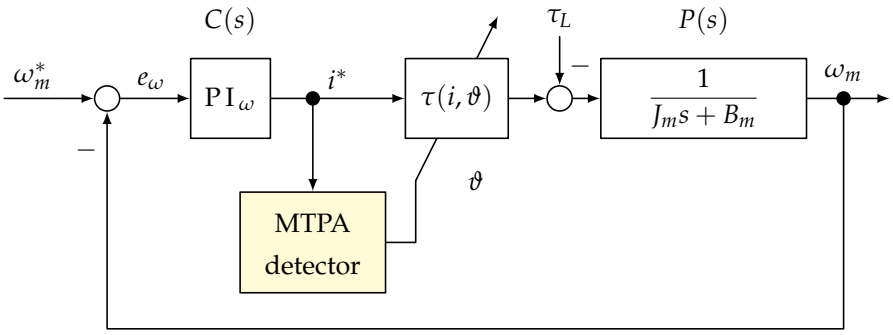

Fig. 2.5: Simplified model of the overall control system, used for the convergence analysis of the proposed MTPA-tracking control scheme.

The simplified analysis reported in this section is aimed to give some highlights on the operating principle of the MTPA detector and the effect of different choices of the design parameters, rather than providing a formal stability proof.
In order to ease the analysis, three simplifying assumptions are considered in the following:

1. the dynamics of the current loops in the overall control system of Fig.2.2 is sufficiently faster than the dynamics of the speed and MTPA-tracking control loops,

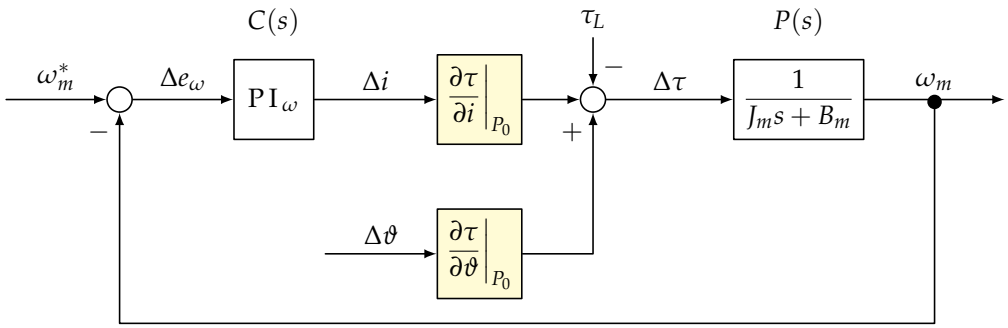

Fig. 2.6: Small-signal linearized dynamics of the speed control loop of the proposed ESC scheme about the operating point P_0.

and therefore it can be neglected. With reference to Fig.2.2, this assumption implies that the currents i_d and i_q are equal to their references i_d^* and i_q^*.

2. at steady state, the overall control system of Fig.2.2 operates in the 2$^{\text{nd}}$ quadrant of the $(i_d; i_q)$ plane. With reference to Fig.2.2, this assumption implies that $i^* = |i^*|$ and $\vartheta_i^* \in [\pi/2; \pi]$. Moreover, because of the previous assumption, it holds that

$$i = i^* = |i^*|\,, \qquad \vartheta_i = \vartheta_i^* = \beta + \pi/2 + d(t) \tag{2.14}$$

In the following, the symbol $\vartheta = \beta + \pi/2$ will be used to denote the unperturbed component of the phase ϑ_i.

3. only the integral action is considered in the PI_{MTPA} regulator of Fig.2.2, so that the updating law for β is

$$\frac{d\beta}{dt} = -\gamma\,\varepsilon_f\,, \qquad \gamma > 0 \tag{2.15}$$

The first assumption allows to approximate the overall system of Fig.2.2 with the simplified model of Fig.2.5, in which the block $\tau(i, \vartheta)$ denotes the mechanism of torque generation described by (2.11), expressed in rectangular coordinates.
Because of (2.11), the dynamics of the speed control loop in the simplified model is non-linear, but it can be linearised about an equilibrium state which is a steady state operating point of the control loop.
Among the infinite equilibrium states, related to the pairs (i, ϑ_i) that yield the same motor torque, the MTPA detector adaptively adjusts the phase ϑ_i to select the MTPA condition.
Let the set of equilibrium values associated to a generic equilibrium state be denoted by

$$P_0 \triangleq \left\{\omega_m = \omega_{m_0}, x_I = x_{I_0}, i = i_0, \vartheta = \vartheta_0, \tau_0 = \tau(i_0, \vartheta_0)\right\} \tag{2.16}$$

where x_I is the integrator state of the speed PI controller. Then, the linearisation of the simplified model about P_0 is

$$\begin{aligned} \Delta\tau &= J_m \frac{\Delta\omega_m}{dt} + B_m \Delta\omega_m \\ \Delta e_\omega &= \frac{\Delta x_I}{dt} \end{aligned} \tag{2.17}$$

with

$$\begin{aligned}\Delta e_\omega &= -\Delta\omega_m \\ \Delta i &= K_{P,\omega}\,\Delta e_\omega + K_{I,\omega}\,\Delta x_I \\ \Delta\tau &= \left.\frac{\partial\tau}{\partial i}\right|_{P_0}\Delta i + \left.\frac{\partial\tau}{\partial\vartheta}\right|_{P_0}\Delta\vartheta\end{aligned} \tag{2.18}$$

and where $\Delta\omega_m$, Δx_I, Δi, $\Delta\vartheta$, Δe_ω, $\Delta\tau$ denote small variations with respect to the equilibrium values (2.16), while $K_{P,\omega}$ and $K_{I,\omega}$ are the proportional and integral gains of the speed PI controller. The linearised model can be used to determine the (small) current perturbation Δi induced by a (small) phase perturbation $\Delta\vartheta$ around the equilibrium value. To this aim, the Transfer Function (TF) relating the two quantities is considered

$$W(s) \triangleq \frac{\Delta i(s)}{\Delta\vartheta(s)} = \underbrace{-\frac{\left(\left.\frac{\partial\tau}{\partial\vartheta}\right|_{P_0}\right)}{\left(\left.\frac{\partial\tau}{\partial i}\right|_{P_0}\right)}}_{=k}\ \underbrace{\frac{\left(\left.\frac{\partial\tau}{\partial i}\right|_{P_0}\right)P(s)C(s)}{1+\left(\left.\frac{\partial\tau}{\partial i}\right|_{P_0}\right)P(s)C(s)}}_{=G(s)} \tag{2.19}$$

It can be shown (similarly to (2.3) that the gain k is equal to the derivative of the current i with respect to the phase ϑ at the operating point P_0; it can be explicitly computed by resorting to (2.3) and (2.11)

$$k \triangleq \left.\frac{di}{d\vartheta}\right|_{P_0} = -\left.\frac{i\left[\Lambda_{mg}\cos\vartheta - i\chi L_d\cos 2\vartheta\right]}{\sin\vartheta\left[\Lambda_{mg} - 2i\chi L_d\cos\vartheta\right]}\right|_{P_0} \tag{2.20}$$

which it can be proved (by using the implicit function theorem) to be equal to the derivative of the current i with respect to the phase ϑ at the operating point P_0, namely $k = di/d\vartheta|_{P_0}$. In fact, by defining the following equivalent function:

$$f(i,\theta) = 0 \qquad \text{where} \qquad f(i,\theta) := \tau(i,\theta) - \tau \tag{2.21}$$

for a given τ, the previous equation implicitly defines a function of the type $i = g(\theta)$, withθ as the independent variable. For the *implicit function theorem*, it holds that

$$\left.\frac{dg}{d\theta}\right|_{P_0} = -\frac{\left.\frac{\partial f}{\partial\theta}\right|_{P_0}}{\left.\frac{\partial f}{\partial i}\right|_{P_0}} \tag{2.22}$$

Note that $\left.\frac{\partial f}{\partial\theta}\right|_{P_0} = \left.\frac{\partial\tau}{\partial\theta}\right|_{P_0}$ and $\left.\frac{\partial f}{\partial i}\right|_{P_0} = \left.\frac{\partial\tau}{\partial i}\right|_{P_0}$; therefore

$$\left.\frac{dg}{d\theta}\right|_{P_0} = -\frac{\left.\frac{\partial\tau}{\partial\theta}\right|_{P_0}}{\left.\frac{\partial\tau}{\partial i}\right|_{P_0}} \equiv k(P_0) \tag{2.23}$$

Neglecting the initial transient response, the small amplitude sinusoidal perturbation of (2.7) (with $\Delta\theta = \epsilon\sin(\omega t)$, with $\epsilon > 0$ a small constant), injected by the MTPA detector shown in Fig.2.2 at steady state produces the current perturbation

$$\Delta i(t) = k\,k_G\,A\,\sin\left(\omega_{AC}t + \varphi_G\right) \tag{2.24}$$

where $k_G = |G(j\omega_{AC})|$ and $\varphi_G = \angle G(j\omega_{AC})$.

2.4.2 *The MTPA operating point*

The current perturbation is actually the output of the HPF in the MTPA detector, apart of a possible attenuation $k_{HF} = |H_{HF}(j\omega_{AC})|$ and a phase lag $\varphi_{HF} = \angle H_{HF}(j\omega_{AC})$ introduced by the filter itself. Including both the attenuation and the phase lag of the HPF, the multiplier (i. e. mixer) output becomes

$$\begin{aligned}\varepsilon(t) &= \Delta i(t) \cdot \Delta\vartheta(t) \\ &= -\frac{1}{2} k_{HF}^2 \, k \, k_G \, A^2 \times \left[\cos\left(2\,\omega_{AC} t + \varphi_G + 2\,\varphi_{HF}\right) - \cos\varphi_G\right]\end{aligned} \tag{2.25}$$

Ideally, the harmonic component at twice the perturbation frequency is completely rejected by the LPF, so it holds that

$$\varepsilon_f(t) = \frac{1}{2} k_{HF}^2 \, A^2 \, k \, k_G \cos\varphi_G \tag{2.26}$$

Because of (2.20), the LPF output is proportional, to the derivative $di/d\vartheta|_{P_0}$.
The term $(1/2)\, k_{HF}^2 \, A^2 \, k_G \cos\varphi_G$ being the proportionality constant. If such constant is different from zero for any admissible phase ϑ, which happens only if

$$\Re\left[G(j\omega_{AC})\right] = k_G \cos\varphi_G \neq 0 \tag{2.27}$$

where $\Re(\cdot)$ denotes the real part, then the convergence of ε_f to zero implies that the system converges at an operating point P^* where $di/d\vartheta|_{P^*} = 0$, i. e. a stationary point of the function $i(\vartheta)$.
This point is actually a minimum, because the function $i(\vartheta)$ is convex: in fact, by differentiation of (2.20), it follows that:

$$\begin{aligned}\frac{d^2 i}{d\vartheta^2} = \frac{i \, \csc^2\vartheta}{(\Lambda_{mg} - 2\kappa\cos\vartheta)^3} \Big[&-\kappa^3 (5 + \cos 4\vartheta)\cos\vartheta + \cdots \\ &\cdots + \frac{1}{2}\kappa^2 \Lambda_{mg} \left(13 + 8\cos\vartheta + 3\cos 4\vartheta\right) - \cdots \\ &\cdots - \kappa\Lambda_{mg}^2 (5 + 3\cos 2\vartheta)\cos\vartheta + \Lambda_{mg}^3 \left(1 + \cos^2\vartheta\right)\Big]\end{aligned} \tag{2.28}$$

where $\kappa = i\chi L_d$.
According to assumption 2, which states that the system operates in the 2nd quadrant of the $(i_d; i_q)$ plane (i. e. $\theta^* \in [\pi/2; \pi]$) and $L_d < L_q$, it is immediate to verify that $d^2 i/d\vartheta^2 > 0$ for any admissible current phase $\vartheta \in [\pi/2; \pi]$ (in the range of interest), i. e. the function $i(\vartheta)$ is convex.

2.4.3 *Convergence to the MTPA operating condition*

To verify that $\varepsilon_f(t)$ actually converges to zero, the following quadratic Lyapunov function candidate is considered

$$V(t) = \frac{1}{2}\left(\varepsilon_f(t)\right)^2 \tag{2.29}$$

By applying the composition rule and equations (2.15) and (2.26), the time derivative of (2.29) is equal to

$$\frac{dV}{dt} = \frac{dV}{d\varepsilon_f}\frac{d\varepsilon_f}{d\beta}\frac{d\beta}{dt} = -\gamma\,\varepsilon_f^2\,\frac{1}{2}\,k_{HF}^2\,A^2\,\frac{d}{d\beta}(k\,k_G\cos\varphi_G) \tag{2.30}$$

If the condition

$$\frac{d}{d\beta}\Re\left[W(j\omega_{AC})\right] = \frac{d}{d\beta}(k\,k_G\cos\varphi_G) > 0 \tag{2.31}$$

holds for any admissible value of the phase ϑ, then $dV/dt < 0$, then ε_f converges asymptotically to zero, for the Lyapunov's stability theorem [39].
In general, the conditions (2.27) and (2.31) are difficult to prove, because of their involved expressions. Nevertheless, they can be verified numerically, by using the nominal motor parameters and different values of the steady state motor torque; results are shown in Fig.2.7.
It can be noticed that both (2.27) and (2.31) hold, which implies the convergence of the system to the MTPA condition. Since (2.31) is always positive, then it is verified that ε_f converges asymptotically to zero; moreover, since (2.27) is always different from zero, then the the convergence of ε_f to zero implies the convergence of the system to the MTPA condition.
The previous analysis can be further extended to infer about the convergence rate of the control system to the MTPA operating point. In fact, by using (2.30) and by observing that (2.31) is always lower bounded by a positive constant (as prove by Fig.2.7 for two different machines), and then:

$$\frac{dV}{dt} < -m\,\gamma\,A^2\,\frac{1}{2}\varepsilon_f^2 = -m\,\gamma\,A^2\,V \tag{2.32}$$

where

$$m = k_{HF}^2 \min_{\vartheta}\left[\frac{d}{d\beta}\Re\left[W(j\omega_{AC}]\right)\right] > 0 \tag{2.33}$$

By the comparison lemma [39], from (2.32) it follows that

$$V(t) < V(t_0)\,e^{-m\gamma A^2(t-t_0)} \tag{2.34}$$

and then, by (2.29),

$$|\varepsilon_f(t)| < |\varepsilon_f(t_0)|\,e^{-(1/2)\,m\gamma A^2(t-t_0)} \tag{2.35}$$

Therefore, the required time $T = t - t_0$ for $|\varepsilon_f|$ to be less than a specified value $\bar{\varepsilon}_f > 0$ has the following upper bound

$$\bar{T} = -\frac{2}{m\gamma A^2}\log\frac{\bar{\varepsilon}_f}{|\varepsilon_f(0)|} \tag{2.36}$$

Note that such time is inversely proportional to the value of the product γA^2, which is related to the design parameters A and γ of the MTPA detector. The remaining parameter m in (2.36) depends only on the motor and speed controller characteristics, and can be computed independently of the design of the MTPA-tracking controller. To appreciate the effective validity of the method above mentioned, in the experimental section Sec.

2.7 of this chapter will be presented a series of experimental results and validation tests to demonstrate the practical feasibility of the proposed solution.
In Tab.2.4 are summarized the results of the comparison between the experimental convergence times (as the time required for the MTPA integrator output β to reach the 90% of its final value) and its theoretical upper bound, evaluated with (2.36) directly on the experimental test bench.
The experimental validation have been repeated for several values of the integral gain γ in the MTPA detector, while the amplitude A of the phase perturbation was kept constant, in order to prove the practical feasibility of (2.36).

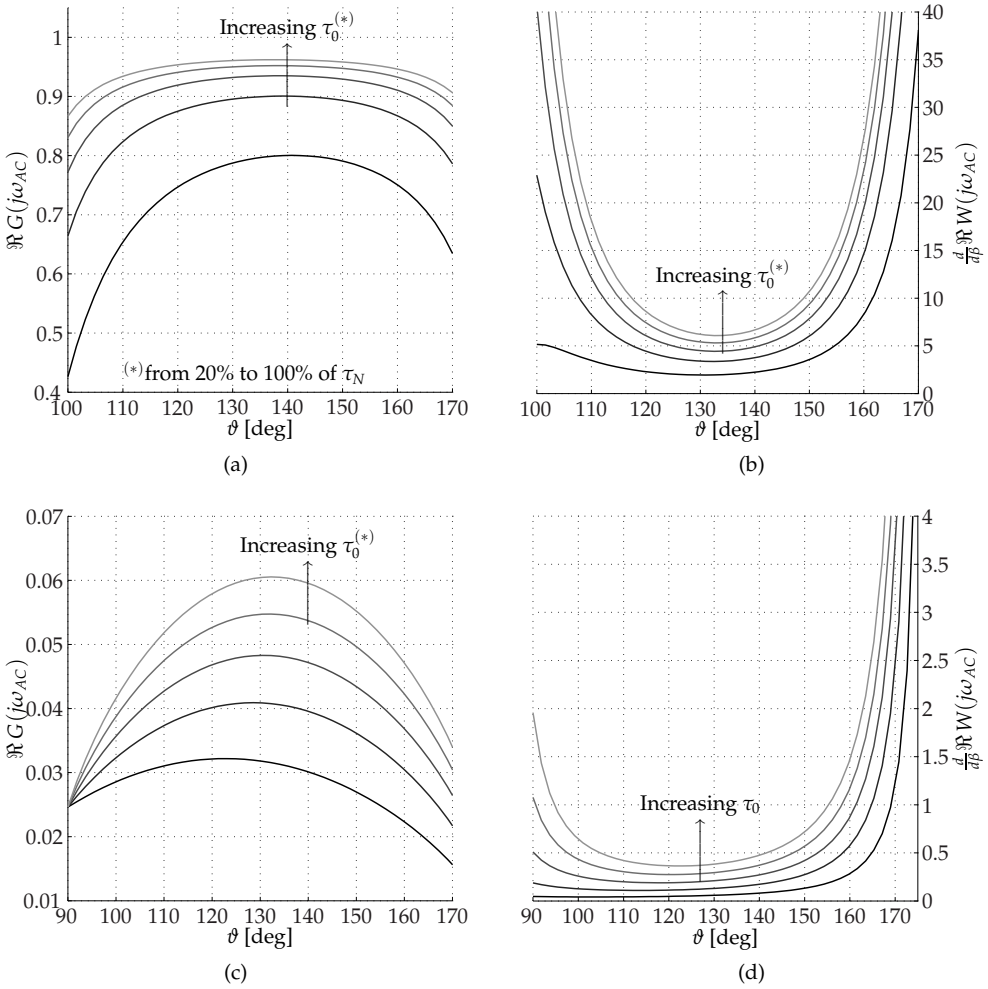

Fig. 2.7: Plots of $\frac{d}{d\beta}\Re\, G(j\omega_{AC})$ and $\Re\, W(j\omega_{AC})$ as ϑ varies within the range $]\pi/2;\pi[$. Plots refer to the nominal values of the motor parameters for the motor in Tab.2.1 and Tab.2.2.

2.5 PARAMETRIC AND SENSITIVITY ANALYSIS

From an industrial perspective, it is relevant to investigate the robustness of the MTPA-tracking algorithm against variations of the magnetic parameters, namely the PM rotor flux linkage Λ_{mg} and the inductance ratio L_q/L_d. In particular, it is important to understand what are the ranges of variation that the control system can tolerate, while

still guaranteeing the attainment of the MTPA condition with a satisfactory convergence time.
For such purpose, it is sufficient to analyse how the two quantities (2.27) and (2.31) are affected by such parametric variations, since both the convergence property and the convergence rate depend on them. With respect to the nominal values reported in Tab.2.1, the following parametric variations have been considered

$$\Lambda_{mg}/\Lambda_{mgN} \in [0.5;\, 1.5]\,, \qquad L_q/L_{dN} \in [2;\, 10] \tag{2.37}$$

where Λ_{mgN} and L_{dN} denotes the nominal values of the parameters. Within these parametric uncertainty intervals, it has been verified that (2.27) is always strictly positive (i. e. different from zero), as reported in Fig.2.7.
The influence of the parametric variations of (2.37) (occurring not simultaneously) on the quantity

$$\min_{\vartheta \in I_\vartheta} \left\{ \frac{d}{d\beta} \Re\left[W(j\omega_{AC}) \right] \right\} \tag{2.38}$$

when $I_\vartheta =]\pi/2; \pi[$ (i. e. for all the admissible operating points within the 2$^{\text{nd}}$ quadrant of the dq plane) is shown in Fig.2.8.
Fig.2.8 demonstrates that (2.38) is always positive, then, according to the results of Sec. 2.4, it is guaranteed that the convergence property to the MTPA condition is robust against the parametric variations (2.37). This is verified except for small values of the saliency ratio ξ, for which a small value of the steady state torque τ_0 may yield a negative value of (2.38). Therefore, at least for a saliency ratio approximately $\xi = L_q/L_d > 4.5 \div 5$ it is guaranteed that the convergence property to the MTPA condition (Fig.2.8b and Fig.2.8d) is robust against the parametric variations of (2.37). Moreover, since the upper bound (2.36) of the convergence time is inversely proportional to (2.38), it is expected that the convergence rate slows down for either large values of the PM flux linkage Λ_{mg}, or small values of the saliency ratio ξ.
Alternatively, the robustness of the proposed control structure can be analysed in terms of sensitivity function, by defining as $W(s;\alpha)$ the TF depending on the model parameter $\alpha \in \mathbb{R}^4$.
Regarding the automatic MTPA tracking controller structure, the problem of evaluating the sensitivity of the amplitude of the current perturbation to variations of the motor parameters Λ_{mg} and $\chi = \dfrac{L_q - L_d}{L_d}$ is now reconsidered. By denoting with $W(s;\Lambda_{mg},\chi)$ the transfer function from the input phase perturbation $\Delta\theta$ to the current magnitude output perturbation Δi; such transfer function depends on the particular working point of the outer speed control loop, and on the motor parameters Λ_{mg} and χ.

4 The *sensitivity* function of $W(s;\alpha)$ to variations of α with respect of its nominal value α_n is defined as the ratio of the percentage change of $W(s;\alpha)$ to a percentage change in α

$$S_\alpha^W(s) = \lim_{\Delta\alpha \to 0} \frac{\dfrac{\Delta W(s;\alpha)}{W(s;\alpha_n)}}{\dfrac{\Delta\alpha}{\alpha_n}} = \frac{\alpha_n}{W(s;\alpha_n)} \frac{\partial W(s;\alpha)}{\partial \alpha}\bigg|_{\alpha=\alpha_n} \tag{2.39}$$

where, for a sufficient small amplitude of $\Delta\alpha$ it follows that:

$$\Delta W(s;\alpha) \approx W(s;\alpha_n)\, S_\alpha^W(s)\, \frac{\Delta\alpha}{\alpha_n} \tag{2.40}$$

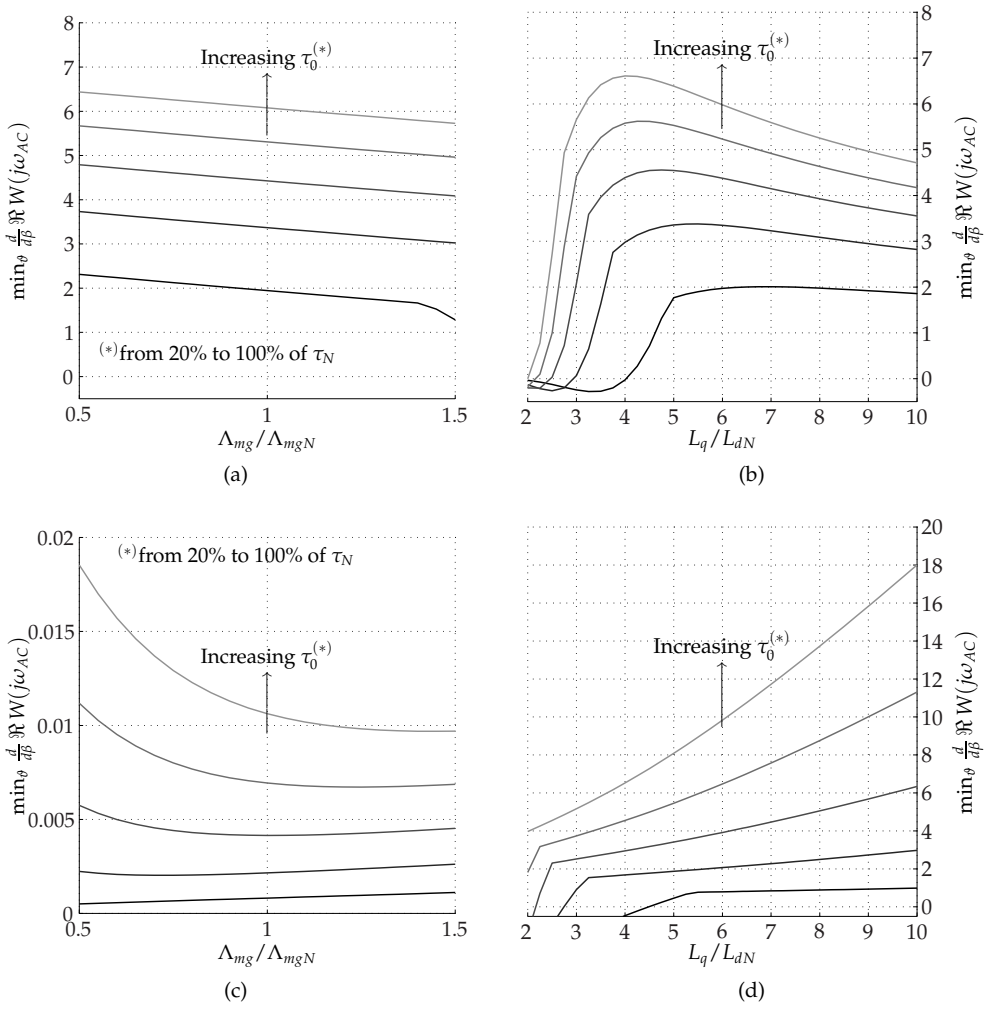

Fig. 2.8: Plots of $\min_\vartheta \dfrac{d}{d\beta} \Re\left[W(j\omega_{AC})\right]$ vs. variations of the motor parameters Λ_{mg} (left plot, with nominal L_q and L_d) and L_q/L_d (right plot, with nominal Λ_{mg}) for the motor in Tab.2.1 (a) - (b) and Tab.2.2 (c) - (d).

From the definition, the couple of sensitivity functions $S^W_{\Lambda_{mg}}(s)$ and $S^W_\chi(s)$ are defined, with respect of (2.19), as:

$$\begin{aligned} S^W_{\Lambda_{mg}}(s) &= \frac{\Lambda_{mgN}}{W(s;\Lambda_{mgN})} \frac{\partial W(s;\Lambda_{mg})}{\partial \Lambda_{mg}}\bigg|_{\Lambda_{mg}=\Lambda_{mgN}} \\ S^W_\chi(s) &= \frac{\chi_N}{W(s;\chi_N)} \frac{\partial W(s;\chi)}{\partial \chi}\bigg|_{\chi=\chi_N} \end{aligned} \tag{2.41}$$

and calculated analytically although their expression is complicated and unnecessary for the purposes of this paragraph.
Their knowledge allows to evaluate numerically the (percentage) variations of the amplitude of the current perturbation Δi due to small (percentage) variations of the parameters Λ_{mg} and χ, under the assumption of a sinusoidal input perturbation $\Delta i(t) = A\sin(\omega_{AC}t)$ in the control loop. From (2.40) and (2.19) it follows that

$$\begin{aligned}\Delta_{\Lambda_{mg}}(A_{\Delta i}) &\approx \left|W(j\omega_{AC};\Lambda_{mgN},\chi_N)\, S^W_{\Lambda_{mg}}(j\omega_{AC})\right| A\,\frac{\Delta\Lambda_{mg}}{\Lambda_{mgN}}\\ \Delta_{\chi}(A_{\Delta i}) &\approx \left|W(j\omega_{AC};\Lambda_{mgN},\chi_N)\, S^W_{\chi}(j\omega_{AC})\right| A\,\frac{\Delta\chi}{\chi_N}\end{aligned} \tag{2.42}$$

where $\Delta_{\Lambda_{mg}}(A_{\Delta i})$ and $\Delta_{\chi}(A_{\Delta i})$ denote the variations of the amplitude $A_{\Delta i}$ of the (sinusoidal) current perturbation Δi to, respectively, the variations of Λ_{mg} and χ.

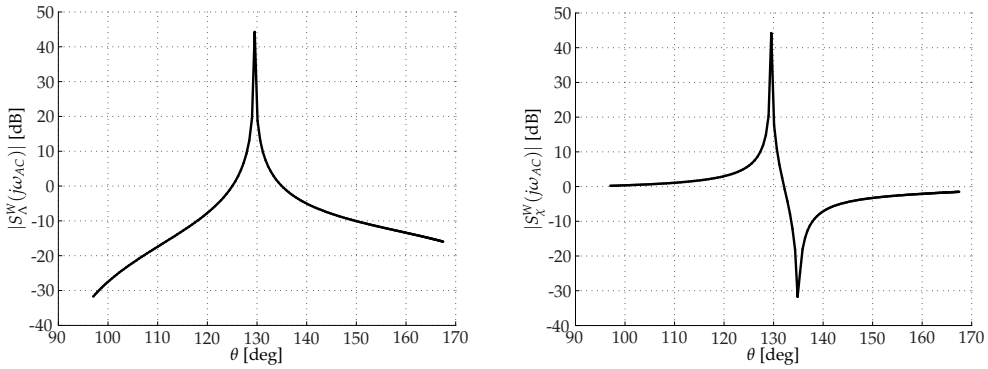

(a) $S^W_{\Lambda_{mg}}(j\omega_{AC})$ (b) $S^W_{\chi}(j\omega_{AC})$

Fig. 2.9: Magnitude of the sensitivity functions $S^W_{\Lambda_{mg}}(j\omega_{AC})$ and $S^W_{\chi}(j\omega_{AC})$ vs. steady state current phase angle θ for the machine of Tab.2.1 and a motor torque of $\tau_0 = \tau_N/2$ [Nm]

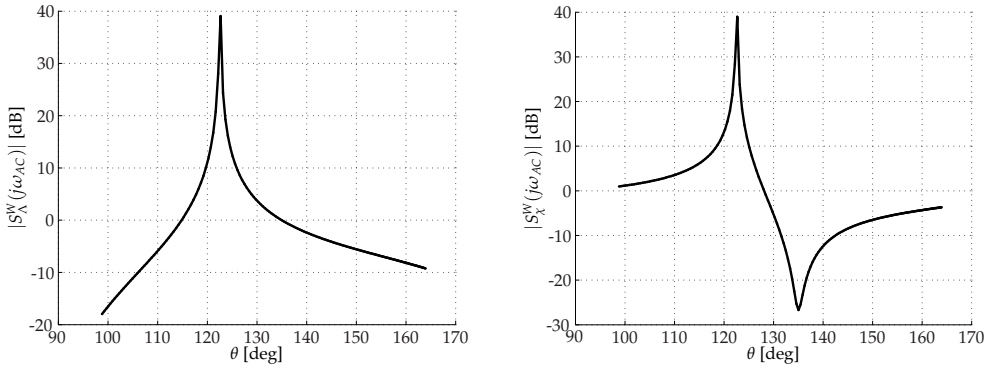

(a) $S^W_{\Lambda_{mg}}(j\omega_{AC})$ (b) $S^W_{\chi}(j\omega_{AC})$

Fig. 2.10: Magnitude of the sensitivity functions $S^W_{\Lambda_{mg}}(j\omega_{AC})$ and $S^W_{\chi}(j\omega_{AC})$ vs. steady state current phase angle θ for the machine of Tab.2.2 and a motor torque of $\tau_0 = \tau_N/2$ [Nm]

Fig.2.9 and Fig.2.10 report the numerical plots of the normalized amplitude of the two sensitivity functions $S^W_{\Lambda_{mg}}(j\omega_{AC})$ and $S^W_{\chi}(j\omega_{AC})$ considering the motor data ofTab.2.1 and Tab.2.2 and a constant torque $\tau_0 = \tau_N/2$.
In particular, it is evident that the maximum sensitivity is always in correspondence of the MTPA angle (β_{MTPA}), meaning that the effects of the parameter variations of Λ_{mg} and χ have their maximum effect exactly in the tracking of the MTPA operating point with respect of a small variation of $A_{\Delta i}$ on the control loop.
Equivalent results and considerations can be achieved by considering the previous problem in terms of additive and multiplicative uncertainties of the transfer function

$W(s;\Lambda_{mg},\chi)$ caused by variations of the parameters Λ_{mg} and χ around their nominal values Λ_{mgN} and χ_N.
With reference to the linearised model of the speed control loop in fact, $W(s;\Lambda_{mg},\chi)$ denotes the TF from the input phase perturbation $\Delta\theta$ to the current magnitude output perturbation Δi; and such transfer function depends on the particular working point of the outer speed control loop, and on the motor parameters Λ_{mg} and χ. By considering and additive uncertainty defined as:

$$\Delta W(s;\Lambda_{mg},\chi) \triangleq W(s;\Lambda_{mg},\chi) - W(s;\Lambda_{mgN},\chi_N) \tag{2.43}$$

and multiplicative uncertainty:

$$\frac{\Delta W(s;\Lambda_{mg},\chi)}{W(s;\Lambda_{mgN},\chi_N)} = \frac{W(s;\Lambda_{mg},\chi)}{W(s;\Lambda_{mgN},\chi_N)} - 1 \tag{2.44}$$

with $\Lambda_{mgN} \in \left[\Lambda_{mg_{\min}};\Lambda_{mg_{\max}}\right]$ and $\chi \in [\chi_{\min};\chi_{\max}]$, the plots in Fig.2.11 and Fig.2.12 show the magnitude of the additive and multiplicative uncertainties evaluated at the frequency ω_{AC} of the input phase perturbation (for the sake of compactness only the motor in Tab.2.1 is considered). The numerical values vary with the working point of the control system, i. e. the current phase θ, and with the particular choice of the motor parameters Λ_{mg} and χ. As expected, the maximum variation is always in correspondence of the MTPA operating point, and this means that the parameter sensitivity of the proposed control action is more relevant in the optimum point.

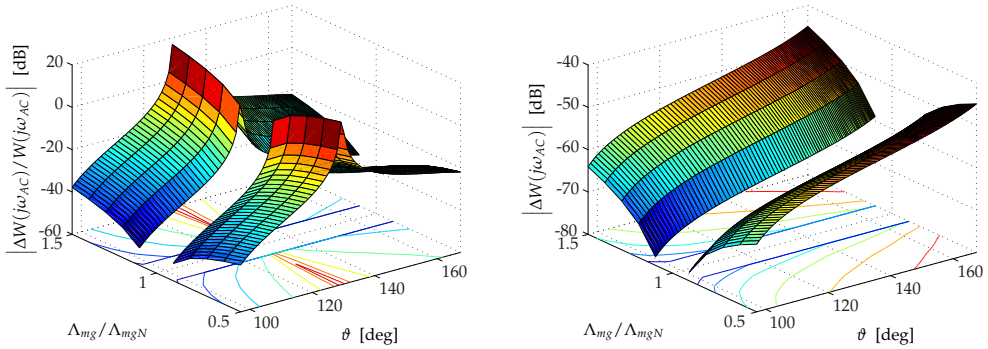

(a) (b)

Fig. 2.11: Magnitude of the multiplicative (left) and additive (right) uncertainties of $W(s;\Lambda_{mg},\chi)$ due to variations of Λ_{mg}, when χ is equal to its nominal value χ_N. for the machine of Tab.2.1

2.6 SIMULATION RESULTS

The aim of this section is to prove the feasibility of the proposed MTPA-tracking algorithm in the Matlab/Simulink simulation environment, by simulating the whole modified FOC drive system refined and completed with the devices illustrated in Sec. 2.6.2. The control algorithm has been written in equivalent C code for the sake of portability (the same code was used for the experimental tests in the dSPACE platform), and a non-linear model of the motor has been adopted insted of the canonical linear approximation. In particular, to emulate the real dynamic of the PMSM-IPM, the non-linear model of Fig.1.7 has been used. The main parameters of the motor and load used for simulations are reported in Tab. 2.1 and Tab.2.2.

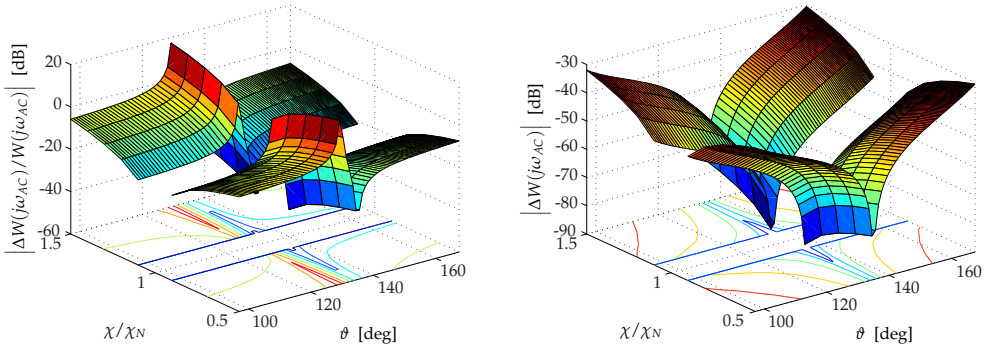

Fig. 2.12: Magnitude of the multiplicative (left) and additive (right) uncertainties of $W(s;\Lambda_{mg},\chi)$ due to variations of χ, when Λ_{mg} is equal to its nominal value Λ_{mgN} for the machine of Tab.2.1

Tab. 2.1: Anisotropic PM synchronous motor $PMSM_2$ parameters

Parameter	**Value**
Nominal ph-ph voltage U_N	400 Veff
Rated current I_N	4 Aeff
Pole pairs p	2
Saliency ratio $\xi = L_q/L_d$	5.8
PM flux linkage Λ_{mg}	0.175 Vs
Rotor Inertia J_m	0.00156 kgm^2
Viscous friction B_m	0.0012 Nms

Tab. 2.2: Anisotropic PM synchronous motor $PMSM_3$ parameters

Parameter	**Value**
Nominal ph-ph voltage U_N	400 Veff
Rated current I_N	5 Aeff
Pole pairs p	2
Saliency ratio $\xi = L_q/L_d$	7.5
PM flux linkage Λ_{mg}	0.28 Vs
Rotor inertia J_m	0.002 kgm^2
Viscous friction B_m	0.0024 Nms

A decoupling and *bemf* feedforward action were included in the current control loops, and the PI regulators were tuned for a bandwidth of about $\approx$ 600 Hz (the alternative calibration method used in the control scheme is briefly summarized in Sec. 2.6.1). The control parameters used in simulation are the same used in the following experimental tests (Sec. 2.7), and their numerical values are collected in Tab. 2.3. Different operating conditions were simulated, while the system is started up without any knowledge of the actual angular compensation β, that is equal of zero at the beginning of the control action.

Fig.2.13 reports the current phase ϑ_i^* and the direct and quadrature currents i_d and i_q when the system is working at constant speed but and variable load torque. Specifically, the load torque was subjected to successive equal step variations from 0 to τ_N at equal steps of $\tau_N/5$ (Fig.2.13a), while the speed was maintenance constant at his reference value of $\omega_m^* = 500\,\text{rpm}$, as reported in Fig.2.13b.
After the first tracking transient, the actual steady-state MTPA operating condition (β_{MTPA}) is always reached in correspondence of each successive torque variation while a low and smooth speed variation appears.

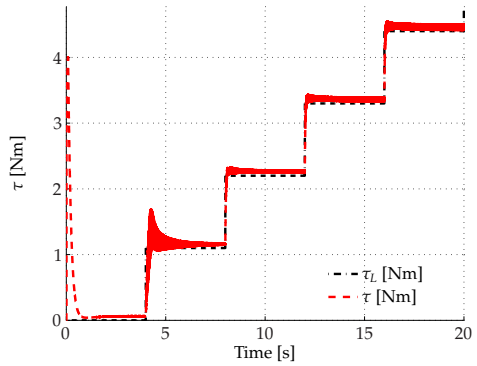

(a) *Different load torque τ_L steps.*

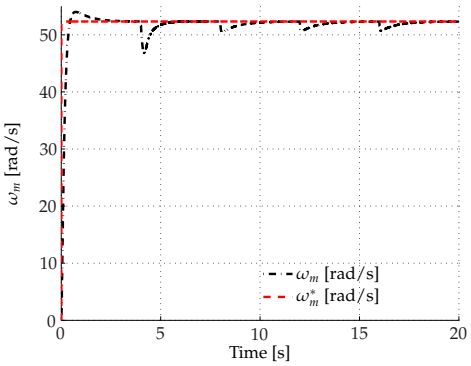

(b) *Fixed speed ω_m during the transients.*

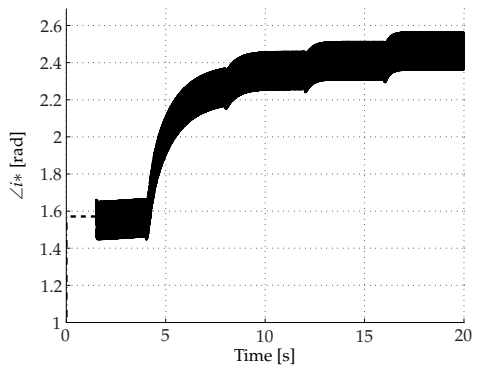

(c) *Phase variation ϑ_i^* in MTPA condition.*

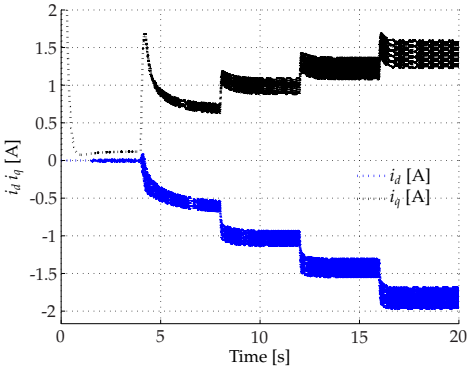

(d) *Current phase ϑ_i^* and resulting currents (i_d, i_q) during the transients.*

Fig. 2.13: Torque, speed and current during load torque transients for the machine in Tab. 2.1.

The enable mechanism described in Sec. 2.6.2 makes the tracking algorithm work properly in a broad range of load conditions. The algorithm takes also advantage from the maintenance of the previous phase β during the successive transients, which are very short for reduced torque changes.
This means that only during the first torque variation the angle β has to move of several degrees from the FOC condition to the MTPA operating condition, while the maintenance of the previous optimal angle leads to a quick and smooth variation (equivalently a reduction in the torque oscillation) after the successive steps. Other batches of simulations have confirmed perfect tracking also in case of sinusoidal load torque variations within the bandwidth of the speed loop, as reported in Fig.2.14. The load torque sinusoidal perturbation is equal of $20\%B_\omega$.
The possibility given by the convergence analysis of 2.4.1 to skip manual settings will be proved with a series of experimental validations, while the simulations here described are only the starting point for an extensive analysis of the overall control architecture.

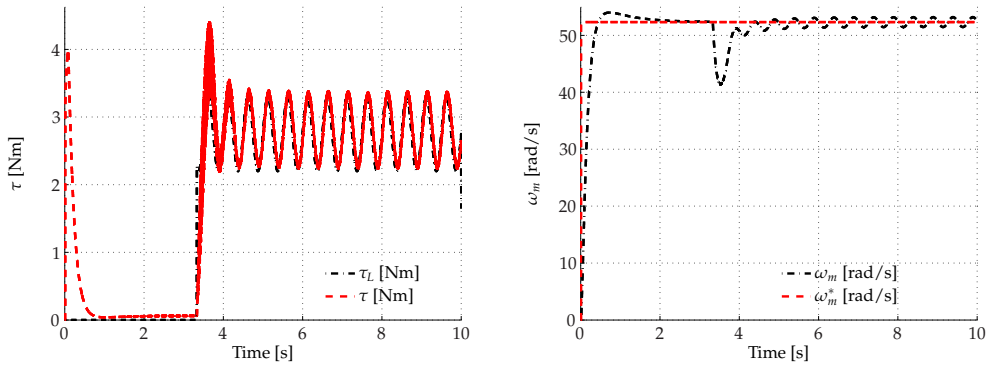

(a) τ_L *perturbation.*

(b) *Fixed speed* ω_m *during the transients.*

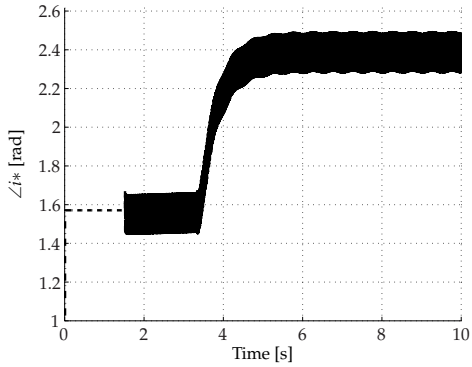

(c) *Phase variation* ϑ_i^* *in MTPA condition.*

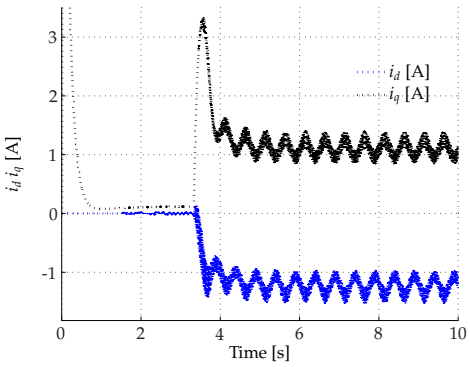

(d) *Current phase* ϑ_i^* *and resulting currents* (i_d, i_q) *during the load torque variation.*

Fig. 2.14: Torque, speed and current during the sinusoidal load torque perturbation (20%B_ω) for the machine in Tab. 2.1.

2.6.1 *Tuning of the current loops*

In order to maintain a direct correspondence between simulations and experimental implementation, the decoupling action is considered into the control scheme.
It leads to a simplification into design strategy of the current PI controls, and so, to calibrate the current control loops a different approach has been adopted instead of the canonical tuning techniques, based on the synthesis in frequency according to the method of the phase margin.
The coupling terms $\omega_{me} L_q i_q$ and $\omega_{me} L_d i_d + \omega_{me} \Lambda_{mg}$ disappear if a decoupling action in inserted in the control scheme, and the voltage balance equations (1.26) becomes:

$$\begin{cases} u_d = R_s i_d + L_d \dfrac{di_d}{dt} \\ u_q = R_s i_q + L_q \dfrac{di_q}{dt} \end{cases} \tag{2.45}$$

By applying the Laplace transformation of both sides of (2.45) (the upper-case letters indicate the Laplace transform variable), the s-domain voltage balance is:

$$\begin{cases} I_d(s) = \mathcal{L}\left(i_d\right) = \dfrac{U_d(s)}{R_s + sL_d} \\ I_q(s) = \mathcal{L}\left(i_q\right) = \dfrac{U_q(s)}{R_s + sL_q} \end{cases} \tag{2.46}$$

Solving the (2.46) as a function of $I_d(s)$ and $I_q(s)$ gives the TF between currents and voltages among the d-axis and q-axis. Since the dynamics of the d-axis has the same behaviour of the q-axis as direct consequence of the decoupling terms, the TF which links the current error $E_d(s)$ and the corresponding value of $I_d(s)$ (assuming that the regulator has a simple PI controller, expressed as $\dfrac{sk_{pd} + k_{id}}{s}$) is:

$$L_d(s) = \frac{I_d(s)}{E_d(s)} = \frac{sk_{pd} + k_{id}}{s} \frac{1}{R_s + sL_d} \tag{2.47}$$

By imposing the condition of unitary amplitude of the function $L_d(s)$ at ω_i ($|L_d(j\omega_i)| = 1$, where $\omega_i = 2\pi B_{HZi}$ and B_{HZi} indicates the bandwidth desired for the current loop), follows that:

$$\begin{aligned} |L_d(j\omega_i)| = 1 &\Leftrightarrow k_{id}^2 + \omega_i^2 k_{pd}^2 = \omega_i^2 R_s + \omega_i^4 L_d^2 \\ &\Leftrightarrow L_d^2\omega_i^4 + (R_s^2 - k_{pd}^2)\omega_i^2 - k_{id}^2 = 0 \end{aligned} \tag{2.48}$$

In order to obtain (2.48) equal of zero, $k_{pd} = L_d\omega_i$ e $k_{id} = R\omega_i$ and the phase of (2.47) is $\angle L_d(j\omega_i) = \angle 1/j = \pi/2\,\text{rad}$. The phase margin of the system in this condition is $m_\Phi = 90\,\text{deg}$, and therefore the dynamic of the system can be considered as that of a first order system. The same procedure can be applied to tune the q-axis PI regulator. Reiterating the procedure at the second of (2.46), the gain for the q branch are: $k_{pq} = L_q\omega_i$ and $k_{iq} = R\omega_i$.

2.6.2 *MTPA enable mechanism*

The proposed on-line adaptive MTPA techniques is based on a cause-and-effect mechanism, and if external factors, as load or speed reference variations interfere with the minimizing variable, the algorithm convergences could be corrupted. Moreover, in a PMSM-IPM motor the high value of the inductance L_q with respect to the L_d one, may easily lead to a saturation of the voltage demand by the current regulators, causing a significant slowdown in the current response due to a reduction of the stability margin and the current perturbation injected with the purpose of tracking the MTPA point definitely produce an extra Joule losses in the motor stator windings. For these reasons, it is possible to devise an enabling mechanism to be added to overall control scheme of Fig.2.2 that turns *ON* the MTPA tracking controller once an almost steady state condition is reached (both on the speed and on the load torque), and that turns it off again when the MTPA operating point is reached.
In this way, the extra Joule losses due to the current perturbation eventually occurs only for the time required by the extremum seeking controller to seek for the MTPA operating condition.
It is obvious that the steady-state identification must be automatic, and a rough-and-ready solution is to monitor the speed error $err_\omega = \omega_m^* - \omega_m$, as a variable to switch the control operation to "MTPA OFF" to "MTPA ON". It has been found that the mechanism

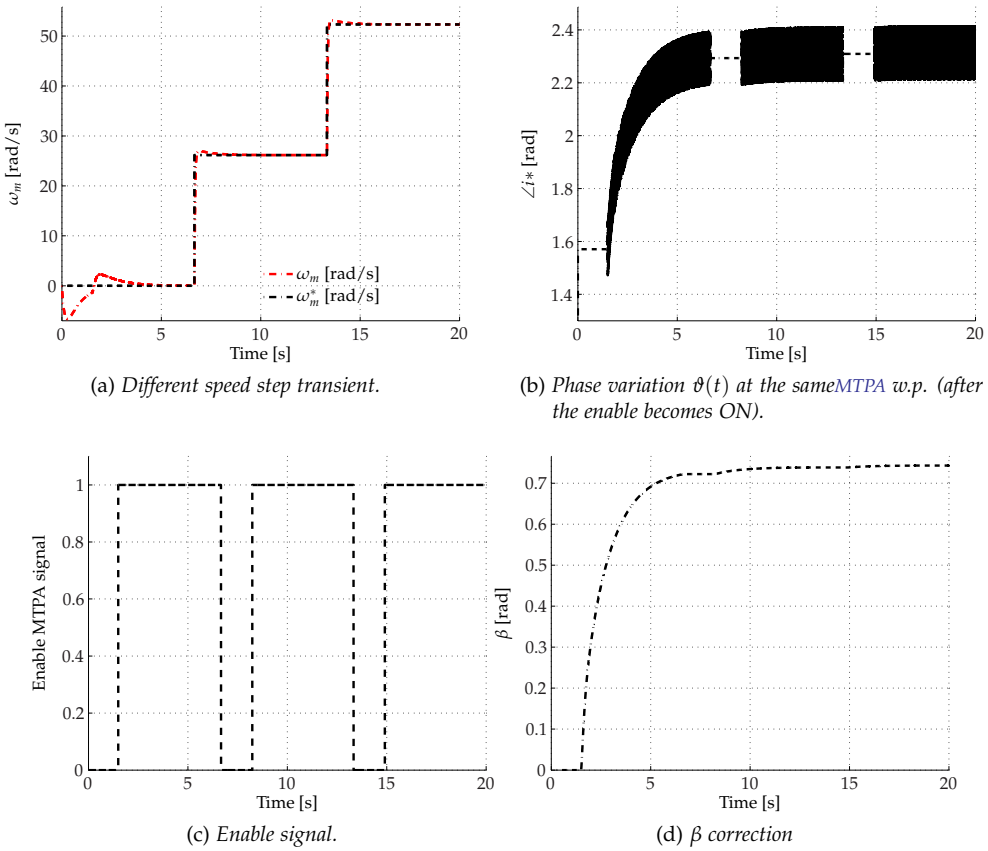

(a) *Different speed step transient.*

(b) *Phase variation $\vartheta(t)$ at the sameMTPA w.p. (after the enable becomes ON).*

(c) *Enable signal.*

(d) *β correction*

Fig. 2.15: Speed response, phase correction and enable signal behaviour following repeated step-changes of the speed reference (constant load torque $\tau_L = \tau_N/3$; injected signal $\Delta\vartheta(t) = Asin(\omega_{AC}t)$ with $A = 0.1$ rad.el., $\omega_{AC} = 2\pi 110$ rad.el/s). Test conduced with the machine in Tab. 2.1.

quality is quite improved when err_ω is filtered by using a band-limited high pass filter, so that the output includes a rough approximation of the load torque. The suggested TF is:

$$W_{hf}(s) = k_{hf}\frac{J_m(1+s\hat{\tau}_m)}{\left(1+s\tau_{hf}\right)^2} \tag{2.49}$$

The zero is designed to compensate as much as possible the mechanical pole $s = -1/\tau_m$, using the best available guess $\hat{\tau}_m$ of the mechanical time constant, while the double pole is placed at a frequency $1/(2\pi\tau_{hf})$ as high as possible, consistent with the sensitivity to the disturbances superposed to the speed measurement. The constant k_{hf} is selected to have a unity gain at low frequency.
When the output of (2.49) remains within the predefined limits (here, fixed to $\pm 3\%$ of the nominal speed) for a suitable time (in the present case, about $50/B_\omega$, where B_ω denotes the speed loop bandwidth), the enable to MTPA algorithm is activated. Just after a MTPA disable, due for example to a change in the speed reference, the input of the integrator PI_{MTPA} is reset and hooked to zero until next enable. Meanwhile, the last value of the phase correction β is frozen and used during the whole transient. It has been found that this simple solution shortens the convergence to the new working point and it also plays a stabilising rule after MTPA reactivations.

Fig.2.15 shows the behaviour of the enable signal in the presence of repeated step-changes of the speed reference. The same figure shows the phase correction β issued by the tracking algorithm, by using the machine in Tab. 2.1.

2.7 EXPERIMENTAL RESULTS

The experimental test bench used for test the studied algorithm was equipped with a Fast Control Prototyping (FCP) dSpace DS1104 R&D controller board, with two DSPs in a master and slave configuration.
The master processor (PowerPC 603e at 250 MHz) calculates the main operations of the control algorithm, while a slave processor (Texas Instruments TMS320F240 fixed point unit at 20 MHz) manages only the PWM routine and the I/O interfacing with the actual speed and current measurements.

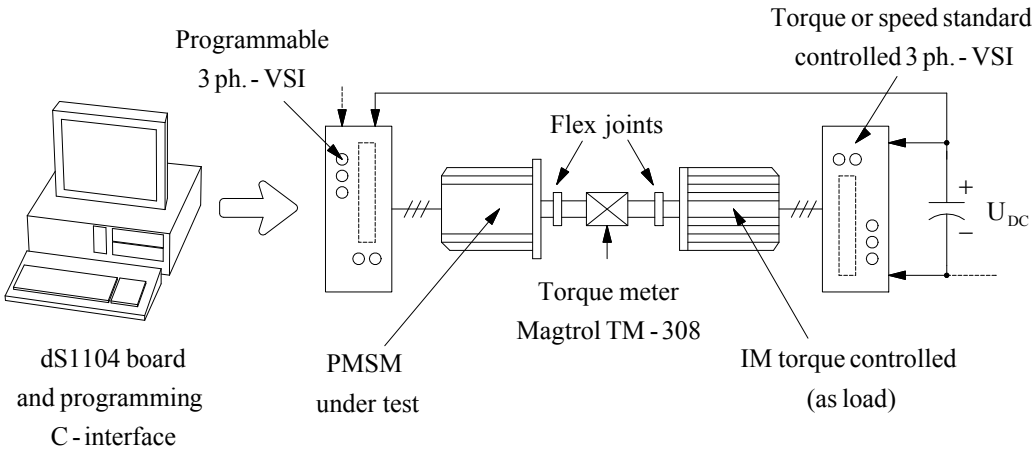

Fig. 2.16: Sketch of the experimental test bench.

Although Simulink models can be compiled and downloaded directly on the dSPACE DS1104 R&D controller board, this rapid solution has the disadvantage to lose the control of the generated code that could lead to unexpected errors. By writing the entire control routine in C code this problem can be overcome.
The MTPA routine has been merged into a conventional dSPACE FOC scheme, that is not described and reported in detail, but a brief general description of the control programming architecture is reported.
The code is structured so that all the calculation are performed during a PWM interrupt routine that calls the macro-C instructions, where are stored the different sub-routines of the algorithm. The main program initialization that calls the PWM interrupt routine is necessary for the DSP card, in order to define the communication between master and slave, digital I/O assignments and converter initialization.
At the beginning, all the A/D converters are started at the same time, and according to the scale factors associated to the current measuring, the current value is acquired at the start of the PWM period. This current measurement is then compared with the current limits of the inverter. If the bounds are respected, the inverter is started and the algorithm is executed at every T_c.
The experimental results have been recorded (and saved on a standard PC for graphic post-processing) using a trace options panel of the control board (namely ControlDesk) and a Tektronix DPO4034 oscilloscope (equipped with an accurate voltage and current probe) for other types of measurements.

An asynchronous induction motor, serving as a programmable load, was coupled on the same shaft of the PMSM-IPM motor under test, through a sensible Magtrol TM308 torque meter (Fig.2.16) to store the torque data in memory.

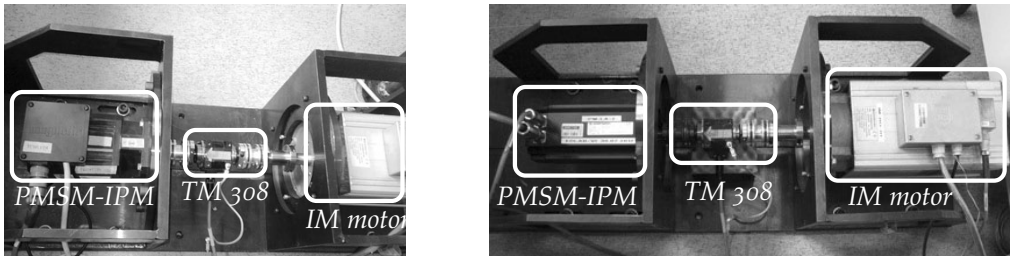

(a) (b)

Fig. 2.17: Experimental test bench configurations. The two PMSM tested are keyed on the same shaft of an IM (controlled in torque, as virtual load).

The torque measure was filtered by using a notch filter tuned around at 178 Hz and finally averaged over a sufficient number of T_c so that the torque reading was satisfactory. The algorithm execution time (worst case) was of 36 μs, while the sampling time and inverter switching period were both $T_c = 100\,\mu s$. With reference to the symbols of Fig.2.2, the MTPA detector parameters are reported in Tab. 2.3.
The experiment layout has been of utmost relevance, in order to ensure repeatability and accuracy in the measurements. For both the PMSM machines available for the experimental tests, rotor position and speed are measured using a resolver-to-digital converter. This solution is well known and usually applied in the industrial application (otherwise an incremental encoder can be replace the resolver interface), and it requires that a sinusoidal reference signal is injected to a rotor mounted coil.

Tab. 2.3: MTPA parameters used in the experimental tests

Parameter	**Value**
Frequency f_{AC} of the disturbance $\Delta\vartheta(t)$	110 Hz
Amplitude A of the disturbance $\Delta\vartheta(t)$	0.5 rad
HPF time constant τ_{HPF}	$\frac{1}{2\pi\ 80}$ s
LPF filter time constant τ_{LPF}	$\frac{1}{2\pi\ 10}$ s
PI proportional gain k_p	0
PI integral gain γ	$500 \div 10000$
Current loop bandwidth BW_i	500 Hz

To obtain the real MTPA curve of the PMSM-IPM machine, a first characterization of the motor must be performed, in order to validates the results produced by the algorithm. In particular, using the dSpace experimental system described above, the PMSM-IPM motor is dragged at a fixed speed ($\omega_m = 300$ rpm) by the IM machine.
In steady state condition, the phase of the current reference is then varied (from π to $\pi/2$) and the two components of the current in the dq reference frame are stored in a LUT with the value of the measured torque (measured with the torque-meter).
The procedure is then repeated by varying the amplitude of the current reference, from zero to the nominal current of the motor, in order to map the entire range of interest.

The results are then post processed to analytically derive the MTPA locus, obtained as a standard search of the minimum in the dq plane. Fig.2.18 collects the torque loci and the MTPA curve obtained following these experiment with respect of the PMSM-IPM in Tab.2.2 and in Tab.2.1. In the same figure are also reported the theoretical curves obtained applying the (2.6) at the nominal parameters reported in Tab.2.2 and Tab.2.1, overlapped with the MTPA curves calculated with the proposed algorithm. The experimental MTPA locus are obtained by monitoring the steady state operating points reached by the MTPA tracking controller under different loading conditions (using the PMSM-IPM machines in Tab.2.2 and Tab.2.1). In particular, the drive has been first brought to a constant speed reference, in conventional FOC with a specific load torque condition (imposed by the induction motor); then, the MTPA tracking controller has been enabled, and the evolution of the current vector on the dq plane has been monitored (while the induction motor has been made to generate a variable torque from 0% to the 100% of the rated torque). Plotting on the dq plane the currents obtained, the MTPA experimental locus is shown in Fig.2.20.
The results shows the perfect matching between the curve produced by the algorithm and that obtained with the measurements. Fig.2.19 shows the MTPA experimental locus in polar and cartesian coordinates, where each point of the MTPA curve has been calculated by averaging the current and phase measurements (at steady state), in order to get rid of the ripple caused by the perturbation injected by the MTPA tracking controller. In both cases, the accuracy of the analytic method suffers the influence of the saturations of the two inductances (Sec. 1.3) and the phenomena of the cross coupling, that occurs during the normal operating.

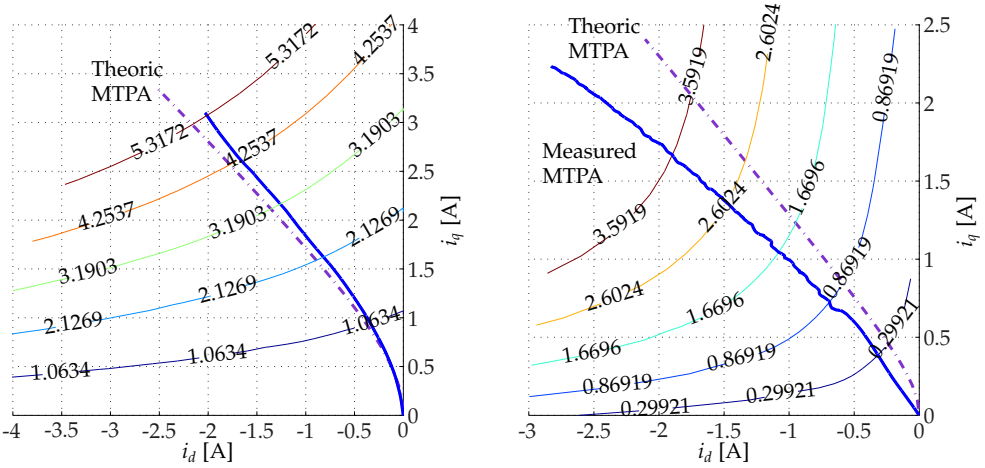

(a) *Constant measured torque loci oberlapped with the MTPA curve obtained with the algorithm by testing of the machine in Tab.2.2*

(b) *Constant measured torque loci oberlapped with the MTPA curve obtained with the algorithm by testing of the machine in Tab.2.1*

Fig. 2.18: Experimentally MTPA curves obtained using the PMSM-IPM machines in Tab.2.2 and Tab.2.1.

The suggested experimental procedure reflects what is considered the conventional mode of operation of the proposed solution in a typical industrial situation, namely tracking the MTPA point against slow variations of the load torque. This situation is typically found in industrial applications involving, among others, pumps, conveyors, extruders, air conditioning and packaging systems, bunchers and stranders, etc. Although a current ripple is in general undesired, in this circumstance it is indeed necessary for the correct operation of the control system. Nevertheless, it is worth noticing that once the MTPA operating point is attained, the MTPA control action could be dis-

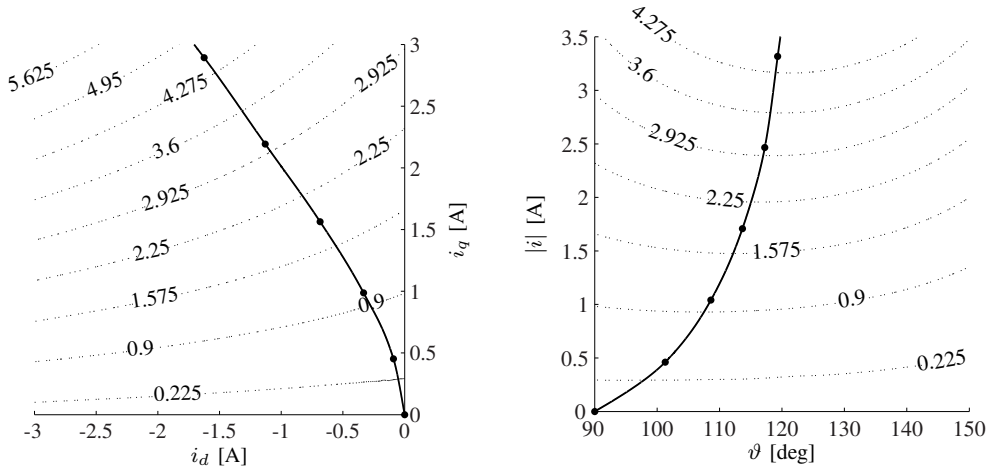

(a) *Experimental MTPA curve in cartesian coordinates*

(b) *Experimental MTPA curve in polar coordinates*

Fig. 2.19: Experimentally MTPA curves obtained using the PMSM-IPM machines in Tab.2.2 in polar and cartesian coordinates (by averaging the currents in single points).

abled, thus avoiding the injection of a persistent disturbance into the system. For such purpose, the enabling mechanism of the Sec. 2.6.2 could be devised in the experimental tests, whose aim is to turn on the MTPA tracking controller once a steady state operating condition is reached (both on the speed and load torque), and to turn it off again when the MTPA point is reached.

In the first batch of measurements, the motor was driven at 500 rpm, while the IM-based virtual load generates a slowly varying ramp torque from 0% to 100% of the rated torque τ_N, to get the MTPA curve. To test the tracking capability and its dependence on the MTPA parameters, the slope of the load torque curves was made progressively steeper, and the results were reported in Fig.2.20. It can be noticed that ramps of decreasing durations lead to a narrow bundle of curves, meaning that the MTPA detector is not affected by the slowly varying load. The curves start to deviate for smaller ramp times, as the rate of change of the load interferes with the dynamic of the MTPA detector, as shown in Fig.2.20 for the 1.25 s ramp time.

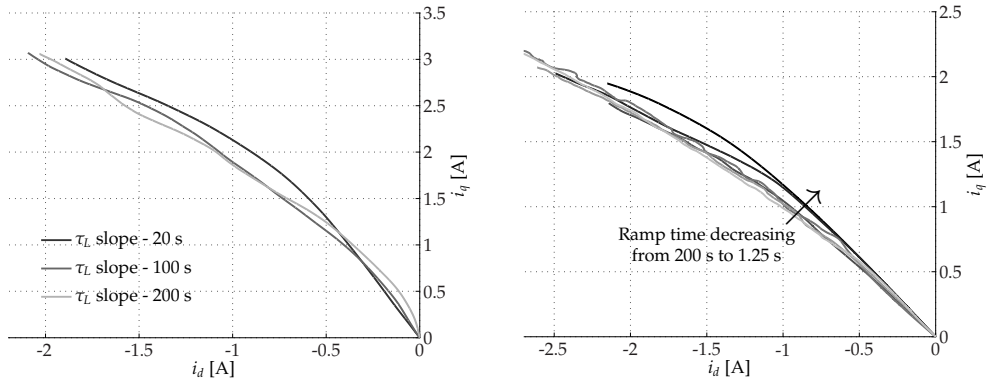

(a) *Experimental MTPA curve of the machine of in Tab.2.2*

(b) *Experimental MTPA curve of the machine in Tab.2.1*

Fig. 2.20: Experimentally MTPA curves (for different time of the load torque slope) using the PMSM-IPM machines in Tab.2.2 and Tab.2.1.

A second batch of measurements has been performed by imposing a $0.1\tau_N$ step load torque pattern (instead of a ramp), from 0% to full load. The results are shown in Fig.2.21a, where the direct and quadrature currents exhibit a heavy ripple, obviously due to the disturbance superimposed to the phase of the current vector.
The effect could be greatly mitigated by adopting the enable algorithm of Sec. 2.6.2 (deactivated during these experiments), which switch on the MTPA once a steady state condition is reached (both in speed and in load torque) and that switch it off again after the MTPA convergence. As a consequence, it follows that the ideal application for a MTPA-based drive works mainly at steady state and has not to be much influenced by a small and short-lived torque ripple.
On the contrary, the experiment shown in Fig.2.21a was aimed to get the point by point MTPA current trajectory (shown in the upper graphic), and the detector was never disabled. Fig.2.21a reports the measured shaft torque, averaged to eliminate the high frequency component coming from the disturbance injection.
The MTPA curve is almost a straight line for low torque levels, and the sensitivity (that is, the response of the speed loop to the disturbance of (2.7)) remains low. These aspects are reflected on the the current ripple, which increases with the torque level. Moreover, these effects could be reduced by adopting a programmed smooth reduction of the amplitude A as a function of the estimated load torque or, more easily, as a function of the output of the speed PI regulator (if necessary).
Sec. 2.4 shows that the phase ϑ of the current vector i asymptotically converges to the actual MTPA angle, which is identified by the condition $\varepsilon_f = 0$. Therefore, the achievable accuracy in the "angle estimation" is theoretically infinite (at least asymptotically); however, in practice such accuracy will be limited mainly by the precision of the current measurement, which is related to the resolution of the A/D converter and the noise rejection capability of the measurement system.
Moreover, it is worth to note that the phase ϑ of the current vector converges *on average* to the actual MTPA angle: in fact, while the extremum seeking controller is enabled, the phase ϑ is always perturbed by an additional perturbation term, which is deliberately introduced by the controller.

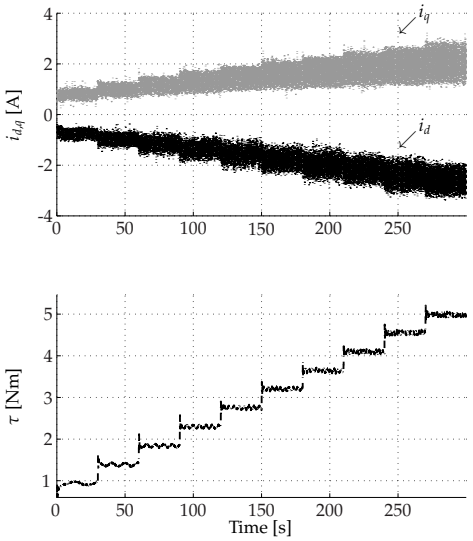

(a) *MTPA point, currents i_d, i_q and average torque τ.*

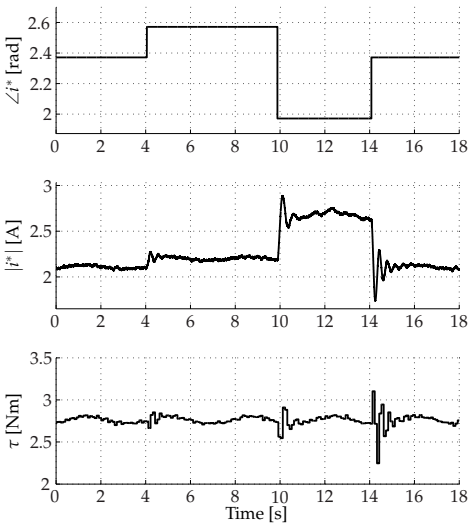

(b) *$\angle i^*$, $|i^*|$ and average torque τ in steady state condition with a constant load torque equal of $\frac{\tau_N}{2}$. $\omega_m = 500\,\text{rpm}$.*

Fig. 2.21: Comparison of the MTPA curves for different conditions for the motor in Tab.2.1.

The convergence accuracy must be referred to the average value of the phase ϑ. The instantaneous value of the phase ϑ is reached at steady state, as neighbourhood of the MTPA angle, whose amplitude is equal to the amplitude A of the phase perturbation.
To establish that a steady state working point was actually on the MTPA curve, a simple experiment has been designed. At steady state, and after that the MTPA detector output was stable, the PI_{MTPA} regulator was disabled and the phase $\angle i^*$ was slightly forced upward ($+0.2$ rad) and downward (-0.4 rad), respectively. Fig.2.21b reports the results, showing a case in which the point selected by the MTPA detector was actually a minimum for the current amplitude.
The test has been carried out at the constant speed of 500 rad, with $\tau = \tau_N$ and repeated under different loading conditions, using the motor in Tab.2.1 and repeated for the machine in Tab.2.2, as documented.
The experiment returned a sensitivity of about 1 A/rad, with a tendency to decrease with the torque level, as mentioned above.

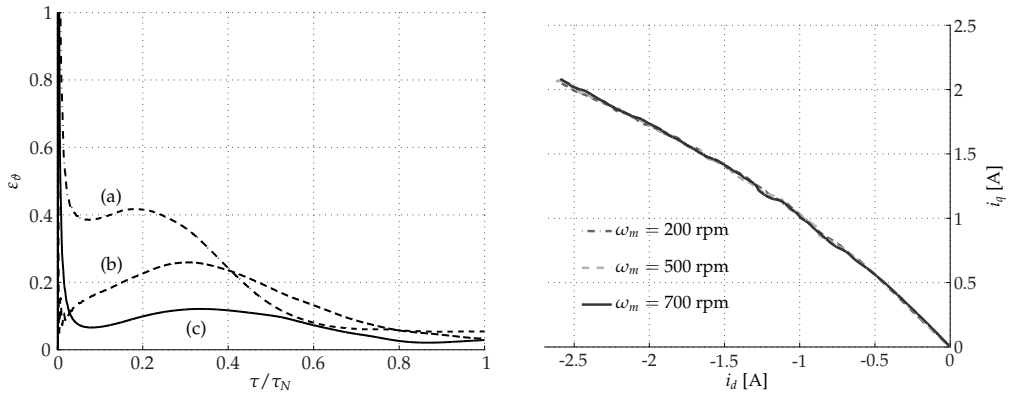

(a) *Effects of parameter variations, in the experimental conditions reported in Tab. 2.3 with (a) $\gamma' = 4\gamma$, (b) $A' = 5A$ and (c) $k'_p = 0.5k_p$ $\gamma' = 0.5\gamma$, $f'_{AC} = 1.5f_{AC}$.*

(b) *Comparison of the MTPA curves for different speed.*

Fig. 2.22: Effects of parameter variations and MTPA curves for different operating speed for the motor in Tab.2.1.

As last design hint, the effect of some parameters on the MTPA detector accuracy was investigated. To this aim, each parameter in Tab. 2.3 was modified in sequence, and a load torque ramp was imposed to explore the whole operating range of the drive.
The monitored quantity was the normalised error ε_ϑ between $i_q/i_d = \tan(\angle i)$, relative to the modified parameter, and the same ratio obtained from Fig.2.20, whose correctness was formerly proved by the test reported in Fig.2.21b. The results are shown in Fig.2.22a.
It is worth noting that an exceedingly high value of the integral gain γ, while improving the convergence speed, reduces the precision in the tracking during the first stretch (Fig.2.22a). Opposite to expectations, a too high value of A may worsen the accuracy, not to mention the unacceptable current ripple, while it has been found that a higher frequency of injection signal f_{AC}, in combination with a decrease of both PI_{MTPA} gains k_p and γ, maintains a quite good accuracy, while improving the MTPA detector dynamic.
For the sake of completeness, some other tests were performed to evaluate the possible influence of the speed in the MTPA detector operations. The tests were conducted by changing the speed of the PMSM-IPM drive, which is always applied a load torque variation in ramp of 100 s. The MTPA loci obtained in three different working conditions ($\omega_m = 200$ rad, $\omega_m = 500$ rad and $\omega_m = 700$ rad) are nearly identical, and it is therefore

possible to conclude that the proposed control action is not influenced by the speed of the motor, as shown in Fig.2.22b.
The experimental tests have been also conceived to prove and analyse the convergence of the proposed control scheme to the MTPA operating condition, in terms of both accuracy and speed of convergence with the aim to demonstrate the practical feasibility of the (2.36).

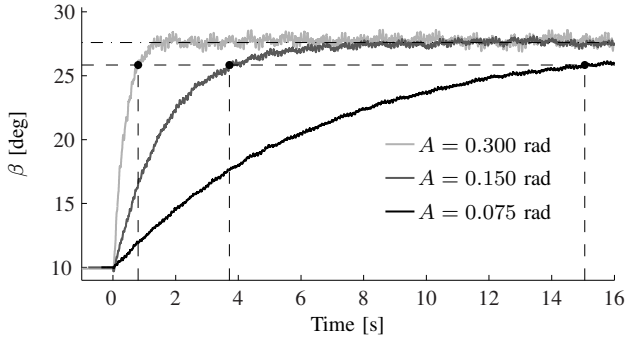

(a) *Different conditions of the perturbation amplitude obtained changing* A. $\gamma = 500$ *and* $\tau_L = 50\%\tau_N$

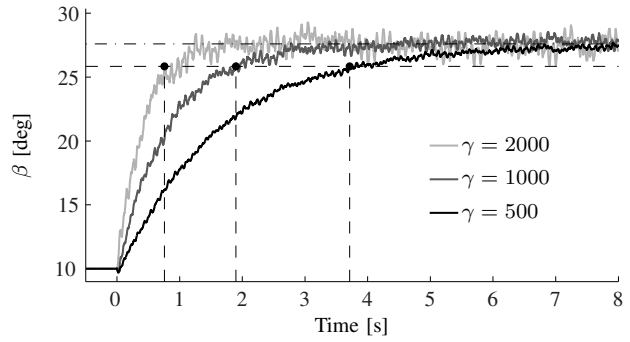

(b) *Different conditions of the perturbation amplitude obtained changing* γ *with* $A = 0.150$ *and* $\tau_L = 50\%\tau_N$

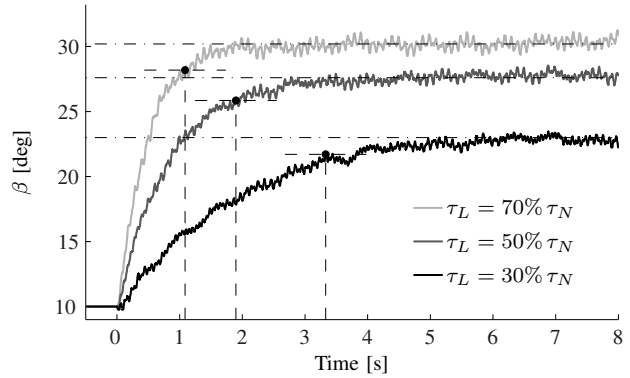

(c) *Different conditions of the perturbation amplitude obtained changing the load torque* τ_L *with* $A = 0.150$ *and* $\gamma = 1000$

Fig. 2.23: Time evolution of the angle β during the approaching phase to the MTPA point. For each plot, the measured convergence time (time required to cover 90% of the angular distance between the initial condition and the steady state condition) is highlighted with dashed lines (Results obtained with the motor in Tab.2.2).

In particular, while the steady state operation of the MTPA tracking controller is described by the results shown in the previous series of experiments, its transient response

Tab. 2.4: Measured/estimated convergence times [s] (motor in Tab.2.2)

$\tau_L = 30\%\tau_N$

A \ γ	500	1000	2000
0.075	>30 / 35.75	15.22 / 17.83	8.98 / 8.90
0.150	7.64 / 8.96	3.33 / 4.50	1.44 / 2.24
0.300	1.73 / 2.25	0.69 / 1.13	0.49 / 0.56

$\tau_L = 50\%\tau_N$

A \ γ	500	1000	2000
0.075	15.05 / 17.81	7.05 / 8.93	3.31 / 4.47
0.150	3.71 / 4.55	1.90 / 2.28	0.76 / 1.14
0.300	0.87 / 1.15	0.48 / 0.57	0.18 / 0.28

$\tau_L = 70\%\tau_N$

A \ γ	500	1000	2000
0.075	8.65 / 10.90	4.15 / 5.45	2.03 / 2.73
0.150	2.01 / 2.73	1.09 / 1.37	0.44 / 0.68
0.300	0.48 / 0.69	0.22 / 0.34	0.08 / 0.17

can be analysed with the aid of the plots reported in Fig.2.23. The plots show that the phase correction β, during the approaching phase to the MTPA point is affected by different choices of the three control parameters: the perturbation amplitude A, the controller gain γ and the load torque τ_L.
In each plot, the convergence time is measured as the time required to cover 90% of the angular distance separating the initial condition from the steady state (MTPA) condition. As correctly predicted by (2.36), from Fig.2.23a it can be noticed that the convergence time is inversely proportional to A^2: in fact, by halving the value of the amplitude A, the convergence time quadruples. In Fig.2.23a, the convergence time has been directly investigated by recording the MTPA trajectory with a constant load torque of 50% of the rated torque, at the constant speed of 500 rad, repeating the test for different amplitudes of the injected phase disturbance. In the same manner, Fig.2.23b shows that the convergence time is inversely proportional to γ, because its value doubles by halving the value of the gain γ. Indeed, it can be verified (Tab.2.4 described below) that the convergence time is inversely proportional to the product γA^2, i. e. the convergence time remains unchanged if, for example, the amplitude A is halved and the gain γ is quadrupled. Moreover, since the load torque affects the value of the parameter m in (2.36) and the convergence time $\bar{T}$ (as evident by the left plot of Fig.2.7), the steady state values are different because the angle of the MTPA point depends on the loading condition.

2.8 CONCLUSIONS

The research on the MTPA automatic attainment has focused on the mathematical aspects of an injection-based MTPA control technique. The strategy includes the zeroing of an error function, which is usually performed by a PI controller, since the inherent system non-linearity makes difficult the a-priori choice of the PI parameters. This research proposes a link between the convergence error time function and the PI parameters, smoothing the way for an automatic - instead of empirical - tuning of the MTPA controller. If compared with other techniques (relying on an off-line computation of the MTPA curve), the proposed solution has the following advantages:

- it does not require any preliminary measurement campaign aimed to find the MTPA operating point for any given load torque. This feature obviously implies savings in terms of time and costs required to carry out the experimental tests, since the experimental characterization of the MTPA curve is usually time-consuming and needs a specific and expensive test bench (equipped with a torque meter and an additional motor operating as a virtual load / brake).
- it can cope with motor parameters variations. A solution based on a pre-computed MTPA curve actually implements an open-loop control scheme, and hence it is unable to compensate any motor parameter variation that may occur during its prolonged operation.
- it can be used almost immediately with any motor: in fact, the proposed controller, being adaptive, requires only a small parameter tuning during its commissioning phase, and then it adjusts its operation according to the motor characteristics. On the contrary, a solution based on a precomputed MTPA curve obviously depends on the specific motor on which the curve has been determined, and cannot be used on a different motor.

The only disadvantages of this method can be found considering the current perturbation injected with the purpose of tracking the MTPA point. In fact, it produces an extra Joule losses in the motor stator winding. Also in this case, using the enable mechanism described in Sec. 2.6.2, it is possible to deactivate the MTPA tracking controller once an almost steady state condition is reached (both on the speed and on the load torque), and that turns it off again when the MTPA operating point is reached. In this way, the extra Joule losses due to the current perturbation eventually occurs only for the time required by the extremum seeking controller to seek the MTPA operating condition. It is important to remarks that in literature exist many other types of control algorithms that can be valuable alternatives in order to minimize the copper losses, as that proposed in [40] or [41].

3 HIERARCHICAL PREDICTIVE CONTROL

3.1 INTRODUCTION AND LITERATURE REVIEW

In view of the increasing demand of energy-efficient drives, predictive control techniques are arousing keen interest in wide sectors of the research in advanced electric drives. Even if the general concept of Model Predictive Control (MPC) exists in many engineering fields (as chemical engineering) since many years ([42] [43]), it is emerged in the electrical drive systems as a promising alternative to the popular and widely used vector control schemes [44] and direct torque control DTC [45], [46]. Recently, this control technique has been successfully applied in different fields, as an example in applications for the automotive industry [47] [48].
First examples of applications of the MPC technique can be found in [49], and they mainly deal with techniques that modern classification [50] indicates as Pulse-width Predictive Control (PPC), or dead-beat control. This class of predictive schemes calculates the voltages required to reach the desired currents after a sampling period and a PWM is used to translate these voltages into switching patterns. The advantage of using the PWM lies in the reduction of current ripple, especially if careful delay compensation is considered, since an appropriate voltage amplitude can be selected even at low speed. The main drawback is that usually the PPC is adopted in case of relatively slow digital implementation, so that an error in the model affects the voltage reference and this, in turn, may cause sensible current errors, precisely because of the large sampling periods. The MPC version for power electronic and drive systems can be divided in two main areas. The modulator Based (PWM or Space Vector Modulation (SVM)) schemes [43] and the direct predictive control schemes DPC, where there is no PWM modulation [51], [52]. The classical approach of MPC identifies a controller law that solves a Constrained Finite Time Optimal Control (CFTOC) problem, where a cost function defines the control goals with respect to the future states and inputs, and the optimization is performed over a prediction horizon of N_{pd} time steps (i. e. over kT_c, $(k+1)T_c$, ... $(k+j)T_c$ steps). A numerical solver is considered to compute the optimal feasible solution [53], by considering the receding horizon concept and evaluated with respect to the initial state plant [54]. At the end of the computation, the first control input of the resulting optimal sequence (saved into a LUT) is applied to the plant and iterated over the next sampling instant. If the entire control region of the power converter is considered, a significant computational effort is required and only simple and linear problems can be solved by considering the explicit MPC toolbox ([53]). This approach cannot takes into account the real time changing of the parameters involved into the control equations, leading to a lack of robustness with respect of the parameters variations.
Recently, an evolution of PPC has led to a modern class of predictive controllers, within the MPC theory [55]. Among the advantages, they let combine speed and current controller in a single MPC, instead of keeping the typical cascade structure of a speed and a current controller. It is possible to enforce in the controller the constraints due to current and voltage limits [56]. Moreover, the system non-linearity can be included in the model, without linearising the equations around any given operating point. This causes the best control input to be found iteratively, and the computational requirements exceed by far those offered by the available processors.

As a compromise, under certain simplifying assumptions, a huge part of the mathematical effort can be shifted off-line, as suggested first in [57]. In this case, the main drawback is the complexity of the computation to be performed off-line, which severely limits the inclusion of non-linearity and constraints, and the sensibility of the control to parameter variations, as in the MPC classic approach. The MPC has the main advantage that can be also used to design any non-linear control objective, i. e. the DC-link voltage control, speed, power or hybrid control, but in this case a linear current controller is used to design the nominal and robust MPC controller for simplicity, and further control goals are assumed to be implemented as external control loops [58].
As previously mentioned, the alternative to the MPC or PPC is the DPC (that also has its roots in the past), named also as finite control set model predictive control ([57]). As the name suggests, this class consists in predicting the future value of the currents for all of the eight voltage vectors that the inverter can generate. Then, the one that minimizes a specific target cost function or a specified object is selected. In this case the problem is a trade-off between the current ripple and the computational requirements (related to the capability to extend the prediction N_{pd} steps ahead, during the interrupt routine). Only analogue or very fast digital systems as FPGA ([59]) can bear an algorithm running at a sampling rate sufficiently high to maintain the current ripple within acceptable limits, while low-cost microprocessor or DSPs suffer of a hardware limitation and could not match the requirements for this type of control.
This thesis work is an attempt to merge the simple, on-line, finite control set approach of DPC with the interesting "global" view of MPC, through a hierarchical structure that entails energy savings, and the name of this new control structure is HDPC. Here the minimisation of a quadratic cost function [51] is replaced by a multi-level decisional structure, where the next control input within a finite set of voltage vector is selected by successive refinements. Moreover, the proposed control architecture avoids the use of an external speed control loop by considering a prediction model that swallows and mixes the electrical and mechanical equations of the motor, as described in Sec. 3.3.
In combination with a new hierarchical decisional structure and an increased number of voltage vectors (Sec. 3.4 and Sec. 3.5), the proposed algorithm has been tested by considering a standard industrial AC drive, without limitations related to the DC link bus voltage, which plays a key role in the performances and quality of the control.
In order to examine the different distinctive features of the HDPC, many simulation results performed either with isotropic motor and anisotropic motor are reported and commented in Sec. 3.6, while a complete and detailed description of the proposed control structure in a FPGA-based experimental bench is at the end of the chapter as well as the experimental evidences (Sec. 3.7).

3.2 BASIC CONTROL STRUCTURE

The predictive control has many advantages if an electric drive with an high dynamic control is required and the knowledge of the electric machine's parameters is available. The main difference between predictive control and traditional strategies is the pre-calculation of the system behaviour, considered in the control algorithm control structure. The difference between the reference and the measured value is used as input in the control decisional structure, that returns the optimal control input.
Basically, many non linear constraints and separated control actions can be included in the control law, without too many modifications on the algorithm structure, but an extremely high number of calculations are required to compute and test all the possible configurations. From the computation point of view and compared to the traditional cascade control strategies, the practical feasibility of the control could be compromised, but in the last years the power of the new DSP and the recent development of new

FPGA platform allows the implementation of this new real time control technique. This research focuses on the application of the direct predictive control implemented as speed and current control for a PMSM drive. Basically, the scheme of Fig.3.1 is considered for the modelization of the system. The PMSM-IPM motor with sinusoidal stator flux distribution is directly fed by the three-phase VSI, in which each of the three phase legs is characterized by two switches that connect the voltage source U_{DC} of the DC link with the neutral point (N), and so the voltage produced in each phase is $\pm U_{DC}/2$.
The two Insulated Gate Bipolar Transistor (IGBT) are complementary, and so, if the upper switch is off, the lower switch has to be turned on.

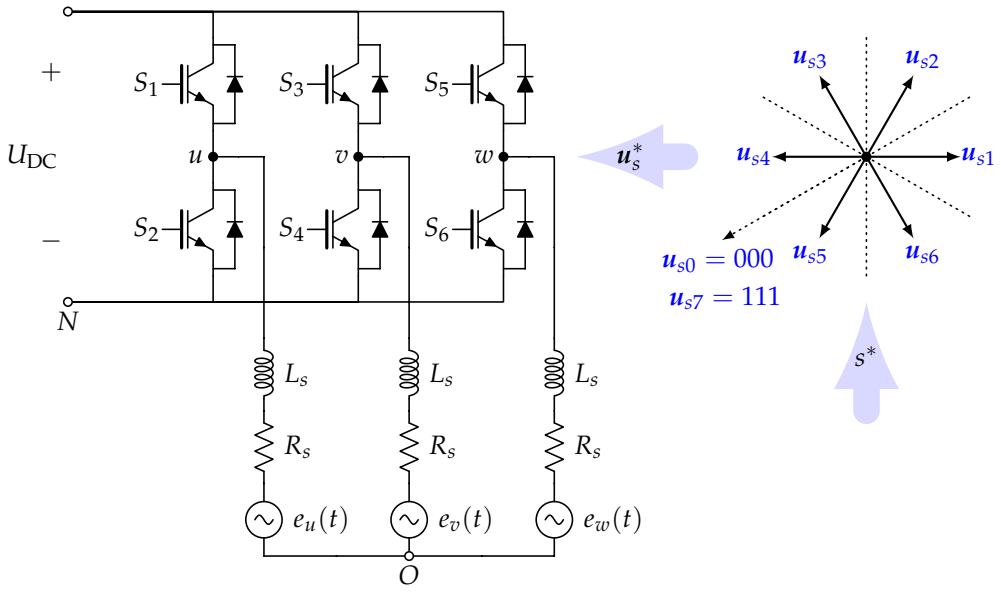

Fig. 3.1: Generic configuration of a DPC control scheme with PMSM machine direct fed by a VSI.

With respect of this basic configuration, the minimum number of switching possibilities generated without modulation is $N_s = 2^3 = 8$. Each switching state of the IGBT is representative of a set of phase voltages that can be produced using this finite set of possibilities (indicated with s_u, s_v and s_w), and so, the output voltage space vector is defined as:

$$\boldsymbol{u}_{si} = \frac{2}{3} U_{DC} \left(u_{su} + u_{sv} e^{j\frac{2\pi}{3}} + u_{sw} e^{j\frac{4\pi}{3}} \right) \qquad i = 1...7 \tag{3.1}$$

Basically, the DPC evaluates each of the (3.1) by considering the finite number of voltage vectors ($\boldsymbol{u}_{s0}, \boldsymbol{u}_{s1}....\boldsymbol{u}_{s7}$) represented in Fig.3.1 (on the right side).
The switching states $\boldsymbol{u}_{s0} = \boldsymbol{u}_{s7}$ are called "zero states", since they produce zero voltage vectors, and so the minimum number of possible switching states is reduced to $N_s = 7$, considering only $\boldsymbol{u}_{s0}$. The control algorithm structure has two main targets. The first is to ensure a quickly and smooth transient speed profile, by guaranteeing at the same time the stability under transient operation; the second, in steady state conditions is to reach different control objectives. The prediction procedure firstly computes the speed and current trajectories for each of the VSI vectors and then selects the optimal switching state vector by considering a novel hierarchical decisional structure.
The optimal voltage vector is then applied during the next whole sampling period but calculated in the previous one, i. e. these calculations must be completed and executed on each sampling time interval T_c.

3.3 MATHEMATICAL BACKGROUND

With the aim to synthesize correctly the prediction model to be used in the HDPC algorithm, the time continuous model of the PMSM-IPM motor of Sec. 1.2 is here reconsidered. The discrete-time domain model can be derived assuming that currents and position are sampled at every instant $k\,T_c$ (T_c defines the sampling interval), and by defining with $\langle\cdot\rangle_k$ the average operator over the time interval $[kT_c,\ (k+1)T_c]$. Assuming that:

$$\langle x\rangle_k \triangleq \frac{1}{T_c}\int_{kT_c}^{(k+1)T_c} x(t)\,dt \tag{3.2}$$

the time integration of (1.19) over the sampling interval $[(k-1)T_c,\ kT_c]$ yields:

$$\begin{aligned}
\frac{1}{T_c}\int_{k-1}^{k} u_d dt &= \frac{1}{T_c}\int_{k-1}^{k}\left(R_s i_d + L_d\frac{di_d}{dt} - L_q\omega_{me} i_q\right)dt \\
\frac{1}{T_c}\int_{k-1}^{k} u_q dt &= \frac{1}{T_c}\int_{k-1}^{k}\left(R_s i_q + L_q\frac{di_q}{dt} + \omega_{me} L_d i_d + \Lambda_{mg}\omega_{me}\right)dt
\end{aligned} \tag{3.3}$$

and after some easy algebraic manipulations, the (3.3) returns the couple of discretized currents in the dq reference frame, rewritten as:

$$\begin{aligned}
i_{d,k} &= i_{d,k-1} + \frac{T_c}{L_d}\left(L_q\langle\omega_{me} i_q\rangle_{k-1} - R_s\langle i_d\rangle_{k-1} + \langle u_d\rangle_{k-1}\right) \\
i_{q,k} &= i_{q,k-1} + \frac{T_c}{L_q}\left(\langle u_q\rangle_{k-1} - R_s\langle i_q\rangle_{k-1} - L_d\langle\omega_{me} i_d\rangle_{k-1} - \Lambda_{mg}\langle\omega_{me}\rangle_{k-1}\right)
\end{aligned} \tag{3.4}$$

The (3.4) can be reorganized and simplified, assuming that the mechanical (or electromechanical) speed be constant between two sampling periods (i.e. $\langle\omega_{me}\rangle_{k-1} \approx \omega_{me,k-1}$) and considering that the applied voltage vector changes only at the beginning of the next algorithm calculation (i.e. $\langle u_d\rangle_{k-1} = u_{d,k-1}$ and $\langle u_q\rangle_{k-1} = u_{q,k-1}$)[1]. In compact form:

$$\begin{aligned}
\langle i_d\rangle_{k-1} &\approx \frac{i_{d,k-1} + i_{d,k}}{2} \\
\langle i_q\rangle_{k-1} &\approx \frac{i_{q,k-1} + i_{q,k}}{2} \\
\langle\omega_{me} i_d\rangle_{k-1} &\approx \omega_{me,k-1}\langle i_d\rangle_{k-1} \\
\langle\omega_{me} i_q\rangle_{k-1} &\approx \omega_{me,k-1}\langle i_q\rangle_{k-1}
\end{aligned} \tag{3.5}$$

By replacing the (3.5) in the (3.4), after some algebraic manipulations the current discretized equations can be rewritten as:

1 These assumptions have general validity but they are particularly truthful at low switching frequencies (i.e. $f_s < 5\,\text{kHz}$), although for high frequency switching (considering that the sampling period is in general smaller of the electrical time constants of the machine) the currents can be considered constant between two successive sampling periods. It follows that $\langle i_d\rangle_{k-1} \approx i_{d,k-1}$, $\langle i_q\rangle_{k-1} \approx i_{q,k-1}$, $\langle\omega_{me} i_d\rangle_{k-1} \approx \omega_{me,k-1} i_{d,k-1}$ and $\langle\omega_{me} i_q\rangle_{k-1} \approx \omega_{me,k-1} i_{q,k-1}$. This, of course, leads to a strong simplification of the model.

$$\begin{cases} i_{d,k} = -\dfrac{i_{d,k}R_sT_c}{2L_d} + \dfrac{u_{d,k-1}T_c}{L_d} + \dfrac{i_{q,k}\omega_{me,k-1}L_qT_c}{2L_d} \\ \qquad + \dfrac{i_{q,k-1}\omega_{me,k-1}L_qT_c}{2L_d} + i_{d,k-1}\left(1 - \dfrac{R_sT_c}{2L_d}\right) \\ i_{q,k} = -\dfrac{i_{q,k}R_sT_c}{2L_q} + \dfrac{u_{q,k-1}T_c}{L_q} - \dfrac{\Lambda_{mg}\omega_{me,k-1}T_c}{L_q} - \dfrac{i_{d,k}\omega_{me,k-1}L_dT_c}{2L_q} \\ \qquad - \dfrac{i_{d,k-1}\omega_{me,k-1}L_dT_c}{2L_q} + i_{q,k-1}\left(1 - \dfrac{R_sT_c}{2L_q}\right) \end{cases} \tag{3.6}$$

Defining as $\boldsymbol{i}_{dq,k} \triangleq \left[i_{d,k},\, i_{q,k}\right]^T$ and $\boldsymbol{u}_{dq,k} \triangleq \left[u_{d,k},\, u_{q,k}\right]^T$ the current and voltage vectors, the two equations in (3.6) can be considered as a linear system in the unknown variables $i_{d,k}$ and $i_{q,k}$.
In state space form the solution returns:

$$\boldsymbol{i}_{dq,k} = \boldsymbol{A}_{k-1}\boldsymbol{i}_{dq,k-1} + \boldsymbol{g}_{k-1} \tag{3.7}$$

where

$$\boldsymbol{A}_{k-1} \triangleq \begin{bmatrix} \dfrac{2L_d\kappa_q}{\Psi_{k-1}} - 1 & \dfrac{4L_q^2T_c}{\Psi_{k-1}}\,\omega_{me,k-1} \\ -\dfrac{4L_d^2T_c}{\Psi_{k-1}}\,\omega_{me,k-1} & \dfrac{2L_q\kappa_d}{\Psi_{k-1}} - 1 \end{bmatrix} \tag{3.8}$$

$$\boldsymbol{g}_{k-1} \triangleq \begin{bmatrix} \dfrac{\left(\kappa_q + L_qT_c^2\,\omega_{me,k-1}\right)u_{d,k-1}}{\Psi_{k-1}} \\ \dfrac{\left(\kappa_d - L_dT_c^2\,\omega_{me,k-1}\right)u_{q,k-1}}{\Psi_{k-1}} \end{bmatrix} - \begin{bmatrix} \dfrac{2\Lambda_{mg}L_qT_c^2\,\omega_{me,k-1}}{\Psi_{k-1}} \\ \dfrac{\kappa_d\Lambda_{mg}L_qT_c}{\Psi_{k-1}} \end{bmatrix} \tag{3.9}$$

and

$$\begin{aligned} \Psi_{k-1} &\triangleq 4L_dL_q + 2R_s\left(L_d + L_q\right)T_c + \left(R_s^2 + L_dL_q\,\omega_{me,k-1}^2\right)T_c^2 \\ \kappa_q &\triangleq 2T_c\left(R_sT_c + 2L_q\right) \\ \kappa_d &\triangleq 2T_c\left(R_sT_c + 2L_d\right) \end{aligned} \tag{3.10}$$

Since the right hand side of (3.7) depends only on measured quantities at the instant $(k-1)T_c$ (i. e. the currents $\boldsymbol{i}_{dq,k-1}$, the voltages $\boldsymbol{u}_{dq,k-1}$ and the velocity $\omega_{me,k-1}$), then it can be used to predict the currents at the instant kT_c, i. e. in state space form:

$$\hat{\boldsymbol{i}}_{dq,k|k-1} = \boldsymbol{A}_{k-1}\boldsymbol{i}_{dq,k-1} + \boldsymbol{g}_{k-1} \tag{3.11}$$

where $\hat{\boldsymbol{i}}_{dq,k|k-1}$ (in general the suffix "$\hat{\cdot}$") denotes the vector of predicted currents at the instant kT_c, given the measurements up to the instant $(k-1)T_c$. In particular, by expanding the previous terms gives:

$$\begin{cases} \hat{i}_{d,k|k-1} = \dfrac{4i_{q,k-1}\omega_{me,k-1}L_q^2T_c}{\Psi_{k-1}} + \dfrac{2u_{q,k-1}\omega_{me,k-1}L_qT_c^2}{\Psi_{k-1}} \\ -\dfrac{2\Lambda_{mg}\omega_{me,k-1}^2L_qT_c^2}{\Psi_{k-1}} - \dfrac{u_{d,k-1}\left(-4L_qT_c-2R_sT_c^2\right)}{\Psi_{k-1}} \\ - \dfrac{i_{d,k-1}\left(-4L_dL_q-2R_sL_dT_c+2R_sL_qT_c+R_s^2T_c^2+\omega_{me,k-1}^2L_dL_qT_c^2\right)}{\Psi_{k-1}} \\ \hat{i}_{q,k|k-1} = \dfrac{4i_{d,k-1}\omega_{me,k-1}L_d^2T_c}{\Psi_{k-1}} - \dfrac{2u_{d,k-1}\omega_{me,k-1}L_dT_c^2}{\Psi_{k-1}} \\ - \dfrac{u_{q,k-1}\left(-4L_dT_c-2R_sT_c^2\right)}{\Psi_{k-1}} - \dfrac{4\Lambda_{mg}\omega_{me,k-1}L_dT_c+2R_s\Lambda_{mg}\omega_{me,k-1}T_c^2}{\Psi_{k-1}} \\ - \dfrac{i_{q,k-1}\left(-4L_dL_q+2R_sL_dT_c-2R_sL_qT_c+R_s^2T_c^2+\omega_{me,k-1}^2L_dL_qT_c^2\right)}{\Psi_{k-1}} \end{cases} \tag{3.12}$$

To complete the modelization, the mechanical part of the equations must be considered. The torque expression (1.21) is averaged applying the same methodology exposed for the voltage equations by considering the operator of (3.2). It follows that:

$$\frac{1}{T_c}\int_{k-1}^{k}\tau dt = \frac{J_m}{T_c}\int_{k-1}^{k}\frac{d\omega_m}{dt}dt + \frac{B_m}{T_c}\int_{k-1}^{k}\omega_m dt + \frac{1}{T_c}\int_{k-1}^{k}\tau_L dt \tag{3.13}$$

and then:

$$\langle\tau\rangle_{k-1} = J_m\left(\frac{\omega_{m,k}-\omega_{m,k-1}}{T_c}\right) + B_m\langle\omega_m\rangle_{k-1} + \langle\tau_L\rangle_{k-1} \tag{3.14}$$

It is worth nothing that, for the previous hypothesis, the speed is considered constant between two sampling instants (i. e. $\langle\omega_m\rangle_{k-1} \approx \omega_{m,k-1}$), and so the discretized speed equation at the instant kT_c derived:

$$\omega_{m,k} = \omega_{m,k-1}\left(1-\frac{T_cB_m}{J_m}\right) + \frac{T_c}{J_m}\left(\langle\tau\rangle_{k-1} - \langle\tau_L\rangle_{k-1}\right) \tag{3.15}$$

The prediction of the speed derived assuming that the estimated load torque is considered constant $\langle\tau_L\rangle_{k-1} = \hat{\tau}_L$ (estimated with the method in 3.3.1), and the hypothesis that $\langle\tau\rangle_{k-1} = \dfrac{\tau_{k-1}+\tau_k}{2} \approx \tau_{k-1}$. Since the torque measure τ_{k-1} is not available, the torque produced by the motor is estimated and not predicted at the instant $(k-1)T_c$. Defining the estimated torque as $\hat{\tau}_{k-1}$, the speed prediction returns:

$$\hat{\omega}_{m,k|k-1} = \left(1-\frac{T_cB_m}{J_m}\right)\omega_{m,k-1} + \frac{T_c}{J_m}\left(\hat{\tau}_{k-1}-\hat{\tau}_L\right) \tag{3.16}$$

By averaging the expression of the electromagnetic torque between the instants $(k-1)T_c$ and kT_c ($\langle\tau\rangle_{k-1} \approx \tau_{k-1}$), it follows that:

$$\tau_{k-1} = \frac{1}{T_c}\int_{k-1}^{k} \tau dt = \frac{3p}{2T_c}\left(\Lambda_{mg}\int_{k-1}^{k} i_q dt + \left(L_d - L_q\right)\int_{k-1}^{k} i_d i_q dt\right) \tag{3.17}$$

and so:

$$\begin{aligned}\tau_{k-1} &= \frac{3}{2}p\Lambda_{mg}\left\langle i_q\right\rangle_{k-1} + \frac{3}{2}p\left(L_d - L_q\right)\left\langle i_d i_q\right\rangle_{k-1} \\ &= \frac{3}{2}p\left\{\Lambda_{mg}\frac{\left(i_{q,k-1} + i_{q,k}\right)}{2} + \left(L_d - L_q\right)\frac{\left(i_{d,k-1}i_{q,k-1} + i_{d,k}i_{q,k}\right)}{2}\right\} \\ &= \frac{3}{4}p\Lambda_{mg}\left(i_{q,k-1} + i_{q,k}\right) + \frac{3}{4}p\left(L_d - L_q\right)\left(i_{d,k-1}i_{q,k-1} + i_{d,k}i_{q,k}\right)\end{aligned} \tag{3.18}$$

Using the previous expression, the torque estimation at step $(k-1)T_c$ is:

$$\begin{aligned}\hat{\tau}_{k-1} &= \frac{3}{4}p\Lambda_{mg}\left(i_{q,k-1} + \hat{i}_{q,k|k-1}\right) \\ &+ \frac{3}{4}p\left(L_d - L_q\right)\left(i_{q,k-1}i_{d,k-1} + \hat{i}_{d,k|k-1}\hat{i}_{q,k|k-1}\right)\end{aligned} \tag{3.19}$$

By replacing the torque expression (3.19) into the (3.16), the prediction of the speed in $(k+1)T_c$ becomes:

$$\begin{aligned}\hat{\omega}_{m,k+1|k-1} &= f_\omega\left(\omega_{m,k-1}, i_{d,k-1}, i_{q,k-1}, \hat{i}_{d,k|k-1}, \hat{i}_{q,k|k-1}, \hat{\tau}_L\right) \\ &= \frac{2J_m}{2J_m + T_c B_m}\left\{\omega_{m,k-1}\left(1 - \frac{T_c B_m}{J_m}\right) - \frac{T_c}{J_m}\left[\frac{3}{4}p\left(i_{q,k-1} + \right.\right.\right. \\ &\left.\left.\left.\hat{i}_{q,k|k-1}\right)\left(\Lambda_{mg} + \frac{\left(L_d - L_q\right)}{2}p\left(i_{d,k-1} + \hat{i}_{d,k|k-1}\right)\right) - \hat{\tau}_L\right]\right\}\end{aligned} \tag{3.20}$$

The (3.20) shows that the speed prediction at step kTc does not depends by the voltages applied at step $(k-1)T_c$, and for this reason it is important to remark that in the stator currents dynamics (3.31), the voltage actuation has an immediate effect at step kT_c but in the electromechanical equation (3.20) this not happen in kT_c.
For the motor speed in fact, the effect of the voltage actuation in the currents depends by the mechanical dynamics of (3.19), and then only at the $(k+1)T_c$ step of prediction the effects of a voltage application on the mechanical variables become visible.
The same behaviour is by considering in the position, where only at the step $(k+2)T_c$ the effects of a voltage application on the electromechanical position $\vartheta_{me} = p\vartheta_m$ are visible. For the sake of completeness the equation of the update electromechanical position is reported.

$$\begin{aligned}&\frac{1}{T_c}\int_{k-1}^{k}\frac{d\vartheta_{me}}{dt}dt = \frac{1}{T_c}\int_{k-1}^{k}\Omega_{me}dt \\ &\Rightarrow \hat{\vartheta}_{me,k+1|k-1} = \vartheta_{me,k-1} + p\left(\frac{\omega_{me,k-1} + \hat{\omega}_{me,k+1|k-1}}{2}\right)T_c\end{aligned} \tag{3.21}$$

The prediction model introduced in this paragraph shows that, as every model-based technique, the predictive control requires the knowledge of the main parameters of the

motor for an effective operating. Any mismatch leads to inaccuracy that can nullify the advantages of the prediction. This was surely one of the main drawbacks in the past, and it still represents a heavy prejudice of the off-line techniques.
Appropriate and modern estimation techniques, as those described in [60], [61], [9] or [62] assure a rather good tracking of both the parameters. As a valid alternative, integral compensation, as that proposed in [49] and the corresponding improved version [63], can (indirectly) fixed the problem of the parameters inaccuracy, by adding a term to the references produced as the integral of the error between the predicted and measured output.
Although these parameters are very important, their influence have no impact on the implementation (the only small impact is the size of the fixed point data types that need to be used in the real FPGA implementation).

3.3.1 *Load torque estimation*

Another issue that has to be addressed is the load torque estimation, that takes a crucial role in the dynamic performance of the drive, influencing the correctness of the prediction as well. In a typical cascade control scheme (e. g. the FOC for PMSM drives) the external speed loop has the primary object in minimize the difference between the speed reference and the measured (or estimated) speed, but the integral action of the PI controller also compensates disturbances or sudden load torque variations.
In the proposed control architecture, the load torque term appears in (3.16) and can be considered as a general disturbance. If not correctly compensated, this term could leads to a steady state speed error. To overcome this problem, a possible solution consist into adopt a disturbance observer, which uses the difference between the actual output and the output of the nominal model as an equivalent disturbance applied to the nominal model torque equation.
It estimates the load torque, which is utilized as a compensation value in the prediction equation (3.16). By considering the mechanical balance:

$$\tau - \tau_L = \underbrace{\frac{3}{2} p \left(\Lambda_{mg} i_q \left(L_d - L_q \right) i_q i_d \right)}_{\tau(i_d, i_q)} - \tau_L = J_m \frac{d\omega_m}{dt} + B_m \omega_m \tag{3.22}$$

and the basic Disturbance Observer (DOB) concepts described in [64], the estimated torque $\hat{\tau}_{k-1}$ (calculated with the (3.14)) can be used into the block diagram represented in Fig.3.2 and subtracted to the estimate value of the reverse mechanical model. This control action returns the correct estimation of the load torque disturbance.

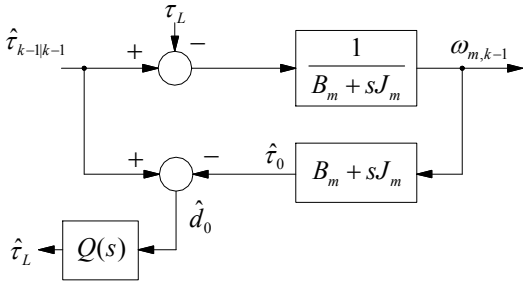

Fig. 3.2: Proposed disturbance observer (DOB) for the estimation of the load torque τ_L.

Assuming that the load torque remains constant or slowly variable (i. e. $d\tau_L(t)/dt \approx 0$), $\hat{\tau}_L$ can be computed retrieving the inverse speed model. Since the direct feedback of

$\hat{d}_0$ cannot be realized (the inverse model plant is non-proper), the control action can be realized by introducing a transfer function $Q(s) = \dfrac{1}{1+s\tau_Q}$, which should have a relative degree ρ_Q greater or equal to the relative degree of the model plant (i. e. in the present case $\rho_Q \geq 1$). It follows that $Q(s)$ can be considered as a first order LPF, and the dynamic of the DOB can be describes with the following set of equations:

$$\begin{cases} \hat{\tau}_0 = J_m \dfrac{\omega_{m,k-1} - \omega_{m,k-2}}{T_c} + B_m \omega_m \\ \hat{d}_0 = \hat{\tau}_{k-1} - \hat{\tau}_0 \\ \hat{\tau}_L = \dfrac{\tau_Q}{\tau_Q + T_c} \hat{\tau}_{L,k-1} + \dfrac{T_c}{\tau_Q + T_c} \hat{d}_0 \end{cases} \tag{3.23}$$

The hypothesis that $\dfrac{d\tau_L(t)}{dt} \approx 0$ leads to consider only the speed measured at step $(k-1)T_c$ and $(k-2)T_c$, and not the prediction of the speed $\hat{\omega}_{m,k|k-1}$ (that requires the estimation of τ_L). As mentioned before, the design of the disturbance observer is reduced to the design of $Q(s)$, or in other terms in the choice of the constant time τ_Q [64]. The choice of the cutting frequency f_Q depends by the measurement noise, by the disturbances of the system and by the amount of uncertainty in the model plant. Moreover, the bandwidth of $Q(s)$ has to be lower than the regulated bandwidth of the input signal $\hat{\tau}_{k-1|k-1}$. For the purposes of the present case, a simple first order low pass filter with a cutting frequency of $f_Q = 1/(2\pi\tau_Q) = 10\,\text{Hz}$ is considered [64].

3.4 THEORY OF OPERATIONS AND DESIGN HINTS

The generalized version of the discrete-time model of the PMSM described in the previous section is used to predict currents and speed at every sample time kT_c. The proposed control scheme, in fact, does not uses an external speed control loop and the speed is directly computed by the algorithm, where many control targets and restrictions have to be included to force the desired speed dynamic by considering the decisional control objects. The future plant states are computed for $k+1, ..., k+1+N_{pd}$ steps (N_{pd} denotes the prediction control horizon), and for each of the N_s possible states that the power converter can generates at every step. The main target is to find the best voltage vector to apply at each sampling instant, considering the optimality criteria, here named HDPC. The main characteristic of the HDPC decisional controller is the way it selects the control law based on a prediction of the system behaviour.
In literature exists many solutions based on the use of a cost function that is generally considered in order to test and select every admissible voltage vector. This function is usually a quadratic cost term, composed by a series of weighting factors that give different priority at every contribution (e. g. speed error, MTPA condition or switching vector) [52], although one of the main disadvantages in this solution is the choice of the weights of the different terms that compose the cost function (as described in [65]).
The proposed decisional algorithm does not rely on a cost function definition, since an hierarchical decisional structure is considered to find and selects the best voltage vector that met the imposed control constraints. During the normal operating, the control routine check the speed reference tracking (transient or steady state condition) and the MTPA condition (only in steady state operations), by reducing step by step the number of admissible states in a hierarchical way.
By focusing on the execution routine in a sampling instant $(k-1)T_c$ (at the same instant are measured the currents and the mechanical position), the goals of the DPC control is to find the best voltage vector to apply at the instant kT_c, selected considering the

HDPC structure. The highest priority in fact, is given to minimize the speed error under mandatory current constraints. If two or more voltage vectors fit the reduction of the speed error and respect a specified speed boundary, the second level of hierarchy is entered, selecting the bunch of vectors that minimises an extra constraints (e. g. the MTPA condition). It is important to considered that, in the more general case (with a horizon of prediction grater than one), the algorithm has to find the first input of the optimal trajectory, calculated using the hierarchy criteria in a recursive way, by testing every node of the possible paths with the decisional structure. This means that at every step on of prediction, the algorithm recursively evaluates the equations of Sec. 3.3 for each of the N_s state vectors of the voltage inverter, so that the total number of iterations grows exponentially with N_{pd} ($N_s^{N_{pd}}$, where N_{pd} indicates the prediction horizon and N_s the number of the voltage states).
In particular, to calculate the optimal path, the result of the hierarchical decisional is added to the previous one, easily tested with a recursive software routine (as detailed in Sec. 3.5.2). Extra constraints can be added to the hierarchical decision process in order to achieve interesting energy savings objects, even if one has to bear in mind that the complexity grows exponentially. A concept scheme of the algorithm timing diagram is summarized in Fig.3.3.

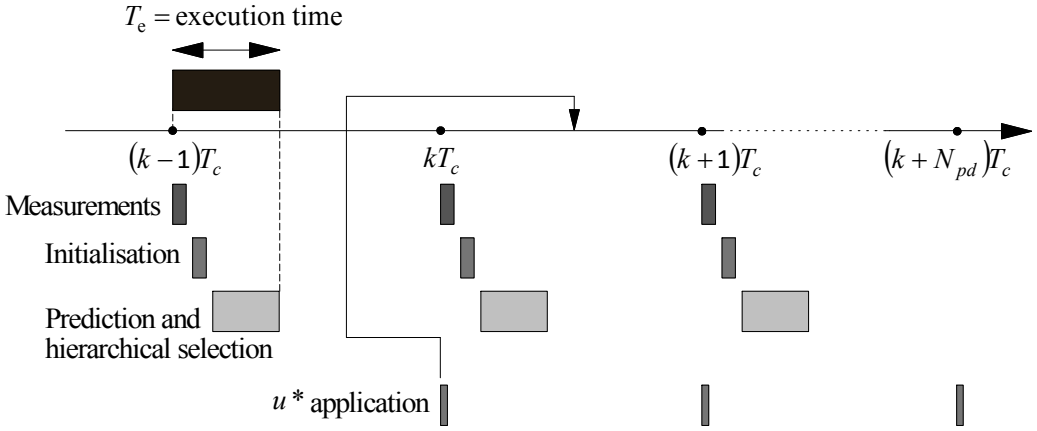

Fig. 3.3: Timing diagram of the HDPC control actions (the length of a single rectangle is magnified and not corresponds to the real execution time of the algorithm).

With respect to Fig.3.3 the control algorithm works as follows. Firstly, since the measurements from the sampling instant are available, as detailed in Sec. 3.4.1 the controlled states change as direct effect of the application of the previous optimal voltage state.
At the same instant, the load torque, is compensated (i. e. at step $(k+1)T_c$, two steps of prediction is the minimum time that ensures that the applied voltage vector has an effects at step $(k+1)T_c$) and the routine calculates all the possible evolutions of currents and speed predictions. The main steps of the execution routine are summarized in the following two sub sections.

3.4.1 *Initialization*

The future control plant depends by his previous value and by the values of the applied voltage. Since the control algorithm has a finite execution time (i. e. it can be assumed comparable with the sampling frequency T_c) a delay time between the instant at which the currents are measured and the instant of application of the new switching vector appears.

Assuming to be in the time instant $(k-1)T_c$, the first part of the control action (called Initialisation in Fig.3.3) estimates the values of the currents at time instant kT_c (through the (3.12)) and of the speed at time instant $(k+1)T_c$ (through the (3.20)). During the step kT_c, in fact, the applied voltages remain constant and equal to $u^{s^*}_{d,k-1}$ and $u^{s^*}_{q,k-1}$ (i. e. those computed in $(k-2)T_c$) and then, the change of the currents and on the speed up to the instant kT_c is only related on the measurements and the previous predicted voltages.

3.4.2 *Prediction*

From the update instant kT_c, the algorithm performs the prediction of current and speed by testing each term of the (3.11) and (3.16) for all the N_s possible voltage configurations.
In the case of $N_{pd} > 1$, the set of equations (3.25) are exploded in a recursive way to explore all the possible configurations, considering each possible state evolution with a prediction horizon N_{pd} greater of one single step. In this latter case, the iterative test is performed for all the possible paths over the entire prediction horizon N_{pd} (that in the more general case could be greater than a single step of prediction), and the complexity increases exponentially, as detailed in Sec. 3.5.2. Regardless of the number of steps of prediction, at the beginning of the prediction step the equations (3.11) and (3.25) are re-considered by using as inputs the estimated values of speed and current calculated in Sec. 3.4.1.
In detail, the prediction of speed refers to the time step $(k+2)T_c$ while the current refers to the step $(k+1)T_c$. These predictions are derived considering the (3.11) and (3.25) by changing the voltage terms with the equivalent ones associated to each of the $\boldsymbol{u}_{s1}, \boldsymbol{u}_{s2}....\boldsymbol{u}_{sN_s}$ finite state configurations of the power converter. This means that each voltage combination of $u^{s^*}_{d,k}$ and $u^{s^*}_{q,k}$ is calculated as:

$$u^s_{d,k} + j u^s_{q,k} = \frac{2}{3} U_{dc}\, e^{j\left(\frac{\pi}{3}s\right)}\, \boldsymbol{T}_{uvw/dq}\left(\hat{\vartheta}_{me,k+1|k-1}\right) \tag{3.24}$$

where the apex $s = 0....N_s$ denotes the voltage state associated at each prediction. The complete set of equations is represented by:

$$\begin{cases} \hat{i}^s_{d,k+1|k} = f_d\left(\hat{\boldsymbol{i}}_{dq,k|k-1}, \boldsymbol{u}^s_{dq,k|k-1}, \hat{\omega}_{me,k|k-1}\right) \\ \hat{i}^s_{q,k+1|k} = f_q\left(\hat{\boldsymbol{i}}_{dq,k|k-1}, \boldsymbol{u}^s_{dq,k|k-1}, \hat{\omega}_{me,k|k-1}\right) \\ \hat{\tau}^s_{k|k-1} = \frac{3}{4} p\left\{\Lambda_{mg}\left(\hat{i}_{q,k|k-1} + \hat{i}^s_{q,k+1|k}\right) + (L_d - L_q)\left(i_{q,k|k-1} i_{d,k|k-1} + \hat{i}^s_{d,k+1|k} \hat{i}^s_{q,k+1|k}\right)\right\} \\ \hat{\omega}^s_{me,k+2|k+1} = f_\omega\left(\hat{\omega}_{me,k+1|k-1}, \hat{i}^s_{q,k+1|k}, \hat{i}^s_{q,k+1|k}, \hat{\tau}_L\right) \end{cases} \tag{3.25}$$

The torque equation (3.18) at step $(k+1)T_c$ becomes a "prediction value", since the inputs of (3.11) are the initialized currents in kT_c (now predicted and not measured).

3.5 THE HIERARCHICAL DECISIONAL STRUCTURE

To determine the couple of voltage vectors $\boldsymbol{u}^{s^*}_{dq,k}, \boldsymbol{u}^{s^*}_{dq,k+1}$ best suited to minimize the generic speed error at step $(k+N_{pd})T_c$ (equivalently the best control input s^*) and to limit the oscillations of the current $|i|^{s^*}_{k+N_{pd}}$, the algorithm performs a hierarchical series of tests using the prediction model of Sec. 3.3. Firstly, the predicted current for each of the N_s voltage states is checked for compliance with the motor thermal limit. This means that the voltage vectors that not ensure a specific bound (i. e. of $k_I I_N$, with $K_I = 1 \div 2$) on the current amplitude are not considered suitable for the hierarchical test. Analytically:

$$\left|\hat{\boldsymbol{i}}^s_{k+N_{pd}}\right| = \sqrt{\left(\hat{i}^s_{d,k+N_{pd}}\right)^2 + \left(\hat{i}^s_{q,k+N_{pd}}\right)^2} \leq k_I I_N \tag{3.26}$$

It follows that, any of the $s = 0...N_s$ possible configurations that exceeds the current limit is excluded from a possible application at kT_c.
The remaining one constitute the subset S_{k,I_N} on which the speed error is evaluated. Fig. 3.4 summarizes the different steps described up to here.
Considering the discrete nature of the algorithm, the predicted speed error is calculated at step kT_c for the step $(k+N_{pd})T_c$, assuming that the speed reference ω^*_m remains constant within the prediction horizon N_{pd}. For this reason, to create a hierarchical structure, a maximum allowable boundary on the speed error (namely e_L) is fixed a priori, in order to guarantee a degree of freedom in the choice of vectors that give this minimum error for the *second hierarchical level*.
In particular, if more than one of the $N_s \in S_{k,I_N}$ voltage vectors ensure the e_L bound, the control adopts the decisional condition of the *second hierarchical level*. Otherwise, if $|e_\omega| > e_L$ the electric drive is in a transient condition (i. e. a speed transient condition or a sudden load torque variation), and only the vector that guarantees the minimum speed error defined by (3.27) is chosen.
Up to this point the algorithm operates in the *first hierarchical level*, and in transient the optimal voltage vector $s^* \in S_{k,I_N}$ is simply calculated as:

$$\begin{cases} s^* = min\left\{e^s_{\omega m,k+1+N_{pd}}\right\} \\ e^s_{\omega m,k+1+N_{pd}} = \left|\hat{\omega}^s_{m,k+1+N_{pd}} - \omega^*_m\right| \quad s \in S_{k,I_N} \end{cases} \tag{3.27}$$

At the end of the transient the speed error is in the e_L boundary. All the voltage configurations that produce an error within e_L will form a subset $S_{k,\omega} \subset S_{k,I_N}$ that satisfies both thermal and speed constraints.
Additional demands on the control algorithm are in the choosing a specific combination of voltage vectors, although in this research the current has been considered as a basic requirement, since this leads to a small torque ripple.
One possible solution is to force the PMSM-IPM to work close to the MTPA trajectory. This feature represents the target of the *second hierarchical level*. The MTPA condition is derived by considering the same polar notation for the currents i_d and i_q described in Sec. 2.3 (i. e. (2.12)), readopted for the purpose of this control as:

$$M^s_{k+N_{pd}} := \begin{cases} \hat{i}^s_{d,k+N_{pd}} + \dfrac{(L_d - L_q)}{\Lambda_{mg}}\left[\left(\hat{i}^s_{d,k+N_{pd}}\right)^2 - \left(\hat{i}^s_{q,k+N_{pd}}\right)^2\right] \\ 2\dfrac{(L_d - L_q)}{\Lambda_{mg}}\hat{i}_{d,k+N_{pd}} < -1 \end{cases} \tag{3.28}$$

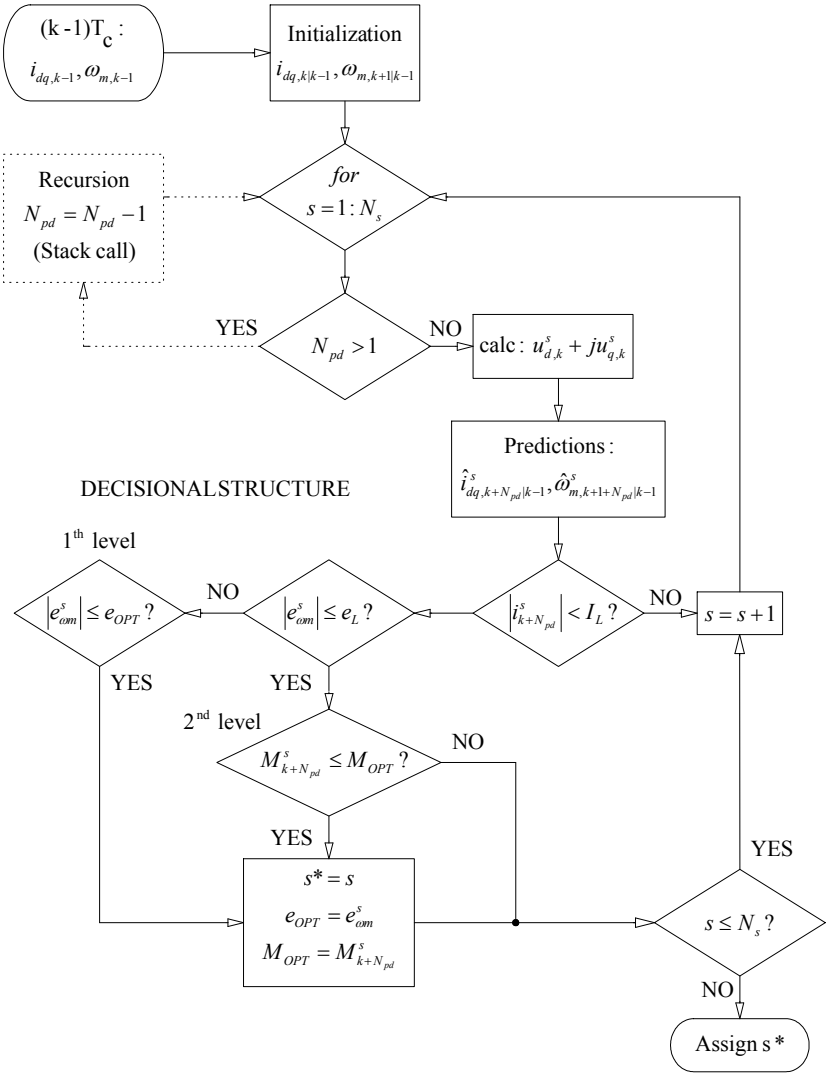

Fig. 3.4: Block diagram of the hierarchical control structure.

The (3.28) is evaluated for each of the remaining voltage configurations ($S_{k,\omega} \subset S_{k,I_N}$), and the second hierarchical subset $S_{k,M}$ is then:

$$S_{k,M} = \left\{ M^s_{k+N_{pd}} \ | s \in S_{k,\omega} \right\} \tag{3.29}$$

The hierarchical subset $S_{k,M}$ is constituted by all the configurations (i. e. the possible state voltage vectors) that fall within a prefixed range of speed error and that produce an approximated MTPA condition. From these alternatives, the control simply selects the optimal voltage vector $s^* \in S_{k,M}$ that represents the minimum into the subset $S_{k,M}$:

$$s^* = min \left\{ M^s_{k+N_{pd}} \right\} \tag{3.30}$$

In theory, if a sufficient high number of alternatives (at least two) remain in the *second hierarchical level*, a second bound can be used in the "MTPA" subset of vectors and the control action could predict an extra selection, for example by evaluating the number of commutations $n^s_{k,cc}$ that each voltage projection would require, finally choosing the

most advantageous one. Both zero vectors 000 and 111 should be evaluated, and a boundary on the MTPA condition should be inserted as in the *second hierarchical level*.

3.5.1 *The HDPC with augmented state vectors set*

The conventional DPC schemes avoid the use of modulation techniques [44], restricting the control input to the only seven state voltage vectors. The reduced set causes high ripple at steady state states, which can be mitigated only by a higher switching frequency. This approach is quite similar to the original DTC scheme, and as direct consequence of the variable switching frequency [66] an high current spread with a relatively high torque ripple are always present in this type of control. Moreover, when the number of states is only $N_s = 7$ and the voltage vector is already near to the requested value for steady-state condition, each voltage change induces a large deviation from the reference point. It is worth to note that many papers on finite-state DPC do not present results obtained at a full industrial DC-link bus voltage of 560 V, due the unacceptable high current ripple.
The correspondence between voltage configurations and equivalent switching states that the VSI can generate in absence of external modulation strategy is given in Fig.3.5 (for the case of $N_s = 7$). With the aim of reducing the current ripple without undermining the simplicity of the finite-state solution, the proposed speed and current predictive control algorithm overcomes the problems related to the limited use of the control region of the converter by introducing the possibility to use an extended number of states of the VSI within one sample period [67].

Voltage s	$u_{s\alpha}$	$u_{s\beta}$	S_2	S_4	S_6
$\boldsymbol{u}_{s0}$	0	0	0	0	0
$\boldsymbol{u}_{s1}$	$\frac{2U_{DC}}{3}$	0	1	0	0
$\boldsymbol{u}_{s2}$	$\frac{U_{DC}}{3}$	$\frac{\sqrt{3}U_{DC}}{3}$	1	1	0
$\boldsymbol{u}_{s3}$	$-\frac{U_{DC}}{3}$	$\frac{\sqrt{3}U_{DC}}{3}$	0	1	0
$\boldsymbol{u}_{s4}$	$-\frac{2U_{DC}}{3}$	0	0	1	1
$\boldsymbol{u}_{s5}$	$-\frac{U_{DC}}{3}$	$-\frac{\sqrt{3}U_{DC}}{3}$	0	0	1
$\boldsymbol{u}_{s6}$	$\frac{U_{DC}}{3}$	$-\frac{\sqrt{3}U_{DC}}{3}$	1	0	1
$\boldsymbol{u}_{s7}$	0	0	1	1	1

(a) *Switching states configuration with $N_s = 7$ voltage vectors.*

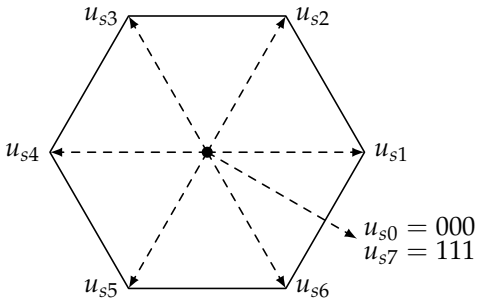

(b) *Equivalent graphic representation.*

Fig. 3.5: Voltage vectors configurations with $N_s = 7$ and equivalent graphical representation.

The use of a single switching vector during the whole period makes unfeasible the use of a standard DC-link bus voltage of the industrial inverters ($\approx 600\,\mathrm{V}$) unless the DC-link bus voltage has not been reduced. In other terms, the absence of an intermediate vector into a discrete sampling period leads to an acceptable current ripple and the torque quality deteriorates immediately by increasing the U_{DC}. One possible solution consists in reducing the sampling period T_c (equivalently increasing the sampling frequency f_{sw}, if supported by the VSI), but this requires a sufficiently powerful hardware in order to execute the algorithm in an execution time T_e compatible with the sampling period T_c. This is one of the reasons for FPGA implementation of control.
As an alternative, the current ripple may be reduced by increasing the number of voltage states applied into a sampling period T_c [68]. This work explores and exploits the use of six extra voltage vectors allocated in the middle of each conventional $\pi/3$ sector of voltage $\alpha\beta$ plane, as shown in Fig.3.6. These extra vectors are introduced as voltage configurations to be tested during the control decisional structure as equivalent projections in the dq plane.
In Fig.3.6 is also reported the relationship between the switching configuration and the equivalent voltage projection in the $\alpha\beta$ reference frame. The equivalent control scheme with $N_s = 14$ states is represented in Fig.3.7, where basically two adjacent voltage configurations corresponding to zero (or non-zero) voltages are applied during a modulation period. It follows that, the application time of an intermediate vector is fixed a priori and it is equal to $0.5T_c$ (equivalently in the middle of every sector of the hexagon), as graphically reported in Fig.3.6. Moreover, it is worth noting that the linear combination of the two nearest physical switching states is equivalent to commutation frequency of $2f_{sw}$. This control strategy leads to avoid an PWM modulator, since in theory, the use of a modulator could produce infinite configurations of voltage states, negating the concept on which is founded this control algorithm. Furthermore, the number of states that can be tested is limited by the available computational resources, which limits the number of possible iterations N_s in according with the execution time T_e. Moreover the use of only few vectors leads to have a more robust control with respect to the parameter variations, as verified during the experimental tests.
Sec. 3.6 reports a collection of tests that prove the practical unfeasibility of the canonical solution with $N_s = 7$ voltage vectors and other simulations that show the improvement by using $N_s = 14$.
The application of the entire DC-link bus voltage is required only to balance the BEMF at the nominal speed or during the transient conditions, in the remaining intermediate cases (as steady-state conditions without load, slow speed or torque variations, etc.) the amplitude of the voltage vector can be reduced percentually. In order to obtain this result, the control region of the converter is reduced by multiplying the amplitude of each voltage state by a coefficient $0 < k_M \leq 1$ fixed at priori. In this way the number of voltage states to be tested by the prediction algorithm remains equal to $N_s = 14$, while the actual converter region is extended (i. e. not limited to peripheral vertices). The adaptive coefficient k_M is calculated by considering the prediction of the speed (i. e. the slope of the speed by considering the difference between the previous steps) and the DOB load torque estimation, assuming that the maximum value of k_M (i. e. $k_M = 1$) is associated to every torque or speed variation while at every intermediate or steady-state operation condition (identified by the estimation and prediction equations) is associated a $k_M \in 0.3 \div 0.5$.
In other terms, k_M is changed during the normal operation and depends by the requirements of the algorithm (e. g. during the *second hierarchical level* the voltage balance depends only by the Electromotive Force (EMF), and the amplitude can be reduced), although it is normally equal of $k_M = 1$. Fig.3.6 shows the graphical representation of the extra added vectors with the equivalent voltage states indicated with the circles.

Voltage s	$u_{s\alpha}$	$u_{s\beta}$	S_2	S_4	S_6
$\boldsymbol{u}_{s0}$	0	0	0	0	0
$\boldsymbol{u}_{s1}$	$\frac{2U_{DC}}{3}$	0	1	0	0
$\boldsymbol{u}'_{s1}$	$\frac{U_{DC}}{2}$	$0.2886U_{DC}$	1	0.5	0
$\boldsymbol{u}_{s2}$	$\frac{U_{DC}}{3}$	$\frac{\sqrt{3}U_{DC}}{3}$	1	1	0
$\boldsymbol{u}'_{s2}$	0	$\frac{\sqrt{3}U_{DC}}{3}$	0.5	1	0
$\boldsymbol{u}_{s3}$	$-\frac{U_{DC}}{3}$	$\frac{\sqrt{3}U_{DC}}{3}$	0	1	0
$\boldsymbol{u}'_{s3}$	$-\frac{U_{DC}}{2}$	$0.2886U_{DC}$	0	1	0.5
$\boldsymbol{u}_{s4}$	$-\frac{2U_{DC}}{3}$	0	0	1	1
$\boldsymbol{u}'_{s4}$	$-\frac{U_{DC}}{2}$	$-0.2886U_{DC}$	0	0.5	1
$\boldsymbol{u}_{s5}$	$-\frac{U_{DC}}{3}$	$-\frac{\sqrt{3}U_{DC}}{3}$	0	0	1
$\boldsymbol{u}'_{s5}$	0	$-\frac{\sqrt{3}U_{DC}}{3}$	0.5	0	1
$\boldsymbol{u}_{s6}$	$\frac{U_{DC}}{3}$	$-\frac{\sqrt{3}U_{DC}}{3}$	1	0	1
$\boldsymbol{u}'_{s6}$	$\frac{U_{DC}}{2}$	$-0.2886U_{DC}$	1	0	0.5
$\boldsymbol{u}_{s7}$	0	0	1	1	1

(a) *Switching states configuration with $N_s = 14$ voltage vectors, associated by a VHDL specific routine.*

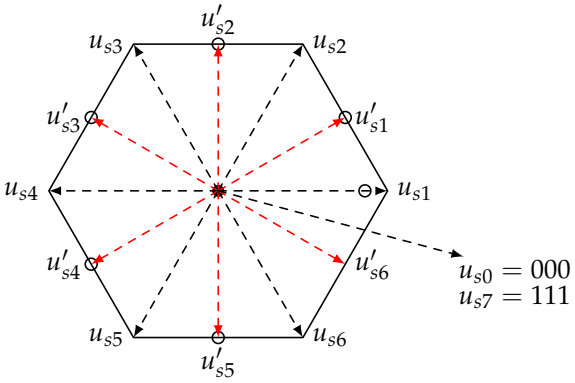

(b) *Equivalent graphic representation.*

Fig. 3.6: Voltage vectors configurations with $N_s = 14$ and equivalent graphical representation.

In conclusion, this modulation strategy avoids the use of a conventional PWM modulator, while giving the finite-state DPC the possibility of reducing the current and speed ripples by resizing the optimal voltage vectors depending on the drive operating point.

3.5.2 *The length of the prediction horizon*

This paragraph details the behaviour of the control prediction algorithm when the prediction horizon is greater of a single step of prediction. If $N_{pd} \geq 1$ the (3.4) must be further exploited to get the prediction of current and speed at step $k + N_{pd}$. A possible solution is to explore all the combinations and ramifications in a recursive way, whose number and arrangement depends by the prediction horizon N_{pd} and by the number of

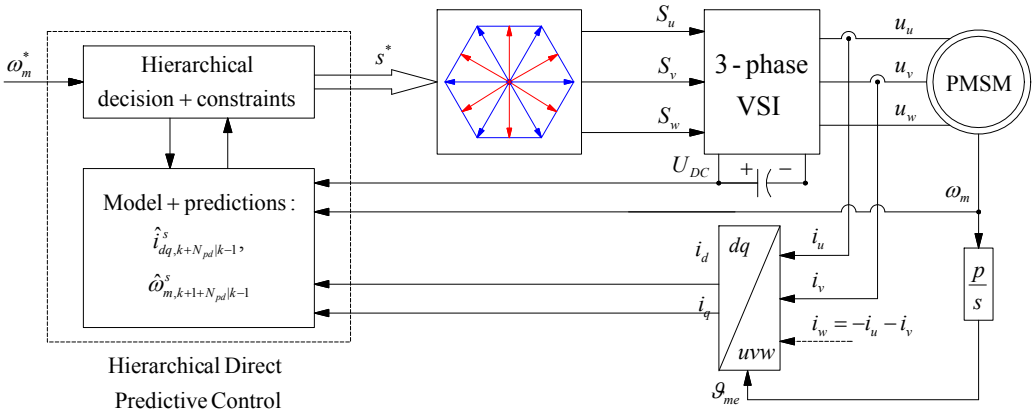

Fig. 3.7: Block diagram of the structure of the HDPC with $N_s = 14$ voltage vectors.

considered voltage states N_s. In other terms, the prediction and the control decisional structure are repeated and evaluated $N_{pd} - 1$ times for each of the $s = 0...N_s$ state voltage vectors of the VSI.
This situation can be represented by the following set of equations:

$$\begin{cases} \hat{i}^s_{d,k+N_{pd}|k+N_{pd}-1} = f_d\left(\hat{\boldsymbol{i}}_{dq,k+1|k}, \boldsymbol{u}^s_{dq,k+1|k}, \hat{\omega}_{me,k+1|k}\right) \\ \hat{i}^s_{q,k+N_{pd}|k+N_{pd}-1} = f_q\left(\hat{\boldsymbol{i}}_{dq,k+1|k}, \boldsymbol{u}^s_{dq,k+1|k}, \hat{\omega}_{me,k+1|k}\right) \\ \hat{\omega}^s_{me,k+1+N_{pd}|k+N_{pd}} = f_\omega\left(\hat{\omega}_{me,k+1|k}, \hat{i}^s_{dq,k+N_{pd}|k+N_{pd}-1}, \hat{\tau}_L\right) \end{cases} \tag{3.31}$$

The hierarchical decisional structure of Sec. 3.5 is repeated N_s times, and this means that the branch and bound exploration grows exponentially, since $N_s^{N_{pd}}$ possible configuration must be evaluated, and this critical feature of the algorithm (for $N_{pd} \geq 1$) is an aspect that must be taken into account for a real-time implementation. The prediction horizon N_{pd} is usually limited to only few steps, but for the purposes of this research a more detailed simulative analysis has been performed to understand the influence and the advantages in the use of a $N_{pd} \geq 1$.
In order to weigh the contribution of the choice of a vector in every node of the trajectory, the exploration starts from the last level of the entire tree of possibilities. The situation can be explained supposing to be in the second-last exploration tree position, where the algorithm is testing one of the N_s voltage vectors and it has in memory the "weight term" associated to the forward node (i. e. that of N_{pd}).
The "weight term" w_N is calculated as product between the speed error and the equivalent MTPA condition $w_{N_{pd}} = |e^s_{\omega m,k+1+N_{pd}} M^s_{k+N_{pd}}|$, and takes into account the averaged distance between the tracking reference and the optimal trajectory that can be achieved using the N_s voltage vectors available.
It follows that, every intermediate result of the hierarchical decision of the node is added to the result of the HDPC routine of Sec. 3.5 to the actual state decision. To give the highest priority at the choice of the first vector of the optimal trajectory, a percentage reduced weight is considered in the recursive creation of the trajectory. At the end of the $N_s^{N_{pd}}$ calculations, the "weight term" w_N takes into account the contribution of the trajectory associated to every of the ($s = 0...N_s$) voltage vectors, and the first optimal vector on N_s possible trajectories is selected choosing the one that returns the lowest

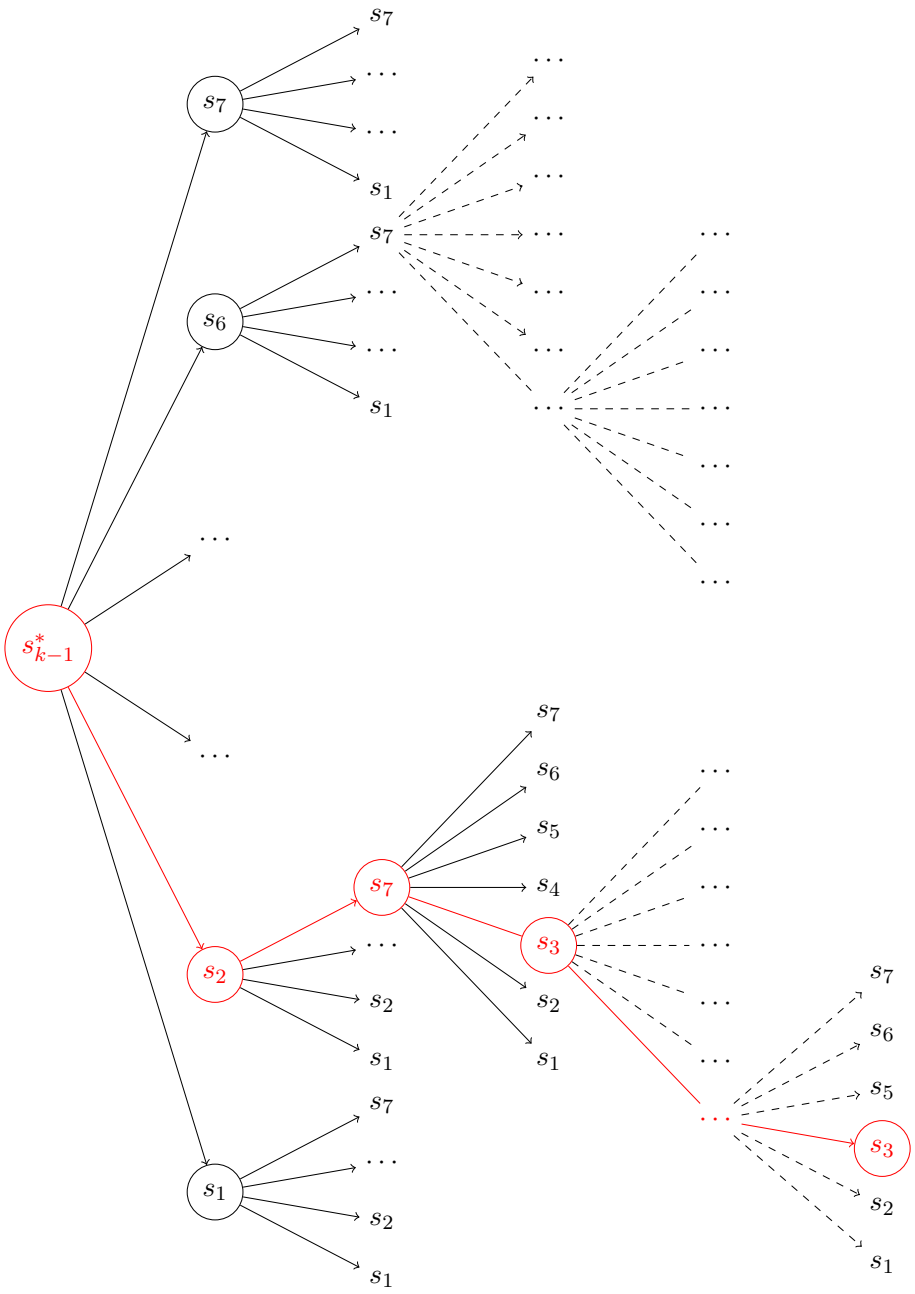

$\mathcal{O}(k+1) = 7^1$ $\mathcal{O}(k+2) = 7^2$ $\cdots$ $\cdots$ $\mathcal{O}(k+N_p) = 7^{N_{pd}}$

Fig. 3.8: Possible evolution of the states of the HDPC algorithm considering only $N_s = 7$.

w_N. Better results in term of torque quality and reduced computational demands can be achieved by choosing carefully the optimal length of the prediction horizon.
In theory, the consideration of a prediction horizon $N_{pd} > 1$ should avoid nervous effects on the control behaviour, since the choice of a optimal voltage vector for $N_{pd} = 1$ could lead to a breach of the thermal limits of the machine and a sudden variation in

the control action if the same horizon had been analysed by considering two or more step of predictions, adopting the structure described above.
The main concept is that the optimal vector could not be the optimal vector compared with the single step of prediction, but in general it is representative of a trajectory that is the optimal over the prediction horizon.
A sketch of the simple case with $N_s = 7$ voltage vectors is represented in Fig.3.8, where the path that matches all the requirements of the control is highlighted in red. Fig.3.8 it is also useful to understand that the recursive iteration of the algorithm produces an optimal voltage vector associated at every step of prediction, and that is used for the calculation of the previous step of prediction, in order to obtain the optimal trajectory.
The simulation was performed by considering a series of functions that contains the prediction of the equations of Sec. 3.3 together with the function that implements the HDPC to selects the optimal vector s^*. A flexible structure has been created in order to easily change different types of parameters (as the number of vectors N_s or the prediction horizon N_{pd}), although a simulation time of many hours is required only to test the predictive algorithm with $N_{pd} = 4$.
Anyway, there are no significant differences in the control current and speed quality if a prediction horizon of $N_{pd} = 1$ or $N_{pd} = 4 \div 5$ is considered. From the mechanical point of view, this control behaviour can be understood by observing that the mechanical time constant of the motor is sufficiently greater of few sampling periods, and so the action of the control has not a sufficient long observation period to change the predicted trajectory in an efficient way. Furthermore, the dynamic of the currents with the increased number of prediction steps has been verified in Sec. 3.6, by simulating the behaviour of the control considering the number of commutations in a fixed time interval.
Anyway, although this choice not influences significantly the dynamic and the currents or torque control quality, the computational requirement grows exponentially. This means that complexity and hardware requirements grows rapidly with the increased number of N_{pd} without having a direct advantage in terms of torque ripple reduction that could justify the use of $N_{pd} \geq 1$.

3.5.3 *Current ripple estimation*

In order to know with precision and in advance the minimum current ripple, during the normal operating of the control routine can be estimated analytically with accuracy. If we assume to be in steady state conditions, the time continuous equations (1.19) and (1.21) can be rewritten as:

$$\begin{cases} U_d = R_s I_d - \Omega_{me} L_q I_q \\ U_q = R_s I_q + \Omega_{me} L_d I_d + \Omega_{me} \Lambda_{mg} \\ \tau_0 = B_m \Omega_m + \tau_L = \dfrac{3}{2} p (\Lambda_{mg} I_q + (L_d - L_q) I_q I_d) \end{cases} \tag{3.32}$$

where the symbols U_d, U_q, I_d, I_q, Ω_{me} and τ_0 denote the variables in steady state operating condition. By defining as $\Delta_{ud,k} \triangleq u_{d,k} - U_d$ and $\Delta_{uq,k} \triangleq u_{q,k} - U_q$ the voltage variations, the reverse triangle inequality[2] returns:

2 The reverse triangle inequality states that, $\forall\, x, y \in \mathbb{R}: |x - y| \geq ||x| - |y||$

$$\begin{cases} \left| \left| u_{q,k} \right| - \left| U_q \right| \right| \leq \left| \Delta_{uq,k} \right| = \left| u_{q,k} - U_q \right| \\ \left| \left| u_{d,k} \right| - \left| U_d \right| \right| \leq \left| \Delta_{ud,k} \right| = \left| u_{d,k} - U_d \right| \end{cases} \tag{3.33}$$

The steady-state voltage U_d and U_q depends by the mechanical steady-state balance of (3.32), derived by substituting the I_d and I_q expressions from the mechanical equation in the first and second of (3.32).

$$\begin{cases} U_d = \dfrac{R_s \left(B_m \Omega_m + \tau_L - \dfrac{3}{2} p \Lambda_{mg} I_d \right)}{\left(L_d - L_q \right) I_q} - \Omega_{me} L_q I_q \\ U_q = \dfrac{R_s \left(B_m \Omega_m + \tau_L \right)}{\dfrac{3}{2} p \left(\Lambda_{mg} + \left(L_d - L_q \right) I_d \right)} + \Omega_{me} L_d I_d + \Omega_{me} \Lambda_{mg} \end{cases} \tag{3.34}$$

From (3.4), the couple of discretized currents $i_{d,k+1}$ and $i_{q,k+1}$ at the instance $(k+1)T_c$ are[3]:

$$\begin{cases} i_{d,k+1} = \left(1 - \dfrac{R_s T_c}{L_d} \right) i_{d,k} + \dfrac{T_c}{L_d} \left(u_{d,k} + \omega_{me,k} L_q i_{q,k} \right) \\ i_{q,k+1} = \left(1 - \dfrac{R_s T_c}{L_q} \right) i_{q,k} + \dfrac{T_c}{L_q} \left(u_{q,k} - \omega_{me,k} L_d i_d - \omega_{me,k} \Lambda_{mg} \right) \end{cases} \tag{3.35}$$

that, after some algebraic manipulations can be rewritten by substituting the steady-state values of (3.32) into the (3.35):

$$\begin{cases} i_{d,k+1} = I_d + \dfrac{T_c}{L_d} \left(u_{d,k} - \left(\underbrace{R_s I_d + \Omega_{me} L_q I_q}_{U_d} \right) \right) = I_d + \dfrac{T_c}{L_d} \Delta_{ud,k} \\ i_{q,k+1} = I_q + \dfrac{T_c}{L_q} \left(u_{q,k} - \left(\underbrace{R_s I_q + \Omega_{me} L_d I_d + \Omega_{me} \Lambda_{mg}}_{U_q} \right) \right) = I_q + \dfrac{T_c}{L_q} \Delta_{uq,k} \end{cases} \tag{3.36}$$

From (3.36), the current ripple variation can be written as:

$$\begin{cases} \Delta_{id,k+1} \triangleq i_{d,k+1} - I_d = \dfrac{T_c}{L_d} \Delta_{ud,k} \leq \dfrac{T_c}{L_d} \left(u_{d,k} + U_d \right) \\ \Delta_{iq,k+1} \triangleq i_{q,k+1} - I_q = \dfrac{T_c}{L_q} \Delta_{uq,k} \leq \dfrac{T_c}{L_q} \left(u_{q,k} + U_q \right) \end{cases} \tag{3.37}$$

and then, the current ripple dependencies from the voltage ripple variation $\Delta_{u,k}$ and the sampling period T_c is shown. Since the applied voltage vectors $u_{q,k}$ and $u_{d,k}$ are chosen from a finite alphabet of voltage configuration (i. e. $s = 0 \ldots N_s$, as defined by (3.24)),

3 $\langle i_d \rangle_{k-1} = i_{d,k-1}$, $\langle i_q \rangle_{k-1} = i_{q,k-1}$, $\langle \omega_{me} i_d \rangle_{k-1} = \omega_{me,k-1} i_{d,k-1}$ and $\langle \omega_{me} i_q \rangle_{k-1} = \omega_{me,k-1} i_{q,k-1}$.

by applying the reverse triangular inequality and the triangle inequality[4] to (3.33), it follows that:

$$\begin{cases} \left|u^s_{d,k+1}\right| + |U_d| \geq \left|\Delta_{id,k+1}\right| \geq \dfrac{T_c}{L_d}\left|\left|u^s_{d,k+1}\right| - |U_d|\right| \\ \left|u^s_{q,k+1}\right| + |U_q| \geq \left|\Delta_{iq,k+1}\right| \geq \dfrac{T_c}{L_q}\left|\left|u^s_{q,k+1}\right| - |U_q|\right| \end{cases} \tag{3.38}$$

and then, since the maximum voltage value is on the bound of the modulation hexagon, (i. e. that shown in Fig.3.5 or Fig.3.6), the previous inequality can be rewritten as:

$$\begin{cases} b_{dm} = \dfrac{T_c}{L_d}\left|\dfrac{2}{3}U_{dc} - |U_d|\right| \leq \left|\Delta_{id,k+1}\right| \leq \dfrac{2}{3}U_{dc} + U_d = b_{dM} \\ b_{qm} = \dfrac{T_c}{L_q}\left|\dfrac{2}{3}U_{dc} - |U_q|\right| \leq \left|\Delta_{iq,k+1}\right| \leq \dfrac{2}{3}U_{dc} + U_q = b_{qM} \end{cases} \tag{3.39}$$

The (3.39) estimates a minimum current ripple and shows that the ripple is related to the sampling time T_c and the DC-bus voltage U_{DC}. This means that the improvements of the control action in terms of current quality are strictly related to these two parameters which bind the overall control behaviour. It is worth noting that the (3.39) gives an important information on the minimum and maximum current ripple (b_m and b_M), which cannot have a current limit less of b_m and higher of the right hand side of (3.39) (i. e. b_M, in the dq components). Moreover, the relationship (3.39) is verified without considering the boundary on the voltage vectors, although the reduction of the current undulation, which depends by the control action during the different hierarchical levels remains the main control goal.

3.6 SIMULATION RESULTS

A complete fixed point model of the control has been created in Matlab/Simulink environment together with the Xilinx System Generator toolbox to emulate the real behaviour of the algorithm described in Sec. 3.3, when programmed into the FPGA platform (including I/O interfacing and quantisation effects).
The Xilinx tool provides an environment to graphically build up the desired functionality in Simulink and to generate the FPGA compiled project, allowing the inclusion of low level VHDL code or the use of pre-compiled Xilinx/Simulink blocks. For the purposes of this research, is useful to adopt different strategies of implementation, by including both pre-compiled Xilinx blocks, m-code equivalent blocks and VHDL code.
The entire prediction and initialization blocks are written in equivalent m-code from Xilinx, where all the variables are programmed and scaled to be in the Q-N notation. The Q-N notation is a particular fixed point number format, which has a number of fractional bits (and integer bits also) specified at priori, and it is particularly useful for this case, since the floating point representation is not admissible in the m-code equivalent structure (instead of the typical Matlab m-functions). In the algorithm implementation the number of bits used for the fractional part is equal of Q=8 and N=10, although in some routines the number of bits is increased to Q=14 and N=14. The number of bits is motivated by the numerical value of the products and constants in the equations of Sec. 3.3, by considering that the function is structured in order to resize the result of every mathematical operation, in order to avoid arithmetic overflows.

4 The triangle inequality states that, $\forall\, x,\, y \in \mathbb{R}$:$|x + y| \leq |x| + |y|$

The control simulation parameters have to be realistic, and the maximum commutation frequency (f_{sw}) of a commercial inverter of a few kW is generally limited to only 10 kHz. The value of f_{sw} is then selected in agreement with the experimental setup, and for the purposes of the control a sampling period of $T_c = 100\,\mu s$ (i. e. $f_{sw} = 8 - 10\,\text{kHz}$) has been considered (although the performance of the control, in terms of current ripple can only be better if the switching frequency is increased) with a prediction horizon $N_{pd} = 1$, as specified in Sec. 3.5.2.
As remarked in the previous paragraphs, although the finite set current predictive control schemes avoid the use of modulation techniques and only one of the seven discrete switching configurations of the power converter is applied during the whole switching period, most of the literature papers does not use the full industrial standard DC-link bus voltage of 560 V, due to the unacceptably high current ripple. Unfortunately, the choice of working at lower DC-link bus voltage does not fit for industrial applications, although to overcome this problem the feature of Sec. 3.5.1 must be considered.
The PMSM-IPM motor parameters are reported in Tab.2.2, while the design control parameters are reported in Tab.3.1. The boundary on the speed error e_L has to be chosen carefully, since it has an an essential role into splitting the transient and steady state operating condition, and then in the choice of the *first* or *second hierarchical level*. It has been selected proportionally to the nominal speed of the motor, in order to ensure sufficient resolution and to emulate the real speed variation around the steady state value.
In order to generalize as more as possible the present study, the special situations with a high switching frequency will not be considered, since, as remarked before, if the control has good performance with a sampling period of $T_c = 100\mu s$, the results achievable with a lower sampling period will be obviously better. For a first evaluation and tuning of the proposed algorithm, the overall control system has been simulated considering a prediction horizon $N_{pd} = 1$ with the minimum finite number of voltage vectors (i. e. $N_s = 7$).
The aim of these simulations is to show the effects of the basic control implementation with only $N_s = 7$ possible voltage states, using the real parameters of a industrial converter without the possibility to change the DC-link bus voltage. The first simulation deals with the speed response to a step reference of 600 rpm and two consecutive steps of load torque (from 0 to the nominal torque at steps of $\tau_N/2$).

Tab. 3.1: Simulation and experimental reference HDPC control parameters

Parameter	**Value**
Switching frequency f_s	10 kHz
State voltages N_s	14
Prediction horizon N_{pd}	1
Speed boundary e_L	$(0.001 \div 0.01)\,\omega_{mN}$ rpm
Current limit I_L	$(0.8 \div 1.5)\,I_N$ A
DC-link voltage U_{DC}	560 V
Modulation index k_M	$0.1 \div 1$

The results are summarized in Fig. 3.9, which reports the machine mechanical speed, the electromechanical generated torque, the currents behaviour in the dq reference frame and the load torque compensated with the DOB.

During the speed transient the machine is controlled exclusively by the *first hierarchical level*, since the speed error did not reach the e_L boundary (the speed error condition is dominant with respect to the other goals of the control, which become negligible).
The currents have a nervous behaviour with a high harmonic contents, and this effect is partially reflected on the generated torque that remains close to the rated limits (and the control does not follows the MTPA trajectory, since it is focuses on maximum torque generation to reaches the minimum speed error). The two positives load torque step of $\frac{\tau_N}{2}$ applied in sequence to the system are necessary to show the influence and the reaction of the DOB on the speed behaviour.
During these sudden load torque variations, the control operates in the *first hierarchical level* since the speed error for the transient time does not respect the boundary on e_L.
In particular, as mentioned in Sec. 3.3.1, the load torque disturbance leads to a steady state speed error (if not correctly compensated), but from Fig. 3.9e it is evident that DOB first-order response is sufficient to compensate the sudden load torque variation.
Fig. 3.10 shows the effects of a reduction in the U_{DC} voltage in terms of current quality and ripple reduction.
In detail, in Fig.3.10a is shown the same transient of Fig. 3.9, but considering a very low DC-link voltage of only $U_{DC} = 130\,\text{V}$. The simulation is then repeated in Fig.3.10b by considering a DC-link voltage of only $U_{DC} = 200\,\text{V}$, and in both cases the results show a sensible current ripple with respect of Fig. 3.9b. These simulations are considered only to prove that in absence of a major number of possible switching vectors, the current ripple is not acceptable if the standard industrial parameters are considered.
The set of simulations with $N_s = 7$ voltage vectors have been performed to appreciate the improvement achievable by introducing six extra voltage vectors, as described in Sec. 3.4. As previously mentioned the intermediate configurations are obtained in the simulation/experimental control architecture by applying two configurations of non-zero voltages or adjacent voltage vectors of Fig.3.6 during a modulation period. In the simulation plant the coefficient $k_M \in 0 \div 1$ is varied by considering the prediction of the speed and the on the load torque estimation, and it is reduced proportionally with the torque demand in the different operating conditions. The simulations have been repeated by considering the modulation strategy of Sec. 3.5.1, a standard DC-link bus voltage of 560 V and a sampling period of $T_c = 100\,\mu s$. Fig.3.11 collects the results obtained by testing the PMSM-IPM motor in Tab. 2.2, with a speed step variation followed by two consecutive torque transients of $\tau_N/2$ each, from zero to the nominal torque of the motor by considering $N_s = 14$ voltage vectors.
As expected, the current ripple of Fig.3.11b and Fig.3.11c is significantly reduced in comparison with that of 3.9b and 3.9c, and it is now acceptable from an industrial perspective, with a peak to peak current ripple of $0.6 \div 0.7\,\text{A}$ and a perfect match of the MTPA trajectory.
Fig.3.11c shows the successive working points of the drive in the $i_d - i_q$ plane (i. e. the accumulations of the consecutive currents variation steps): at the start up (maximum torque of Fig.3.11f, during the speed transient the motor is controlled exclusively by the *first hierarchical level*), then at steady state with no load and finally at increasing load torque (i. e. in the *second hierarchical level*). All points lie close to the theoretical MTPA curve (dotted line), confirming the correctness and the effectiveness of the proposed algorithm.
The same improvements are evident in the torque response of Fig.3.11f, while the usual high dynamic in the speed response (Fig.3.11a) is preserved as well as the DOB action of Fig.3.11e. In particular, the speed behaviour is quite smooth but the high bandwidth of this control is appreciable and fast as expected by a bang-bang controller. It is worth to note that the algorithm is capable of operating either with isotropic or anisotropic machines with no difference, for its inherent capability of reaching the minimum cur-

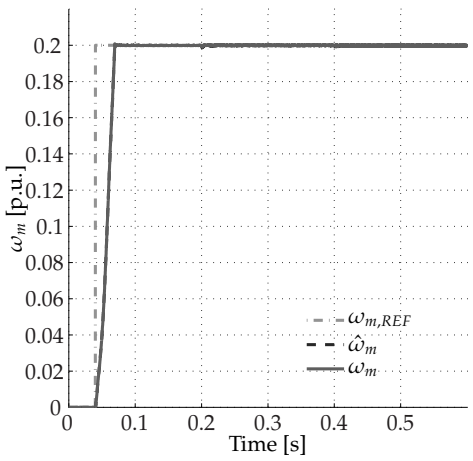

(a) *Mechanical speed* ω_m

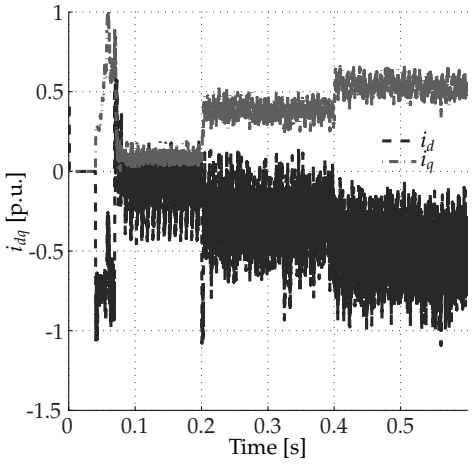

(b) *Currents transients of* i_d *and* i_q

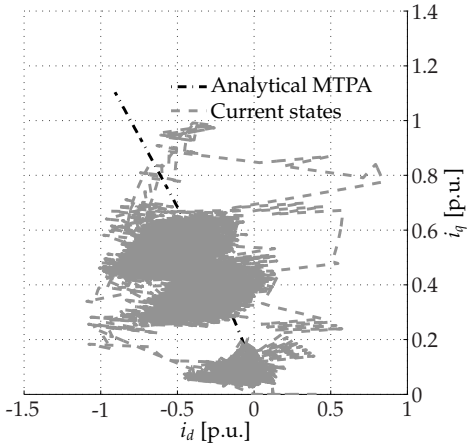

(c) *Overlapping of the analytic* MTPA *trajectory with the currents path*

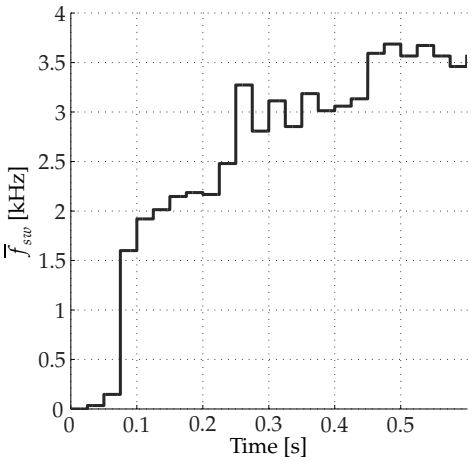

(d) *Switching frequency* f_{sw} kHz, *calculated with the* (3.40)

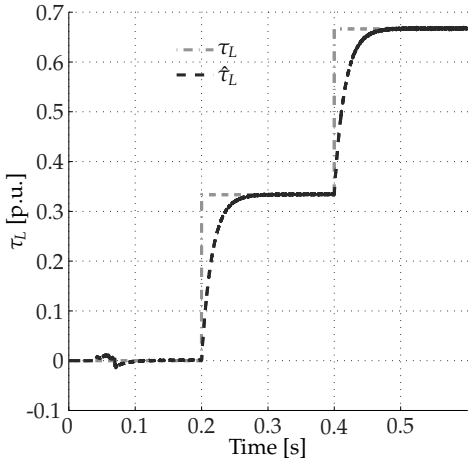

(e) *Load torque estimation with the* DOB

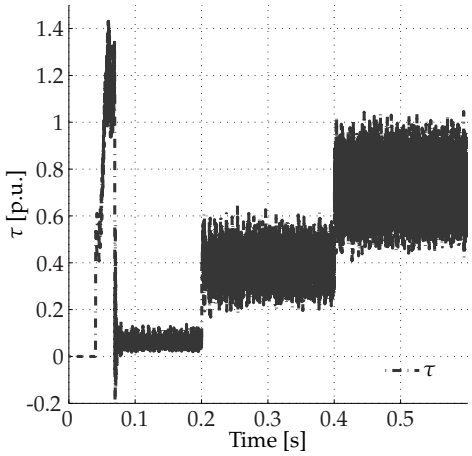

(f) *Electromagnetic torque of the PMSM drive*

Fig. 3.9: Speed, currents and torque during different transients using a HDPC configured with $N_s = 7$ voltage vectors. Machine in Tab.2.2, $T_c = 100\,\mu s$, $N_{pd} = 1$ and $U_{DC} = 560\,\text{V}$

rent vector at steady state in any case To testify and appreciate the feasibility of the algorithm, a series of simulations performed by using the PMSM-SPM motor in Tab.3.2 (the same available in the laboratory bench) has been also reported.

Tab. 3.2: Isotropic PM synchronous motor $PMSM_2$ parameters

Parameter	Value
Nominal ph-ph voltage U_N	400 Veff
Rated current I_N	3.7 Aeff
Pole pairs p	4
Saliency ratio $\xi = L_q/L_d$	≈ 1
Rotor inertia J_m	0.00795 kgm^2
Viscous friction B_m	0.0024 Nms

Although in the case of PMSM-SPM the MTPA condition is reduced to the standard FOC control, the results obtained by applying the algorithm are shown in Fig.3.12, where the same transients of torque and speed proposed in the previous cases are repeated again. Due to the low inductance value of this machine ($L_d \approx L_q$ in Tab.3.2), the control algorithm exhibits a deteriorated current quality, direct consequence of the particular type of machine adopted for the experiments.

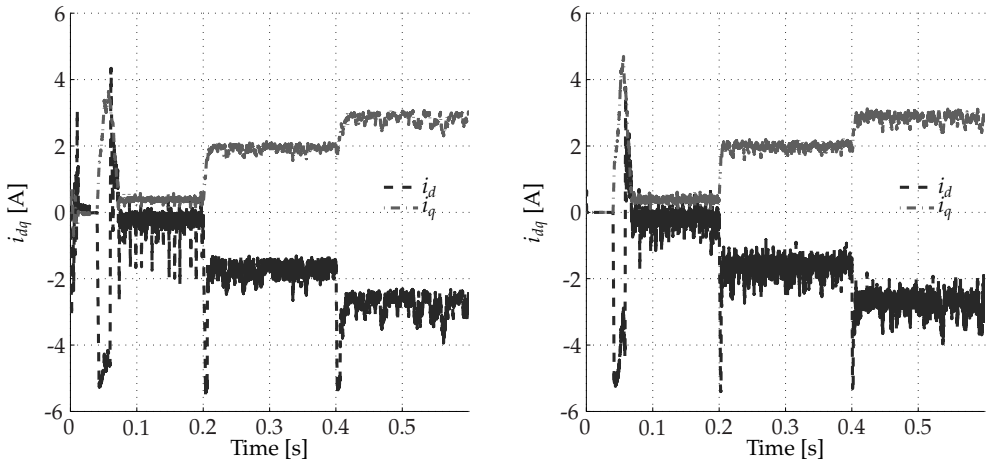

(a) *currents i_d and i_q with $U_{DC} = 130$ V* (b) *currents i_d and i_q with $U_{DC} = 200$ V*

Fig. 3.10: Currents dynamic of the machine in Tab.2.2 during the same transient of Fig. 3.9. $T_c = 100\,\mu s$, $N_{pd} = 1$ and a DC-bus voltage $U_{DC} = 130$ V and $U_{DC} = 200$ V

Due to intrinsic non-linearity of the proposed control algorithm, a direct comparison of its dynamic performances with respect to a conventional PI-cascade control is quite difficult (e. g. during a speed transient). A possibility is to set a small reference speed variation at no-load condition, in order to perform a small-signal evaluation similar to the one applicable to the case of field-oriented control. In this condition, the bandwidth of the control is calculated in a condition of quasi-linear relationship, and considering the raise time t_r, the equivalent bandwidth of the speed f_{Bw} can be calculated as $f_{Bw} = 0.3/t_r$. Since the average raise time (in presence of little step variations) is about $t_r = 2$ ms, the corresponding bandwidth is $f_{Bw} \approx 175$ Hz.
To testify the conjectures on the wantonness of using a high number of prediction steps of Sec. 3.5.2, in Fig.3.13 is shown the same current transient of Fig.3.11 in response of

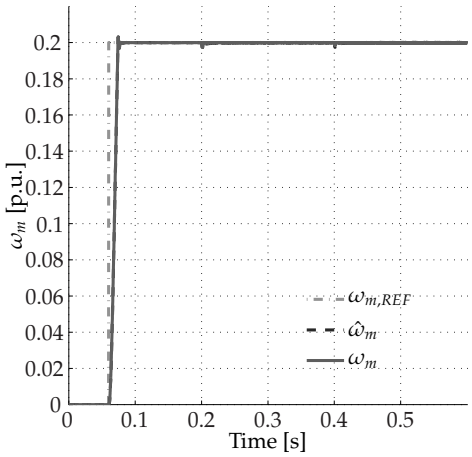

(a) *Mechanical speed* ω_m

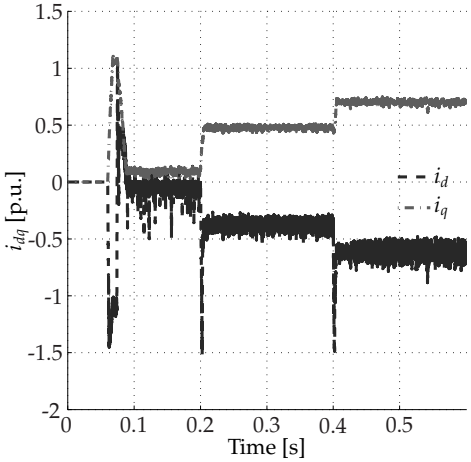

(b) *Currents transients of* i_d *and* i_q

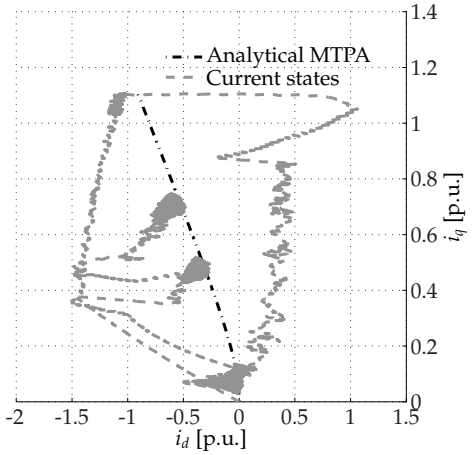

(c) *Overlapping of the analytic* MTPA *trajectory with the currents path*

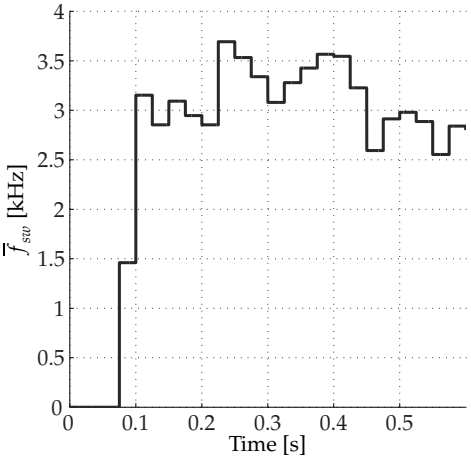

(d) *Switching frequency* f_{sw} kHz, *calculated with the* (3.40)

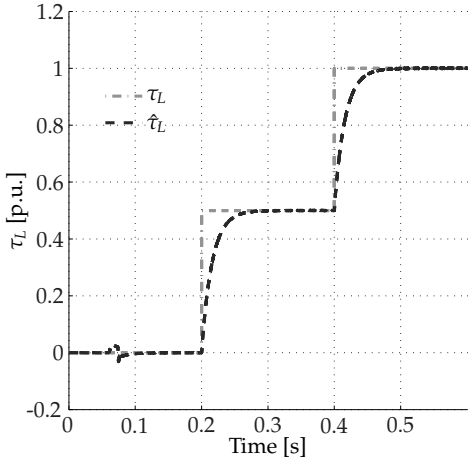

(e) *Load torque estimation with the* DOB

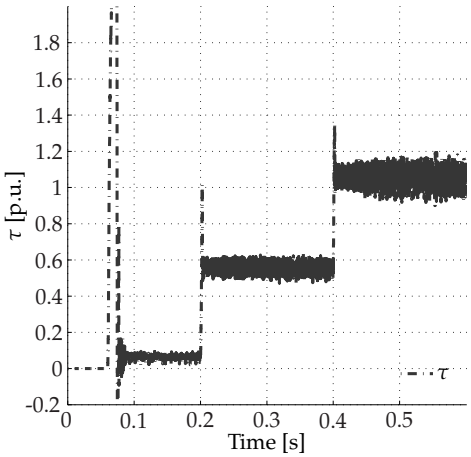

(f) *Electromagnetic torque of the PMSM drive*

Fig. 3.11: Speed, currents and torque during different transients using a HDPC configured with $N_s = 14$ voltage vectors. Simulation performed with the machine parameters of Tab.2.2 and control parameters in Tab.3.1.

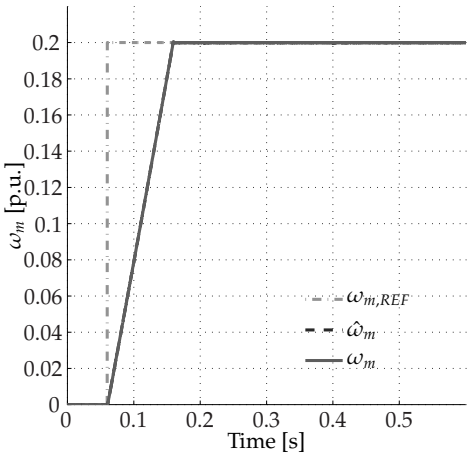

(a) *Mechanical speed* ω_m

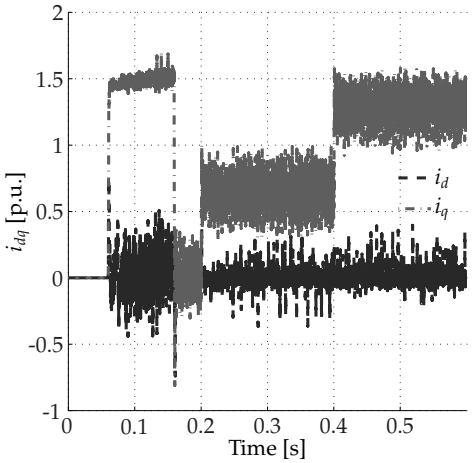

(b) *Currents transients of* i_d *and* i_q

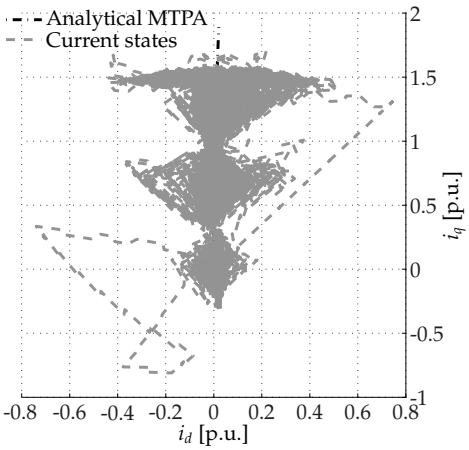

(c) *Overlapping of the analytic* MTPA *trajectory (i. e.* FOC *condition) with the currents path*

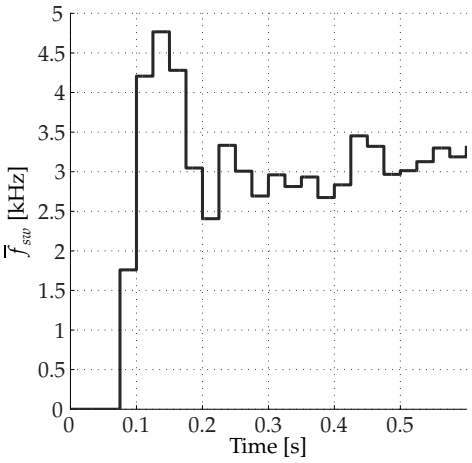

(d) *Switching frequency* f_{sw} kHz*, calculated with the* (3.40)

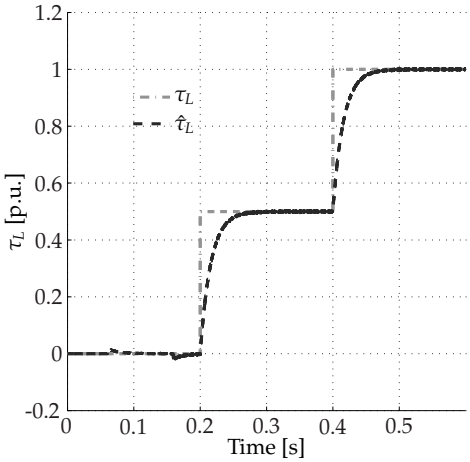

(e) *Load torque estimation with the* DOB

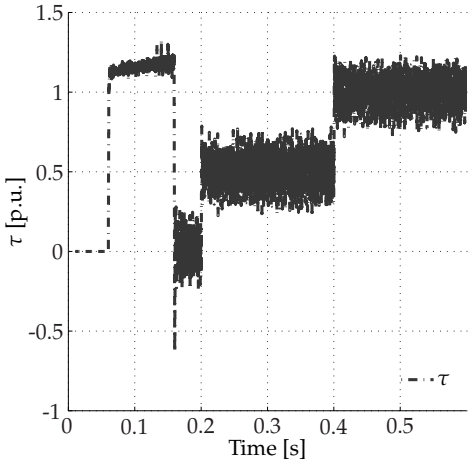

(f) *Electromagnetic torque of the PMSM drive*

Fig. 3.12: Speed, currents and torque during different transients using a HDPC configured with $N_s = 14$ voltage vectors. Simulation performed with the machine parameters of Tab.3.2 and control parameters in Tab.3.1.

the same speed step variation, but with the HDPC control algorithm configured as in Sec. 3.5.2, with $N_s = 14$ voltage vectors. It is quite evident that there are no benefits in term of current ripple reduction or torque quality (e. g. by direct comparison of Fig.3.11f and Fig.3.13b) if a greater prediction horizon ($N_{pd} = 3$) is considered but the computational requirement increase a lot.
The conjectures on the length of the prediction horizon of Sec. 3.5.2 are further supported by considering the total number of commutations in a fixed temporal window on the simulation time. As mentioned in Sec. 3.5.2, the absence of improvements in the speed behaviour can be easily justified by considering the mechanical time constant of the system, while the worsening of the currents must be properly analysed.
To this purpose, the total number of commutations of the VSI switches have been recorded among a fixed time interval, i. e. by considering the control with $N_{pd} = 1$ and $N_{pd} = 3$ prediction steps. The results in Fig.3.13 prove that despite the optimal voltage vector is the first on the trajectory trajectory on N_{pd} steps, the choice of a prediction horizon of $N_{pd} = 3$ steps leads to a deterioration in the quality of the currents and to a significant increasing in the number of switching commutations. Numerically, the number of commutations N_T is of $N_T = 597.42 \cdot 1e^6$ with $N_{pd} = 1$, $N_T = 850.38 \cdot 1e^6$ with $N_{pd} = 2$ and $N_T = 1084 \cdot 1e^6$ with $N_{pd} = 3$, and then the increment is $\approx 35\%$ at each increasing of the prediction step.

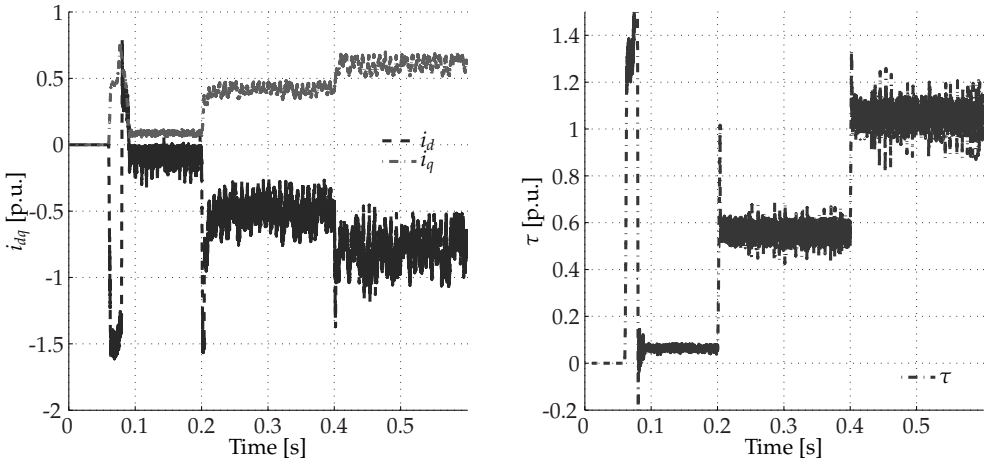

(a) *currents i_d and i_q with $N_{pd} = 3$*

(b) *Torque τ generated by the motor with $N_{pd} = 3$*

Fig. 3.13: Currents and torque dynamic of the machine in Tab.2.2 during the same transient of Fig. 3.11. $T_c = 100\,\mu s$, $N_{pd} = 3$ and DC-bus link of $U_{DC} = 560\,\text{V}$

Since the proposed control architecture has been studied to be implemented in a FPGA platform, the main advantage brought by this hardware platform is the achievable limited execution time T_e (as proved in 3.7).
This means that, if the hardware configuration of the VSI could guarantee a sufficient high sampling frequency (i. e. the average commutation of the switches must be in compliance with the sampling frequency f_{sw}), then it could be possible to take advantage of the limited execution time and improve the performances of the HDPC by reducing the sampling interval T_c (as analytically demonstrated in Sec. 3.5.3). To this purpose, a final batch of comparison simulations were carried out changing the sampling frequency f_{sw}. Fig.3.14 shows the same transient conditions of Fig.3.12 but repeated considering a reduced sampling period, in order to testify and appreciate the improved control behaviour.

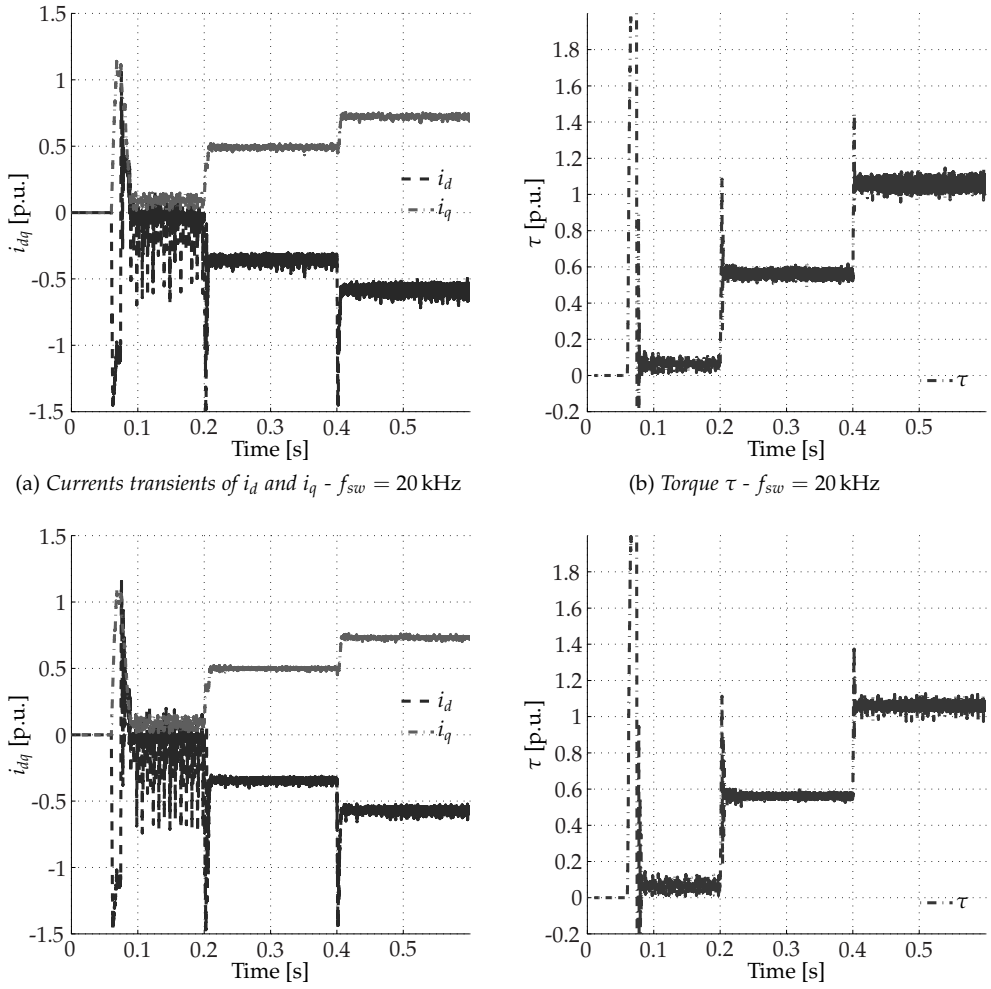

(a) *Currents transients of i_d and i_q - $f_{sw} = 20\,\text{kHz}$*

(b) *Torque τ - $f_{sw} = 20\,\text{kHz}$*

(c) *Currents transients of i_d and i_q - $f_{sw} = 40\,\text{kHz}$*

(d) *Torque τ - $f_{sw} = 40\,\text{kHz}$*

Fig. 3.14: Currents and torque during different transients by considering the HDPC configured with $N_s = 14$ voltage vectors with respect of different sampling frequencies f_{sw}. Motor of Tab.2.2, prediction horizon $N_{pd} = 1$ and DC-bus link of $U_{DC} = 560\,\text{V}$

The current quality and the electromagnetic torque show a linear improvement that is directly correlated to the increased sampling frequency. The speed and the DOB response are not influenced by the variation of the sampling period, and for the sake of compactness the related simulation results are not reported.

3.6.1 *Switching frequency analysis*

An aspect to be considered and investigate is related to the influence of the proposed choice of the vectors on the switching frequency of the converter. In the canonical modulation techniques (e. g. the SVM) the frequency is maintained constant, but the structure of the HDPC leads to a randomized choice of the voltage vector (i. e. at each sampling time the commutation frequency changes as direct effect of the choice of the voltage vector between the N_s alternatives), although the maximum switching frequency of the control is indirectly limited by the sampling frequency. In theory a constant switching frequency is always desirable for a better design and selection of the switching devices (i. e. the stress of the IGBTs is known a priori), and for this reason it is important to

understand the limitations of the proposed control strategy in terms of spectral distribution and switching frequency analysis.
To measure the effect of the control strategy on the switching frequency and reference tracking performance, it is important to define the average switching frequency of the converter $\overline{f}_{sw}$ as the average value of the switching commutations of all the six controlled power semiconductors in the converter into an observation period. Analytically:

$$\overline{f}_{sw} = \frac{1}{6N_{TC}T_c} \sum_{i=1}^{N_{TC}} (N_{cu,i} + N_{cv,i} + N_{cw,i}) \tag{3.40}$$

where N_{TC} defines the number of periods considered to calculate the commutations, while $N_{cu,i}$, $N_{cv,i}$ and $N_{cw,i}$ define the number of commutations of a single leg of the power converter. In the simulation results of the previous paragraphs (Fig.3.9d, Fig.3.11d and Fig.3.12d) is reported the averaged switching frequency calculated with the (3.40). An other advantage in the use of $N_s = 14$ vectors (instead of only $N_s = 7$) is the reduction of the $\overline{f}_{sw}$, as visible in Fig.3.9d and Fig.3.11d. Moreover, it can be observed that the amplitude of the currents display a spread spectrum as the one shown in Fig.3.15, where different sampling frequencies have been considered, presenting different ranges and magnitudes of the spectral content in each case.
In particular, the harmonics are spread over the entire spectrum (instead of the SVM), where they are concentrated around the fixed frequency. In some applications, a current spectrum as that of Fig.3.15 is not desirable because it can produce oscillations and complicate the design of components. Furthermore, if required by the specific application, it is important to control or limit the number of commutations of the power switches of the VSI and a possible solution consists into shape the spectrum by introducing an extra hierarchical level that takes into account the number of commutations. In this way, different frequencies have different weights in the control decisional structure allowing the control of the harmonic content of the variables.
To better understand the harmonic content caused by the random structure in the decisional architecture, a simple spectral analysis can be performed by considering the three-phase currents in the *uvw* reference in a steady state condition with the speed at a constant value (considering the amplitude of the *dq* currents in Fig.3.11b and Fig.3.12b), Fig.3.15 shows the current spectra obtained after a Fast Fourier Transform (FFT) post-elaboration. The normalized spectra at the fundamental frequency exhibit many low frequency harmonics, with an amplitude of few percent with respect to the fundamental one and a distributed noise (consequence of the choice of the optimal voltage vectors in a finite alphabet) with a low magnitude in the entire spectra range. The absence of high order harmonics (with respect to the standard SVM control technique at the same T_c), represents an aspect of improvement of the proposed control, since these harmonics are directly related to the losses in the electrical machines. Unfortunately, the low frequencies in the harmonic content could lead to mechanical resonances, which are often at a low frequency. This latter aspect could penalize the evaluation of the overall drive system from a mechanical point of view.

3.7 EXPERIMENTAL RESULTS

The FPGA implementation of the proposed HDPC control architecture promises to guarantee very good performances (in terms of current and speed quality) and to have a flexible and reconfigurable structure, but in order to appreciate this features, the first part of this section is devoted to understand the main difference with a standard microprocessor implementation.

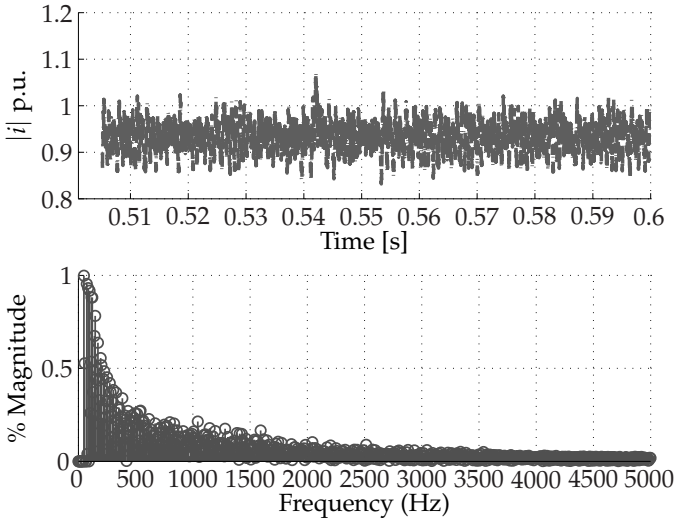

(a) *Current spectrum of the absolute value of the dq currents in Fig.3.11b, relative of the machine in Tab.2.2*

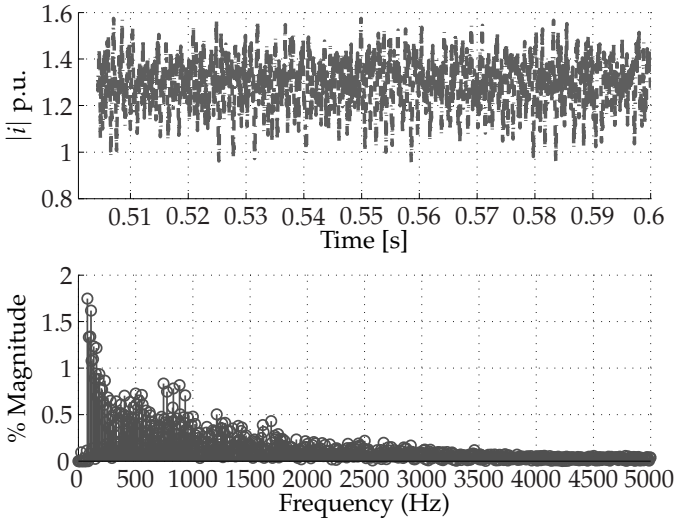

(b) *Current spectrum of the absolute value of the dq currents in Fig.3.12b, relative of the machine in Tab.3.2*

Fig. 3.15: Current spectrum of the HDPC configured with $N_s = 14$ voltage vectors, normalized to the foundamental tone. Simulation performed with the machine parameters of Tab.2.2 and control parameters in Tab.3.1.

3.7.1 *Limits of microprocessor implementation*

In this paragraph are commented the experimental results obtained with a rough version of the proposed HDPC control algorithm previously implemented in a microprocessor platform. A detailed description of that algorithm can be found in [69], although the relevant aspect is related to the experimental results, that were performed on a laboratory test bench equipped whit the PMSM of Tab.1.1 supplied by a three-phase inverter and controlled by a Fast Control Prototyping (FCP) board. The FCP was the dSPACE DS1104 R&D Controller Board of Sec. 2.7, based on a 603 PowerPC floating-point processor running at 250 MHz and an I/O interfacing managed by a slave-DSP subsystem based on the TMS320F240 DSP microcontroller.

A vector-controlled induction motor drive was used as a programmable mechanical load, while the whole digital control of the PMSM drive was implemented by adopting a prediction horizon of $N_{pd} = 1$. Although the computing power of this board is sufficient to test the major part of the studied control algorithms, in practice it suffers from some limitations, that have moved the implementation of the proposed HDPC control on a FPGA prototyping platform. As in Sec. 3.5, the algorithm in [69] performs a series of tests on the speed and current predicted vectors by evaluating the number of commutations in a hierarchical way. The optimal voltage vector was calculated by testing only the $N_s = 7$ discrete states of the VSI, although the preliminary results obtained with that approach were not satisfactory in terms of current quality (the DC-bus linkage was of only $U_{DC} = 100\,\text{V}$).
One batch of experimental results from [69] is reported in Fig. 3.16c, obtained by considering the motor driven with a speed reversal from $-300\,\text{rpm}$ to $300\,\text{rpm}$. As documented in Fig. 3.16d the steady-state speed error is close to zero, but the current quality is unacceptable from an industrial prospective, as expected by Sec. 3.6, since the use of only $N_s = 7$ voltage vectors leads to a high current ripple.

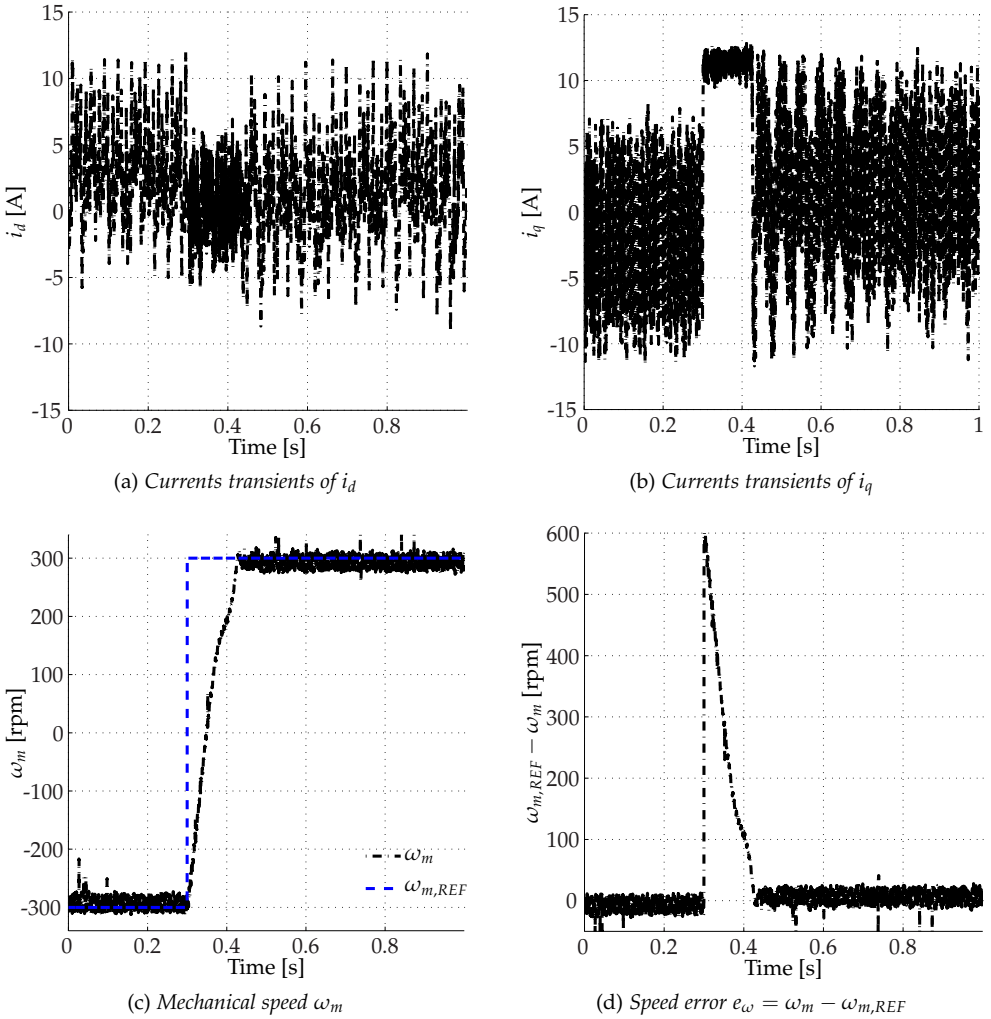

(a) *Currents transients of* i_d

(b) *Currents transients of* i_q

(c) *Mechanical speed* ω_m

(d) *Speed error* $e_\omega = \omega_m - \omega_{m,REF}$

Fig. 3.16: Currents and speed behaviour during a transient using a HDPC implementation into the dSPACE 1104 FCP board, configured with $N_s = 7$ voltage vectors. Machine in Tab.1.1, $T_c = 100\,\mu s$, $N_{pd} = 1$ and $U_{DC} = 100\,\text{V}$

In other terms, the low switching frequency and the high execution time T_e lead to have remarkable ripple in the currents, except during the transient, when the drive is pushed to its maximum performances.
Nevertheless, the experiments were performed to show the principle and the validity of that rough version of the algorithm, but they also proved that the hardware resources of the DSP-based board limits the possibility to obtain better performances (e. g. the use of $N_s = 14$ voltage vectors described in Sec. 3.5.1).
Furthermore, the main complication was related to the board programming architecture, that requires the complete execution of the code in the first half of the PWM period T_c.
Actually, it means that the whole algorithm has to be computed in half of the selected sampling period T_c, and the implementation of the easiest version of the algorithm with only $N_s = 7$ voltage vectors requires a computational time of about $T_e = 40\mu s$, which leads to a minimum sampling period of $T_c = 100\,\mu$s (equivalently $f_{sw} = 10\,$kHz).
In practical terms, a refinement of that control architecture (i. e. by considering the control technique with $N_s = 14$ vectors of Sec. 3.5.1) was unfeasible.
The large number of calculations that requires this algorithm to perform all the steps described above are prohibitive for an implementation with reasonable update period on microcontroller and then, the proposed algorithm has been tested and implemented in a FPGA platform as detailed in the next paragraph.

3.7.2 *FPGA implementation*

For the experimental validation, a customized test bench composed by two PMSM connected in back-to-back configuration with a torque meter mounted on the shaft was used to test the HDPC algorithm. Unlike the simulations, the experimental measurements were carried out on a PMSM with reduced anisotropy, since a PMSM-IPM was not available for the laboratory tests.
However, the HDPC algorithm can be used without limitations and a changing in the PMSM motor type (i. e. isotropic or anisotropic type) requires only a least amount of effort, since the use of a PMSM instead of the PMSM-IPM in the experimental setup does not reduces neither compromises the quality of the achievable results.
The PMSM used as a load machine was fed by a 4 kW commercial VSI, while the PMSM under test (whose parameters are in Tab.3.2) was driven by a customised inverter that received the control signals from the FPGA.
The FPGA-based control system is represented by a Virtex-6 FPGA ML605 Evaluation Kit with FMC (FPGA Mezzanine Card I/O) connector, on which the compiled bit stream file project was directly downloaded by using a USB/JTAG interface module and by means of a customized Matlab Graphical User Interface (GUI).
It is worth noting that the programming code described introduced in Sec. 3.6 (composed by Xilinx blocks, m-code equivalent blocks and VHDL code) has been refined and completed with the necessary sub-routines (e. g. the A/D conversion, the rotary reference frame transformations, the Dead Time (DT) compensation and the resolver to digital driver), in order to ensure the necessary communications with the VSI and the alarm interfaces.
The programming of the Matlab Graphical User Interface (GUI) has been necessary for the experimental development and implementation of the proposed control algorithm, since in the customized FPGA-based control system is needful to have a friendly interface to control all the parameters and variables involved in the control routine or to be able to load/save and then post-process the data.
To this aim, the internal variables that have to be controlled were stored into the Virtex-6 FPGA by using the available First In First Out data buffer (FIFO), directly linked to the

Matlab GUI interface which manages the real–time communication and the data logging of the main HDPC control signals.
The GUI interface has been configured to communicate with these elements in real time, and the control signals have been managed in the Matlab instructions by means of specific blocks inserted in the Xilinx System Generator overall scheme.
It is worth noting that the use of these FIFO should be limited as more as possible, since the HDPC control routines already uses many hardware resources, and an excessive utilization of these elements could lead to an overflow of the area occupation.
In the experimental tests have been considered the same simulation parameters reported in Tab.3.1, with a switching frequency f_{sw} limited to 10 kHz (equivalent of a sampling time to $T_c = 100\,\mu s$) as direct consequence of the physical hardware limitations of the VSI.
Due of the overall complexity of the Matlab/Simulink scheme, the block diagram in Fig.3.17 will be considered as logic synthesis of the operations performed by the algorithm in a sampling period.
The Finite State Machine (FSM) in Fig.3.17 manages the activation of the different VHDL subroutines in the Xilinx System Generator control scheme by considering that all the I/O interfacing are completely programmed into the Virtex-6 device (with a clock period of $T_s = 5\,\text{ns}$), completed by the A/D routine interface and the resolver to digital data conversion.
More in detail, the FSM is synchronized with a main counter that counts from zero to T_c/T_s , where T_s defines the sampling time of the FPGA clock (i. e. $T_s = 5\,\text{ns}$), and at every predefined time interval generates a short pulse to activate separately each of the VHDL routines in Fig.3.17.
It follows that, the FSM manages the necessary latency times and provides the correct timing of the operations in order to ensure the deterministic execution time of the algorithm.
The input signals have to be properly scaled in order to obtain a fixed-point internal representation of the variables, and the current scaling factor $fsg_{i,uvw}$, which only depends by the number of bits of the A/D converter can be easily calculated as:

$$fsg_{i,uvw} = \frac{2^{Nb,i}}{2\,MAX_i} \tag{3.41}$$

where MAX_i defines the maximum allowable current.
The prediction and optimization blocks have the largest computational burden, and then, in order to improve the algorithm execution time, the calculation of many routines is performed in parallel. the current and DC-link bus are performed in parallel
The first task is the A/D conversion, where the currents i_{uvw} and the DC-link bus voltage U_{DC} are acquired with $N_b = 12$ bit resolution and the absolute position is recorded with the on-board programmable resolver-to-digital converter with $N_b = 14$ bit of resolution.
In the proposed implementation, the A/D conversion processes, the speed calculation and the sin / cos are then activated at the same time, while the remaining part of the algorithm is executed in different times and it is synchronized with the FSM, as summarized in Fig.3.17.
The routines with the highest priority can stops the acquisition until the next activation signal of the FSM, but during the execution of these routines, all the information are stored into the FPGA I/O registers, to be used in the subsequent control blocks or directly stored for the data logging.
In the diagram of Fig.3.17 the resolver interface computes the electrical position by multiplying the mechanical position (provided via the $N_b = 14$ bits word) with the

number of pole pairs. An electrical offset position is then added, in order to align correctly the electrical position with the *d*-axis of the PMSM.

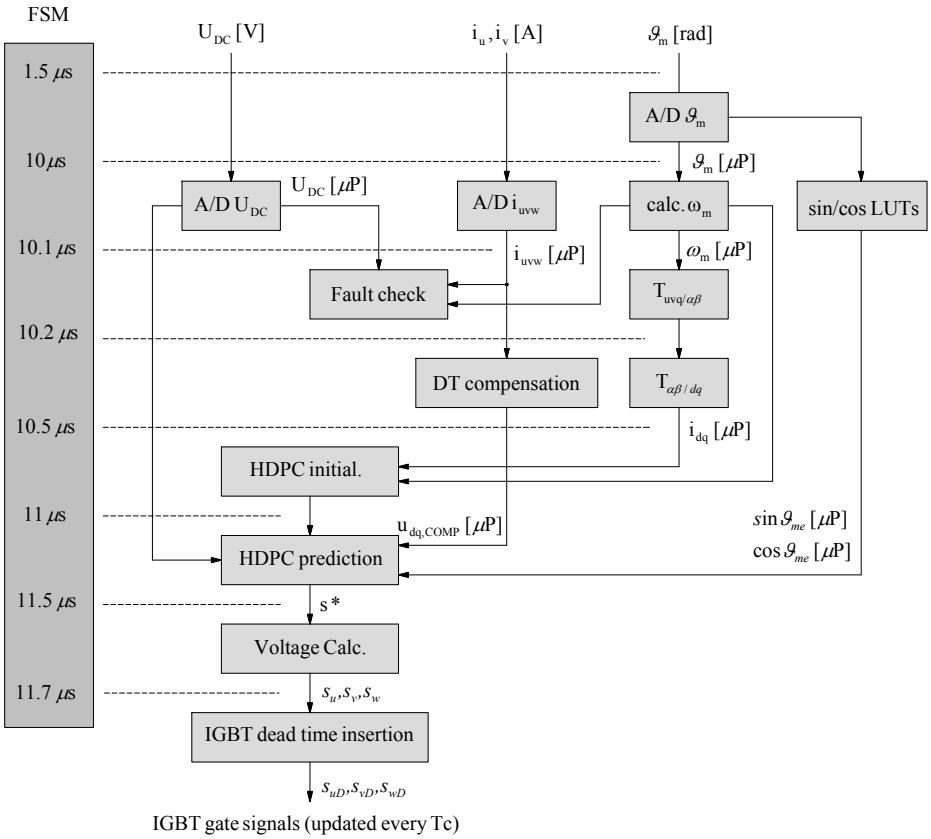

Fig. 3.17: Algorithm control diagram of the FPGA implementation.

The acquired currents (in the *uvw* reference frame) are then converted in the *dq* reference frame by means of the $T_{uvw/\alpha\beta}$ and $T_{\alpha\beta/dq}$ VHDL routine. The voltage distortion caused by the DT effects and the IGBT non-linearities is compensated into the *dq* reference frame on the basis of the sign of the currents and a pre-compiled LUT [70].
The compensation action is included as VHDL routine inside the Xilinx control scheme, calculated as difference between the selected optimal voltage component and reference value. This voltage reference correction is necessary since the predictions of Sec. 3.3 is strictly dependant by the voltages applied to the motor.
The initialization and prediction blocks (with decisional structure) receive the measured U_{DC} DC-link value, the i_{dq} currents and the measured speed ω_{me}, in order to calculate the optimal vector s^*.
At the end, a specific VHDL routine adds the DT from the reference IGBT signals and the IGBT gate signals (s_u, s_v and s_w calculated as summarized in Sec. 3.5.1), which are finally used to drive the VSI interface board.
The electromechanical speed ω_{me} is derived by the measured position scaled in the fixed-point notation. In particular, since the digital word that represents the mechanical position is acquired with an opto-isolated board, by defining as $N_{b,\vartheta}$ the number of bits used for the binary resolver data, the scaling global position factor fsg_{ϑ_m} can be calculated as:

$$fsg_{\vartheta_m} = \frac{2^{Nb,\vartheta} - 1}{2\pi} \tag{3.42}$$

The numerical speed derivation is approximated by a numerical filtered interpolated derivative, with the assumption that T_{cw} defines the sampling period of the speed. T_{cw} must be equal to the sampling period T_c (i. e. $T_{cw} = T_c$) since a delay in the speed measurement could compromises the control action. It follows that:

$$\begin{aligned} \omega_m &= \frac{\vartheta_{m,k} + 3\vartheta_{m,k-1} - 3\vartheta_{m,k-2} - \vartheta_{m,k-3}}{6T_{cw}} \text{ rad/s} \\ &= \frac{\vartheta_{m,k} + 3\vartheta_{m,k-1} - 3\vartheta_{m,k-2} - \vartheta_{m,k-3}}{6T_{cw} fsg_{\vartheta_m}} \mu\text{P} \end{aligned} \tag{3.43}$$

with an equivalent scaling speed factor (derived by (3.43)) of:

$$fsg_{\omega_m} = \frac{6\left(2^{Nb,\vartheta} - 1\right)}{2\pi} T_{cw} \tag{3.44}$$

It is important to remark that, instead of the canonical FOC or DTC control schemes, the speed measurement cannot be filtered because the delay introduced by the LPF action could leads to a control instability, as shown in Fig.3.18.
In detail, Fig.3.18a and Fig.3.18b show a speed transient of $\omega_m = 200\,\text{rpm}$ with the mechanical speed filtered by considering the LPF settled with a first cutting frequency of $f_{LPF,1} = 100\,\text{Hz}$ and a second of $f_{LPF,2} = 10\,\text{Hz}$.

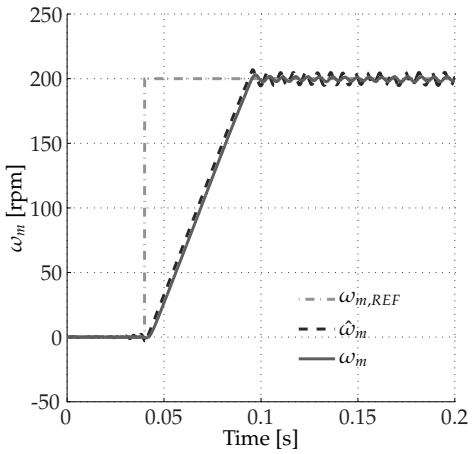

(a) *Mechanical speed transient of* $\omega_m = 200\,\text{rpm}$, *LPF settled at* $f_{LPF,1} = 100\,\text{Hz}$

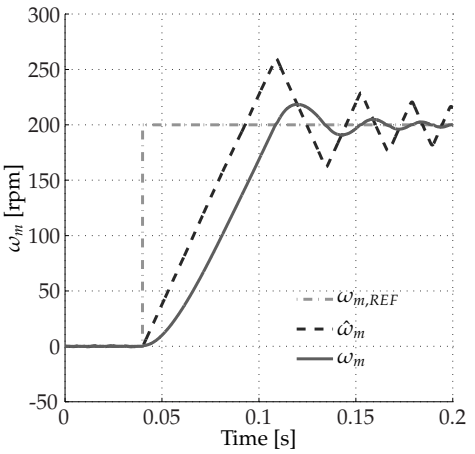

(b) *Mechanical speed* ω_m, *LPF settled at* $f_{LPF,2} = 10\,\text{Hz}$

Fig. 3.18: Speed transients using a HDPC configured with $N_s = 14$ voltage vectors and two different LPF actions. Motor in Tab.3.2, $T_c = 100\,\mu s$, $N_{pd} = 1$ and $U_{DC} = 560\,\text{V}$

The simulation results (i. e. in the same conditions of Fig.3.12) prove that the delay introduced by the LPF leads to an oscillatory and non-stable response of the speed that depends by the control action. The predicted speed is compared with a delay measurements, and the result is a wrong choice of the optimal voltage vector.
The practical feasibility of the speed derivation by using the resolver-to-digital binary word is a trade off between several factors, as the quality of the resolver measurement, the number of bits used to represent the angle ϑ_{me} and the admissible delay in the speed measurement.
At the end, the use of (3.43) seem to be a good compromise, although the boundary e_L on the speed error has been enlarged to ensure the use of the *second hierarchical*

level. Inside the VHDL control routines there are also the trigonometric transformation $\sin(\vartheta_{me})$ and $\cos(\vartheta_{me})$ of the electromechanical position ϑ_{me}.
This pair of functions are easily derived from the measurement of ϑ_{me} by saving on memory a LUT the numerical values of these trigonometric identities, but the memory area in which they are stored is divides into $2^{Nb,sc}$ sectors. A scaling factor $fsg_{sin,cos}$ is then also introduced, and it is equal of:

$$fsg_{sin,cos} = 2^{Nb,sc-1} \tag{3.45}$$

From (3.45) it is immediately to obtain the scaling factor (fsg_{dq}) of the currents i_d and i_q in the rotary reference frame dq, equal of:

$$fsg_{dq} = fsg_{i,uvw}2^{Nb,sc-1} \tag{3.46}$$

In Fig.3.19a and Fig.3.19b are reported a speed and current transient obtained with the PMSM of Tab.3.2. Fig.3.19c is shown a reversal speed transient and the equivalent optimal switching activity selection (Fig.3.19d).
The speed profile of In Fig.3.19a shows that the drive quickly reacts to the reference change, exhibiting a non-linear transient typical of bang-bang control. The steady-state error is closed to zero, as expected by the DOB compensation action (i. e. as consequence in the wrong parameter estimation).
The direct and quadrature currents of Fig.3.19b show a reasonable ripple, in particular during the speed transient, in good agreement with that calculated in the simulation case of Fig.3.12b. As expected, the control algorithm operates in MTPA condition after the initial speed transient (i. e. the FOC condition since the motor tested is a PMSM), as evident from Fig.3.19b, with a current $i_d \approx 0$ in absence of load torque.
The good matching between simulations and experimental tests confirmed the accuracy and the practical feasibility of the HDPC control architecture. Fig.3.19c shows a reversal speed transient of ± 100 rpm by considering a filtered speed signal with LPF tuned with a cut frequency of $f_{LPF} = 200$ Hz. The deterioration in the speed commented in Fig.3.18 is verified twice also in the experimental case, if compared with the speed quality visible in Fig.3.19a.
For the sake of completeness, in Fig.3.19d is shown the equivalent switching activity in a zoomed area of Fig.3.19c, in order to prove the randomized nature in the decisional structure. These preliminary results prove the practical feasibility of the control algorithm and its successfully implementation in to the FPGA platform.
It is worth noting that from the log summary file generated by the compiler, the project occupies about the 10% of the available slices and the 61% of the DSP48E1 slices (used for wide math functions, DSP filters, and complex arithmetic without the use of general FPGA logic). Many connections were produced mainly due to the programming approach, which optimised the fast execution of the prediction algorithm (with a parallelisation of the prediction for the $N_s = 14$ voltage vectors obtained at once) penalising the FPGA resources, the other term of the design trade-off.
In case of less area occupation, if desired, the project could be reprogrammed exploiting the prediction model recursively. However, that solution would impose a limitation on the maximum number of predictions, which is approximately given by the ratio between the switching period and the time execution of one prediction step.
The final implementation of the proposed control architecture ensures an execution time of $T_e = 11.7\,\mu s$, with a bottleneck in the AD conversion, that requires approximately $10\,\mu s$. Obviously, if the hardware configuration of the VSI could guarantee a sufficient high sampling frequency, then it could be possible to take advantage of the limited execution time T_e and improve the performances of the HDPC by reducing the sampling interval T_c.

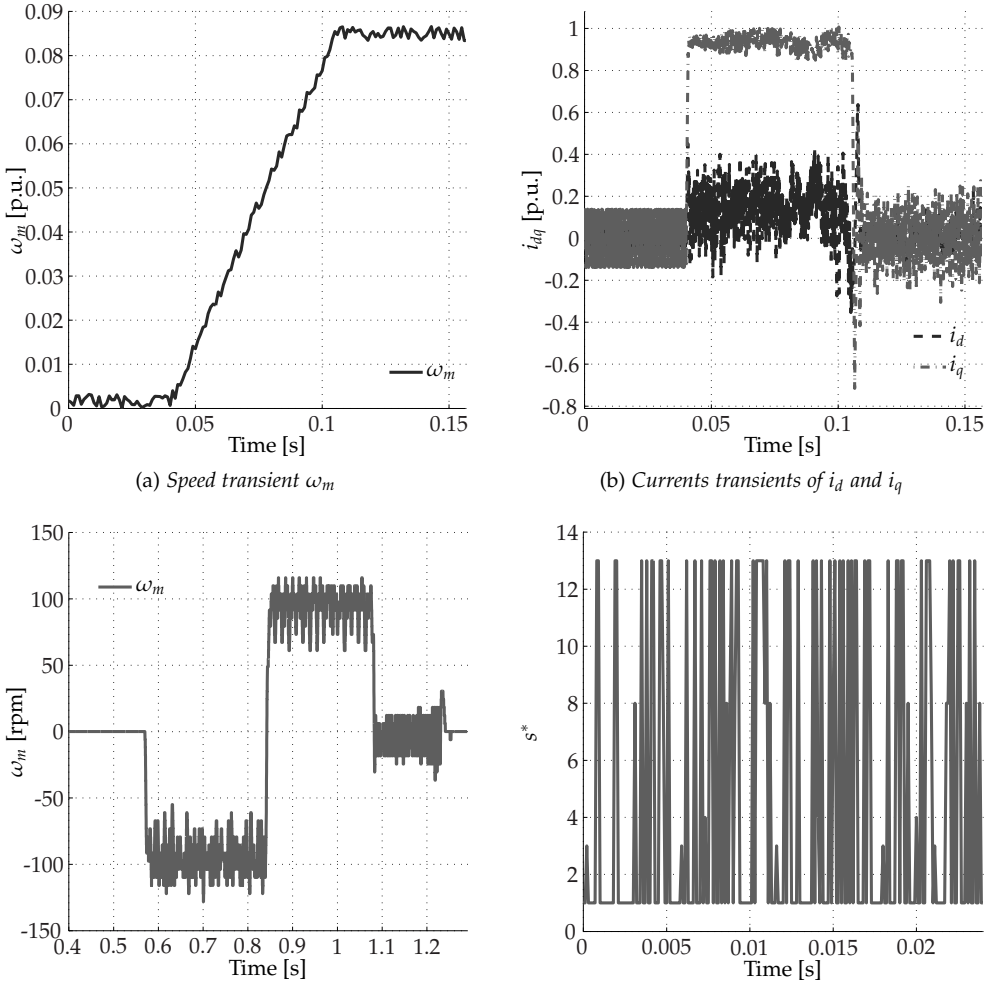

(a) *Speed transient* ω_m

(b) *Currents transients of* i_d *and* i_q

(c) *Mechanical reversal speed* ω_m *of* ± 100 rpm. *Introduction of a* LPF *settled at* $f_{LPF} = 200$ Hz

(d) *Zoom of the optimum switching states* s^* *with respect of Fig.3.19c*

Fig. 3.19: Experimental speed and currents behaviour during a speed reversal transients with the machine of Tab.3.2. The HDPC is configured with $N_s = 14$ voltage vectors, sampling period $T_c = 100\,\mu s$, $N_{pd} = 1$ and $U_{DC} = 560$ V.

3.8 CONCLUSIONS AND FUTURE DEVELOPMENTS

A combined speed-and-current direct predictive control for PMSM with isotropic or anisotropic structure was presented. Instead of the typical predictive control scheme, the proposed control architecture eliminates the external speed loop and predicts both currents and speed dynamic in each sampling period, employing a particular decisional structure. Speed current and current vector amplitude minimisation are considered in a hierarchical way, instead of using cost functions.

The proposed scheme is capable of operating in industrial conditions (i. e. standard DC-link voltages) by resizing the amplitude of the optimal vectors. The number of possible vectors has also been increased from $N_s = 7$ to $N_s = 14$ for further minimising the current spread. Simulation and experiments proved the feasibility of the proposed algorithm and this latter feature distinguishes the proposed control architecture by the conventional predictive control schemes.

The reasonable length of the prediction horizon has been studied and clarified as well as the complete modelization of the drive, supported and validated by many simulation and experimental results.
An improvement of currents and torque quality has been achieved with the extra modulation strategy here presented, that also guarantees a good improvement in terms of harmonic content reduction of the stator currents.
Although many laboratory tests were performed, the real implementation exhibits many complications which have been solved, and it was then possible to prove the concept and its feasibility into a faster device as a modern FPGA. For the FPGA implementation of the algorithm, much attention was paid to achieve high efficiency in the execution time and resource utilization, with the aim to have a control architecture capable to operate at high sampling frequency without too many adjustments in the code structure.
Simulation and experimental results suggest that the proposed HDPC architecture is deeply related to the specific application as well as to the available hardware resources, and to this purpose a small AC motor drive with high dynamic demands could be the optimal application field for this control architecture.
Future works will include an experimental test of the algorithm by considering a PMSM-IPM as well as the possibility of automatic identification of the two boundaries into the different two (or three) hierarchical levels. At the same time the proposed algorithm should be tested by reducing the sampling period of the currents, by adopting a power converter with higher switching frequency capability.

Part II

PARAMETER IDENTIFICATION OF INVERTER-FED INDUCTION MOTORS AT STANDSTILL

This part of the research describes an automated self-commissioning procedure for voltage-fed vector-controlled IM drives directly connected to the mechanical load, which represents a step over for the development of intelligent drives capable of operating without external modification in different working operations.
Induction motors parameter estimation, in fact, can be considered one of the most widely studied topics in electric drive literature, mainly due to the widespread use of IMs in many industrial applications, although the wide diffusion of the PMSM in the modern industrial and mechatronic applications.
As an example, the motors used in the hybrid or electric vehicles must have high power density in compact geometrical dimensions, and the typical PMSM motors are preferred, although the increased price of the rare earths has lead to reconsider the IM as valid alternative [71]. In this sense, the knowledge of the motor parameters must be accurate enough in order to ensure its accurate exploitation when controlled by a standard indirect vector control scheme
Usually, the IM electric and mechanical parameters are calculated from the data sheet or using the typical no-load and locked-rotor experimental tests, although in both cases, the accuracy of the results is inadequate for modern servo drives.
The problem is not new at all, and first papers devoted to parameter and commissioning analysis, as [72] or [73], were focused on the need for correct identification to ensure the best performances, but in very few of them a comprehensive estimation of motor parameters has been reached, also considering the inherent parameter non-linearities. Moreover, in [73] the identification was not performed at standstill and the motor was in rotation during the tuning process, while in general the standstill operations are preferred in order to obtain an intelligent and flexible AC drive.
Alternatively, in [74] is presented an algorithm to estimate the parameters at standstill using a PWM inverter and injecting DC and sinusoidal currents, although in this example the major drawbacks are the simplifications introduced in the model and estimation equations and the global linearisation of the whole system.
In general, approach of the literature is to consider the induction motor by adopting the constant parameter models without taking into account core losses and magnetic saturation, which depend on the current magnitude, frequency and by the operating conditions.
The results achievable cannot be considered acceptable or satisfactory in the presence of sudden flux level variations (e. g. in transient conditions, flux weakening operating or during the on-line starting of the drive), where the parameters and magnetic path linearity is lost.
A linear model of the motor could be considered accurate enough since, for IM drive applications with a low dynamic, the flux level is maintained constant at its nominal value and only in limited cases (e. g. during the flux weakening phase) some parameters, such as the inductance values, increase or decrease.
In fact, the industrial applications at constant speed with slowly variable torque are the typical application field of drives with IM machines, and in these cases, the inductances can be considered constant and the rotor currents frequency is small enough to not consider the skin effect on rotor bars resistance [75]. Unfortunately, if an IM is considered for high-dynamic applications (e. g. robotic or mechatronic applications) this last assumption is no more valid, and new commissioning strategies have to be reconsidered.

Moreover, the commissioning procedure has to be studied considering the motor already connected to the mechanical load, with few or no possibilities of disconnecting it to perform some off-line no-load or varying-load measurements. Standstill self-commissioning techniques are aimed at solving this problem, while at present, in many applications, a vector control method that considered only a simple linear models of the IM is widely used, and only constant parameters are used to modelling the machine.
As focused on before, motor parameters are intimately related to the most advanced control techniques and not only into the FOC, but also in the direct torque control DTC or model predictive control MPC, and they influence the overall system performance [72], [76]. In the torque or flux control strategies in fact, the standard *dq* reference frame concept and rotor flux orientation requires a precise knowledge of parameters as the rotor time constant. To this aim, in the estimation procedure this parameter should also be identified online to obtain better performances, although this feature represent a step-over and not influences the real efficiency advantages of the self-commissioning techniques.
Wrongly estimated values, in fact, cause inefficiency which is nothing than the loss of energy related to an inaccurate voltage compensation (e. g. due of a non-compensated saturation of same parameters of the control scheme).
Other papers have debated on the need of supporting the standard FOC or DTC schemes with an algorithm of self calibration [73], while in [77] the standard no-load and locked-rotor are exceeded by considering three frequency-domain tests, performed at standstill. [78] combines an adaptive observer with a flux estimation in the rotor speed reference frame, although the non-linear magnetic saturation of other motor parameters is not accounted.
Anyway, the literature splits and consider the self-commissioning techniques into two main categories: the "on–line" and the "off–line" approach. The first solution is devoted to an on-line tracking of the most critical parameters of the IM, as the stator and rotor resistances, in order to update and tuning the parameters of the control algorithm. In [79] and [80], can be found interesting solutions for the on-line estimation of the stator and rotor resistances, together with a comparison with the benefits of a real vectorial scheme application are included Other examples of the "on-line" estimation technique are proposed in [81] and [82], where the estimation is formulated as a non-linear least squares identification problem, and applied during regular operation of the machine. The parameter values can be continuously updated assuming a constant excitation of the machine, and the optimum parameter vector is the solution that minimizes a residual error.
The off-line approach uses test signals to compute a detailed map of IM parameters non-linearities, prior to or during the final commissioning phase, as in [83], where is described a full deterministic identification method to derived the mechanical and main electrical parameters of a high power induction motor. In [84] there is an interesting standstill solution, which takes into account the magnetising inductance saturation only. The debated solution considers the flux linkage-current relationship and estimated it by means of a third-order polynomial retrieved by a sinusoidal current injection combined with a recursive least square algorithm. However, the procedure needs a prior knowledge of other IM parameters.
In [85] is proposed a fully comprehensive series of laboratory tests performed on an IM, with the aim of obtain a complete description of the motor parameters, but unfortunately, the procedure is not suitable for the self-commissioning operation, since it is not performed with the motor at standstill and the mechanical load must necessarily be varied during the estimation procedure. Moreover, the solution of [85] requires an high computational demand, beyond the standard AC drive resources or specifically developed for a known machine geometry, as explained in [86] and [87]. However,

the results clearly show a non-negligible non-linear dependence of every IM parameter with respect to the IM working point. Since the literature exhibits a lack in estimation procedures capable to derive correctly the non-linear parameters of the IM motor at standstill, the research in this thesis propose an off-line estimation technique, with the aim to be a complete, cheap and highly accurate self-commissioning procedure for IM parameters estimation. Unlike most of the cited works, it does not rely on either special test rigs, or high computational resources, since the procedure is performed completely at standstill and without any change in motor connections, so that it fits for motors already placed on site, too.

As a distinctive feature, the identification routines make use of a non-ideality compensation map and of a software routine that reconstructs the voltage drops by avoiding any direct voltage measurement. In particular, to get a commissioning of the inverse-Γ magnetic model of the motor and overcome some operative limitations contained, for example in [88], in this research the attention is focused on some details that make the procedure a step beyond in terms of accuracy with respect to the results described in [89] and [90]. As an example, in some routines is used an extremely focused digital version of the DFT ([91] and [92]), to enhance the industrial feasibility and reduce the computational time.

In detail, Chap.4 recalls the basics of the IM, focusing on the magnetically saturated machine model and its equivalent circuit representation at standstill, while Chap.5 describes the theory of operations, the core of the proposed algorithm and the step-by-step sequence of operations executed during the self commissioning procedure.

The theoretical conjectures and their general validity have been explored by applying the identification algorithm to three different IM machines, and the experimental results obtained by a fast-control prototyping (FCP) test bench are reported and compared with alternative tests that prove the practical feasibility and correctness of the method.

4 THE INDUCTION MOTOR

4.1 INDUCTION MOTOR STRUCTURE

Squirrel-cage induction motors are simple, rugged and robust type of electric machine [93], well known and used already a century ago but still widely used in the modern motor industry for their manifold advantages [20] [94]. At present, although the basic control structure of an induction motor is complicated (if compared with the PMSM motor), these motors are preferred to other categories of electric machines in classical heavy-duty industry productivity sectors for their robustness.
They can be also used in high performance electric drives, but the typical vectorial control schemes (sensored or sensorless) require with high accuracy the motor parameters knowledge. In particular, in the traditional direct vector FOC schemes the parameters accuracy is not high and the flux linkage identification is performed with specific sensors (e. g. tapped stator windings or Hall- effect sensors) [20]. The indirect FOC partially overcomes the hardware complications, but as main drawback, this solution requires many motor parameters, which have to be estimated with good accuracy. The model and the equivalent circuit of IM derived in this chapter is the starting point for the automatic procedures of parameters estimation described in Chap.5. Here is simply collected the necessary background to understand the proposed identification algorithm, but a complete and accurate description to derive the main equations of an IM motor can be found in many books and papers in literature (e. g. [20] or [95]). A sketch of an IM section is shown Fig.4.1, where are also highlighted the stator and the squirrel cage rotor. Both these elements are composed by compacted stack of ferromagnetic laminations separated by an air gap g. As in the PMSM machines, the stator winding is excited from a balanced three phase source of voltages. The three rotating currents induced by the voltages, generate a magnetic field in the air gap rotating at synchronous speed as determined by the number of stator poles and the applied stator frequency f.
The basic operating principle of the induction motor is based on the well-known physical phenomena of the Faraday's Law and the Lorentz Force on a conductor. Briefly, the magnetic field generated by the three-phase voltage source sweeps across the cage rotor conductors, and a voltage drop is induced in each conductor while it is being invested by the flux (i. e. the Faraday's principle) while the currents generated by the induced voltage produces produce a mechanical force for the Lorentz's law. As final result, an alternating current is supplied to the stator directly and to the rotor by induction from the stator.
The previous general considerations on the flux-linkage transmission can be expressed and translated into an equivalent circuit that describes the three-phase induction machine. This description only refers to machines with symmetric stator windings excited by a symmetric of voltages. The main equations of the induction motor are associated to the sketch of Fig. 4.1, which represents a one pole pair induction motor.
Since the rotor in an IM is usually of squirrel cage type, which is equivalent to a short-circuited three-phase wounded rotor with the same number of pole pairs as the stator, the three stator phases can be indicated with u_s, v_s and w_s, while the equivalent rotor phases are u_r, v_r and w_r. The electromechanical angle ϑ_{me} (between the phase u_s and u_r) is defined as $\vartheta_{me} = p\vartheta_m$, where p are the polar pairs of the machine and ϑ_m is the mechanical position of the rotor. In the section of of Fig. 4.1 is also reported the rotary

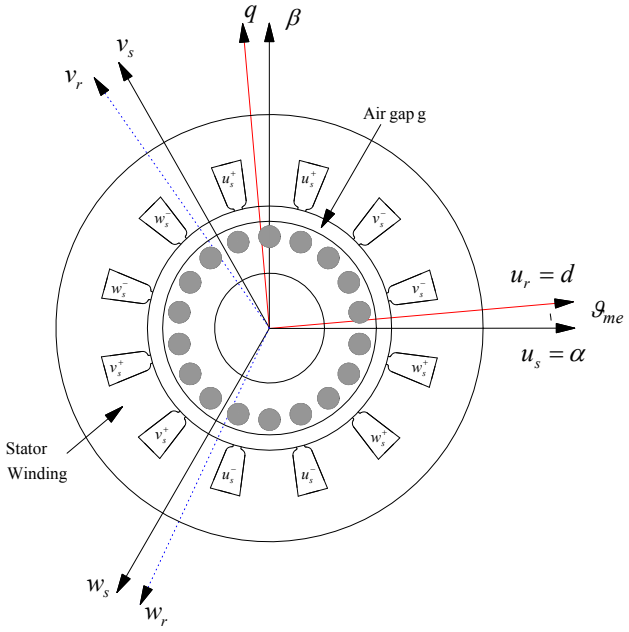

Fig. 4.1: Sketch of an Induction motor with one pole pair ($p = 1$) and $Q_s = 12$ stator slots. In the figure the stator and rotor reference frame are also indicated.

reference frame dq fixed to axes u_r and shifted to the same electromechanical position ϑ_{me} by the phase u_s. The time derivative of ϑ_m and ϑ_{me} is the electromechanical rotor speed ω_{me} and the mechanical rotor speed ω_m. The generic voltage balance equations for the stator phases are:

$$\begin{cases} u_{su} = R_s i_{su} + \dfrac{d\lambda_{su}}{dt} \\ u_{sv} = R_s i_{sv} + \dfrac{d\lambda_{sv}}{dt} \\ u_{sw} = R_s i_{sw} + \dfrac{d\lambda_{sw}}{dt} \end{cases} \tag{4.1}$$

while the equivalent rotor voltage balancing returns:

$$\begin{cases} 0 = R_r i_{ru} + \dfrac{d\lambda_{ru}}{dt} \\ 0 = R_r i_{rv} + \dfrac{d\lambda_{rv}}{dt} \\ 0 = R_r i_{rw} + \dfrac{d\lambda_{rw}}{dt} \end{cases} \tag{4.2}$$

where λ_{su}, λ_{sv} and λ_{sw} are the stator flux linkages, R_s and R_r are the stator and rotor resistances and λ_{ru}, λ_{rv} and λ_{rw} are the rotor flux linkages.
The model can be completely associated to Fig. 4.1 by exploiting the spatial vector notation and by considering a fixed stator reference frame, as described in [4] or [20]. In particular, the vector notation is useful to defines a space vector as a complex number by applying the following transformation:

$$\boldsymbol{u} = \frac{2}{3}\left(u_u(t) + u_v e^{j\frac{2\pi}{3}} + u_w e^{j\frac{4\pi}{3}}\right) \tag{4.3}$$

The (4.3) applied to the (4.1) and (4.2) returns the equivalent compact vector description of the induction motor in the $\alpha\beta$ stationary reference frame depicted by Fig. 4.1.

$$\begin{cases} \boldsymbol{u}_s = R_s \boldsymbol{i}_s + \dfrac{d\boldsymbol{\lambda}_s}{dt} \\ \boldsymbol{\lambda}_s = L_s \boldsymbol{i}_s + L_m \boldsymbol{i}_r \\ \mathbf{0} = R_r \boldsymbol{i}_r + \dfrac{d\boldsymbol{\lambda}_r}{dt} - j\omega_{me}\boldsymbol{\lambda}_r \\ \boldsymbol{\lambda}_r = L_r \boldsymbol{i}_r + L_m \boldsymbol{i}_s \end{cases} \tag{4.4}$$

In (4.4) $\boldsymbol{u}_s$ represents the stator voltage, $\boldsymbol{i}_s$ is the stator current, $\boldsymbol{i}_r$ is the rotor current, $\boldsymbol{\lambda}_s$ is the stator flux linkage, $\boldsymbol{\lambda}_r$ is the rotor flux linkage. According to the space vector notation, the two components in the $\alpha\beta$ reference frame of the stator voltages and current space vectors can be explicated as $\boldsymbol{u}_s = u_{s\alpha} + ju_{s\beta}$ and $\boldsymbol{i}_s = i_{s\alpha} + ji_{s\beta}$. The second and the fourth equations in (4.4) are demonstrated in [4], while the symbol L_s defines the synchronous stator inductance, L_m the synchronous mutual inductance between stator and rotor and L_r the synchronous rotor inductance.

4.2 EQUIVALENT CIRCUITS

For the purposes of this research it is interesting to consider the equivalent circuit representation of the induction motor. Since the operation principle of the induction machine is quite similar as that of a three-phase transformer, apart that in a transformer there is no mechanical motion between primary and secondary windings, the (4.4) can be represented with the equivalent circuit of Fig.4.2.

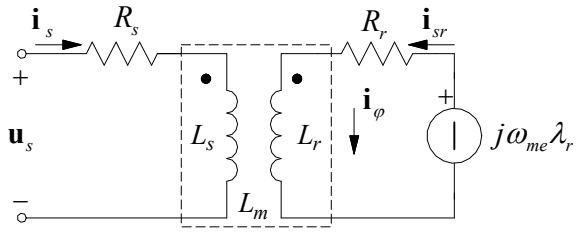

Fig. 4.2: Conventional equivalent circuit of the IM.

The circuit is representative of the stator voltage balance equation and the rotor voltage balance equation, related to each other by a mutual inductor. Since the circuit has been obtained from a state space vector representation (4.4), it is valid also in a non-sinusoidal steady state condition. The mutual inductor of Fig.4.2 can be substituted by the circuit of Fig.4.3. This circuit is composed by L_0, L_1, L_2 and n, that replace the three parameters (L_s, L_r, L_m) of the circuit in Fig.4.2. Since the number of parameters is high, the new degree of freedom is fixed by the transformer ratio n. The relationship between the mutual inductor parameters of Fig.4.3 and Fig.4.2 can easily be derived as:

$$\begin{aligned} L_0 &= nL_m \\ L_1 &= L_s - nL_m \\ L_2 &= L_r - \frac{L_m}{n} \end{aligned} \tag{4.5}$$

The aim is to derive the general inverse-Γ equivalent circuit at stand-still ($\omega_{me} = 0$). The equivalent circuital representation of Fig.4.2 was adopted as the reference model for the estimation procedure of the IM machine.

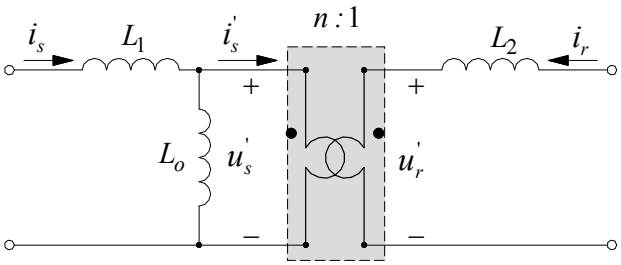

Fig. 4.3: Four-parameter circuit of a mutual inductor.

By setting $n = L_m/L_r$, $L_2 = 0$ and the set of equations (4.5) is reduced to:

$$\begin{aligned} L_0 &= \frac{L_m^2}{L_r} = L_\varphi \\ L_1 &= L_s - \frac{L_m^2}{L_r} = L_t \end{aligned} \tag{4.6}$$

L_0 is generally renamed as L_φ (*magnetising inductance*), while L_1 becomes L_t (*transient inductance*). The rotor resistance R_{sr}, referred to the stator side can be rewritten as:

$$R_{sr} = n^2 R_r = \frac{L_m^2}{L_r^2} R_r \tag{4.7}$$

while the mutual inductor of Fig.4.2 is now omitted. The reference inverse-Γ equivalent circuit at standstill for the IM is that shown in Fig.4.4.

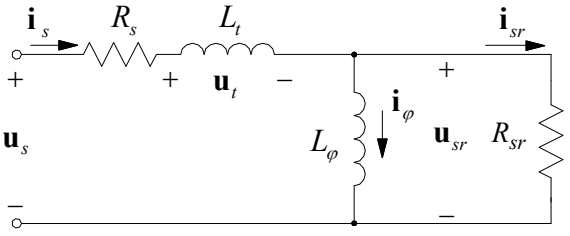

Fig. 4.4: Inverse-Γ equivalent circuit of an IM at standstill.

The inverse-Γ equivalent circuit has a null inductance on the rotor side, and as a final result the rotor time constant can be defined from the ratio between the magnetising inductance and the rotor resistance referred to the stator:

$$\frac{L_\varphi}{R_{sr}} = \frac{L_r}{R_r} = \tau_R \tag{4.8}$$

Moreover, the current and flux linkage vector in Fig.4.4 can be redefined as follows:

$$\begin{aligned} \boldsymbol{i}_{sr} &= -\frac{L_r}{L_m} \boldsymbol{i}_r \\ \boldsymbol{\lambda}_{sr} &= \frac{L_m}{L_r} \boldsymbol{\lambda}_s \end{aligned} \tag{4.9}$$

Both the inductive elements of Fig.4.4 can be replaced with non-linear functions of the current vectors which flow through each of them. The previous relationship can be related either to the magnetic anisotropy of the stator lamination (for some kind of motors) or to the presence of significant space harmonics in the *mmf* distribution. This happens because the iron path saturation is related to both the magnitude and the spatial distribution of the phase currents at each instant. The couple of inductive elements of Fig.4.4 are then replaced with the components represented in Fig.4.5. These two elements are representative of the transient flux linkage space vector $\boldsymbol{\lambda}_t$ and the magnetising flux linkage space vector $\boldsymbol{\lambda}_\varphi$, respectively.

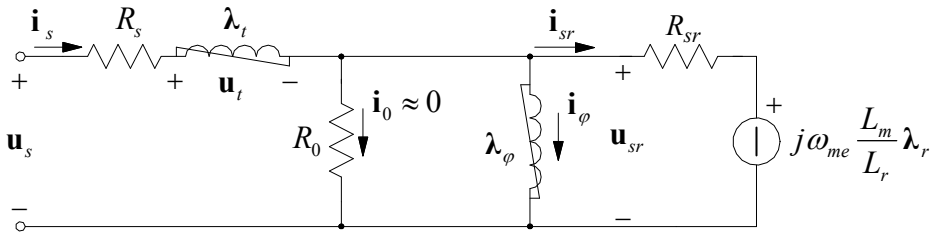

Fig. 4.5: Inverse-Γ equivalent saturated circuit of an IM.

As in the linear version, at standstill, the electromechanical speed $\omega_{me} = p\omega_m$ is null, ω_m being the rotor speed and p the number of pole pairs.
In the circuit of Fig.4.5 also the R_0 resistor has been included to represent the stator iron losses. The presence of this element does not significantly affect the voltage drop across R_s, since the current magnitude which flows through R_0 is very small ($i_0 \approx 0$ since R_0 is very high).
With reference to Fig.4.5, the voltage balance at standstill can be rewritten as:

$$\boldsymbol{u}_s = R_s \boldsymbol{i}_s + \frac{d\boldsymbol{\lambda}_t(\boldsymbol{i}_s)}{dt} + \frac{d\boldsymbol{\lambda}_\varphi(\boldsymbol{i}_\varphi)}{dt} = R_s \boldsymbol{i}_s + \frac{d\boldsymbol{\lambda}_s(\boldsymbol{i}_s)}{dt} \tag{4.10}$$

while the voltage balance for the right-hand mesh gives:

$$\boldsymbol{u}_{sr} = \frac{d\boldsymbol{\lambda}_\varphi}{dt} = R_{sr}\boldsymbol{i}_{sr} \tag{4.11}$$

According to [88] the constitutive equation of a non-linear inductance (as that representing $\boldsymbol{\lambda}_t$ in Fig.4.5) can be expressed in the form

$$\boldsymbol{u}_t(t) = \frac{\boldsymbol{\lambda}_t(\boldsymbol{i}_s(t))}{dt} = L_t(\boldsymbol{i}_s)\frac{d\boldsymbol{i}_s(t)}{dt} \tag{4.12}$$

where $L_t(\boldsymbol{i}_s)$ indicates the differential transient inductance as the function of current through it. The same expression can be written for the differential magnetising inductance $L_\varphi(\boldsymbol{i}_\varphi)$, associated to the magnetising flux linkage $\boldsymbol{\lambda}_\varphi$.

$$\boldsymbol{u}_\varphi(t) = \frac{\boldsymbol{\lambda}_\varphi(\boldsymbol{i}_\varphi(t))}{dt} = L_\varphi(\boldsymbol{i}_\varphi)\frac{d\boldsymbol{i}_s(t)}{dt} \tag{4.13}$$

The substitution of the differential inductances in (4.10) and (4.11) yields the general set of voltage balance equations of the inverse-Γ model:

$$\begin{cases} \boldsymbol{u}_s = R_s \boldsymbol{i}_s + L_t(\boldsymbol{i}_s)\dfrac{d\boldsymbol{i}_s}{dt} + L_\varphi(\boldsymbol{i}_\varphi)\dfrac{d\boldsymbol{i}_\varphi}{dt} \\ L_\varphi(\boldsymbol{i}_\varphi)\dfrac{d\boldsymbol{i}_\varphi}{dt} = R_{sr}\boldsymbol{i}_{sr} \\ \boldsymbol{i}_s = \boldsymbol{i}_\varphi + \boldsymbol{i}_{sr} \end{cases} \tag{4.14}$$

The system (4.14) will be used widely in the next chapter, since all the parameters estimated with the commissioning procedure are contained in these equations.
For the sake of completeness, buy considering the space vector notation the electromagnetic torque of the motor can be represented as:

$$\tau = \frac{3}{2} p \frac{L_m}{L_r} |\boldsymbol{\lambda}_r| \, |\boldsymbol{i}_s| \sin\phi \tag{4.15}$$

where the symbol ϕ defines the difference (in the fixed reference frame $\alpha\beta$ between the phase of $\boldsymbol{i}_s$ and that of $\boldsymbol{\lambda}_r$ [4]. The well-known expression of the mechanical load completes the mechanical set of equations:

$$\tau = J_m \frac{d\omega_m}{dt} + B_m \omega_m + \tau_L \tag{4.16}$$

where J_m and B_m are are the mechanical inertia and viscous friction respectively, and τ_L is the load torque.

5 PARAMETER IDENTIFICATION ALGORITHM

5.1 INTRODUCTION

The control identification algorithm is based on a dynamic model of the IM that refers to the Γ-inverse model of Fig.4.5, and consists in a series of consecutive steps, each exploiting the results of the preceding one. The parameters are estimated by imposing a known voltage vector $\boldsymbol{u}_s$ shifted from the angle ϑ_{me} with respect to the stator phase u, and considering the current amplitude or frequency measurements.
The main contribution of this research is represented by the absence of restrictions related to the angular position of the voltage vector $\boldsymbol{u}_s$ and by the complete tracking of all the non-linear parameters without limitations. Moreover, the proposed control technique allows the calculation of the magnetizing flux linkage $\boldsymbol{\lambda}_s$ without measuring the real voltage applied to the motor.
Finally, by meshing the measurements of the stator resistance R_s, the flux linkage $\boldsymbol{\lambda}_s$ and other equivalent parameters suitably projected along the $\alpha\beta$ reference frame, the complete mapping of all the parameters of 4.4 is obtained.
This chapter summarizes step by step each routine of the proposed estimation algorithm, and the following sections are organized as follows:

- Sec. 5.2: a classic estimation procedure used to obtain the main parameters of the equivalent circuit for a standard FOC. This algorithm is not executed at standstill and returns only the linear parameters.
- Sec. 5.3: detailed mathematical aspects for the derivation of the model used for the estimation procedure.
- Sec. 5.4: a characterization of the inverter non-linear behaviour.
- Sec. 5.5, 5.6, 5.7, 5.8 describes the method adopted to calculate the non-linear parameters of the inverse-Γ circuit of Fig.4.5. Experimental results and the validation tests are included in the realtive sub-sections.
- Sec. 5.7: the influence of the squirrel cage rotor during the calculation of the flux linkage reported in Sec. 5.7 is analysed. A specific prototype of an IM machine is used to validate the conjectures.
- Sec. 5.10: final remarks and future works.

Many experimental results were performed by using three different induction motors (IM_1, IM_2 an IM_3 as report in Tab.5.1, Tab.5.2 and Tab.5.3) to verify the correctness and accuracy of the method and to prove the practical feasibility of the algorithm considering real and industrial induction motors.
The experiments were carried out by considering a three-phase VSI (characterized in 5.4), directly controlled by the same equipment of Sec. 2.7.
The entire automatic drive control algorithm has been written in C code on the same FCP dSpace DS1104 R&D controller board of Sec. 2.7, and the worst execution time length is of 29 μs, considering an inverter switching period of $T_c = 100\,\mu s$.
The code is structured as in Sec. 2.7, so that during every PWM interrupt the main code calls the macro-C instructions, where are stored the different sub-routines of the algorithm.

All the A/D converters are started at the same time, and the accuracy of the current sensor within the inverter have been evaluated to be sure that the parameter estimation is not influenced by the inaccuracy of the measurement. The measurements of the built-in hall current sensors were compared, before the activation of the estimation procedure, to the current measurements obtained with a high-accuracy power analyser KinetiQ PPA2530 (bandwidth of 2 MHz with an accuracy of the 0.03%). The percentage error, that increases at higher current levels, could affect the correct estimation of the magnetizing inductance and the other parameters, and to this aim, a constant bias of $0.035 I_N$ was added to the current measurement.
Other standard parameters used during the tests, a part of the SVM switching frequency of 10 kHz, was the IGBT dead times of $t_d = 4\,\mu s$ and the DC-link Bus voltage of $U_{DC} = 100\,\text{V}$. In particular, it has been proved that the results are not affected by greater values of the DC-bus voltage.
The only main difference with respect of the experimental layout of Sec. 2.7 (apart of the programming C-interface) is that a second machine (e. g. controlled in torque) is not necessary as load, since all tests are completely performed at standstill. A sketch of the experimental setup and equipment is in Fig.5.1.

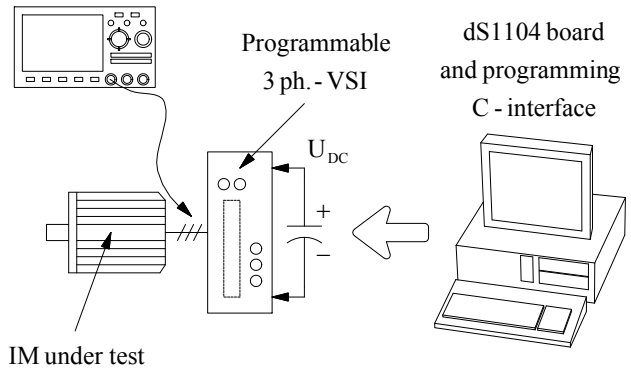

Fig. 5.1: Sketch of the experimental test bench used for the IM self commissioning procedure.

As mentioned before, one distinguishing feature of the control is the absence of limitation in the choice of the voltage vector $\boldsymbol{u}_s$, shifted from the angle ϑ_{me} with respect to the stator phase u. At each subsequent change of the position of the vector the control routine recalculate the main compensation curves and re-initialize the identification routines, while the results obtained at every different angular positioning are saved in order to complete the mapping of the motor.
In terms of time, to complete the mapping with a high precision and a variation of $\vartheta_{me} = 1\,\text{deg.el}$ in the positioning of the voltage vector $\boldsymbol{u}_s$, the entire estimation procedure completes the $\vartheta_{me} = 0 \div 360\,\text{deg.el}$ and return all the non-linear relationship in a few minutes. Anyway, the code can be setted to return only the basic non-linear relationship, and in this latter case in less of a minute the entire standstill identification algorithm gives the results
To have a wide and general term of comparison with other algorithms or estimation procedures, the results and the experimental curves are normalized to the nominal parameters of the induction machines, which were chosen very differently from each other as topologies and application field. The first and the third machines are servo motors (Tab.5.1 and Tab.5.3) designed to have a high dynamic range and a low stator resistance; while the second motor (Tab.5.2) is a typical motor for electric pumps.

Tab. 5.1: Induction motor IM_1 parameters

Parameter	Value
Nominal current I_N	11.8 Aeff
Nominal frequency f_N	52.5 Hz
Nominal speed ω_{mN}	1500 rpm
Nominal ph-ph voltage U_N	280 Veff
Pole pairs p	2
Stator resistance R_s	0.74 Ω
Iron losses equivalent resistance R_0	1115 Ω

Tab. 5.2: Induction motor IM_2 parameters

Parameter	Value
Nominal current I_N	6.6 Aeff
Nominal frequency f_N	50 Hz
Nominal speed ω_{mN}	2900 rpm
Nominal ph-ph voltage U_N	380 Veff
Pole pairs p	1
Stator resistance R_s	1.5 Ω
Iron losses equivalent resistance R_0	832 Ω

Tab. 5.3: Induction motor IM_3 parameters

Parameter	Value
Nominal current I_N	8 Aeff
Nominal frequency f_N	50 Hz
Nominal speed ω_{mN}	1500 rpm
Nominal ph-ph voltage U_N	400 Veff
Pole pairs p	1.98
Stator resistance R_s	1.9 Ω
Iron losses equivalent resistance R_0	1814 Ω

5.2 A TYPICAL IM PARAMETER ESTIMATION PROCEDURE

In this paragraph a series of canonical tests, usually adopted to derive the equivalent circuit parameters are presented. These tests cannot be considered when validating the experimental results obtained with the proposed commissioning algorithm, since they simply return the linear parameters of the machine without taking into account the saturation of the magnetic circuits. Moreover the IM are usually designed to be magnetically saturated in the nominal operating conditions, the non-linear effects are difficult to estimate with great accuracy by using a step by step standard procedure. Nonetheless, these standard tests are useful to have a quick characterization of the machines and to appreciate the accuracy of the results obtainable with the commissioning procedure presented in this chapter.

The traditional way of identifying the parameters is to use the "no-load" and "increasing-load" tests [96] [97], that anyway represents an improvement over the use the manufacturer data to determine the electrical parameters of the machine.

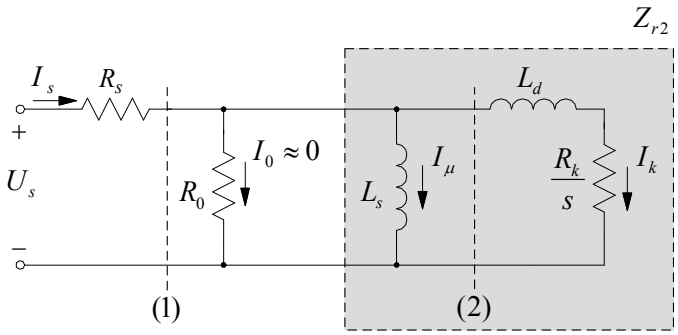

Fig. 5.2: Equivalent circuit of an IM machine used for the “no-load” and “load” tests.

As described in [96], the characterization must be preceded by a DC measurement of the phase to phase resistance, in order to obtain the stator resistance value[1]. At this measurement follows the estimation procedure, capable to extract the set of parameters of the per-phase equivalent circuit shown in Fig.5.2.
In the following the use of capital letters indicated a generic sinusoidal operation mode, and it is important to underline that, instead of the circuit of Fig.4.4 (where there are no limitations in the type of signal applicable, since all the variables are in vectorial representation), this standard procedure is limited at the phasorial notation.
The parameters of Fig.5.2 can be related to the parameters of the canonical inverse-Γ circuit of Fig.4.4 by simply calculating the equivalent impedances of the two circuits as:

$$Z_{r1} = j\Omega_s L_t + j\Omega_s L_\varphi || \frac{R_{sr}}{s} = \frac{(j\Omega_s)^2 L_t + j\Omega_s \frac{R_{sr}}{s} \frac{L_\varphi + L_t}{L_\varphi}}{j\Omega_s + \frac{R_{sr}}{sL_\varphi}} \tag{5.1}$$

$$Z_{r2} = j\Omega_s L_s || \left(j\Omega_s L_d + \frac{R_k}{s} \right) = \frac{(j\Omega_s)^2 \frac{L_s L_d}{L_s + L_d} + j\Omega_s \frac{R_k}{s} \frac{L_s}{L_d + L_s}}{j\Omega_s + \frac{R_k}{s(L_d + L_s)}} \tag{5.2}$$

By comparing (5.1) and (5.2) and after some algebraic manipulation, the equivalence between the parameters of Fig.4.4 and Fig.5.2 is:

$$\begin{aligned} L_t &= \frac{L_s L_d}{L_s + L_d} \\ L_\varphi &= \frac{L_s^2}{L_s + L_d} \\ R_{sr} &= \frac{L_s^2 R_k}{(L_s + L_d)^2} \end{aligned} \tag{5.3}$$

The canonical procedure of identification entails the characterization of the magnetizing curve by means of a series of no-load measurements.

1 The better way to avoid errors caused by wire resistance is the Kelvin, or 4-wire measurement method.

Moreover, due to saturation effects, the magnetizing inductance is affected by the rotor current, and the effect is particularly marked with the rotor slots geometry closed or in the presence of skewing in the design [12][98]. For this reason, the results obtained using the no-load test hold only at low loads level, i. e. only when the rotor current is around zero.
As the load increases, when a current different from zero flows into the rotor circuits, the magnetizing inductance and the rotor leakage inductance will change, and the locked rotor test is the canonical way to obtain the parameters of the machine in this latter case. In the following two sections will be described in detail the "no-load " test and then the "increasing-load" procedure.

5.2.1 *No-load test*

The no-load test returns the active input power P, the phase-to-phase voltage U_{ph-ph} and the *RMS* phase current I_s. Voltage and current measurements are used to derive the impedance of the equivalent circuit of Fig.4.4, since the slip frequency is $s = 0$ for the standstill condition of the test (the difference between synchronous speed and shaft speed is zero).
The no-load identification procedure is performed by considering the IM motor of Tab.5.1. The test execution requires only basic laboratory instrumentation as a simple variable three-phase transformer. In particular, the variable transformer is directly connected to the motor, and a power analyser KinetiQ PPA2530 is used to measure the three-phase input power, voltages and currents. Tab.5.4 summarizes the basic steps and the post-processing data conditioning required by the test.
Since the test is performed at "no-load", the active power at section (1), $P^{(1)}$, is the sum of the iron and mechanical losses ($P^{(1)} = P_{ir} + P_m$), and since the motor speed during the test is manteined constant (and very close to the rated speed) the mechanical losses P_m is constant, while the iron losses P_{ir} vary with the square of the voltage $U^{(1)}$ (it is related to the steady state stator flux linkage of the motor).

Tab. 5.4: No-Load test steps

Parameter	**Formula**
Apparent Power	$S = \sqrt{3} U_{ph-ph} I_s$
Reactive Power	$Q = \sqrt{S^2 - P^2}$
Active Power at section (1)	$P^{(1)} = P - 3R_s I_s^2$
Reactive Power at section (1)	$Q^{(1)} = P$
Apparent Power at section (1)	$S^{(1)} = \sqrt{\left(Q^{(1)}\right)^2 + \left(P^{(1)}\right)^2}$
Current at section (1)	$I^{(1)} = I_s$
Voltage at section (1)	$U^{(1)} = \dfrac{S^{(1)}}{3I^{(1)}}$
Magnetizing current at section (1)	$I_\mu = f(U^{(1)}) = \dfrac{Q^{(1)}}{3U^{(1)}}$

Tab.5.5 collects the post-elaboration numerical results obtained with the machine IM_1 in Tab.5.1. Moreover, in Fig.5.3a is plotted the magnetisation curve $U^{(1)} = f(I_\mu)$, that, after reversing ($I_\mu = f(U^{(1)})$), will be useful for the next increasing load test. In Fig.5.3b is also plotted the equivalent resistance R_0, which is very high and quite independent

by the applied voltage $U^{(1)}$. It is calculates as $R_0 = 3{U^{(1)}}^2/P_{ir}$, and its average value for the IM_1 motor is of $R_0 \approx 1115\,\Omega$. The current I_0 that flows through R_0 (Fig.4.5) can be considered approximately zero.

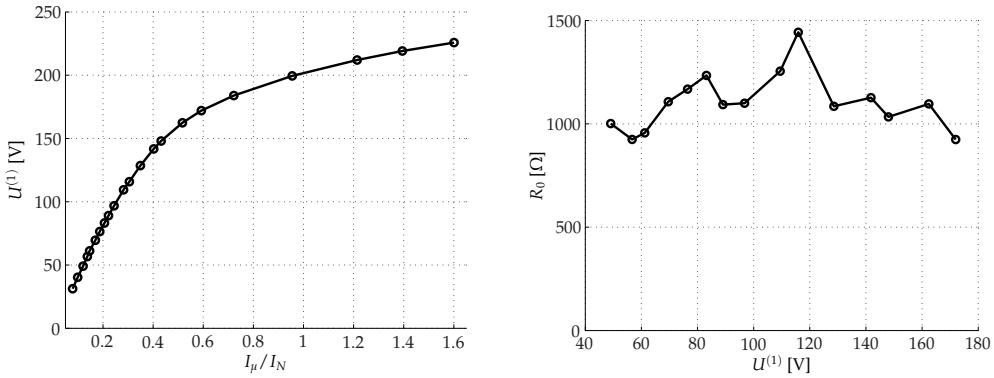

(a) *Magnetisation curve* $U^{(1)} = f(I_\mu)$ (b) *Equivalent losses* $R_0 = f(U^{(1)})$

Fig. 5.3: Curves for the IM_1 machine in Tab.5.1, obtained with the "no-load" test.

5.2.2 *The increasing load test*

The remaining parameters of Fig.5.2 are calculated by considering and by processing a second batch of measurements on the motor, named as "increasing-load" test. The experimental configuration is slightly modified with respect to the previous test, since the IM machine must be braked, while a constant load torque is applied using a second motor. To this purpose, an PMSM controlled motor is used as an active load to brake the IM machine under test, since in the "locked-rotor" version of this test the squirrel cage rotor concatenates back electromotive forces of a frequency higher than the slip frequency. The quality of the results for the presence of secondary effects on the conductors as the skin effect is then deteriorates.
The post-processing procedure first implements the steps summarized in Tab.5.6, and after this preliminary series of calculations, applying the equivalence (5.3) the complete set of parameters of the inverse-Γ circuit in Fig.4.4 is returned. In Tab.5.7 are reported the numerical data of the IM_1 machine in Tab.5.1, obtained by processing the experimental data recorded by the power analyser KinetiQ PPA2530 during the application of the steps in Tab.5.6.
The final numerical values of the inductances and resitance of L_t, L_φ and R_{sr} are derived by averaging the numerical data in Tab.5.7 and considered in a standard FOC control scheme.
The previous two tests returns averaged parameters, although with some additional calculation they could be mapped. As an example, the inductance L_s could be mapped as a function of the magnetizing current, but unfortunately the accuracy of these tests is low, by considering that many parameters vary according to the working conditions of the motor.

5.3 DERIVATION OF THE MODEL TRANSFER FUNCTION

Most of the traditional studies on the IM drives assume motor linearity, but a modern self commissioning algorithm (as that proposed in this research) requires a different formalization of the problem.

Tab. 5.5: Numerical results of the "No-Load test"with the IM_1 in Tab.5.1

U_s [V]	I_s [A]	S [VA]	P [W]	Q [VAR]	$S^{(1)}$ [VA]	$P^{(1)}$ [W]	$Q^{(1)}$ [VAR]	$I^{(1)}$ [A]	$U^{(1)}$ [V]	R_0 [Ω]	P_{ir} [W]	I_μ [A]
31.38	0.95	29.81	6.59	29.07	29.67	5.92	29.07	0.95	31.23	685.34	1.42	0.93
40.42	1.18	47.70	7.28	47.14	47.55	6.25	47.14	1.18	40.30	928.24	1.75	1.17
49.19	1.43	70.34	8.42	69.84	70.18	6.90	69.84	1.43	49.07	1001.59	2.40	1.42
56.84	1.63	92.65	9.95	92.11	92.46	7.98	92.11	1.63	56.72	924.63	3.48	1.62
61.30	1.74	106.66	10.66	106.13	106.46	8.41	106.13	1.74	61.18	956.37	3.91	1.73
69.67	2.00	139.34	11.84	138.84	139.12	8.87	138.84	2.00	69.56	1106.76	4.37	2.00
76.57	2.21	169.22	13.13	168.71	168.98	9.50	168.71	2.21	76.46	1168.08	5.00	2.21
83.29	2.43	202.39	14.49	201.88	202.13	10.10	201.88	2.43	83.18	1234.10	5.61	2.43
89.17	2.62	233.63	16.85	233.02	233.31	11.75	233.02	2.62	89.05	1093.26	7.25	2.62
96.88	2.88	279.01	19.17	278.36	278.66	13.01	278.36	2.88	96.76	1099.96	8.51	2.88
109.56	3.33	364.83	22.28	364.15	364.42	14.04	364.15	3.33	109.44	1254.76	9.54	3.33
115.99	3.60	417.56	23.43	416.91	417.13	13.80	416.91	3.60	115.87	1442.96	9.30	3.60
128.74	4.12	530.41	32.35	529.42	529.79	19.74	529.42	4.12	128.59	1084.86	15.24	4.12
141.95	4.75	674.26	39.10	673.13	673.50	22.34	673.13	4.75	141.79	1126.92	17.84	4.75
148.21	5.10	755.87	45.02	754.53	754.97	25.69	754.53	5.10	148.03	1033.74	21.20	5.10
162.59	6.10	991.80	56.20	990.21	990.62	28.55	990.21	6.10	162.40	1096.26	24.06	6.10
172.25	6.99	1204.03	72.82	1201.82	1202.38	36.52	1201.82	6.99	172.01	924.05	32.02	6.99
184.24	8.52	1569.72	99.74	1566.55	1567.22	45.81	1566.55	8.52	183.95	819.10	41.31	8.52
199.85	11.27	2252.31	146.87	2247.52	2248.13	52.50	2247.52	11.27	199.48	828.94	48.00	11.27
212.54	14.33	3045.70	219.36	3037.79	3038.52	66.79	3037.79	14.33	212.04	721.80	62.29	14.33
219.76	16.46	3617.25	289.02	3605.68	3606.75	87.72	3605.68	16.46	219.12	576.95	83.22	16.46
226.57	18.90	4282.17	373.90	4265.82	4267.20	108.49	4265.82	18.90	225.78	490.16	104.00	18.89

Tab. 5.6: Increasing Load test steps

Parameter	**Formula**
Phase voltage	$U_s = \frac{U_{ph-ph}}{\sqrt{3}}$
Apparent Power	$S = 3U_s I_s$
Reactive Power	$Q = \sqrt{S^2 - P^2}$
Active Power at section (1)	$P^{(1)} = P - 3R_s I_s^2$
Reactive Power at section (1)	$Q^{(1)} = P$
Apparent Power at section (1)	$S^{(1)} = \sqrt{\left(Q^{(1)}\right)^2 + \left(P^{(1)}\right)^2}$
Current at section (1)	$I^{(1)} = I_s$
Voltage at section (1)	$U^{(1)} = \frac{S^{(1)}}{3I^{(1)}}$
Magnetizing current at section (1)	$I_\mu = f(U^{(1)})$, from Fig.5.3a
Reactive power on L_s	$Q_0 = 3I_\mu U^{(1)}$
Stator inductance L_s	$L_s = \frac{U^{(1)}}{\Omega_s I_\mu}$
Loss power in the iron	$P_{ir} = 3\frac{\left(U^{(1)}\right)^2}{R_0}$
Active Power at section (2)	$P^{(2)} = P^{(1)} - P_{ir}$
Reactive Power at section (2)	$Q^{(2)} = Q^{(1)} - Q_0$
Apparent Power at section (2)	$S^{(2)} = \sqrt{\left(Q^{(2)}\right)^2 + \left(P^{(2)}\right)^2}$
Voltage at section (2)	$U^{(2)} = U^{(1)}$
Current at section (2)	$I^{(2)} = \frac{S^{(2)}}{3U^{(2)}}$
Leakage inductance	$L_d = \frac{Q^{(2)}}{3\Omega_s \left(I^{(2)}\right)^2}$
Equivalent rotor resistance	$R_k = \frac{sP^{(2)}}{3\Omega_s \left(I^{(2)}\right)^2}$

Tab. 5.7: Numerical results of the "Load test"with the IM_1 in Tab.5.1

I_f [A]	1.00	2.00	3.00	4.00	5.00	6.00
V_{fu} [V]	160.00	160.00	160.00	160.00	160.00	160.00
I_u [A]	5.83	5.85	6.03	6.25	6.44	6.67
V_{fv} [V]	160.00	160.00	160.00	160.00	160.00	160.00
I_v [A]	5.81	5.84	6.00	6.21	6.40	6.63
V_{fw} [V]	160.00	160.00	160.00	160.00	160.00	160.00
I_w [W]	5.83	5.87	6.04	6.23	6.42	6.65
ω_m [rpm]	1495.00	1492.00	1490.00	1488.00	1487.00	1486.00
Ω_s [rpm]	1500.00	1500.00	1500.00	1500.00	1500.00	1500.00
s	0.00	0.01	0.01	0.01	0.01	0.01
U_s [V]	160.00	160.00	160.00	160.00	160.00	160.00
I_s [A]	5.83	5.85	6.03	6.25	6.44	6.67
P [W]	94.24	126.73	231.10	324.00	400.00	469.17
Q [VAR]	928.03	927.38	936.71	946.06	949.59	958.54
$P^{(1)}$ [W]	69.33	101.64	204.45	295.37	369.60	436.56
$Q^{(1)}$ [VAR]	928.03	927.38	936.71	946.06	949.59	958.54
$I^{(1)}$ [A]	5.83	5.85	6.03	6.25	6.44	6.67
$U^{(1)}$ [V]	159.62	159.48	159.00	158.57	158.23	157.91
I_μ [A]	5.855	5.843	5.805	5.772	5.45	5.21
Q_0 [VAR]	25480.11	25432.60	25280.74	25146.00	25035.88	24936.10
P_{ir} [W]	22.84	22.80	22.66	22.54	22.44	22.35
$P^{(2)}$ [W]	46.49	78.85	181.79	272.83	347.16	414.21
$Q^{(2)}$ [VAR]	-6.501	-4.390	13.704	30.755	40.543	55.119
$U^{(2)}$ [V]	159.62	159.48	159.00	158.57	158.23	157.91
$I^{(2)}$ [A]	153.81	153.66	153.11	152.62	152.24	151.86
L_d [mH]	\	\	33.183	32.658	26.448	25.057
R_k [Ω]	1.792	1.715	0.922	0.728	0.617	0.552
L_s [mH]	86.788	86.882	87.183	87.449	87.665	87.860
f [Hz]	0.17	0.27	0.33	0.40	0.43	0.47
L_t [mH]	\	\	24.035	23.778	20.318	19.36
L_φ [mH]	\	\	63.148	63.671	67.347	68.4
R_{sr} [Ω]	\	\	0.484	0.386	0.364	0.33

Typical approximation to a single phase of the non-linear inverse-Γ circuit of the IM machine (usually named per-phase) represented in Fig.4.5 is not appropriate and could lead to a wrong consideration of the problem in term of vectorial notation. Moreover, the introduction of non-linear quantities in the circuit of Fig.4.4 leads to the impossibility to find an explicit analytical solution of the problem (currents associated at each element of the circuit as $i_s(t)$ and $i_\varphi(t)$), and for this reason it is important to formalize correctly the problem.
To this purpose, a different approach based on the use of the spatial vector notation is considered, in order to obtain a general TF of the circuit in different working points without approximations. To this aim, the "Perturbation method" (Chapter 10 of [39]) can be used to find an approximate solution $(i_s(t), i_\varphi(t))$ of the non-linear inverse Γ circuit.
In particular, the linearisation of the parameters is performed by adding a "small" term (named ε) to the mathematical equations of (4.14), in order to derive the equivalent "formal power series" of the desired solution, that can be truncated and solved explicit with the common linear mathematical instruments and obtain an approximated solution around the operating condition.
It is important to underline that a first-order "Perturbation method" not differs from the canonical linearisation approach, since the two methodologies deliver the same output.
If you consider a general voltage vector $\boldsymbol{u}_s = \boldsymbol{u}_{s0}(t) + \varepsilon \boldsymbol{u}_{s1}(t)$ applied to the circuit in Fig.4.5, where $\boldsymbol{u}_{s0}(t) = \text{const.}$ defines a DC component, ε a small parameter and $\boldsymbol{u}_{s1}(t)$ a general high frequency component.
The solution $(\boldsymbol{i}_s, \boldsymbol{i}_\varphi)$ of the non-linear Γ-inverse circuit depends on ε, and this mathematical approach aims to find an approximated solution when $\varepsilon \to 0$. If you consider:

$$\begin{aligned} \boldsymbol{i}_s(t) &= \sum_{k=0}^{N-1} \boldsymbol{i}_{sk}(t)\varepsilon^k + \mathcal{O}(\varepsilon^N) \\ \boldsymbol{i}_\varphi(t) &= \sum_{k=0}^{N-1} \boldsymbol{i}_{\varphi k}(t)\varepsilon^k + \mathcal{O}(\varepsilon^N) \end{aligned} \tag{5.4}$$

and a first order approximation is applied to the equations (5.4), by defining as $\boldsymbol{i}_{sk}(t)$ and $\boldsymbol{i}_{\varphi k}(t)$ the current expansion terms. The (5.4) truncated at the second order term ($N = 2$) returns:

$$\begin{aligned} \boldsymbol{i}_s(t) &= \boldsymbol{i}_{s0}(t) + \boldsymbol{i}_{s1}(t)\varepsilon + \mathcal{O}(\varepsilon^2) \\ \boldsymbol{i}_\varphi(t) &= \boldsymbol{i}_{\varphi 0}(t) + \boldsymbol{i}_{\varphi 1}(t)\varepsilon + \mathcal{O}(\varepsilon^2) \end{aligned} \tag{5.5}$$

Also considering the ε-expansion of the non-linear inductances $L_t(\boldsymbol{i}_s)$ and $L_\varphi(\boldsymbol{i}_\varphi)$

$$\begin{aligned} L_t(\boldsymbol{i}_s(t)) &= L_{t0}(t) + L_{t1}(t)\varepsilon + \mathcal{O}(\varepsilon^2) \\ L_\varphi(\boldsymbol{i}_\varphi(t)) &= L_{\varphi 0}(t) + L_{\varphi 1}(t)\varepsilon + \mathcal{O}(\varepsilon^2) \end{aligned} \tag{5.6}$$

where:

$$\begin{aligned} L_{t0}(t) &= L_t(\boldsymbol{i}_s(t))\Big|_{\varepsilon=0} = L_t\left(\boldsymbol{i}_{s0}(t)\right) \\ L_{t1}(t) &= \frac{\partial L_t\left(\boldsymbol{i}_s(t)\right)}{\partial \varepsilon}\Big|_{\varepsilon=0} = \frac{\partial L_t(\boldsymbol{i}_s)}{\partial \boldsymbol{i}_s}\frac{\partial \boldsymbol{i}_s}{\partial \varepsilon}\Big|_{\varepsilon=0} = \frac{\partial L_t(\boldsymbol{i}_s)}{\partial \boldsymbol{i}_s}\boldsymbol{i}_{s0}(t)\boldsymbol{i}_{s1}(t) \end{aligned} \tag{5.7}$$

and similarly for $L_\varphi(\boldsymbol{i}_\varphi)$:

$$\begin{aligned} L_{\varphi 0}(t) &= L_t(\boldsymbol{i}_s)\Big|_{\varepsilon=0} = L_\varphi\left(\boldsymbol{i}_{s0}(t)\right) \\ L_{\varphi 1}(t) &= \frac{\partial L_\varphi\left(\boldsymbol{i}_{s0}(t)\right)}{\partial \varepsilon}\Big|_{\varepsilon=0} = \frac{\partial L_\varphi(\boldsymbol{i}_\varphi)}{\partial \boldsymbol{i}_\varphi}\frac{\partial \boldsymbol{i}_\varphi}{\partial \varepsilon}\Big|_{\varepsilon=0} = \frac{\partial L_\varphi(\boldsymbol{i}_\varphi)}{\partial \boldsymbol{i}_\varphi}\left(\boldsymbol{i}_{\varphi 0}(t)\boldsymbol{i}_{\varphi 1}(t)\right) \end{aligned} \tag{5.8}$$

By substituting the previous ε terms expressions in the general voltage balance equation of the Γ-inverse circuit (4.14), it holds that:

$$\begin{aligned} &\boldsymbol{u}_{s0}(t) + \varepsilon \boldsymbol{u}_{s1}(t) + \mathcal{O}(\varepsilon^2) = R_s\left[\boldsymbol{i}_{s0}(t) + \boldsymbol{i}_{s1}(t)\varepsilon + \mathcal{O}(\varepsilon^2)\right]\cdots \\ &\cdots + \left[L_{t0}(t) + L_{t1}(t)\varepsilon + \mathcal{O}(\varepsilon^2)\right]\cdot\left[\frac{d\boldsymbol{i}_{s0}(t)}{dt} + \varepsilon\frac{d\boldsymbol{i}_{s1}(t)}{dt} + \mathcal{O}(\varepsilon^2)\right]\cdots \\ &\cdots + \left[L_{\varphi 0}(t) + L_{\varphi 1}(t)\varepsilon + \mathcal{O}(\varepsilon^2)\right]\cdot\left[\frac{d\boldsymbol{i}_{\varphi 0}(t)}{dt} + \varepsilon\frac{d\boldsymbol{i}_{\varphi 1}(t)}{dt} + \mathcal{O}(\varepsilon^2)\right] \end{aligned} \tag{5.9}$$

Assuming $\frac{d\boldsymbol{i}_{s0}}{dt} = 0$ and $\frac{d\boldsymbol{i}_{\varphi 0}}{dt} = 0$, the previous expanded expression returns:

$$\begin{aligned} &\boldsymbol{u}_{s0}(t) + \varepsilon \boldsymbol{u}_{s1}(t) + \mathcal{O}(\varepsilon^2) = R_s\left[\boldsymbol{i}_{s0}(t) + \boldsymbol{i}_{s1}(t)\varepsilon + \mathcal{O}(\varepsilon^2)\right]\cdots \\ &\cdots + \underbrace{\left[L_{t0}(t) + L_{t1}(t)\varepsilon + \mathcal{O}(\varepsilon^2)\right]\frac{d\boldsymbol{i}_{s0}}{dt}}_{=0} + \varepsilon\frac{d\boldsymbol{i}_{s1}(t)}{dt}L_{t0}(t) + \underbrace{\varepsilon^2\frac{d\boldsymbol{i}_{s1}(t)}{dt}L_{t1}(t)}_{\mathcal{O}(\varepsilon^2)} + \mathcal{O}(\varepsilon^2) \\ &\cdots + \underbrace{\left[L_{\varphi 0}(t) + L_{\varphi 1}(t)\varepsilon + \mathcal{O}(\varepsilon^2)\right]\frac{d\boldsymbol{i}_{\varphi 0}}{dt}}_{=0} + \varepsilon\frac{d\boldsymbol{i}_{\varphi 1}(t)}{dt}L_{t0}(t) + \underbrace{\varepsilon^2\frac{d\boldsymbol{i}_{\varphi 1}(t)}{dt}L_{t1}(t)}_{\mathcal{O}(\varepsilon^2)} + \mathcal{O}(\varepsilon^2) \end{aligned} \tag{5.10}$$

Equating the coefficients of same order at both sides, yields:

$$\begin{aligned} \left[\varepsilon^0\right] \quad &\Longrightarrow \quad \boldsymbol{u}_{s0}(t) = R_s\boldsymbol{i}_{s0}(t) = DC\,\text{component} \\ \left[\varepsilon^1\right] \quad &\Longrightarrow \quad \begin{cases} \boldsymbol{u}_{s1}(t) = R_s\boldsymbol{i}_{s1}(t) + L_{t0}\dfrac{d\boldsymbol{i}_{s1}(t)}{dt} + L_{\varphi 0}\dfrac{d\boldsymbol{i}_{\varphi 1}(t)}{dt} \\ 0 = L_{\varphi 0}\dfrac{d\boldsymbol{i}_{\varphi 1}(t)}{dt} - R_{sr}(\boldsymbol{i}_{s1}(t) - \boldsymbol{i}_{\varphi 1}(t)) \end{cases} \end{aligned} \tag{5.11}$$

and finally, applying the "Laplace transform" to the $\left[\varepsilon^1\right]$ of (5.11), the equivalent s-domain expression of the $\left[\varepsilon^1\right]$ balance is obtained:

$$\mathcal{L}\left\{\left[\varepsilon^1\right]\right\} \quad \Longrightarrow \quad \begin{cases} \boldsymbol{U}_{s1}(s) = (R_s + sL_{t0}\boldsymbol{I}_{s1}(s)) + sL_{\varphi 0}\boldsymbol{I}_{\varphi 1}(s) \\ 0 = R_{sr}\boldsymbol{I}_{s1}(s) - \left(R_{sr} + sL_{\varphi 0}\right)\boldsymbol{I}_{\varphi 1}(s) \end{cases} \tag{5.12}$$

This linear s-domain system (5.12) can easily be solved in the variables $\boldsymbol{I}_{s1}(s)$ and $\boldsymbol{I}_{\varphi 1}(s)$, e. g. by applying the "Cramer's Rule". The solution of $\boldsymbol{I}_{s1}(s)$ returns:

$$\boldsymbol{I}_{s1}(s) = \frac{\begin{vmatrix} \boldsymbol{U}_{s1} & sL_{\varphi 0} \\ 0 & -\left(R_{sr} + sL_{\varphi 0}\right) \end{vmatrix}}{\begin{vmatrix} R_s + sL_{t0} & sL_{\varphi 0} \\ R_{sr} & -\left(R_{sr} + sL_{\varphi 0}\right) \end{vmatrix}} = \frac{\boldsymbol{U}_{s1}(s)\left(R_{sr} + sL_{\varphi 0}\right)}{\left(R_{sr} + sL_{\varphi 0}\right)\left(R_s + sL_{t0}\right) + sL_{\varphi 0}R_{sr}} \tag{5.13}$$

The general impedance of the inverse Γ circuit of Fig.4.5, calculated as ratio between the equivalent voltage $\boldsymbol{U}_{s1}(s)$ and the current $\boldsymbol{I}_{s1}(s)$ is:

$$Z(s) = \frac{\boldsymbol{U}_{s1}(s)}{\boldsymbol{I}_{s1}(s)} = \frac{\mathcal{L}(\boldsymbol{u}_{s1})}{\mathcal{L}(\boldsymbol{i}_{s1})} = \frac{sL_{\varphi 0}R_{sr}}{\left(R_{sr} + sL_{\varphi 0}\right)} + R_s + sL_{t0} \tag{5.14}$$

5.4 INVERTER VOLTAGE DROP ESTIMATION

For the purposes of the proposed self-commissioning algorithm and for the requirements of the routine in Sec. 5.7 (used to identify the flux linkage $\boldsymbol{\lambda}_s$), a simple pre-characterization of the voltage-current relationship of the components in Fig.5.4 is the only requirement before starting the identification procedure.
Actually, the precise correspondence of the voltage drop u_t caused by the IGBT and the threshold voltage u_d of the free-wheeling diode is obtained by considering the non-linear effects and the voltage drop across the active switching components, i. e. IGBT and diodes.

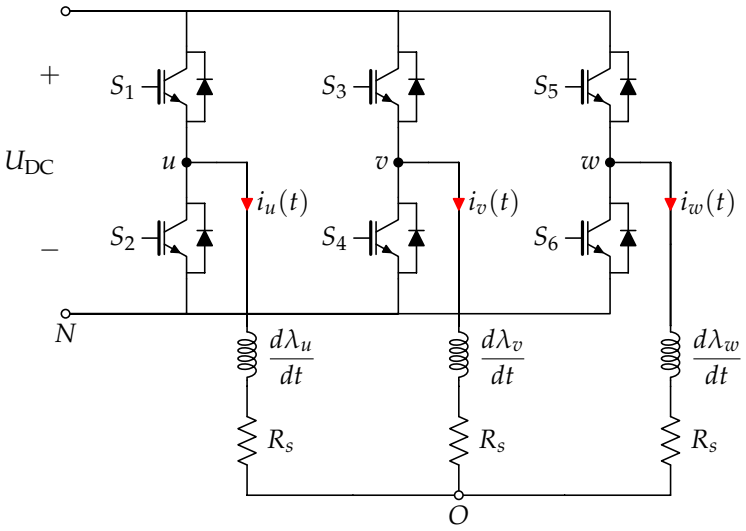

Fig. 5.4: Inverter standard configuration, the IM machine is represented as a three-phase load.

To correctly estimate this drop, a rough-and-ready solution to derive the characteristic curves of the VSI components consists into use of the data-sheets to get the diodes threshold voltage and the IGBTs conduction drop as a function of the current, but unfortunately these informations are usually too rough.
Basically, by supposing that the induction motor is fed by a standard three-phase voltage inverter, and that it lacks of the hardware circuitry for direct phase voltage measurement, as an alternative, an extremely accurate result has been obtained with the

proposed experimental test. By connecting the u, v inverter poles to the corresponding u, v phases of a PMSM, spun by a standard IM at a low and constant speed ($\approx 250\,\text{rpm}$)[2]. The inverter was suitably commanded in the null state configuration (indicated as 000), i. e. with all the bottom switches *ON* and the top switches *OFF*. The phase to phase voltage u_{uN} between the motor phase terminal u and the neutral point N of the VSI was measured by a differential voltage probe, and stored along with the phase current i_u caused by the PMSM electromotive force of the motor in Tab.1.1 (Fig.5.5).

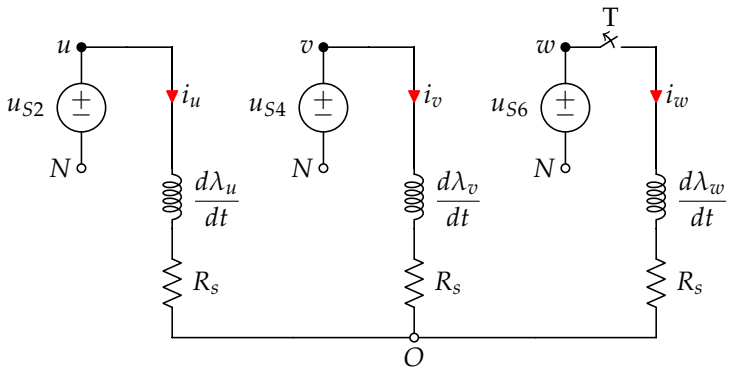

Fig. 5.5: Inverter configuration for a null voltage vector (000 or 111). During the test for the voltage drop determination, phase w is open.

In this particular configuration of the VSI, the current $i_u = -i_v$ flows identically in the IGBT S_2 or in the diode D_2, meaning that the measured voltage represents either the diode or the IGBT voltage drop. Positive values of i_u are associated to the diode threshold voltage.
The results of the measure in the time domain are plotted in Fig.5.6a, while the same curve is replotted in function of the current that flows into the components in Fig.5.6b. By processing the collected data separately, a polynomial approximations of the voltage drops $u_t = f(|i|)$ and $u_d = f(|i|)$ were calculated in Fig.5.6b and separately in Fig.5.6c and Fig.5.6d can be easily derived.
The degree of the polynomials is a trade-off between accuracy and computational effort, but for the purposes of this research, a sixth grade polynomial function has been found to be appropriate:

$$\begin{aligned} f_t(|i|) &= \alpha_{t0}|i|^6 + \alpha_{t1}|i|^5 + ... + \alpha_{t5}|i| + \alpha_{t6} \\ f_d(|i|) &= \alpha_{d0}|i|^6 + \alpha_{d1}|i|^5 + ... + \alpha_{d5}|i| + \alpha_{d6} \end{aligned} \tag{5.15}$$

The coefficients α_{ti} and α_{di} are obtained using a polynomial fitting algorithm, which elaborates the plot of Fig.5.6a as a function of the current. It is worth noting that the approximation of the very first portion of the curve (steep slope, few tens of mA) is quite rough, but it will not be used by the identification procedure, since the flux-linkage estimation algorithm is stopped at very low currents, and therefore that part of the voltage reconstruction is not used at all.
Some inverter non-idealities calculated with the proposed method are non-linear while others are linear with the current that flows into the power components. By focusing

2 From an experimental point of view, the inverter under characterization must be isolated by the VSI used to drag the IM motor.
To this aim, during the experimental identification of the curves in Fig.5.6, the IM was dragged by adopting an external three phase commercial VSI, controlled by a scalar V/Hz control.

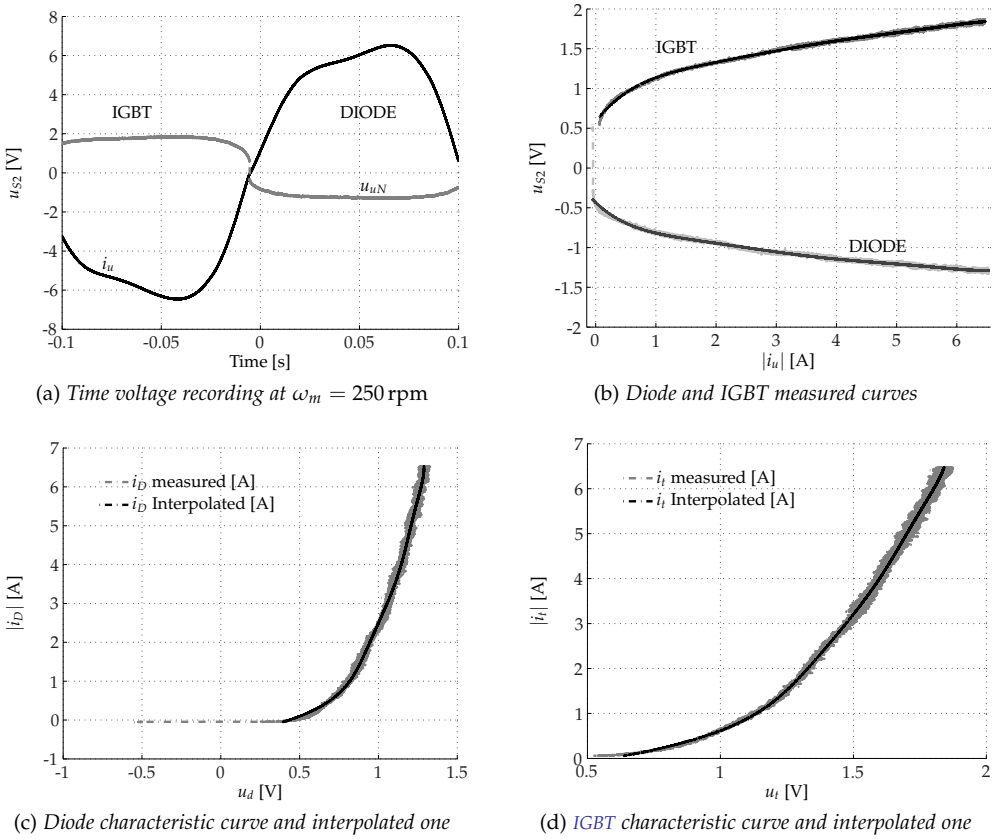

(a) *Time voltage recording at* $\omega_m = 250\,\text{rpm}$

(b) *Diode and IGBT measured curves*

(c) *Diode characteristic curve and interpolated one*

(d) *IGBT characteristic curve and interpolated one*

Fig. 5.6: Identification of the voltage drop of IGBTs and diodes.

only on the behaviour at sufficiently high currents (i. e. for currents greater of 2 A), the upper curve of Fig.5.6a is obtained without switching activity. This means that the behaviour of each power component (either an IGBT, or a diode) can be approximated by a straight line, that is, by the series of a constant voltage drop and a resistive voltage drop.

The feasibility of the method is testified twice, since the results do not change if the speed of the motor is changed (Fig.5.7) and if the compensation curve is compared with that obtained by measuring directly the phase to phase voltage.

In particular, Fig.5.7 shows a time-voltage recording with the voltage probe connected between the phase to phase voltage u_{uv} and the current $i_u = -i_v$ with the VSI, configured as in Fig.5.5 (i. e. with the inverter at $-\pi/6$ and configured in 000 while the PMSM was dragged by the IM).

By processing the collected data separately (i. e. plotting the data of Fig.5.7a in the current-voltage plane), the direct overlapping with the sum of $u_t + u_d$ obtained in Fig.5.6b is shown in Fig.5.7b. The perfect matching of the polynomial approximation in Fig.5.6b with the experimental data (also at different speeds) proves the practical feasibility and the accuracy of the method.

5.5 STATOR RESISTANCE AND DEAD TIME COMPENSATION

The first estimated parameter is the stator resistance R_s. When a DC current is flowing in the circuit of Fig. 4.5, the inductances are short-circuits and no current flows in the R_{sr} branch.

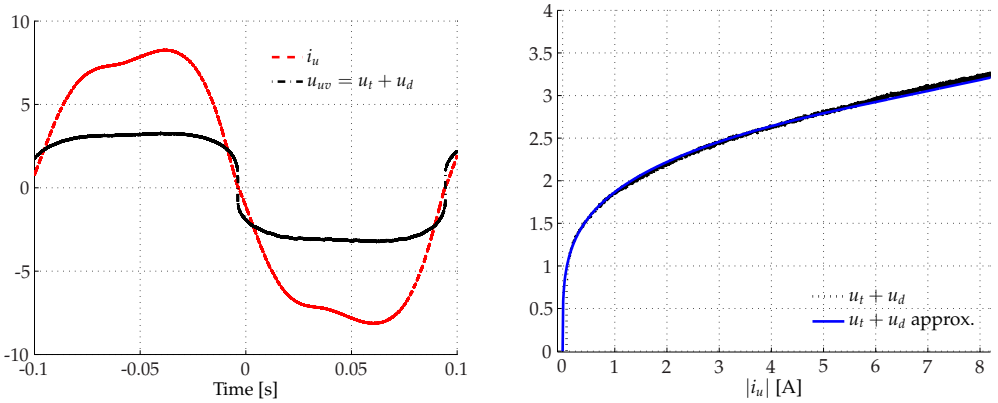

(a) *Time voltage recording at* $\omega_m = 100$ rpm

(b) *Sum of diode and IGBT measured curves*

Fig. 5.7: Alternative validation and identification of the voltage drop of IGBT and diode at $\omega_m = 100$ rpm.

Consequently, the ratio between the phase voltage $\boldsymbol{u}_s$ and the current $\boldsymbol{i}_s$ gives an estimation of the R_s value. The major issue resides in the meaning of the estimated resistance value, which depends upon the section in which the voltage is measured.
If the voltage is directly measured on motor terminals, the estimated resistance value is equal to the stator resistance value.
However, very often the phase voltage is approximated by its reference, providing adequate compensation of inverter non-linearities, as in [80]. In such cases, the $\boldsymbol{u}_s/\boldsymbol{i}_s$ ratio encompasses other resistive contributions which refer to cables and IGBTs linear characteristics.
In particular, the dead-time effects negatively affect the phase voltage generation of the PWM (as documented in [70]), introducing in principle a constant voltage drop, the sign of which depends on the sign of the phase current. However, it is well known [89] that the voltage distortion behaviour at low current levels diverges from the theoretical profile, becoming constant only for high current levels.
The parasitic effects in fact, are usually referred to non-linear phenomena that occur in the components and are quite difficult to describe adopting analytical or mathematical models (e. g. considering an equivalent scheme with equivalent capacitances, inductances and resistance in parallel with the component).
Moreover, these effects are evident only at low currents, but a method to obtain a comprehensive compensation of the inverter non-ideality was proposed in [88], although a modified version has been adopted here as first routine executed by the self-commissioning algorithm.
Basically, a reference voltage vector $\boldsymbol{u}_s^* = U_{s0}e^{j\vartheta_{me}}$ of step-decreasing amplitude and fixed phase ϑ_{me} (with respect to the $\alpha\beta$ stationary reference frame, aligned to the u phase) is applied to the induction motor, while the phase currents are measured and processed to get the corresponding step-increasing current vector $\boldsymbol{i}_s = I_{s0}e^{j\vartheta_{me}}$.
The non-linear ratio between the DC voltage and the steady state current amplitudes (U_{s0}/I_{s0}) encompasses the whole chain of resistive elements, including cables and IGBTs resistances. At the higher current levels, the non-linearity of the switching devices almost vanishes, so that the ratio becomes a constant, as depicted in Fig.5.8 that was obtained for a fixed positioning of $\vartheta_{me} = -\pi/6$.
It is important to highlight that the described non-linearity compensation of this paragraph does not isolate the contribution of each diode or IGBT to the voltage drop, but actually gives only a mean value associated to the position of the applied voltage vector

ϑ_{me}, which in turn determines what components are actually conducting the current, as can be recognized from the schematic of the inverter reported in Fig.5.5. Specifically, the main steps to identify R_s can be summarized as follows.
Subsequently, a series of non-compensated voltages are applied (i. e. the amplitude of $\boldsymbol{u}_s^* = U_{s0}e^{j\vartheta_{me}}$ is varied from a specified range), leading to a different steady-state DC voltage references, stored as voltage-references in a LUT together with the measured currents I_{s0}, as reported in The plot in Fig.5.8a.
The non-linear curve of Fig.5.8a takes accounts for both the voltage distortion effects at low current levels and the constant voltage drop at higher current levels, but it can be used to estimate the resistance R_s, by simply considering the higher current samples.
For higher current values in fact, the distortion is quite constant [88], while the curve slope represents the all-comprehensive stator phase resistance R_s. Therefore, the linear components can be considered the stator phase resistance and part of the power switches drop, while the inverter dead time effect and the constant part of the switches drop constitute the difference between U_{s0} and $R_s I_{s0}$.
The stator resistance R_s can be considered as the general solution of a Ordinary Least Squares (OLS) estimation, by considering the relationship $U_{s0}^* = \hat{R}_{s,est} I_{s0}$ as a linear regression model and the parameter $\hat{R}_{s,est}$ the unknown coefficient (Chap. 1.9 of [99]). The correlation between the voltage references U_{s0}^* and the current measurements I_{s0} is then:

$$\hat{R}_{s,est} = \frac{\frac{1}{N_m}\sum_{k=1}^{N_m}\left(I_{s0,k} - \mu_{I_{s0}}\right)\left(U_{s0,k}^* - \mu_{U_{s0}^*}\right)}{\frac{1}{N_m}\sum_{k=1}^{N_m}\left(I_{s0,k} - \mu_{I_{s0}}\right)^2} \tag{5.16}$$

where $\mu_{I_{s0}} = \frac{1}{N_m}\sum_{k=1}^{N_m} I_{s0,k}$ and $\mu_{U_{s0}^*} = \frac{1}{N_m}\sum_{k=1}^{N_m} U_{s0,k}^*$ are the averaged current and voltage references value on the N_m samples.
The measured currents ($I_{s0,k} = i_{d,k}$) are stored together with the voltage references $U_{s0,k}^*$ and used to derive the correct $R_{s,est}$ value. From an experimental point of view, only the last ten samples ($N_m = 10$ in the right side of the curve in Fig. 5.8a) have been considered to calculate the stator resistance, although an increased number of measurements leads to increase the precision in the estimation.
It can be proved that $\hat{R}_{s,est}$ asymptotically converges to $R_{s,est}$ for $N_m \to \infty$ (i. e. with N_m sufficiently high), and it represents the best linear unbiased estimator, i. e. the one with the lowest variance among the class of linear estimates [100]. In the following will be considered $\hat{R}_{s,est} = R_{s,est}$.
In the identification routine, while the higher part of the curve becomes the linear relationship R_s between the reference voltage and the current, the difference $|U_{s0}^*| - R_{s,est} I_{s0}$ can be considered the non-linear offsetting of the initial voltage reference, as reported in Fig.5.8b.
To compensate the non-ideality inverter (due to the dead time effects), the curve of the reference voltage $|U_{s0}^*|$ (that is the output of the PI current regulators, saved in the LUT) is subtracted from the respective voltage measurements U_{s0}, calculated as:

$$U_{s0} = R_{s,est} I_{s0} \tag{5.17}$$

The current-dependent compensation term is then added to the voltage reference to get an actual voltage equal to the primitive reference signal in the following routines of the

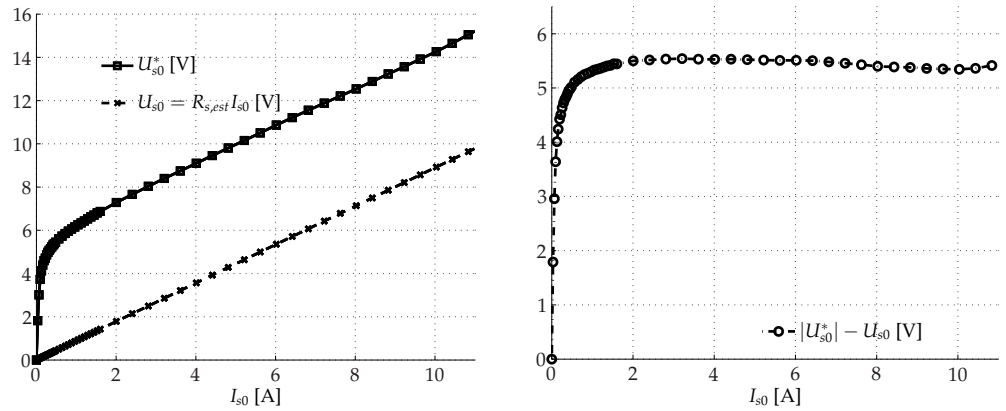

(a) *Dead time voltage drop compensation, calculated as* $|U^*_{s0}| - U_{s0}$

(b) *The two curves represent the voltage reference* $|U^*_{s0}|$ *and the non compensate voltage reference* U_{s0}

Fig. 5.8: Reference voltage-to-current characteristic of the three-phase inverter calculated. The curves are calculated with a DC-link bus voltage of $U_{DC} = 100\,\mathrm{V}$.

estimation algorithm. It is worth noting that the compensation usually fails for very low current values, due to the effect of the parasitics of the switching components that make the dead time effect non-linear, and the related voltage drop falls. Distortion due to the dead time is lost in parasitic effects when the IGBTs are crossed by low currents, while it is parallel to the high current values.

The higher part of the curve in Fig.5.8b is only related to the dead time effects (i.e. $\boldsymbol{u}_{DT} = \dfrac{4t_d U_{DC}}{3T_c} sgn(I_{s0})$) and by the constant bias of the components [4].

Numerically, the value used in the experimental tests for deriving Fig.5.8a were a DC-link bus voltage $U_{dc} = 100\,\mathrm{V}$, a switching period of $T_c = 100\,\mu s$ and the dead times of $t_d = 4\,\mu s$.

As expected, at high current level the voltage drop in Fig.5.8a is approximately $|U^*_{s0}| - U_{s0} \approx 5.5\,\mathrm{V}$, in good agreement with only the dead time contribution of $\boldsymbol{u}_{DT} = 5.33\,\mathrm{V}$. At lower currents, the parasitics of the switching components make the dead time effect non-linear, and the related voltage drop falls. This is automatically included in the inverter model, by taking a difference which is lower and decreased as a quantity proportional of how much the phase current is closed to zero.

As an example, the final result obtained by considering a phase voltage shift of $\vartheta_{me} = 0°$ with the IM_2 motor was of $R_s = R_{s,est} = 1.507\,\Omega$, very close to the one reported in Tab. 5.2.

Since the conduction of the components depends on the electromechanical position ϑ_{me} of the voltage reference vector, a complete mapping of the resistance as a function of the angular position is reported in Fig.5.9. To this purpose, the reference voltage vector is varied by changing the d-axis current reference ($I_{s0} = i_d$), in successive steps, in order to cover the entire electromechanical period and map the resistance and compensation curves (e. g. little variations can be attributed to the temperature variation). The value of R_s has small variations when calculated at different phase angles, as shown for example in Fig.5.9 for motor IM_1 (Tab. 5.1) and IM_2 (Tab. 5.2).

These variations take account of the different DC current paths caused by the different positioning of the voltage vector. The difference between the ideal curve and the measured curve can be used to compensate the voltage references of the control algorithm (via a look-up table or a polynomial approximation), to obtain a perfect match between the reference phase voltage and the measured phase voltage.

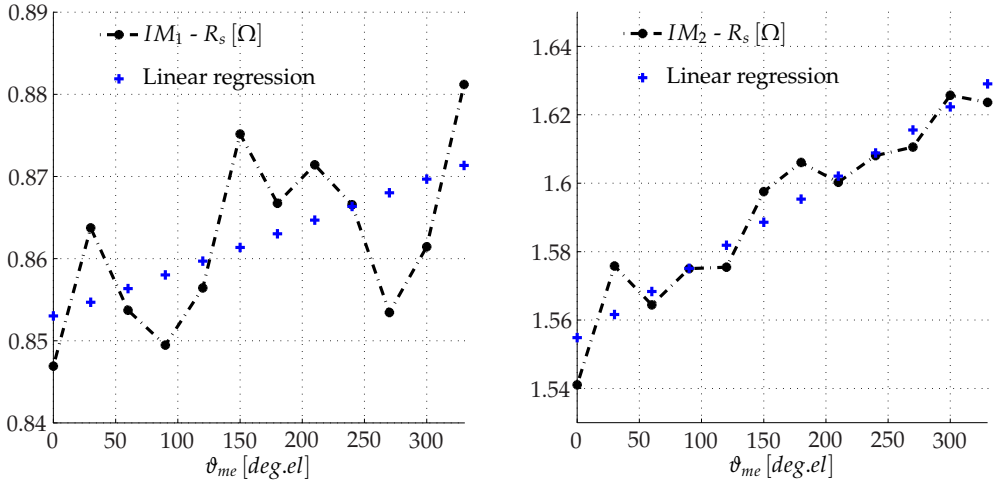

(a) IM_1 (b) IM_2

Fig. 5.9: Comprehensive equivalent resistance R_s as a function of ϑ_{me} for the machine IM_1 and IM_2 (Tab. 5.1 and Tab. 5.2).

From Fig.5.9 it is visible that the initial and final value of the resistance during the estimation is different. This difference depends, in addition to the non-linear effects of the components, by the temperature changing, since it exceeds by far the variations due to the different current distribution in the components.
Therefore, in industrial implementations of this algorithm, an on-line tracking algorithm for the stator resistance should been added to avoid this little discrepancy (the estimated value of R_s remains a good starting point for such an algorithm).
To validate the resistance estimation procedure, the resistances of the three motor have been accurately measured with a 4-wire measurement performed with an ohmmeter Agilent 34401A. The estimated resistance R_s includes neither the cable connection to the inverter, nor the voltage drop due to the inverter switches, and therefore it is slightly less than the mean value of the R_s displayed in Fig.5.9.

5.6 THE IDENTIFICATION OF THE TRANSIENT FLUX LINKAGE

The second parameter estimated by the control algorithm is the transient inductance L_t. L_t is obtained by injecting a sinusoidal high-frequency signal of small amplitude U_{s1} superimposed to a step-varying DC bias U_{s0}, and by measuring the resulting stator current. The (pulsating) reference space voltage vector is applied along the d-axis, with an angular displacement of ϑ_{me} with respect to the stationary reference frame (Fig.5.10).

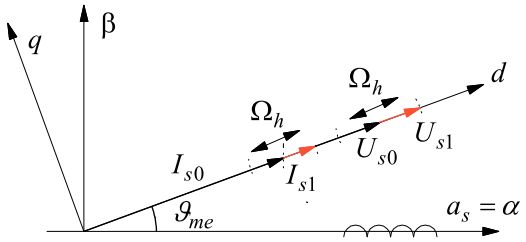

Fig. 5.10: Reference voltage for the identification of the inductance L_t

It produces a corresponding pulsating current vector (along the same direction ϑ_{me}), delayed by an angle $\gamma(\omega)$, that is

$$\begin{cases} \boldsymbol{u}_s^*(t) = \boldsymbol{u}_{s0} + \boldsymbol{u}_{s1}(t) = (U_{s0} + U_{s1}\cos(\omega t))\, e^{j\vartheta_{me}} \\ \boldsymbol{i}_s(t) = \boldsymbol{i}_{s0} + \boldsymbol{i}_{s1}(t) = (I_{s0} + I_{s1}\cos(\omega t - \gamma))\, e^{j\vartheta_{me}} \end{cases} \tag{5.18}$$

The basic idea is to linearise the circuit of Fig.4.5 around consecutive steady-state working points, through the step-varying bias DC voltage U_{s0}, and calculate the differential inductance L_t from the expression of the TF between the Laplace transforms of the imposed stator voltage vector and the measured stator current $Z(s) = \boldsymbol{U}_s^*(s)/\boldsymbol{I}_s(s)$.
The application of the *perturbation method* described in 5.3, provided that U_{s1} is sufficiently small, leads to the voltage balance equations for the first-order components $\boldsymbol{u}_{s1}$ and $\boldsymbol{i}_{s1}$. They are obtained by (5.11), where L_{t0} and $L_{\varphi 0}$ are the differential inductances at the working point $(\boldsymbol{u}_{s0}, \boldsymbol{i}_{s0})$. Forcing a sinusoidal perturbation (5.18) as voltage reference, the frequency response can be obtained by placing $s = j\omega$ in (5.14):

$$Z(j\omega) = R_s + j\omega L_{t0} + \frac{j\omega L_{\varphi 0} R_{sr}}{R_{sr} + j\omega L_{\varphi 0}} \tag{5.19}$$

Now considering the Laplace transform of (5.18) (where $\boldsymbol{u}_{s1}(t)$ defines the first order voltage component and $\boldsymbol{i}_{s1}(t)$ the equivalent delayed current), it follows that:

$$\begin{aligned} \boldsymbol{U}_{s1}(s) &= \mathcal{L}\left(\boldsymbol{u}_{s1}\cos(\omega t)\right) = \boldsymbol{U}_{s1}\frac{s}{s^2+\omega^2} \\ \boldsymbol{I}_{s1}(s) &= \mathcal{L}\left(\boldsymbol{i}_{s1}\cos(\omega t - \gamma)\right) = \boldsymbol{I}_{s1}\frac{s\sin\left(\frac{\pi}{2}-\gamma\right) + \omega\cos\left(\frac{\pi}{2}-\gamma\right)}{s^2+\omega^2} \\ &= \boldsymbol{I}_{s1}\frac{s\cos(\gamma) + \omega\sin(\gamma)}{s^2+\omega^2} \end{aligned} \tag{5.20}$$

Replacing the (5.20) into (5.14), the equivalent impedance can be rewritten as:

$$\begin{aligned} Z(j\omega) &= \frac{\boldsymbol{U}_s^*(s)}{\boldsymbol{I}_s^*(s)}\Big|_{s=j\omega} \approx \frac{\boldsymbol{U}_{s1}(s)}{\boldsymbol{I}_{s1}(s)}\Big|_{s=j\omega} = \frac{s\boldsymbol{U}_{s1}}{\boldsymbol{I}_{s1}\left(s\cos(\gamma) + \omega\sin(\gamma)\right)}\Big|_{s=j\omega} \\ &= \frac{j\omega\boldsymbol{U}_{s1}}{\boldsymbol{I}_{s1}\left(j\omega\cos(\gamma) + \omega\sin(\gamma)\right)} \\ &= \frac{\boldsymbol{U}_{s1}}{\boldsymbol{I}_{s1}}\frac{1}{\cos(\gamma) - j\sin(\gamma)} = \frac{\boldsymbol{U}_{s1}}{\boldsymbol{I}_{s1}}e^{j\gamma} \end{aligned} \tag{5.21}$$

Considering a suitably high frequency $\omega = \Omega_h$, the right-hand term of (5.19) reduces to R_{sr} with good approximation, so that the imaginary part of $Z(j\Omega_h)$ returns the value of $L_t(\boldsymbol{i}_{s0})$ (by considering the same nomenclature used in (5.18):

$$L_t(\boldsymbol{i}_{s0}) = L_{t0} \approx \frac{\Im\left[Z\left(j\Omega_h\right)\right]}{\Omega_h} = \frac{1}{\Omega_h}\frac{U_{s1}}{I_{s1}}\sin\gamma \tag{5.22}$$

In the practical implementation, the accurate determination of the current space vector $\boldsymbol{i}_{s1}$ with respect to $\boldsymbol{u}_{s1}$, has some critical aspects related to the inherently bad signal-to-noise ratio of the measurement system. To estimate correctly the transient inductance,

the solution adopted is represented by the Goertzel algorithm, which is a fast and efficient implementation of the discrete-time Fourier transform ([92]).
The implementative procedure for the calculation of $L_t(\boldsymbol{i}_{s0})$ can be summarized by the diagram in Fig.5.11, that is a block diagram representation of the (5.22).
At steady state and in a given working point $(\boldsymbol{u}_{s0}, \boldsymbol{i}_{s0})$, during every $T_c = 100\,\mu s$ the phase currents are sampled and transformed into a space vector in the (d, q) reference frame. For the particular choice of the d-axis, the q-components of both reference voltage and current are null, and the single-tone component of the $\boldsymbol{i}_s$ current at the angular frequency ω_h is detected by applying, in succession, an IIR and an FIR filter to the $d-$component of the current vector $i_d = I_{s0} + I_{s1}\cos(\omega_h t - \gamma)$ (Fig.5.11). In details, for each of the first $(N-1)$ samples, the algorithm computes the intermediate IIR filter sequence of vectors

$$s(n) = i_d(n) + 2\cos(2\pi k/N)\, s(n-1) - s(n-2) \tag{5.23}$$

where $k = fNT_c$, $0 \leq n \leq (N-1)$ and N is the total number of samples per period of the input signal, as detailed in Sec. 5.6.1.1. The choice of N is a trade-off between the accuracy of the results and the execution time of the DFT; in the present work, a value $N = 100$ was found to be appropriate.
After N samples, a FIR filter is applied to $s(N)$ and $s(N-1)$, conveniently stored apart:

$$\begin{cases} I_{s1}\cos(\gamma) = s(N) - \cos(2\pi k/N)\, s(N-1) \\ I_{s1}\sin(\gamma) = \sin(2\pi k/N)\, s(N-1) \end{cases} \tag{5.24}$$

To better understand the operating principle of the single tone DFT, the next section describes in detail the Goertzel algorithm structure, while in Sec. 5.6.2 are collected the main experimental results obtained in the estimation of L_t.

5.6.1 *The Goertzel DFT algorithm*

The algorithms of the DFT are normally used for the calculation of amplitude and phase of the entire spectrum of a signal. The knowledge of the spectrum might be of interest for some real-time applications, such as certain electrical drives based on advanced control techniques, where it is generally sufficient the knowledge of a single harmonic or a small number of harmonics.
When a single harmonic detection is required, DFT and FFT algorithms are not computationally efficient, and a single-tone of the DFT, known as the Goertzel algorithm, ensures better performances.
The normalised definition of DFT is the following:

$$X(k) = \sum_{r=0}^{N-1} x(r) W_N^{kr}, \qquad 0 \leq k, r \leq N-1 \tag{5.25}$$

where N is the number of samples, $W_N = e^{-j2\pi/N}$, $x(r)$ and $X(k)$ are the sampled signal (sample time $T = 1$) and its frequency-domain transformation (sample frequency $F = 1/N$), respectively.
The Goertzel algorithm is obtained by manipulating the 5.25 by considering the following identity:

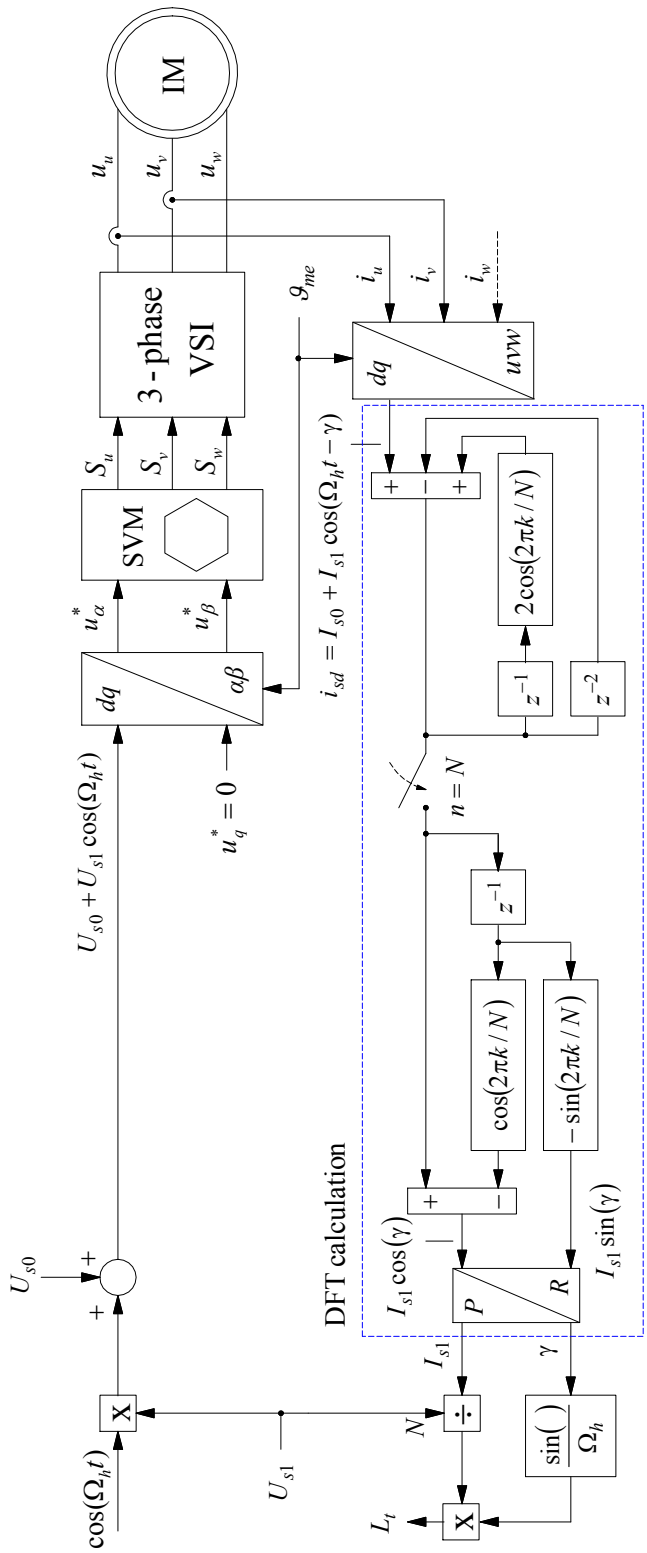

Fig. 5.11: Diagram for the L_t estimation procedure by the Goertzel DFT algorithm.

$$W_N^{-kN} = e^{(j2\pi/N)Nk} = e^{j2\pi k} = 1 \tag{5.26}$$

By replacing the (5.26) into the (5.25), it follows that:

$$X(k) = W_N^{-kN} \sum_{r=0}^{N-1} x(r) W_N^{kr} = \sum_{r=0}^{N-1} x(r) W_N^{-k(N-r)} \tag{5.27}$$

and then, from (5.27), the following sequence can be introduced:

$$y(n) = \sum_{r=0}^{N-1} x(r) W_N^{-k(n-r)} \tag{5.28}$$

The sequence (5.28) is equal to $X(k)$ when $n = N$ and represents a convolution between $x(n)$ and W_N^{-kn}, or equivalently the output of a linear system whose impulse response is equal to W_N^{-kn}. The Z-transform of W_N^{-kn} is:

$$H(z) = \underbrace{\frac{1}{\left(1 - 2\cos\left(2\pi k/N\right) z^{-1} + z^{-2}\right)}}_{\text{IIR filter}} \underbrace{\left(1 - W_N^k z^{-1}\right)}_{\text{FIR filter}} \tag{5.29}$$

(5.29) represents the transfer function between the sequence $y(n)$ and the input $x(n)$ (that is equal of $x(n) = i_d(n)$ for the studied application), split into an IIR filter and a FIR filter, as shown in Fig.5.12.

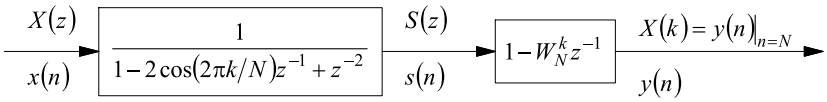

Fig. 5.12: Harmonic relevator as series of an IIR and an FIR filter.

It follows that:

$$X(z) = \left(1 - 2\cos\left(2\pi k/N\right) z^{-1} + z^{-2}\right) S(z) \tag{5.30}$$

Back into the time domain, let $s(n)$ be the output of the IIR filter and $S(z)$ its Z-domain value, then $s(n)$ (in the time domain, from Fig.5.12) can be rewritten as:

$$s(n)\left[1 - 2\cos\left(\frac{2\pi k}{N}\right) z^{-1} + z^{-2}\right] = x(n) = i_d(n) \tag{5.31}$$

and then, after some algebraic manipulations:

$$s(n) = x(n) + 2\cos\left(2\pi k/N\right) s(n-1) - s(n-2) \tag{5.32}$$

With the input $x(n) = i_d(n)$ being sampled during real-time control, the sequence $s(n)$ is computed on-line.
As regards the FIR filter, its output $y(n)$ is computed only for $n = N$, provided that $s(N)$ and $s(N-1)$ were previously saved:

$$X(k) = y(n)\big|_{n=N} = s(N) - W_N^k s(N-1) \tag{5.33}$$

Since W_N^k is a complex number, expression (5.33) is complex, too. The real and imaginary parts are:

$$\begin{aligned} \Re[X(k)] &= s(N) - \cos(2\pi k/N)\, s(N-1) \\ \Im[X(k)] &= \sin(2\pi k/N)\, s(N-1) \end{aligned} \tag{5.34}$$

Since $x(n)$ is a real signal, (5.32) shows that the computation of $s(n)$ requires one multiplication (as $2\cos(2\pi k/N)$ is stored as a coefficient) and two additions. The block scheme of the describe algorithm is represented by Fig.5.13.

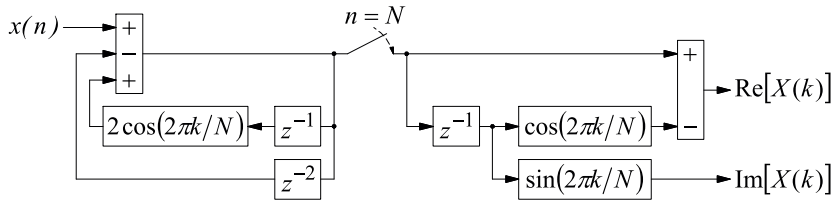

Fig. 5.13: Block diagram of the Goertzel algorithm.

Thus, $s(N)$ is obtained by N multiplications and $2N$ additions. The calculation of $\Re[X(k)]$ and $\Im[X(k)]$ requires two multiplications and one addition.
Altogether, the Goertzel algorithm requires $N+2$ multiplications and $2N+1$ additions to be spread over the whole NT_c time window, while $s(n)$ is updated with only one multiplication and two additions for each sample period.
Moreover, the value of N can be increased as needed with no effects on the computational time requirements, obtaining a very high DFT selectivity [92].
This is a net saving, if compared to the DFT in (5.25), which needs $2N$ multiplications and $2N$ additions to compute a real and imaginary parts of $X(k)$ from a real $x(k)$ signal [92].
However, the real advantage of the Goertzel algorithm for single harmonic analysis resides in its recursive definition (5.32), since in this way, the algorithm can be effectively used in real time without affecting the execution time of control routines.

5.6.1.1 *The phase detection*

With respect of the estimation of the transient inductance, it is relevant to understand the phase results of the computation with the Goertzel algorithm when the signal:

$$\begin{aligned} x[n] &= I_{s1}\cos(2\pi f_0 n T_c - \gamma) \\ n &= 0, \ldots, N-1\,;\, \gamma > 0 \end{aligned} \tag{5.35}$$

is injected in the control chain. In particular, the frequency f_0 is a multiply integer of F_c/N (frequency resolution of the DFT, i. e. $f_0 = k_0 F_c/N$ with $k_0 \in \{0, 1, \ldots, N-1\}$), and the Goertzel algorithm filters the input sequence $x[n] = i_d(n)$ that returns an impulsive response

$$h[n] = W_N^{-kn}\delta_{-1}[n] \qquad n \in \mathbb{Z} \tag{5.36}$$

where $\delta_{-1}[n]$ denotes the unitary sequence:

$$\delta_{-1}[n] = \begin{cases} 1 & n \geq 0 \\ 0 & n < 0 \end{cases} \tag{5.37}$$

As detailed in Sec. 5.6.1, after N steps, the output y of the IIR filter is equal of the k tone of the more general DFT transformation X of the input sequence x (i.e. $y[N] = X[k]$). By using the expansion of (5.35) (considering the cosine angle addition identity[3]), for a generic $k \in \{0, 1, \ldots, N-1\}$ it follows that:

$$x[n] = I_{s1} \left(\cos\gamma \cos(2\pi f_0 n T_c) - \sin\gamma \sin(2\pi f_0 n T_c) \right) \tag{5.39}$$

By considering the Fourier transforms:

$$\begin{aligned} \cos\left(\frac{2\pi}{N} k_0 n\right) &\xrightarrow{\text{DFT}} \quad \frac{N}{2}\delta[k+k_0] + \frac{N}{2}\delta[k-k_0] \\ \sin\left(\frac{2\pi}{N} k_0 n\right) &\xrightarrow{\text{DFT}} \quad j\frac{N}{2}\delta[k+k_0] - j\frac{N}{2}\delta[k-k_0] \end{aligned} \tag{5.40}$$

with $k \in \{0, 1, \ldots, N-1\}$, the DFT transformation X becomes:

$$\begin{aligned} y[N] = X[k] &= I_{s1}\frac{N}{2}\left(\cos\gamma - j\sin\gamma\right)\delta[k-k_0] + \cdots \\ &= I_{s1}\frac{N}{2}\left(\cos\gamma + j\sin\gamma\right)\delta[k+k_0] \end{aligned} \tag{5.41}$$

In this case $\delta[n]$ is the "Kronecker's delta" function (i. e. $\delta[0] = 1$ e $\delta[n] = 0$ for $n \neq 0$). By choosing $k = k_0$, the (5.41) can be rewritten as:

$$y[N] = X[k_0] = I_{s1}\frac{N}{2}\left(\cos\gamma - j\sin\gamma\right) \tag{5.42}$$

and so:

$$\begin{aligned} |y[N]| &= |X[k_0]| = I_{s1}\frac{N}{2} \\ \angle y[N] &= \angle X[k_0] = \operatorname{atan2}\left(-\sin\gamma, \cos\gamma\right) = -\gamma \end{aligned} \tag{5.43}$$

This means that the Goertzel algorithm return exactly the phase shift γ between current and voltage of (5.21).

5.6.2 *Experimental results*

The algorithm was tested on different induction motors, whose nameplate data are reported in Tab.5.1, Tab.5.2 and Tab.5.3. Actually, the choice of the frequency Ω_h is a trade-off between the accuracy of the approximation (5.22), which requires high frequency, and the need of a phase γ not too close to $\pi/2$ rad.el, to avoid computational inaccuracy in the rectangular-to-polar (R/P) conversion (Fig.5.11). Taking a value of

3

$$\cos(\alpha - \beta) = \cos(\alpha)\cos(\beta) + \sin(\alpha)\sin(\beta) \tag{5.38}$$

$\gamma = 1.4\,\text{rad}$ as a good compromise, the frequency $f_l = \Omega_h/2\pi = 100\,\text{Hz}$ was finally selected for the experimental tests.
Voltage and current fundamental harmonics were acquired and processed using the proposed fast DFT, but the choice of frequency and amplitude of the injection signal is a compromise between several factors. The chosen frequency f_l ensures that the phase $\angle \dot{I}_s$ is not too close to $\pi/2\,\text{rad.el}$, while the reference AC voltage $|U_{AC}|$ provides sufficient resolution in the current reading without moving the working point from the linear region.
Anyway, higher values of the injection frequencies f_l require a greater resolution (F) in the Goertzel algorithm, since the current noise reduces the bandwidth centred on the injection frequency. The final value of the current perturbation was in the range of $\in [I_{AC,min} \div I_{AC,max}] = 0.25 \div 0.3\,\text{A}$, and to ensure an equal amplitude in the modulation current at each working point, the algorithm changes the amplitude of the reference AC voltage $|U_{AC}|$ and verifies that before proceeding with the calculation of the DFT the measured perturbation is in the boundary set.
In the final version of the algorithm, in the calculation of L_t the currents $|i_s| < 3\,\text{A}$ were excluded, since the saturation effects are more appreciable for higher currents and it is therefore expected that L_t will remain constant in that range.
The amplitude of the voltage input U_{s1} has to be tuned to get a correspondent sinusoidal current high enough to let the analog-to-digital conversion be accurate, but limited to a value that prevents saturations around the working point. For an A/D resolution of 12 bit, the here was to impose a minimum current around $0.3\,\text{A}$ ($15 - 20\,\text{LSB}$). Being just few percent of the IM rated current, any saturation is avoided.
As a first experimental test, the value of L_t was plotted as a function of the DC bias current I_{s0}, at a fixed position $\theta_{me} = 0\,\text{rad.el}$, i. e. along the α axis. The result is shown in Fig.5.14a, that reports the automatic estimation of L_t for all the available motors.
The L_t trend as a function of the bias DC vector angular position θ_{me} is reported in Fig.5.14b, for the case of IM_1 (Tab.5.1), and it can be concluded that the position of the bias current vector does not substantially affect the inductance calculation. On the other hand, and contrary to the common belief, some motors may suffer a marked saturation effect of L_t, despite the fact that it mainly represents a leakage flux linkage (Fig.5.14a, IM_1).
It can be somewhat physically explained by considering the saturation of the stator slot corners in the motor at higher currents, that affects the value of the total leakage flux linkage in the air gap. The squirrel cage rotor in fact, has the narrow area that, in short circuit closes all the bars that can be saturated with a moderate rotor current.
The complete profile of ($L_t = f(|i_s|, \vartheta_{me})$) is shown in Fig.5.14b and Fig.5.14c, and the marked degree saturation can be explained considering the saturation of the stator slot corners in the motor for higher currents, affecting the value of the total leakage flux linkage in the air gap. In fact, with respect of the details of the IMs geometry, it is expected that those with open slots on the stator and rotor (IM_2 and IM_3) have a rather constant L_t (and greater for IM_3, where the slots are relatively more closed and deeper, [98], [101]). On the opposite hand, IM_1 has closed slots and it will feature high L_t for small currents, which drop with increasing current because of the saturation of the iron bridges.
These measurements confirm that L_t is a delicate parameter in an IM model, since its value is very small and difficult to calculate with an automatic identification routine. To ensure maximum accuracy in the L_t calculation, at every recalculation of the inductance the machine's resistance R_s was also recalculated together with the dead times compensation curves in the $\alpha\beta$ reference frame. At a different angular position ϑ_{me} of the reference vector, in fact, the dead time compensation curve along α or β is proportional to the angular projection and then varies, albeit slightly.

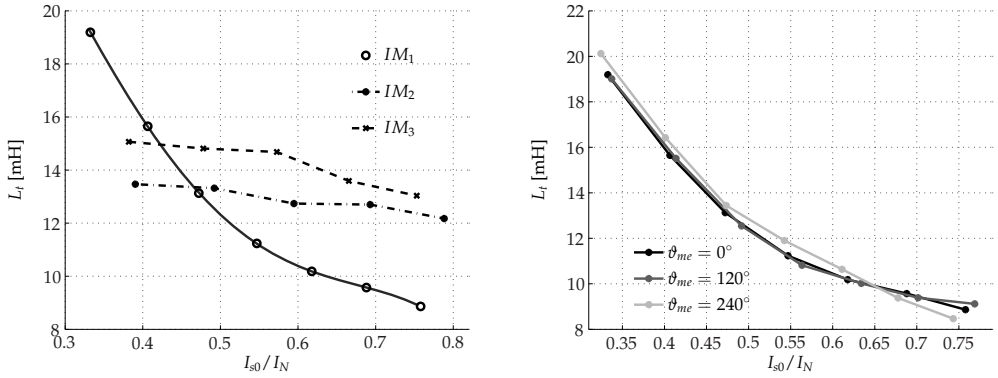

(a) L_t *as a function of current, all motors tested.*

(b) IM_1 *(Tab.5.1):* L_t *as a function of current vector position.*

(c) IM_2 *(Tab.5.2):* L_t *as a function of current vector position.*

(d) IM_3 (Tab.5.3): L_t as a function of current vector position.

Fig. 5.14: Experimental transient inductance L_t identification, various IMs.

For the sake of comparison, the conventional test reported in Sec. 5.2, executed on IM_1, returned a value of $L_t = 20.75\,\text{mH}$ at only a few hertz, in good accordance with that reported in Fig.5.14 for the IM_1 machine.

5.7 THE IDENTIFICATION OF THE MAGNETIZING FLUX LINKAGE

The third parameter that must be identified is $L_\varphi(\boldsymbol{i}_\varphi)$. The same considerations of Sec. 5.7, related to the estimation of $L_t(\boldsymbol{i}_s)$ are valid also for the calculation of this parameter. In particular, this means that the two inductances in Fig. 4.5, when a DC current flows in the circuit, are short-circuited, and so the whole magnetic energy is kept within the two elements without being transformed into mechanical energy.
$L_\varphi(\boldsymbol{i}_\varphi)$ can be derived from the knowledge of the stator flux $\boldsymbol{\lambda}_s$ and the DC magnetizing current value used to calculate the flux linkage relationship, that leads to an estimation of the total apparent inductance[4] [88], which is the sum of $L_t(\boldsymbol{i}_s)$ and $L_\varphi(\boldsymbol{i}_\varphi)$.

4 The instantaneous link between the flux linkage and the current that flows into the inductance can be expressed by the relation $\lambda(i(t)) = L_s^{app}(i(t))i(t)$, in which the *apparent* inductance L_s^{app} is function of the current only. By utilizing the chain differentiation rule, it can be expanded as:

$$u(t) = \frac{d\lambda(i(t))}{dt} = \left[L_s^{app}(i(t)) + i(t)\frac{dL_s^{app}(i(t))}{di(t)}\right]\frac{di(t)}{dt} = L(i)\frac{di(t)}{dt}. \tag{5.44}$$

The equivalent parameter $L_s(\boldsymbol{i}_s)$ can be easily derived as:

$$L_\varphi(\boldsymbol{i}_\varphi(0)) + L_t(\boldsymbol{i}_s(0)) = \frac{\lim\limits_{t\to+\infty} \boldsymbol{\lambda}_s(\boldsymbol{i}_s(t))}{\lim\limits_{t\to+\infty} \boldsymbol{i}_s(t)} \tag{5.46}$$

where the two limits to infinity refers to a steady-state condition. $L_\varphi(\boldsymbol{i}_\varphi)$ is then estimated by subtracting the value of $L_t(\boldsymbol{i}_s)$ from the expression (5.46), previously calculated in 5.6.
There are two main advantages in considering the expression (5.46) for the $L_\varphi(\boldsymbol{i}_\varphi)$ estimation.
The first is that the intrinsic non-linearity of L_φ, due to the iron path saturation within the IM magnetic circuit, not modify the expression (5.46), that returns the correct value of $L_\varphi(\boldsymbol{i}_\varphi)$ by imposing growing DC current values in order to map the entire non-linear characteristic.
The second advantage resides in the possibility of using any current profile to reach the final DC value (or magnetizing current, as will be defined in this chapter), since the system is conservative. Ramps or smoother signals turn out to be useful to reduce the natural tendency of real motors to self-align themselves to stator slots, maintaining the standstill feature during the whole procedure.
Unfortunately, the main problem is the exact deduction of $\boldsymbol{\lambda}_s(\boldsymbol{i}_s(0))$, and some issues have been addressed in papers as [102] and [103], but unfortunately these solutions do not work in a standstill condition. To overcome this problem, a novel approach for the calculation of the flux linkage, without limitation in the choice of the voltage vector $\boldsymbol{u}_s$ is here described.
Starting from the basic definition of the flux linkage, it can be derived as implicit function of time by the direct integration of (5.48):

$$\boldsymbol{\lambda}_s(\boldsymbol{i}_s(t_1)) = \boldsymbol{\lambda}_s(\boldsymbol{i}_s(0)) + \int_0^{t_1} (\boldsymbol{u}_s(t) - R_s\boldsymbol{i}_s(t))\, dt \tag{5.47}$$

Similarly to the previous step, the IM under test is driven to an initial DC steady state condition (U_{s0}, I_{s0}), at a fixed angular position ϑ_{me} of the DC bias vector, so that at time $t = 0$ the flux $\boldsymbol{\lambda}_s(I_{s0}e^{j\vartheta_{me}})$ is established in the motor.
A null voltage vector reference is then issued to the inverter and, at the same time, the integration (5.47) is triggered and continued until the stator current falls below the ADC sensibility (at time t_1). Then, the flux linkage is null ($\boldsymbol{\lambda}_s(t_1) = 0$), so that:

$$\boldsymbol{\lambda}_s(I_{s0}e^{j\vartheta_{me}}) = \lambda_{s\alpha} + j\lambda_{s\beta} = -\int_0^{t_1} (\boldsymbol{u}_s - R_s\boldsymbol{i}_s)\, dt \tag{5.48}$$

It is worth noting that $\boldsymbol{i}_\varphi(0) = \boldsymbol{i}_s(0) = I_{s0}e^{j\vartheta_{me}}$, since the voltage across the resistance R_{sr} is null in the DC steady state condition (see Fig.4.5).
Therefore, at the end of the identification step, the magnetising flux $\boldsymbol{\lambda}_\varphi$ will be derived by the difference from the stator and the transient flux linkage:

The final expression is formally similar to the linear case, with the obvious distinction of an explicit dependence on the current of the *instantaneous* inductance L_s

$$L_s(i) = L^{app}(i) + i(t)\frac{dL_s^{app}(i)}{di}. \tag{5.45}$$

The instantaneous inductance L_s represents the actual inductance around the operating point $P = (I_{s0}, \lambda_{s0})$ and it expresses the derivative $d\lambda_s/di$ of the flux linkage with respect to the current in P.

$$\boldsymbol{\lambda}_{\varphi}(\boldsymbol{i}_s(0)) = \boldsymbol{\lambda}_s(\boldsymbol{i}_s(0)) - \boldsymbol{\lambda}_t(\boldsymbol{i}_s(0)) \tag{5.49}$$

The correct calculation of this parameter requires the exact numerical knowledge of the flux linkage $\boldsymbol{\lambda}_s(I_{s0}e^{j\vartheta_{me}})$, that will be detailed in Sec. 5.7.2.
With respect of the calculation of $\boldsymbol{\lambda}_s(I_{s0}e^{j\vartheta_{me}})$, the integration routine starts with the application, at $t = 0$, of the null voltage vector. It corresponds to an inverter configuration with the three low switches in the *ON* state ($S_2 = S_4 = S_6 = 1$) and the dual high switches in the *OFF* state (Fig.5.5).
Depending on the sign of the current in each inverter leg, it is possible to determine which components are carrying the current. Regarding as positive the currents that flow inward a motor phase, and denoting by T_i and D_i an IGBT or diode of the i-th pole, the results have been collected in Tab.5.8.

Tab. 5.8: Conducting components in the inverter as a function of ϑ_{me}.

Angle [deg]	**Conducting components**	**Current sign**
$\vartheta_{me} = 0°$	D_2, T_4, T_6	$i_u^+, i_v^- i_w^-$
$\vartheta_{me} = 30°$	$D_2, 0, T_6$	$i_u^+, i_v^0 i_w^-$
$\vartheta_{me} = 60°$	D_2, D_4, T_6	$i_u^+, i_v^+ i_w^-$
$\vartheta_{me} = 90°$	$0, D_4, T_6$	$i_u^0, i_v^+ i_w^-$
$\vartheta_{me} = 120°$	T_2, D_4, T_6	$i_u^-, i_v^+ i_w^-$
$\vartheta_{me} = 150°$	$T_2, D_4, 0$	$i_u^-, i_v^+ i_w^0$
$\vartheta_{me} = 180°$	T_2, D_4, D_6	$i_u^-, i_v^+ i_w^+$
$\vartheta_{me} = 210°$	$T_2, 0, D_6$	$i_u^-, i_v^0 i_w^+$
$\vartheta_{me} = 240°$	T_2, T_4, D_6	$i_u^-, i_v^- i_w^+$
$\vartheta_{me} = 270°$	$0, T_4, D_6$	$i_u^0, i_v^- i_w^+$
$\vartheta_{me} = 300°$	D_2, T_4, D_6	$i_u^+, i_v^- i_w^+$
$\vartheta_{me} = 330°$	$D_2, T_4, 0$	$i_u^+, i_v^- i_w^0$

Tab.5.8 covers the whole possible angular positions ϑ_{me} of the DC bias vector, by steps of $\pi/6$ rad.el. Any intermediate angular position maintains the sign of the currents, i. e. the conducting components remain the same.
With this information, the actual voltage drops $u_{S2}(|i_u|)\,, u_{S4}(|i_v|)\,, u_{S6}(|i_w|)$ in the conducting component (either the diode or the IGBT of each inverter leg) can be retrieved either from the curves of Fig.5.6 or from their polynomial approximation.
The next step is the set-up of the algorithm that implements the expression (5.48). During the step transient, voltage and currents space vectors can be derived as[5]:

$$\begin{cases} \boldsymbol{u}_s = \dfrac{2}{3}\left(u_{S2}(|i_u|) + u_{S4}(|i_v|)e^{j\frac{2\pi}{3}} + u_{S6}(|i_w|)e^{j\frac{4\pi}{3}}\right) \\ \boldsymbol{i}_s = i_{s\alpha} + j i_{s\beta} = \dfrac{2}{3}\left(i_u + i_v e^{j\frac{2\pi}{3}} + i_w e^{j\frac{4\pi}{3}}\right) \end{cases} \tag{5.50}$$

The stator flux linkage vector is readily obtained by substituting (5.50) into the right term of (5.48).

5 The (5.50) is derived by applying the Spatial Vector notation to the three legs of the equivalent circuit of Fig.5.5.

If the inverse Clarke transformation $\boldsymbol{T}_{\alpha\beta0/uvw}$ is applied at the real and imaginary part of the (5.48), the three fluxes λ_{su}, λ_{sv} and λ_{sw} in the uvw reference frame can be also derived.

$$\begin{pmatrix} \lambda_{su} \\ \lambda_{sv} \\ \lambda_{sw} \end{pmatrix} = \underbrace{\frac{2}{3}\begin{bmatrix} 1 & -\frac{1}{2} & -\frac{1}{2} \\ 0 & \frac{\sqrt{3}}{2} & -\frac{\sqrt{3}}{2} \\ \frac{1}{2} & \frac{1}{2} & \frac{1}{2} \end{bmatrix}}_{=\boldsymbol{T}_{\alpha\beta0/uvw}} \begin{pmatrix} \lambda_{s\alpha} \\ \lambda_{s\beta} \\ \lambda_{s0} \end{pmatrix} \tag{5.51}$$

The identification algorithm calculates the flux linkage $\boldsymbol{\lambda}_s(I_{s0}e^{j\vartheta_{me}})$ at standstill with respect of the equivalent circuit of Fig.4.5 but the entire estimation procedure miss of the BEMF, that appears when $\omega_{me} \neq 0$.
Since the parameters estimated by the algorithm are used in a typical FOC control scheme, it is relevant to understand if the estimation of the BEMF $j\omega_{me}L_m\boldsymbol{\lambda}_r/L_r$ in Fig.4.5 can be derived by the knowledge of the magnetizing flux linkage.
In fact, the flux linkage $\boldsymbol{\lambda}_\varphi(\boldsymbol{i}_\varphi)$ (from Fig.4.5) can be rewritten as:

$$\boldsymbol{\lambda}_\varphi(\boldsymbol{i}_\varphi) = L_\varphi \boldsymbol{i}_\varphi = \frac{L_m^2}{L_r}(\boldsymbol{i}_s - \boldsymbol{i}_{sr}) \tag{5.52}$$

Moreover, since the rotor current can be expressed in the stator reference frame as [4]:

$$\boldsymbol{i}_{sr} = -\frac{L_r}{L_m}\boldsymbol{i}_r \tag{5.53}$$

it follows that $\boldsymbol{\lambda}_\varphi$ can be expressed as:

$$\boldsymbol{\lambda}_\varphi(\boldsymbol{i}_\varphi) = \frac{L_m^2}{L_r}(\boldsymbol{i}_s + L_m\boldsymbol{i}_r) \tag{5.54}$$

The rotor flux linkage $\boldsymbol{\lambda}_r(\boldsymbol{i}_r)$ can be expressed as:

$$\boldsymbol{\lambda}_r(\boldsymbol{i}_r) = L_m\boldsymbol{i}_s + L_r\boldsymbol{i}_r \tag{5.55}$$

The equating of (5.55) and (5.54) returns:

$$\frac{L_m}{L_r}(L_m\boldsymbol{i}_s + L_r\boldsymbol{i}_r) = \boldsymbol{\lambda}_\varphi = \frac{L_m^2}{L_r}(\boldsymbol{i}_s + L_m\boldsymbol{i}_r) \tag{5.56}$$

that correlates the knowledge of the BEMF $(j\omega_{me}\frac{L_m}{L_r}\boldsymbol{\lambda}_r)$ with the non-linear parameter $\boldsymbol{\lambda}_\varphi$, calculated with the proposed algorithm. It follows that the knowledge of the Γ-inverse circuit parameters at standstill is sufficient for the practical application use of them into a conventional control scheme (i. e. sensored or sensorless FOC), although other implementation aspects should be carefully considered.

In particular, it is worth noting that during the normal operating of the motor, instead of the standstill condition, part of the current $\boldsymbol{i}_s$ is split in $\boldsymbol{i}_\varphi$. Luckily, the estimation procedure is not corrupted by this aspect, since the flux linkage $\boldsymbol{\lambda}_\varphi$ is calculated after the calculation of $\boldsymbol{\lambda}_s$.
The tricky aspect is related to the exact knowledge of $\boldsymbol{i}_\varphi$ during the normal operating of the motor, when $\boldsymbol{\lambda}_\varphi$ is modified by the operating conditions as well as its current $\boldsymbol{i}_\varphi$. This aspect is beyond the scope of this work but it will be covered by future research works.
One aspect neglected so far which should be considered to prove the effective validity of the $\boldsymbol{\lambda}_s(I_{s0}e^{j\vartheta_{me}})$ calculation, is the influence of the homo polar voltage component in the flux linkage estimation.
In the proposed identification algorithm, the real and imaginary part of the flux linkage (5.48), are calculated in the $\alpha\beta$ reference frame and the zero-component are lost.
As known, the homo polar voltage term appears in every non-balanced three-phases systems, and during the step voltage transient, due of the asymmetry in the VSI configuration (i. e. the component in conduction depends by the voltage vector positioning, as reported in Tab.5.8), the induction motor connected to the VSI represents a non-balanced three-phase system, and the influence of the homo polar component must be analysed. For the Kirchhoff's circuit laws the sum of the currents is zero (i. e. $i_u + i_v + i_w = 0$) but the homo polar term is lost during the estimation of the flux linkage $\boldsymbol{\lambda}_s$ of (5.50), since the flux linkage is calculated in the $\alpha\beta$ reference frame. This obvious consequence is easy to prove, and with respect of Fig.5.5 (with all the phases connected) the voltage balance can be written as:

$$\begin{aligned} u_{uO} &= u_{S2}(|i_u|) + u_{NO} = R_s i_u + \frac{d\lambda_{su}(t)}{dt} \\ u_{vO} &= u_{S4}(|i_v|) + u_{NO} = R_s i_v + \frac{d\lambda_{sv}(t)}{dt} \\ u_{wO} &= u_{S6}(|i_w|) + u_{NO} = R_s i_w + \frac{d\lambda_{sw}(t)}{dt} \end{aligned} \tag{5.57}$$

The IM is saturated during the identification tests and then the flux linkage concatenated by each phase has an homo polar component due of the saturation in the magnetic circuit.
The sum of the flux linkages is then expressed as $\lambda_{su}(t) + \lambda_{sv}(t) + \lambda_{sw}(t) + 3\lambda_{sO}(t) = 0$, where $3\lambda_{sO}(t)$ defines the equivalent flux linkage homo polar term due of the saturation effects in the motor (i. e. $\frac{d\lambda_{su}(t)}{dt} + \frac{d\lambda_{sv}(t)}{dt} + \frac{d\lambda_{sw}(t)}{dt} = -3\frac{d\lambda_{sO}(t)}{dt}$). From (5.57), the voltage u_{NO} can be written as:

$$u_{NO}(t) = -\frac{u_{S2}(t)(|i_u|) + u_{S4}(t)(|i_v|) + u_{S6}(t)(|i_w|)}{3} - \frac{d\lambda_{sO}(t)}{dt} \tag{5.58}$$

and with respect of (5.57), the flux linkage in each phase uvw is:

$$\begin{aligned} \lambda_{su}(i_u(t_1)) &= \lambda_{su}(i_u(0)) + \int_0^{t_1} (u_{s2}(t) + u_{NO}(t) - R_s i_u(t))\, dt \\ \lambda_{sv}(i_v(t_1)) &= \lambda_{sv}(i_v(0)) + \int_0^{t_1} (u_{s4}(t) + u_{NO}(t) - R_s i_v(t))\, dt \\ \lambda_{sw}(i_w(t_1)) &= \lambda_{sw}(i_w(0)) + \int_0^{t_1} (u_{s6}(t) + u_{NO}(t) - R_s i_w(t))\, dt \end{aligned} \tag{5.59}$$

Since at the end of the integration process $\lambda_s(t_1) = 0$, the replacement of (5.58) into the (5.59) yields:

$$\begin{aligned}
\lambda_{su} &= -\int_0^{t_1} \left(\frac{2}{3}u_{s2}(t) - \frac{1}{3}u_{s4}(t) - \frac{1}{3}u_{s6}(t) - \frac{d\lambda_{sO}(t)}{dt} - R_s i_u(t) \right) dt \\
\lambda_{sv} &= -\int_0^{t_1} \left(-\frac{1}{3}u_{s2}(t) + \frac{2}{3}u_{s4}(t) - \frac{1}{3}u_{s6}(t) - \frac{d\lambda_{sO}(t)}{dt} - R_s i_v(t) \right) dt \\
\lambda_{sw} &= -\int_0^{t_1} \left(-\frac{1}{3}u_{s2}(t) - \frac{1}{3}u_{s4}(t) + \frac{2}{3}u_{s6}(t) - \frac{d\lambda_{sO}(t)}{dt} - R_s i_w(t) \right) dt
\end{aligned} \tag{5.60}$$

The previous expression shows that the homo polar flux linkage component is actually present in the *uvw* reference frame, but it is not considered in the identification routine[6]. This term, in fact, is lost in the flux linkage calculation of $\lambda_{s\alpha}$ in (5.62), but some experimental validations have proved that the contribute of the zero-voltage component is irrelevant, therefore the flux linkage calculation is not significantly affected by this term.
To this purpose, the homo polar component effects have been considered and evaluated from an experimental point of view, as demonstrated by Fig.5.15, where are shown the voltages at the terminal of the motor $u_{s\alpha}$ and the equivalent voltage drop u_{s2} of the VSI by considering a voltage vector $\boldsymbol{u}_s$ at $-\pi/6$ rad.el.

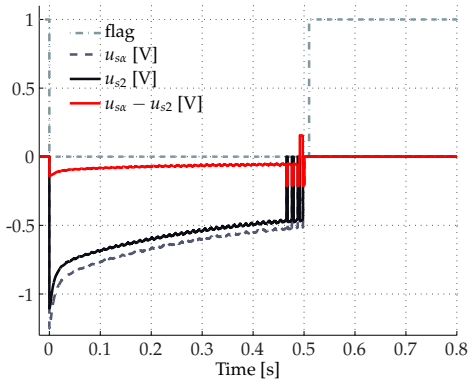

Fig. 5.15: Experimental measurement of the homo polar component $u_{NO} = u_{s\alpha} - u_{s2}$.

6 It is obvious that by considering the expression of the magnetic fluxes in the $\alpha\beta$ reference frame:

$$\begin{aligned}
\lambda_{s\alpha} &= -\int_0^{t_1} (u_{s\alpha}(t) - R_s i_{s\alpha}(t))\, dt = \int_0^{t_1} (R_s \Re(\boldsymbol{i}_s) - \Re(\boldsymbol{u}_s))\, dt \\
\lambda_{s\beta} &= -\int_0^{t_1} (u_{s\beta}(t) - R_s i_{s\beta}(t))\, dt = \int_0^{t_1} (R_s \Im(\boldsymbol{i}_s) - \Im(\boldsymbol{u}_s))\, dt
\end{aligned} \tag{5.61}$$

and replacing the real and imaginary part of the (5.50) into the (5.61), since $i_u + i_v + i_w = 0$ it follows that:

$$\begin{aligned}
\lambda_{s\alpha} &= -\frac{2}{3}\int_0^{t_1} \left(u_{S2}(t) - \frac{1}{2}u_{S4}(t) + \frac{1}{2}u_{S6}(t) \right) dt + \frac{2}{3}\int_0^{t_1} R_s \left(i_u - \frac{1}{2}i_v - \frac{1}{2}i_w \right) dt \\
&= \lambda_{su} - \frac{\lambda_{sv}}{2} - \frac{\lambda_{sw}}{2} \\
\lambda_{s\beta} &= -\frac{2}{3}\int_0^{t_1} \left(\frac{\sqrt{3}}{2}u_{S4}(t) - \frac{\sqrt{3}}{2}u_{S6}(t) \right) dt + \frac{2}{3}\int_0^{t_1} R_s \left(\frac{\sqrt{3}}{2}i_v - \frac{\sqrt{3}}{2}i_w \right) dt \\
&= \frac{\sqrt{3}}{2}\lambda_{sv} - \frac{\sqrt{3}}{2}\lambda_{sw}
\end{aligned} \tag{5.62}$$

The results in Fig.5.15 prove that the difference of the two terms is very low, and considering that the homo polar flux linkage component not affects the torque in an IM (without neutral point linked), it can be neglected.

5.7.1 *Experimental results*

The experimental measurement related to the on-line calculation of the magnetising inductance has been one the most challenging parts of the entire estimation procedure. The experimental setup is the same of Sec. 5.6.2, and after the calculation of the stator resistance and the dead time compensation (carried out using the three-phase voltage inverter characterized in Sec. 5.4), the automatic procedure starts. A first transient from zero to a DC current level $i_s(0) = I_{s0}$ (aligned with d-axis, shifted of the angle ϑ_{me} from the u-axes) is performed.
When the DC steady-state current I_{s0} is reached, the on-line calculation of the real or imaginary part of flux linkage with (5.60) can be performed. To this aim the current is forced to zero, with the inverter configured with the three low switches in the ON state ($S_2 = S_4 = S_6 = 1$) and the dual high switches in the OFF state, as shown in Fig.5.5.
During this transient, all the three currents are measured and the three voltage drops in each conducting leg of the inverter ($u_{S2}(|i_u|)\,, u_{S4}(|i_v|)\,, u_{S6}(|i_w|)$) are reconstructed (as specified in the previous paragraph, Tab.5.8). When the transient is finished (all the currents are zero), a little delay time is imposed and the same step transient is repeated again, and in order to map the entire flux linkage curve in the whole IM current range, a new step transient is applied by changing the I_{s0} value.
After the complete mapping of a curve $\lambda_{s\alpha} = f(i_{s\alpha})$ and $\lambda_{s\beta} = f(i_{s\beta})$ (approximately from 0 to $1.2 \div 1.3\, I_N$ of the machine), the procedure restarts by reconsidering a different angular position ϑ_{me}. The final beam of curves $\lambda_{s\alpha} = f(i_{s\alpha}, \vartheta_{me})$ and $\lambda_{s\beta} = f(i_{s\alpha}, \vartheta_{me})$ is parametrized at the angular position ϑ_{me}, while the stator resistance R_s and the dead time compensation are recalculated at each ϑ_{me} variation.
The on-line implementation of the algorithm for the estimation of the flux linkage presents some drawbacks, and for this reason some details cannot be ignored. In particular, when the voltage reference is set to zero ($\boldsymbol{u}_s = 0$), the integration of the current and voltage drop start, but the time when integration stops is a very delicate question. In fact, the compensation of the three branches must cease as soon as the current of one of them is below a predetermined value, and so the total integration of the flux linkage ends only when in all three branches there is no more significant current, because the current absence in one branch does not ensure that the transient is exhausted.
Another problem is related to the noise of the current measurements, and so the detection of the current below the significant threshold is carried out by adopting a hysteresis bandwidth limited to $i_H \in [i_{H,min} \div i_{H,max}] = 0.02 \div 0.04\,\text{A}$, to be sure that the currents are not considered different to zero due to the overlapped noise.
A first batch of measures was performed to understand the difference between the real voltages applied to the motor and that calculated with the automatic algorithm. During the transient, the application of (5.60) requires the knowledge of the real voltages on the phases of the motor, that are reconstructed by considering the (5.50) in combination with the interpolated curves of Fig.5.6. Fig.5.16 shows a comparison between the voltages obtained with the approach described in Sec. 5.4 and the voltages measured by a voltage probe while the estimation procedure was running. During the execution of the test, the voltage vector $\boldsymbol{u}_s$ generated with the control algorithm was at the fixed position of $\vartheta_{me} = -\pi/6$ rad.el, so that the sum of the three reconstructed voltages $|u_{s2}|$, $|u_{s4}|$ and $|u_{s6}|$ was equal of the phase to phase real measure performed with the oscilloscope. The perfect match between real and estimated voltages for the IM_1 motor in Fig.5.16a and

for the IM_2 motor in Fig.5.16b proves the practical feasibility and the high accuracy of the method.

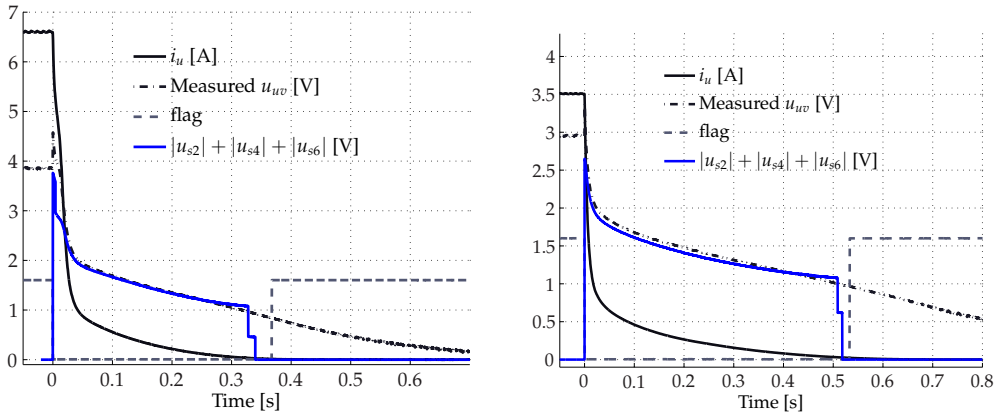

(a) IM_1 *voltage drop.* (b) IM_2 *voltage drop.*

Fig. 5.16: Overlap during a transient between the reconstructed voltages (dSPACE algorithm, using the curves of Sec. 5.4) and the real ones (motor IM_1 and IM_2) at the fixed position $\vartheta_{me} = -\pi/6$ rad.el. A voltage probe has been used to recorded the voltage transient while the algorithm running.

A second batch of experimental results are in Fig.5.17. These figures shows a generic voltage drop of u_{S2} and the current trend of i_u, during the application of (5.48). As mentioned above, the integration is stopped at time t_1 (as visible in Fig.5.17), in correspondence to the current zeroing. It is worth noting that in Fig.5.16 as well as in Fig.5.17 the resultant flux linkage is missing of a part of the voltage contribution, since it is evident that at time t_1 the voltage drop u_{s2} has not yet come to zero.
There are several combined reasons that produce this effect. The main contribution is related to the action performed by the squirrel-cage rotor, that is a short-circuited coil and contrasts every modification of the flux linkage. The result of this action is represented by an induced BEMF at the primary winding. The second one is represented by the particular VSI configuration during the step voltage transient. In the 000 configuration of the inverter, in fact, the non linear effects of the diodes lead to a quick change in the stator current behaviour, that in absence of a hardware measurement system cannot be considered.
In Sec. 5.9 this phenomenon will be clarified. The solution is to measure off-line the voltage lost term, store it in a look-up table, and add this compensation during the integration process of (5.48).
Some measurements on IM_1 (Tab.5.1), at different angular positions of the bias DC voltage vector, and relative to increasing current amplitude, were carried out to map the stator flux linkage vector in all possible operating conditions of the motor.
The identification results are reported in Fig.5.18, plotted as a function of both the amplitude I_{s0} (normalised to the rated motor current) and the position ϑ_{me}, respectively. Besides the expected saturation (that appears to be around the 70% of the rated current), the measurements highlight a certain dependence of the flux linkage amplitude on its space position. Neglecting or ignoring this dependency may lead to imprecise models, with direct repercussions on the control side.

5.7.2 *Validation of the method*

Several tests were performed with the aim of validating the results of the identification. Similarly to the transient inductance, the identification of the stator flux linkage

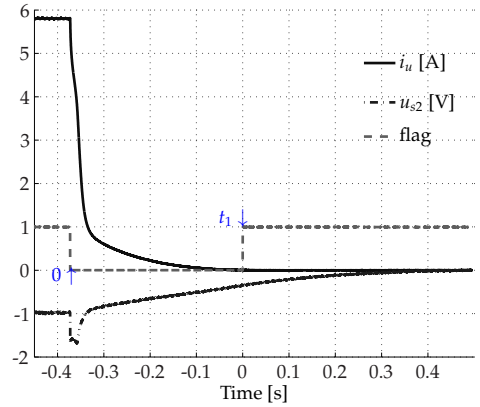

(a) *Voltage drop and current during the λ_s identification procedure, (IM_1, Tab.5.1)*

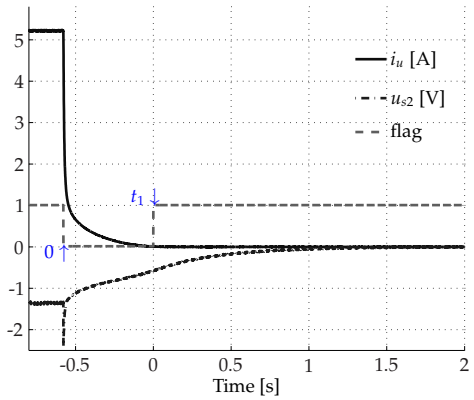

(b) *Voltage drop and current during the λ_s identification procedure, (IM_2, Tab.5.2)*

Fig. 5.17: Voltage drop and current during the switch off transient. Tail effect visible after t_1

was performed on different motors; the relevant data are reported in Tab.5.1, Tab.5.2 and Tab.5.3. As an objective method of comparison to determine whether the estimation procedure returns the correct result, the curves were compared in two different ways, namely, with those obtained using the Finite Element Analysis and those deriving from a comparative DC-test, [11], [88]. In particular, the procedure for the calculation of the flux linkage using a DC test consist in impose different DC currents I_{s0} to the motor by a programmable DC-power supply, directly connected to the phases u and v, to emulate the voltage supply condition of an inverter-fed IM with a constant phase $\vartheta_{me} = -\pi/6$ rad.el. By using the VSI in fact, the same DC step voltage transient is obtained by setting the voltage reference at $\vartheta_{me} = -\pi/6$ rad.el with the states configuration in $00o$, since the phases u and v are short-circuited through diode D_2 and IGBT T_4, as shown in Fig.5.19.
The analytic expression of the flux linkage can be derived by considering the phase u and the current i_u, while the stator resistance is supposed as a known or easily derivable quantity.
It follows that $i_u = -i_v$, while $i_w = 0$. The phase voltages and phase currents were measured by a differential and a current probe, while an off-line post-elaboration returns the correct flux linkage estimation by considering the (5.48) in the specific case of $\vartheta = -\pi/6$ rad.el. From the balance equation of a single phase voltage relative to the neutral point O (Fig.5.5), it follows that:

$$u_{uO} = R_s i_u + \frac{d\lambda_{su}(i_u, i_v, i_w)}{dt} \tag{5.63}$$

The stator flux linkage $\lambda_{su}(t)$ is then:

$$\lambda_{su}(t) - \lambda_{su}(0) = \int_0^t (u_{uO} - R_s i_u)\, dt \tag{5.64}$$

Since in general, the neutral point of the motor is not accessible, the Step voltage transient of both current i_u and the phase-to-phase voltage u_{uv} were recorded. The symmetry of phase feeding ($i_u = -i_v$) makes $\lambda_{su} = -\lambda_{sv}$ true and then the phase-to-phase voltage drop u_{uv} is:

$$u_{uv} = u_{uO} - u_{vO} = 2R_s i_u + 2\frac{d\lambda_{su}}{dt} \tag{5.65}$$

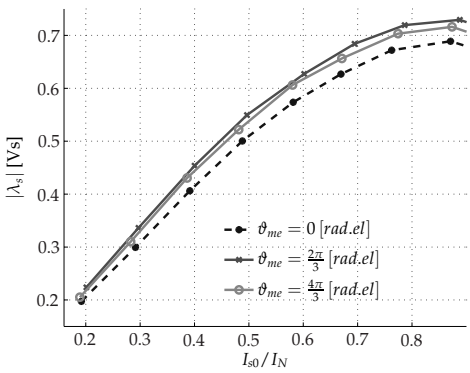

(a) IM_1 - *Flux linkage identification versus current*

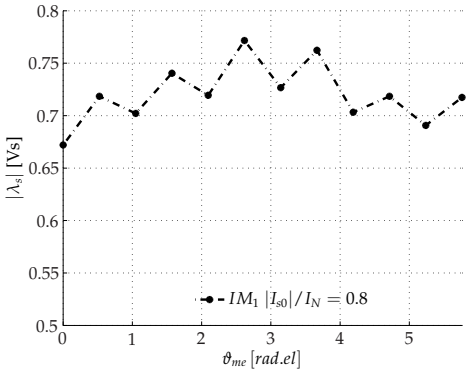

(b) IM_1 - *Flux linkage identification versus* ϑ_{me}

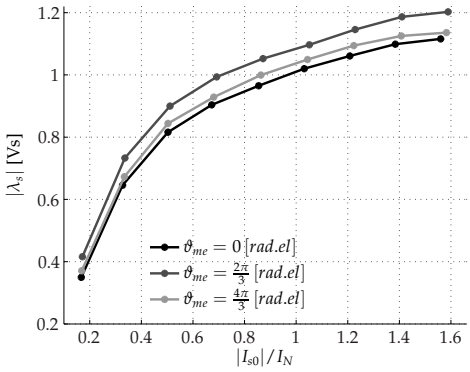

(c) IM_2 - *Flux linkage identification versus current*

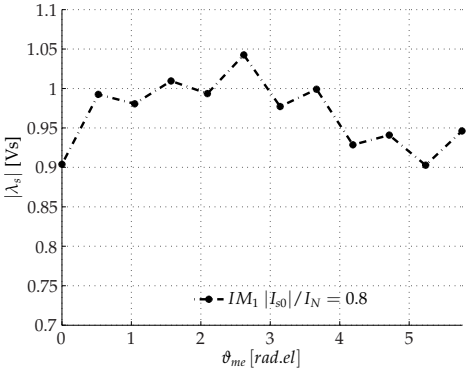

(d) IM_2 - *Flux linkage identification versus* ϑ_{me}

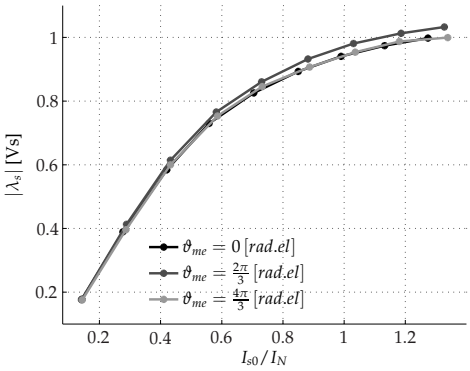

(e) IM_3 - *Flux linkage identification versus current*

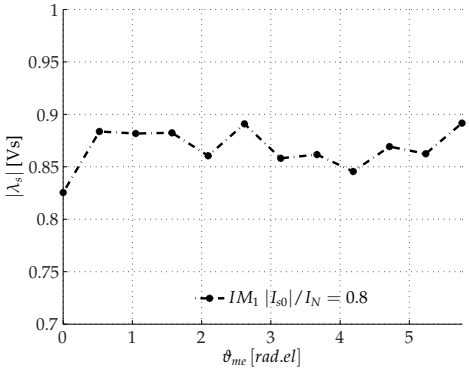

(f) IM_3 - *Flux linkage identification versus* ϑ_{me}

Fig. 5.18: Experimental stator flux linkage identification of IM_1 (Tab.5.1), IM_2 (Tab.5.2) and IM_3 (Tab.5.3), with compensation of the flux linkage added, as reported in Sec. 5.9.

and (5.64) becomes

$$\lambda_{su}(t) - \lambda_{su}(0) = \int_0^t \left(\frac{u_{uv} - 2R_s i_u}{2} \right) dt \tag{5.66}$$

The integration (5.66) stops at time t_1, when both its integrands are zero, and then the (constant) output represents the initial flux linkage $\lambda_{su}(0)$, relative to the initial DC current I_{s0}:

$$\lambda_{su}(I_{s0}) = -\int_0^{t_1} \left(\frac{u_{uv} - 2R_s i_u}{2} \right) dt \tag{5.67}$$

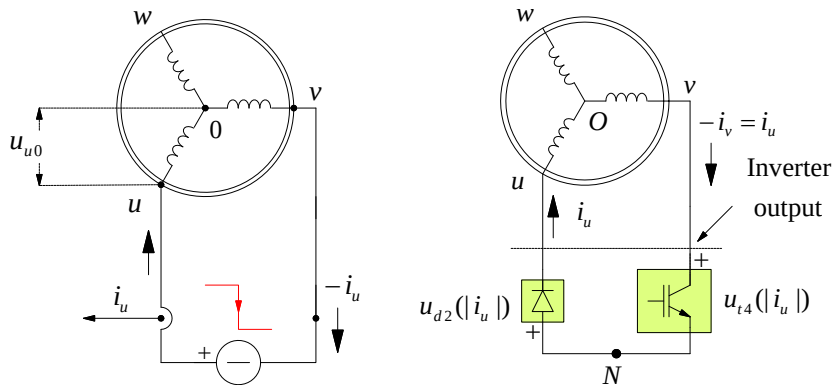

(a) *Before the step voltage transient* (b) *After the step voltage transient*

Fig. 5.19: DC Step voltage representation with the inverter setted in 000 configuration. The phases u and v are short-circuited through diode D_2 and IGBT T_4, or equivalently by considering the switch T of Fig.5.5 open.

Several Step voltage tests at different I_{s0} levels have been performed to get the reference flux linkage-current characteristic reported in Fig.5.20a, Fig.5.20c and Fig.5.20e. The plot also include the results of finite element analysis FEA simulations, described hereafter. Due to the non-linear characteristic and the magnetic saturation effects, the stator and rotor flux linkages are functions of the voltage vector position ϑ_{me} and by the magnetizing current I_{s0}. The FEA of the three machines under test (IM_1, IM_2 and IM_3) have been carried out by means of the same open-source simulation software *Femm33* [5] used in Sec. 1.3, on the base on the geometry data and of the windings distribution by means of the star of slots [7]. The results of the "no–load" FEA simulations allow the calculation of the non–linear stator flux linkage as a function of the stator current, as detailed in [104] and [105].
The "no–load" analyses were performed to different angles of the current vector and by varying its amplitudes, at zero frequency in the dq rotor reference frame. This rotor reference frame is shifted from the angular position ϑ_{me} with respect to the phase u, and growing levels of stator current density aligned with the d-axis are imposed during the analysis, while the current vector is shifted at constant steps of $\vartheta_{me} = 1\,\text{deg.el}$ to cover the entire electrical period of the machine. The stator flux linkage (function of the ideal stator winding distribution) is then computed by integrating the magnetic vector potential $\boldsymbol{A}$ concatenated on each stator slot, by taking into account the winding distribution as depicted in [7]. The amplitude of the currents is then made to vary from a minimum value to a maximum value (i. e. rated current) for each angular position.
This simulation allows the mapping of the machine for the entire range of the electrical period, and a flux linkage beam of curves in the $\alpha\beta$ reference frame (i. e. $\lambda_{s,\alpha} = f(i_\alpha, \vartheta_{me})$, $\lambda_{s,\beta} = f(i_\beta, \vartheta_{me})$ and $|\lambda_s| = f(|i_s|, \vartheta_{me})$) is completely derived. Then, the data are extracted and post-elaborated for a direct comparison with the result of the DC-test described above.
Fig.5.20 summarizes the main results of the comparison. For all of the three motors under test, the DC test and the simulated flux linkages were superposed to the flux linkage obtained by the (5.48), at $\vartheta_{me} = -\pi/6\,\text{rad.el}$. The overlapping is almost perfect, with an error (relative to the nominal flux linkage) that remains within the 0.5% range for IM_1, the $1.5 - 2.5\%$ for IM_2 and $2 - 2.5\%$ for IM_3 (Fig.5.20b, Fig.5.20d and Fig.5.20f). The DC test remains the more accurate term of comparison, while in the case of the comparisons with FEA, eventual mismatches can be attributed to slight discrepancies between theoretical geometries and real dimensions of the machine under test, affected

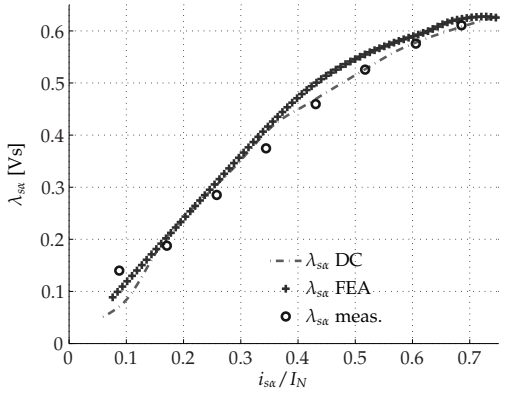

(a) IM$_1$ $\lambda_{s,\alpha} = f(I_{s0}/I_N = 0.8, \vartheta_{me} = -\pi/6\,\text{rad.el})$

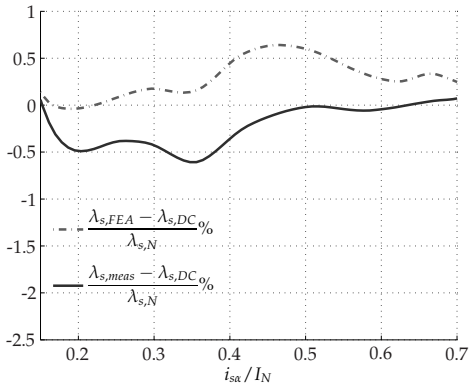

(b) *Percentage error of* IM$_1$

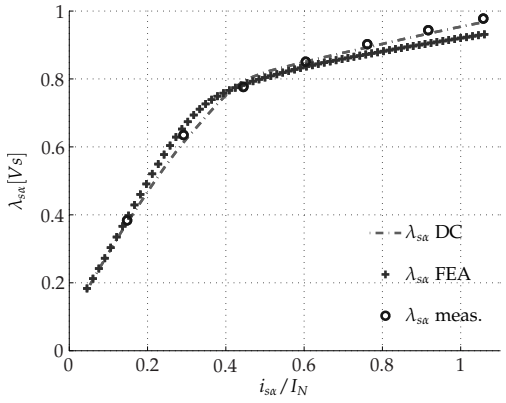

(c) IM$_2$ $\lambda_{s,\alpha} = f(I_{s0}/I_N = 0.8, \vartheta_{me} = -\pi/6\,\text{rad.el})$

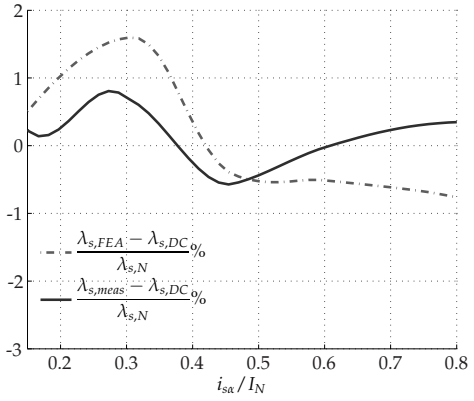

(d) *Percentage error of* IM$_2$

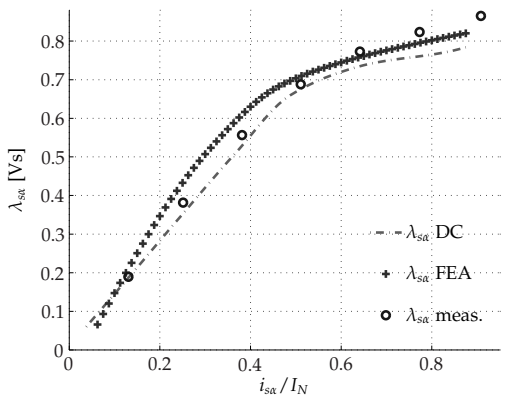

(e) IM$_3$ $\lambda_{s,\alpha} = f(I_{s0}/I_N = 0.8, \vartheta_{me} = -\pi/6\,\text{rad.el})$

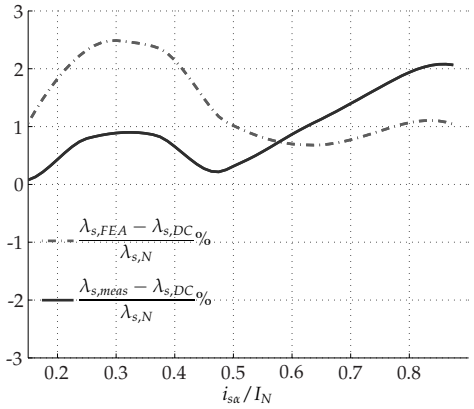

(f) *Percentage error of* IM$_3$

Fig. 5.20: (a), (c), (e): DC test and FEA-related α-axis stator flux linkages superposed to the measured one, at $\vartheta_{me} = -\pi/6\,\text{rad.el}$ with compensation of the flux linkage due of the "Tail" included (as detailed in Sec. 5.9). Percentage errors in (b), (d), (f).

by the manufacturing tolerances. The last step of the identification procedures is the off-line calculation of the inductance $L_\varphi(\boldsymbol{i}_\varphi, \vartheta_{me})$.
While not conceptually difficult, the data post-processing of figurename 5.14 with the data of Fig.5.18 requires an accurate numerical post elaboration of the numerical data. Regarding that in (5.49), at $t = 0$ the currents in the two inductances of the equivalent circuit Fig. 4.5 are the same ($\boldsymbol{i}_s(0) = \boldsymbol{i}_\varphi(0) = I_{s0}$) and they are linked to the flux linkages by the *apparent* inductances, as outlined in Sec. 5.7.
This means that the calculation of L_φ can be performed easily after the estimation of the flux linkages $\boldsymbol{\lambda}_s(\boldsymbol{i}_s(0))$, allowing different DC current values $I_{s0} = \boldsymbol{i}_s(0)$ to be set in order to map $\boldsymbol{\lambda}_s(\boldsymbol{i}_s(0))$, and $L_s^{app}(\boldsymbol{i}_s(0))$. It follows that:

$$\begin{aligned} L_s^{app}(\boldsymbol{i}_s(0)) &= L_\varphi^{app}(\boldsymbol{i}_s(0)) + L_t^{app}(\boldsymbol{i}_s(0)) \\ &= \frac{\lim_{t\to\infty} \int_0^{t_1} (\boldsymbol{u}_s(t) - R_s \boldsymbol{i}_s(t))\, dt}{\boldsymbol{i}_s(0)} = \frac{\boldsymbol{\lambda}_s(\boldsymbol{i}_s(0))}{\boldsymbol{i}_s(0)} \end{aligned} \tag{5.68}$$

and replacing the total flux linkage $\boldsymbol{\lambda}_s(\boldsymbol{i}_s(0))$ as a third-order polynomial function of the current $I_{s0} = \boldsymbol{i}_s(0)$, a numerical approximation can be achieved:

$$\begin{aligned} L_s^{app}(\boldsymbol{i}_s(0)) &= \frac{\boldsymbol{\lambda}_s(\boldsymbol{i}_s(0))}{\boldsymbol{i}_s(0)} = \frac{k_3 \boldsymbol{i}_s^3(0) + k_2 \boldsymbol{i}_s^2(0) + k_1 \boldsymbol{i}_s(0) + k_0}{\boldsymbol{i}_s(0)} \\ &= k_3 \boldsymbol{i}_s^2(0) + k_2 \boldsymbol{i}_s(0) + k_1 + k_0 \boldsymbol{i}_s^{-1}(0) \end{aligned} \tag{5.69}$$

The coefficients (k_3, k_2, k_1, k_0) can be obtained by a polynomial fitting algorithm, which elaborates the measurements of $\boldsymbol{\lambda}_s$ obtained from the previous identification procedure, as confirmed by Fig.5.21a, that shows the accurate numerical interpolation achieved.
The precise numerical derivative of the stator flux as a function of its current that returns the plot of stator inductance L_s reported in Fig.5.21b (refers to IM_1, but the same procedures has been applied to IM_2 and IM_3) represent the starting point for the numerical derivation of $L_\varphi(\boldsymbol{i}_\varphi, \vartheta_{me})$.

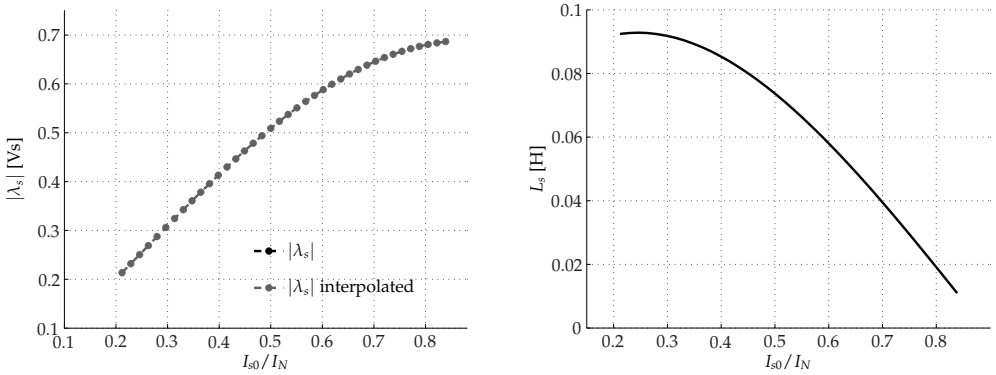

(a) Interpolation of Fig.5.20a with the third-order polynomial function of (5.69)

(b) Inductance $L_s(\boldsymbol{i}_s(0))$ for motor IM_1 calculated with (5.70). Saturation begins at $I_{s0}/I_N \approx 0.38$

Fig. 5.21: Interpolation of the flux linkage at $\vartheta_{me} = 0$) and equivalent inductance L_s for motor IM_1.

By directly applying the relationship (5.46), the final value of the *differential* inductance $L_\varphi(\boldsymbol{i}_s(0), \vartheta_{me})$ is obtained.

$$\begin{aligned} L_s(\boldsymbol{i}_s(0)) &= L_s^{app}(\boldsymbol{i}_s(0)) + \boldsymbol{i}_s(0)\frac{dL_s^{app}(\boldsymbol{i}_s(0))}{di} \\ &= 3k_3\boldsymbol{i}_s^2(0) + 2k_2\boldsymbol{i}_s(0) + k_1 = L_\varphi(\boldsymbol{i}_s(0)) + L_t(\boldsymbol{i}_s(0)) \end{aligned} \tag{5.70}$$

The results of the calculations of the magnetizing inductance are reported in Fig.5.22. They have been obtained by combining the experimental L_t data of Fig.5.14b, Fig.5.14c and Fig.5.14d with the estimated one of Fig.5.18a, Fig.5.18c and Fig.5.18e.
The polynomial fitting approximation of (5.70) has been used for each of the three motor tested, and Fig.5.20b, Fig.5.20d and Fig.5.20f collects the inductances $L_\varphi = f(I_{s0}, \vartheta_{me})$ obtained by considering three different angular positions: $\vartheta_{me} = 0$ rad.el, $\frac{2\pi}{3}$ rad.el and $\frac{4\pi}{3}$ rad.el.
The coherence among the data collected in these tests and the real parameters of the machine is rather precise, as one can easily verify. A final remark and comparison with the standard tests described in Sec. 5.2 is here reported. In particular, by considering the motor IM_1 in the linear region (up to about 4 A, equivalent of $I_{s0}/I_N = 0.34$), the numerical stator inductance value of Fig.5.21b can be compared, at low currents, with the experimental data of Tab.5.7.
The measured inductance of Fig.5.21b in fact, is around 0.91 mH (considering a ratio $I_{s0}/I_N = 0.34$), which is very close to that reported in Tab.5.7. The small discrepancy (a few percent) with respect to the no-load test may be ascribed to several reasons (stator resistive drop and quality of the measurements in the no-load test, a moderate imprecision in the *tail voltage* compensation in the proposed method.
In nominal conditions, i. e. at nominal speed, current, load and voltage, the saturation of the iron leads to have no more sinusoidal variables and therefore the stator flux linkage shall not be computed by considering a standard approach (i. e. as ratio of a voltage to a frequency). In other terms, when saturation intervenes, every non-linear quantity can be computed by only considering instantaneous relationships, such as those used in (4.10).
The correctness of the stator flux linkage λ_s measurements have been verified twice, by both FEA and DC measurements, as explained before, but in order to obtain accurate results by the DC measurements, some important aspects have been considered:

- For the off-line processing of the measures the number of the oscilloscope's saved points must be sufficiently high to have enough resolution in the off-line post-processing of the measures (e. g. 100000 points are sufficient to ensure a great accuracy).

- the repeatability of a single measurement must be ensured and verified with high accuracy. After every measured recording in fact, the current and voltage probes must be re-calibrated and zeroed. This guarantees a percentage error variability to only 0.1 % with respect to a reference flux linkage (related to the maximum value of the current of the motor).

The DC tests described could be expanded to any position by using three synchronized DC voltage generators, although this latter option required the possibility to record at the same time three transients of voltages and currents to performs off-line the integration of the variables. The experimental validation of the method in fact, if carried out at any specific angular position with evidence in DC would be complete, but it remains anyway satisfactory. In fact, the results obtained with the FEA provide sufficient reliability for the purpose of research.

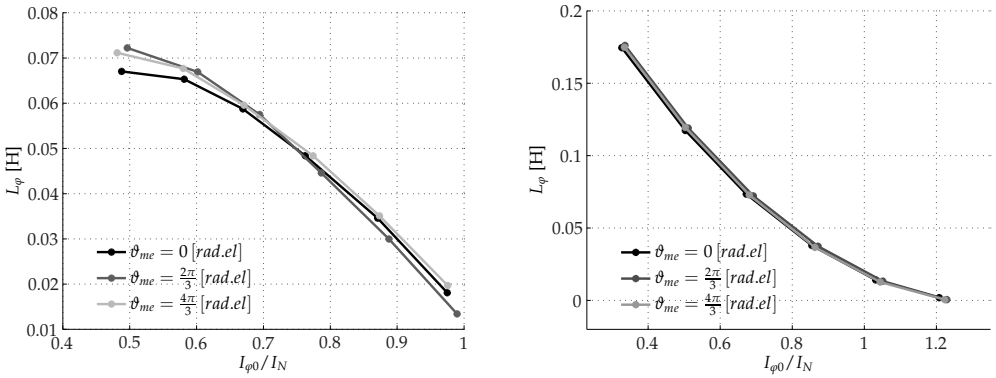

(a) $L_\varphi = f(I_{s0}, \vartheta_{me})$ *of* IM_1

(b) $L_\varphi = f(I_{s0}, \vartheta_{me})$ *of* IM_2

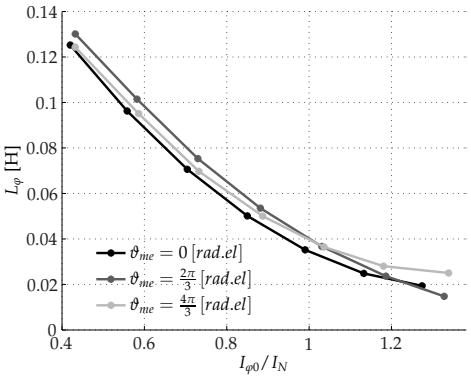

(c) $L_\varphi = f(I_{s0}, \vartheta_{me})$ *of* IM_3

Fig. 5.22: $L_\varphi = f(I_{s0}, \vartheta_{me})$ of the three machines obtained with (5.49).

The flux linkage identification at three different angular positions of the bias DC voltage vector, and relative to an increasing current amplitude was carried out on IM_1 (Tab. 5.1). The results are reported in Fig.5.23a (blue balls), where the flux linkage in two different working points has been calculated by the direct hardware measurements of the phase voltages, obtained by means of three differential voltage probes (one for each phase and the neutral point) and two current probes, while the algorithm was running.
The superposition of the data is quite fair, while some unavoidable differences can be ascribed to both the non-perfect "tail" voltage compensation, and the inverter voltage drop reconstruction.
Alternatively, Fig.5.23b shows the complete parametrized flux linkage λ_{su} for the entire electrical period of the machine at a fixed magnetizing current, and the overlapping with the FEA results confirms the general validity of the proposed algorithm.
The FEA results can be used also to check the validity of the proposed estimation algorithm by plotting the flux linkage of a single phase in the entire electric period, for different values of current. The results are reported in Fig.5.24 and Fig.5.23.
As final remark it is important to underline that if a direct hardware phase voltage measurement were available in the standard industrial VSI drives [106], the little discrepancy related to the reconstruction of the phase voltages disappear, although this solution remains a trade-off between cost and benefits.

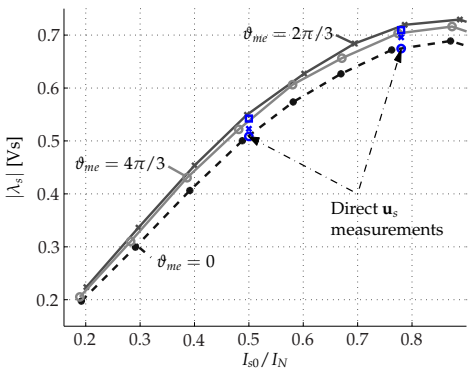

(a) *Overlapping of the three curves of* $|\lambda_s|$ *for* IM_1 *with the off-line integration results*

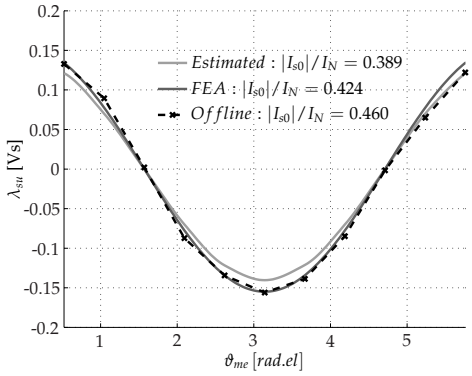

(b) *Overlapped* λ_{su} *calculated with the* FEA *and with the estimation procedures for the machine* IM_1

Fig. 5.23: Overlapped λ_{su} calculated with the direct off-line measurement of the flux linkage and an extra validation compared with the FEA analysis.

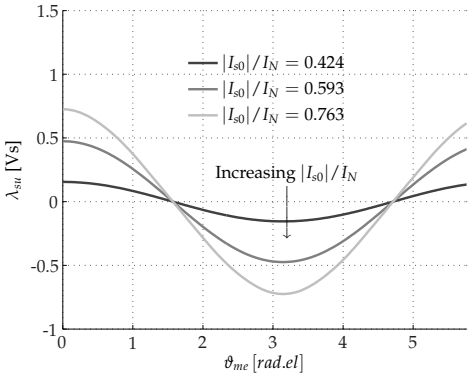

(a) λ_{su} *calculated with the* FEA *for* IM_1

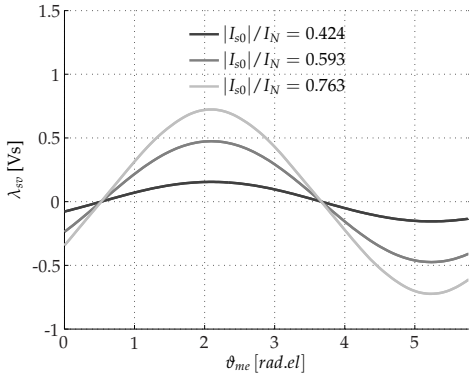

(b) λ_{sv} *calculated with the* FEA *for* IM_1

Fig. 5.24: λ_{su} and λ_{sv} calculated with the FEA for the machine IM_1 in Tab. 5.1 for different current levels.

5.8 ROTOR RESISTANCE REFERRED TO THE STATOR

Similarly to the transient inductance, the rotor resistance referred to the stator R_{sr} can be obtained by exciting the system with a pulsating sinusoidal signal of the form (5.18). Inverting the expression (5.12):

$$\begin{cases} \boldsymbol{I}_{\varphi 1}(s) = \dfrac{\boldsymbol{U}_{s1}(s) - (R_s + sL_{t0})\,\boldsymbol{I}_{s1}(s)}{sL_{\varphi 0}} \\ R_{sr}(s) = \dfrac{sL_{\varphi 0}\boldsymbol{I}_{\varphi 1}(s)}{\boldsymbol{I}_{s1}(s) - \boldsymbol{I}_{\varphi 1}(s)} = \dfrac{sL_{\varphi 0}}{\dfrac{\boldsymbol{I}_{s1}(s)}{\boldsymbol{I}_{\varphi 1}(s)} - 1} \end{cases} \tag{5.71}$$

results:

$$\frac{\boldsymbol{I}_{s1}(s)}{\boldsymbol{I}_{\varphi 1}} = \frac{sL_{\varphi 0}\boldsymbol{I}_{s1}(s)}{\boldsymbol{U}_{s1}(s) - (R_s + sL_{t0})\,\boldsymbol{I}_{s1}(s)} = \frac{sL_{\varphi 0}}{Z(s) - (R_s + sL_{t0})} \tag{5.72}$$

and replacing (5.72) into (5.71), the expression of $R_{sr}(s)$ is obtained. As in 5.6, a sinusoidal perturbation (in the form of (5.18)) is forced as voltage reference.
The reference space voltage vector is applied along the $d-$ axis, with an angular displacement of ϑ_{me} with respect to stationary reference frame, and the corresponding pulsating current vector (along the same direction ϑ_{me}) is delayed by an angle $\gamma(\omega)$. The frequency frequency response is obtained by placing $s = j\omega$ in the $R_{sr}(s)$ expression.

$$R_{sr}(s)\Big|_{s=j\omega} = \frac{j\omega L_{\varphi 0}\left(Z(j\omega) - (R_s + j\omega L_{t0})\right)}{j\omega L_{\varphi 0} - Z(j\omega) + R_s + j\omega L_{t0}} \tag{5.73}$$

Since the resistance (5.73) is a rotor parameter, a low-frequency sinusoidal reference voltage $\omega = \Omega_L$ is chosen (around the nominal slip frequency of the motors under test), for the sake of a closer match to normal operating conditions.
Furthermore, since R_{sr} is a real quantity, the imaginary part of (5.73) is necessarily null, and this condition leads to eliminating $L_{\varphi 0}$ from (5.73). Expanding (5.73), the previous hypothesis returns the final expression used in the automatic algorithm for the calculation of R_{sr}[7]:

$$\begin{aligned} \Im\left(R_{sr}(j\omega)\right) &= 0 \\ \Re\left(R_{sr}(j\omega)\right) &= \frac{U_{s1}^2 + I_{s1}^2\left(R_s^2 + \Omega_L^2 L_{t0}^2\right) - 2U_{s1}\left(R_s I_{s1}\cos\gamma + \Omega_L L_{t0} I_{s1}\sin\gamma\right)}{U_{s1} I_{s1}\cos\gamma - R_s I_{s1}^2} \end{aligned} \tag{5.76}$$

which can be directly computed from the parameters $R_s, L_t(I_{s0})$ obtained in the previous steps of the identification, and the currents $I_{s1}\sin\gamma, I_{s1}\cos\gamma$, as output of the Goertzel algorithm described in Sec. 5.6.1. The experimental tests were performed at different frequencies and the DC bias was extended up to the nominal current. The amplitude U_{s1} of the sinusoidal perturbation was as large as possible, under the constraint of maintaining the linearity of the system. A lower bound in I_{s1} was imposed by the 12-bit resolution of the A/D converters used in the current measurement. The experimental tests have highlighted that the Goertzel algorithm (5.32) requires a current amplitude I_{s1} of at least 20 LSB. The voltage U_{s1} was chosen accordingly, resulting in a rather small signal, due to the low frequency of the pulsating signal.
As a consequence, the algorithm exhibit a quite high sensibility to errors in the inverter voltage compensation (Sec. 5.4, as for L_t, but in that case the injection frequency is higher, and the non-linearity effects of the inverter are less significant). The final values chosen for the frequency $\Omega_l/(2\pi) = 5\,\text{Hz}$ while the amplitude U_{s1} vary in automatic way and the procedure of estimation starts only when the the linear region is reached. It is obvious that a direct measurement of the phase voltages, while more expensive,

7 Alternatively, R_{sr} can be calculated as:

$$\Re\left(R_{sr}(j\omega)\right) = R_{sr} = \frac{u_{srd}^2 + u_{srq}^2}{u_{srd} i_{sd} + u_{srq} i_{sq}} \tag{5.74}$$

with

$$\begin{cases} u_{srd} = U_{s1} - I_{s1} R_s \cos\gamma - I_{s1} L_{t0}\Omega_L \sin\gamma \\ u_{srq} = I_{s1} R_s \sin\gamma + I_{s1} L_{t0}\Omega_L \cos\gamma \\ i_{sd} = I_{s1}\cos\gamma \\ i_{sq} = -I_{s1}\sin\gamma \end{cases} \tag{5.75}$$

would represent the best solution. The behaviour of R_{sr} as a function of the injected frequency, at $I_{s0} = 0.6 I_{sN}$, $\vartheta_{me} = 0\,\text{rad.el}$, for all the machines tested, is reported in Fig.5.25a. From the substantial set of experiments carried out on the prototypes, some conclusions can be drawn:

- In principle, different working points could lead to different R_{sr} values, due to either possible iron saturation or structure asymmetry. These aspects, often disregarded, usually lead to rough mistakes in measurement interpretation. In the present case, the problem was tackled by calculating all the parameters of (5.76) at any given working point and spatial position, thus including the saturation effect on L_{t0}. In this way, the trend of R_{sr} remained strictly related to the proper physical causes only.

- The plots in Fig.5.25b exhibit a certain dependence on the pulsating frequency Ω_L. Different frequencies are used to map the R_{sr} in the range of interest, which is usually from zero to the IM nominal slip frequency (from 5% to 10% of the nominal IM speed).

  Frequencies higher than the nominal slip speed are not meaningful since the IM rotor will never work in those conditions. It is evident that the R_{sr} parameter suffers from the skin effect even in the range of Ω_L injection, but it is worth noting that skin effect represents only a part of the R_{sr} increment during normal operation, the other effect being the resistance increase as a function of the temperature, due to persisting loading conditions at standstill. Fig.5.25b shows that the R_{sr} curve always drops down for low frequencies. This not only depends on the skin effect, but is mainly due to the rather low voltage values at low frequency, that must be used during this step to avoid over current. Low voltage magnitudes are very difficult to measure, leading to incorrect estimations. Thus, it is suggested to neglect the first measurements, considering only those obtained from a quarter of the slip frequency on.

- Fig.5.25c shows that the skin effect is evident for every angular position of the voltage vector U_{s1}, but it is independent of the angular position. The same behaviour can be appreciated observing Fig.5.25d, where the R_{sr} as a function of the current is plotted in three different angular positions. In the considered frequency range $(10 - 40\,\text{Hz})$ the increase spans from the 22% of IM_3 to 100% of IM_1, mirroring the "deep bar" geometry of the latter motor.

- As far as the iron losses are concerned, it is worth recalling that the measurements were obtained at standstill and at low frequency, so that the iron losses do not affect the identification of R_{sr}. Actually, a standard no-load test returned (conducted for the motor IM_1) a value of $R_0 = 1115\,\Omega$ (derived from eddy current losses and hysteresis losses, as reported in Tab.5.1), which should placed in parallel to R_{sr} as shown in the scheme in Fig.4.5. It is evident that its influence is negligible, in the specified conditions

- The execution of the Goertzel algorithm took about 4 s, a time far beyond the usual rotor thermal constants. Hence, the effects of temperature increase during the test can be neglected as well. Anyway, in view of an on-line tracking algorithm, both the cited items, i. e. the iron losses and the dependence on the temperature, should be properly taken into account, by implementing one of the several alternatives present in literature.

Unfortunately, in literature there are no ways of measuring the rotor resistance directly, and so it is impossible to have a direct and real measure of R_{sr}. To validate the results

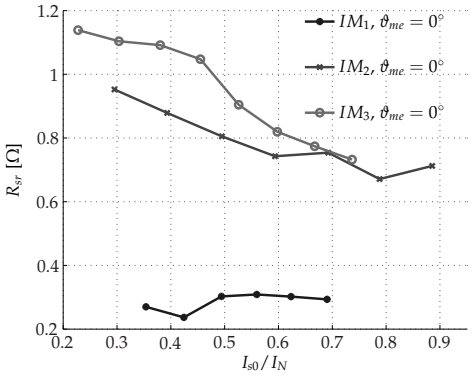

(a) $R_{sr} = f(|I_{s0}|, \vartheta_{me} = 0)$ *estimation for* IM_1, IM_2 *and* IM_3

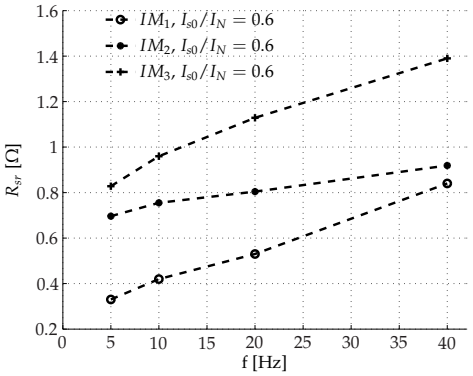

(b) R_{sr} *estimation for different frequency of the injection signal for* IM_1, IM_2 *and* IM_3

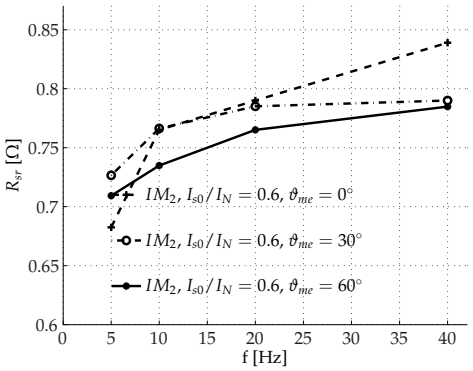

(c) R_{sr} *estimation for different frequency and different angular position using the motor in Tab. 5.2*

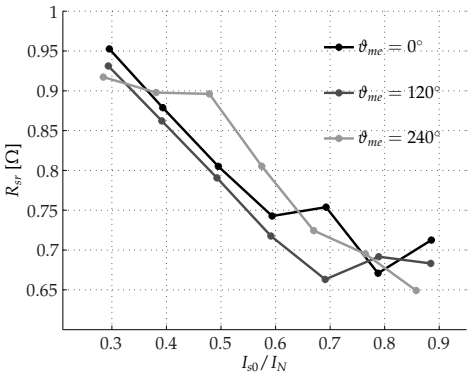

(d) $R_{sr} = f(|I_{s0}|, \vartheta_{me})$ *estimation for* IM_2

Fig. 5.25: Experimental results of the R_{sr} calculation.

obtained in Fig.5.25 the test described in Sec. 5.2 has been applied to IM_1, and the identified rotor resistance was of $R_{sr} = 0.37\,\Omega$ (see Tab.5.1) at a rotor frequency of few Hz, in good agreement with the extrapolation of the IM_1 curve reported in Fig.5.25.
While the magnetic parameters can be completely determined off-line, the stator and rotor resistances, in theory, do need an on-line tracking algorithm, not only for frequency but even more for temperature variations.
Anyway, if the temperature variation is slow, the rotor resistance R_{sr} does not change so fast and it is possible to solve the problem by adopting a simple on-line closed-loop adaptation, as described in [107]. The values of R_{sr} and R_s obtained in this research should therefore be considered as good starting values for one among the many different tracking algorithms present in the literature.

5.9 THE SQUIRREL CAGE ROTOR INFLUENCE

The automatic detection of the magnetising inductance described in 5.7 has the problem related to the estimation of the "tail effect", mentioned in the same paragraph.
On the basis of the estimation procedures described in 5.7 (at the fixed phase $\vartheta_{me} = -\pi/6$ rad.el for a direct comparison with the DC tests), different transients were repeated for different current levels, in order to get the profile of the integration result in the whole IM current range. While the automatic integration (5.67) was running, to get an insight of the integration mechanism, phase voltage and current curves, as a

function of time, were recorded by connecting a differential probe to the terminals u and the neutral point of the two IMs used in this experiment.
The accuracy of the current sensors available in the inverter has been verified by comparison with a high precision instrument (as mentioned at the beginning of this chapter), to avoid inaccuracy in the flux estimation. An initial offset measurement and reset procedure was also included, while two specific machines were manufactured to investigate to which extent the presence of the rotor influences the accuracy in the aforementioned step response-based procedures.
Both the motors have the same stator configuration and the main electric parameters are reported in Tab. 5.2. The relevant difference is that the first motor has a classic squirrel cage rotor with aluminium bars, while the second one has a squirrel cage rotor without die-cast aluminium bars in the rotor stack. This rotor configuration leads to obtaining rotor currents identically zero, and therefore the effects of energy balance due to the rotor flux linkage will be missing. Fig.5.26a and Fig.5.26b show the particular configuration of the squirrel cage rotor without bars, while the stator is manteined the same for both the machines.

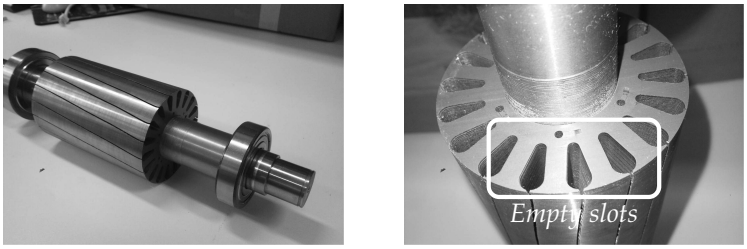

(a) *Modified squirrel cage rotor* (b) *Particular of the rotor slots*

Fig. 5.26: Modified machine used for the experimental tests. The stator is the same in Tab. 5.2, but the cage rotor is without aluminium bars.

The results obtained applying different step voltage transients are collected in Fig.5.27. These four time-plots refer to two different I_{s0} currents for both the machines tested, and the "flag integration" signal added is necessary to monitor the end of the integration time ("t_0" defines the initial integration time, while "t_1" indicates the moment in which the current falls below the sensibility of the inverter current probes an the hysteretic bandwidth).
Fig.5.27b and Fig.5.27d (no rotor bars) shows that at time "t_1" the voltage is zero, but in the case of machine with the standard squirrel cage rotor the phase-to-phase voltage is still non-zero (Fig.5.27a and Fig.5.27c), as for the transients of Fig.5.16 and Fig.5.17.
In principle, stopping time t_1 should be induced by a zero current, so that each integrand term in (5.67) is equally zero, but this does not seem to be entirely correct. This means that in a standard IM, the residual magnetization of the rotor flux linkage has not been completely expired when the stator current zeroing blocks the integration of (5.67). As a result, the estimated flux linkage is lower than the real one.
As expected, by comparing the results of the automatic flux integration with the reference one obtained using the DC test (representation of Fig.5.19 or Fig.5.5 with the switch T open) reported in Fig.5.28a, the actual flux linkage λ_{su} of the IM with rotor bars is greater than the flux linkage obtained with the estimation algorithm on the same motor (ball marks, in Fig.5.28a). On the other hand, the DC-test flux linkage and the estimated one coincide almost perfectly if the estimation procedures of 5.7 is applied to the IM with the modified rotor structure (without die-casting rotor bars), as reported in Fig.5.28b. This evidence triggered further investigations, described hereafter.

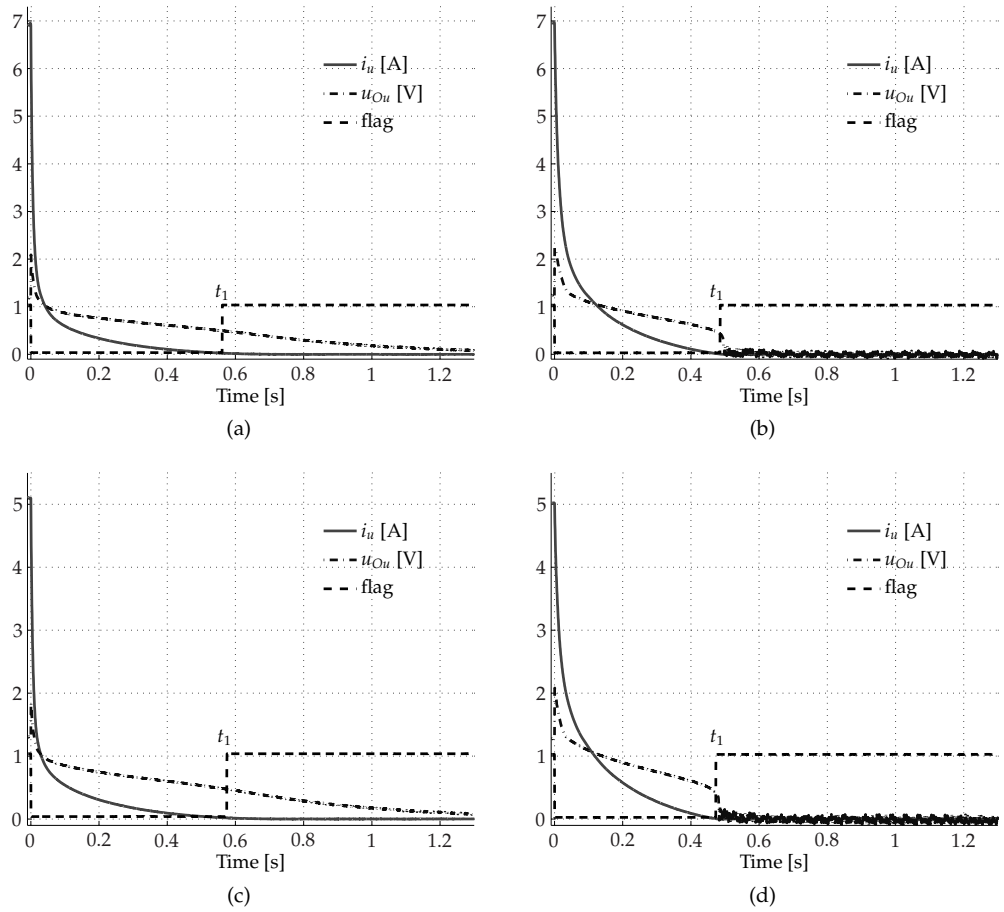

Fig. 5.27: Time trend of voltage and current of the motor in Tab. 5.2 with the classic squirrel cage rotor (Fig.5.27a) and without bars (Fig.5.27b) for an initial current of 7 A and 5 A (Fig.5.27c and Fig.5.27d with no bars). The "tail" effect is visible only in the case of machine with rotor bars.

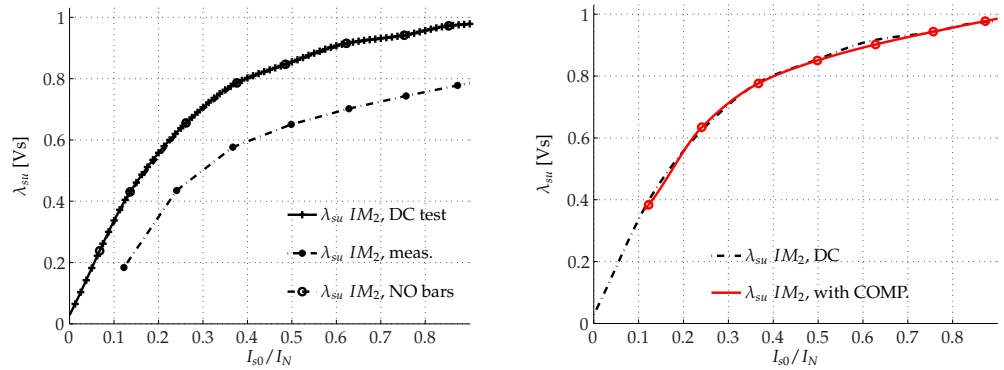

(a) *DC test and flux curve produced with the estimation algorithm applied to the machine in Tab. 5.2 with and without rotor bars*

(b) *Effects of compensation at the estimation algorithm result in red line*

Fig. 5.28: Stator magnetising flux linkage λ_{su} at fixed position of $\vartheta_{me} = -\pi/6$ rad.el.

It is quite obvious that the energy stored in the rotor during the initial i_{u0} setting, Joule losses apart, is returned to the stator during the Step voltage, but the effects are not yet clarified in literature.

To this purpose, the squirrel cage induction motor can be considered as a three-phase winding in short circuit, aligned with the magnetic field produced by the stator of the machine. In absence of the "rotor element", the electric machine accumulates magnetic energy on the windings of the stator in the form of flux-linkage and this energy is not transferred to the secondary circuit (the squirrel cage rotor in the case of an induction motor).
To better understand this phenomenon, the impact of the rotor element in the integration procedure of Sec. 5.7, a three-phase transformer with the secondary winding not short circuited is considered as substitute of the three-phase IM without the squirrel cage rotor.
In this simply experiment, by short-circuiting only one phase of the secondary winding, it is possible to measure the current that flows into the windings and, as expected, by applying the algorithm routine of Sec. 5.7 with the voltage vector $\boldsymbol{u}_s$ aligned at $\vartheta_{me} = -\pi/6$ rad.el, the rotor current exhibit a stretched decay time with respect of that of the stator, avoiding the effect of diode conduction at the primary side.
During the estimation procedure of Sec. 5.7, at the instant t_0 the PWM modulation is stopped, but as known, the surge voltage generates sudden stator current variation, and it is important to understand if these surge voltages are different in the two identical motors with different rotors.
Experimental tests have proven that these phenomenon is strictly dependent on the presence of the rotor, since the phase voltage in the windings is tied only to the variation of flux linkages. In fact, at instant t_0, the inverter is in configuration (000) or (111) (there's no PWM modulation), and the passive component (diode or IGBT) is manteined in conduction by the energy of the magnetic field at the time t_0, as reported in Fig.5.27.

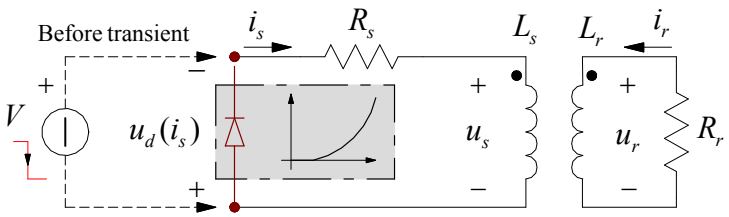

Fig. 5.29: Equivalent representation of the motor related to the primary during the voltage transient.

The results of Fig.5.27 demonstrate that, with the same stator winding configuration but with different rotor topologies (with and without rotor bars), the magnetization flux linkage at time t_0 is the same in both the motors as well as the initial magnetizing current I_{s0}. The application of the same voltage vector generates the same magnetic field, that is only linked to the reluctance of the magnetic circuit.
It can be observed, that at the instant t_0, a EMF is induced on the rotor, and in the bars short-circuited bars of the squirrel cage rotor flow a current (linked to the electric time constant of the rotor τ_R and the coupling factor between stator winding and rotor), that modifies the current transient in the stator windings.
If it were possible to measure them, it might be observed that from t_0 and t_1 (t_0 and t_1 the instants in which the integration of (5.47) is applied), the currents of the rotor would assume a dynamic dependent on the time constant of the rotor correlated to a decreasing exponential decay linked to this constant, different to that of the induced currents of the stator.
This means that the exponential decay of the stator current depends on the stator resistance and by the mutual inductance, but the conduction of the diode in each phase (e. g. the diode D_2 in Fig.5.19 at $\vartheta_{me} = -\pi/6$ rad.el) is ensured by a negative voltage drop, to which the effect of the induced current of the rotor is added.

In other terms, the effects of the rotor current is manifested in a negative voltage contribution to the stator side. This reaction generates a progressive lengthening of the time of discharge $t_1 - t_0$, and justifies the difference between the decay of the machine with rotor bars and without rotor bars visible in Fig.5.27a and Fig.5.27b.
To better understand this aspect, an equivalent linear representation of the motor from t_0 and t_1 is reported in Fig.5.29. The comments on the circuit of Fig.5.29 can be considered valid although the secondary non-linear effects related to the saturation of the magnetic circuits have been neglected (for the sake of simplicity).
With respect of Fig.5.29, the voltage and current balancing during the Step voltage transient can be written as:

$$\begin{cases} u_s = L_s \dfrac{di_s}{dt} + L_m \dfrac{di_r}{dt} \\ u_r = L_r \dfrac{di_r}{dt} + L_m \dfrac{di_s}{dt} \\ u_d + R_s i_s + u_s = R_r i_r + u_r \end{cases} \tag{5.77}$$

It follows that, during the conduction of the diode (i. e. when the VSI is configure in 000 or 111, after t_0):

$$u_d = -R_s i_s - u_s = -L_s \frac{di_s}{dt} - L_m \frac{di_r}{dt} - R_s i_s \tag{5.78}$$

and by considering the non-linear diode characteristic of Fig.5.6c together with the equation set of (5.77), the behaviour of the motor can be simulated. In particular, the diode is maintained in conduction until its voltage drop $u_d(i_s)$ is greater of the lower limit of the diode characteristic in Fig.5.6c, but this clearly depends by the effects of the secondary winding on the primary circuit.
Fig.5.30a shows the current at the primary and secondary windings during a step voltage response that emulates the situation illustrated in Sec. 5.6.
At the same time, the voltage at the primary and secondary winding are shown in Fig.5.30b. As expected, in Fig.5.30a the rotor current i_r changes only during the current variation of i_s, when the diode conduction is not influenced by the secondary winding effects.
After the first current transient (before the ending of the step voltage), an equilibrium condition is established at both the primary and secondary windings (i. e. they have the same magnetic field), while the absence of rotor current avoids any flux linkage variation at the primary winding.
At the end of the application of V, an electromotive force is induced on the short-circuited rotor that leads to a non-zero rotor current, while the diode is maintained in conduction by the negative voltage balance of (5.78).
The decay of the stator current i_s depends only by the negative voltage drop of u_s, which contributes to maintain in conduction the diode. The u_d voltage (that is function of the current passing through it) in fact, is balanced by the resistive voltage drop and by the negative voltage arose on the primary inductance, as visible in Fig.5.30b.
The negative voltage drop u_r at the secondary side is the direct effect of the mutual coupling term $L_m \dfrac{di_s}{dt}$, that is strictly dependant by the rotor current i_r induced at the secondary winding.
This latter particular explains the shortening of the decay time in Fig.5.27b with respect of Fig.5.27a.

The integrated absolute value of the "tail" at the end of the conduction of diode not remains constant with respect of the initial current I_{s0}, since it is related to the exponential decay of the stator voltage, that depends by the rotor time constant and by the mutual coupling term L_m. When the stator current is approximately zero, in fact, the voltage value remains equal of $u_d = V_D = L_m \frac{di_r}{dt}$ with a stator current $i_s \approx 0$ (V_D represents the voltage drop of the diode, approximately $V_D \approx 0.45\,\text{V}$).

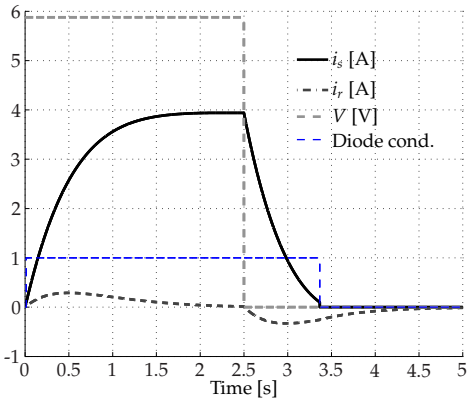

(a) *Currents i_s, i_r and voltage reference V*

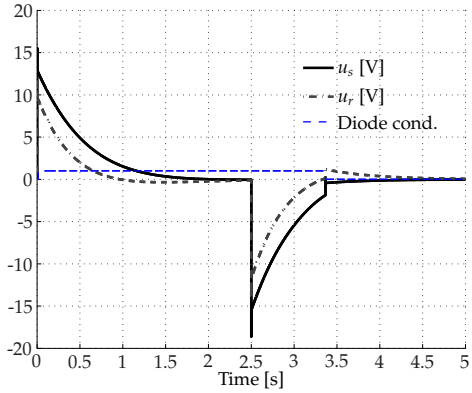

(b) *Primary and secondary voltages u_s and u_r*

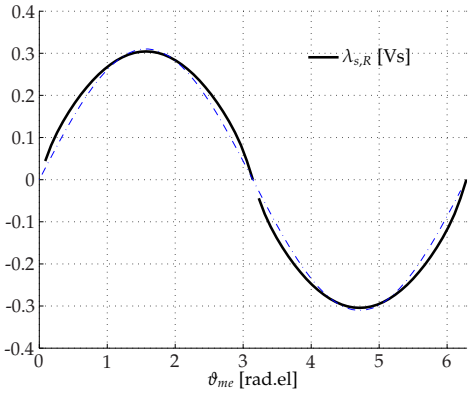

(c) *Integrated flux linkage $\lambda_{s,R}$ overlapped with the interpolated sinusoidal approximation (dotted).*

Fig. 5.30: Transient behaviour obtained by simulating the equivalent scheme of Fig.5.29 and rotor integrated flux linkage $\lambda_{s,R}$.

To prove this last feature, an other batch of simulations have been performed. The "tail effect" depends by the initial current which, in a three-phase distributed winding as the stator and squirrel cage rotor is the projection on each phase of the absolute current generated by the stator voltage $\boldsymbol{u}_s$.
In Fig.5.30c is shown the residual flux linkage $\lambda_{s,R}$ of the "tail", calculated by integrating the residual voltage u_s when the stator current i_s is zero (i. e. by applying the (5.47) when the diode flag of Fig.5.27a becomes zero).
As expected, by applying a consecutive series of voltage steps $V = A \sin \vartheta_{me}$ the residual flux linkage $\lambda_{s,R}$ exhibit a sinusoidal trend, due of the proportionality of the rotor current with the magnetizing stator current.
Many experimental tests have been performed to correlate the "tail effect" with the angular position of the voltage vector $\boldsymbol{u}_s$ used in the tests of the calculation of the stator flux linkage $\boldsymbol{\lambda}_s$ of 5.7 (i. e. by the initial current in each phase, as demonstrate in Fig.5.30c).

The measurements of voltage and current curves have been performed with a differential voltage and current probe while the estimation algorithm was running, by recording the data at a different angular position of $\boldsymbol{u}_s$. The post-elaboration of these data (i. e. after the instant t_1) return the residual flux linkage $\lambda_{s,R}$ of each phase (after the instant t_1, by applying the (5.48) at the stored measurements).
As expected, the compensation term $\lambda_{s,R}$ is independent of the initial magnetizing current I_{s0}, that represents the absolute value of the current associated to the voltage vector $\boldsymbol{u}_s$, although the projection in each phase of the current changes the final integrated value of the "tail" (as expected by the simulation in Fig.5.30c).
The experimental validation is reported in Fig.5.31a, where the off-line integration of the "tail" is repeated for the entire electrical period by considering two different initial magnetizing current I_{s0}.
The sinusoidal compensation value can be used to correct the flux linkage integration in the uvw reference frame, as described in or by directly considering the $\alpha\beta$ reference frame used in Sec. 5.7, by applying the inverse Clarke transformation at the three sinusoidal curves Fig.5.31b, and by adding the equivalent compensation value of $\lambda_{s,R}$ to $\lambda_{s,\alpha}$ or $\lambda_{s,\beta}$.
The curves of Fig.5.31b have been derived by interpolating the experimental compensations of Fig.5.31a with three sinusoids shifted of $2\pi/3$ rad.el.

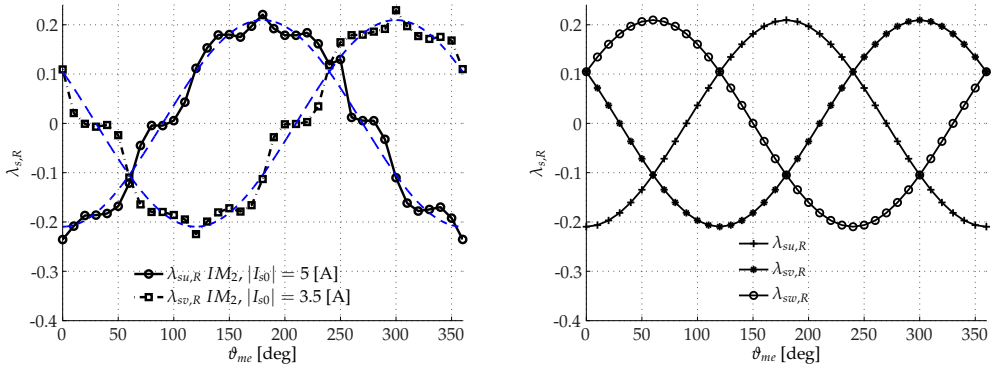

(a) *Integration of the rotor Tail flux for the machine in Tab.5.2, phase u and v at two different initial current level I_{s0}*

(b) *Interpolation of the three phases residual flux linkage (λ_{sR}) for* IM_2

Fig. 5.31: Experimental integration of the residual rotor flux linkage of IM_2, (Tab.5.2) to prove the independences of the compensation with respect of the initial magnetizing current.

The same procedure was then repeated for the other two motors (IM_1 and IM_3), and for the sake of completeness in Fig.5.32 is shown the off-line integration $\lambda_{s,R}$ in an entire electric period of the motors IM_1.
Anyway, due of the nature of three-phase system of the compensation curves, it is sufficient to calculate only the maximum value of the compensation and uses it to calculate the equivalent compensation in the entire electrical period.
To be sure that this last approximation were right, while the routine of Sec. 5.7 was running, the voltage drops and the current transients on each of the three phases of the motor (from phase u, v, w and neutral point O) were recorded, by considering two different angular positions ($\vartheta_{me} = \pi/4$ rad.el and $\vartheta_{me} = -\pi/6$ rad.el). The resulting flux linkage obtained with an off-line integration of voltage and current drop is identical in the two different angular positions, since the equivalent absolute value of voltage and currents is the same (as visible in Fig.5.32b).

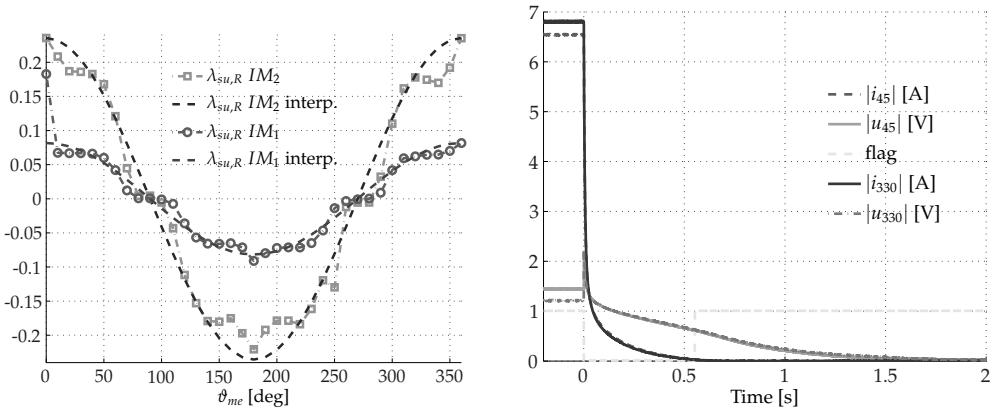

(a) *Rotor tail flux for of phase u for the machines* IM_1 *and* IM_2*, overlapped with the interpolated ones*

(b) *Voltage and current amplitude of* IM_2*, (Tab.5.2), at two different angular position with compensation added*

Fig. 5.32: Residual rotor flux linkage λ_{su} for the motor IM_1 and IM_2. Validation of the method at specific voltage and current.

This last experiment confirms the nature of the tail as a general three-phase system, and leads to consider the compensation of the "Tail" as the projection of the residual flux linkage on each of the three axes.
Is it also clear that, if it were possible to measure the real phase-to-phase voltage (as suggested in [106]), the integration might end at the right moment, without any error, avoiding the problems related to the "tail", that only depends by the specific motor that must be identified. It is also worth noting that the "tail" has no effect in the case of the DC test, since the integration was performed on measured voltage and current, but the added compensation of the wrong flux linkage marked with circles in Fig.5.28 compensates this mismatch. The result testifies the effectiveness of the procedure, since an almost perfect overlap is obtained.

5.10 CONCLUSIONS AND FUTURE WORKS

The automatic procedure for the self-commissioning of the IM parameters presented is totally performed at standstill and it represents an automatic way for the estimation of the main parameters of the IM machine. It is particularly appreciated when the motor is already connected to the load or in a procedure of pre-identification for a sensorless evolute algorithm for IM drives.
The estimation algorithm return the main parameters of the inverse-Γ model, and includes non-linearities of both the motor and the VSI converter for every possible angular position ϑ_{me} of the voltage vector. The obtained parameters are ready-to-use for most common speed and position sensorless algorithms, thus representing a step towards complete drive self-commissioning.
The mutual interaction between rotor and stator during step-based tests, generally an underestimated or ignored argument, is here revisited and revamped, as it gives the means for a justification of the discrepancy between real flux and the curve obtained with direct integration of the *bemf*. Many experimental results have been validated with a direct FEA comparison and a series of DC tests.
Further research activity will be devoted to a refinement of the proposed technique regards the on-line tracking of those parameters which are temperature-dependent, as R_s and R_{sr} and of iron losses influence as well. The study has also highlighted that many

problem resides in voltage measurement, which is normally replaced by a compensated version of the references.
Through a batch of accurate experimental results performed by adopting two custom IMs, this research has proved that to get the flux linkage estimation with the precision required by advanced sensorless AC drives, and as a temporary alternative, a further compensation of the rotor-related *bemf* has been successfully implemented and tested. Anyway, the straight solution remain the measurement of the actual voltage applied to the motor, as a standard which should be included in every advanced AC drive.
In conclusion, the solution proposed in this research is really suitable for the existing industrial applications, although a non-negligible error in flux-linkage estimation must be considered as trade off between costs and benefits.

Part III

FINAL CONCLUSIONS AND REMARKS

CONCLUSIONS

In this dissertation, new and alternative control techniques for modern mechatronic electrical drives have been presented and experimentally validated.
According to the solutions present in literature, the basic notions of the electric machines used in the control algorithms have been given in Chap.1 and Chap.4, while Chap.2 and Chap.3 were focused on advanced control methodologies for PMSM drives. The proposed control architectures have been deeply studied from a theoretical point of view, and an high number of experimental and simulation results have been presented in order to validate the theoretical model plant.
The MTPA control algorithm of Chap.2 brings the system to work in an operating point with the most efficient torque-to-current ratio, yet without giving any explicit information about the torque itself.
As future development, the MTPA algorithm could be combined with an identification procedure that uses the informations in the MTPA operating condition to retrieve the unknown motor parameters and, through them, a precise torque estimation. It follows that, with a proper rearrangement of the MTPA control algorithm it could be possible perform an on-line estimation of the electromagnetic torque, obtained by describing the q-axis flux linkage by a polynomial approximation, merged with a simple least-square algorithm (as suggested in [9]).
The HDPC control technique presented in Chap.3 has also proven to be a viable control alternative for PMSM drives in certain fields of use, in particular when is required an extremely high dynamic combined with a reduced cost of the system.
In this sense, the main contribution of the research was the introduction of a novel hierarchical decisional structure, which yields a choice of the control input voltage and combines dynamic performances considering also the efficiency aspects.
Moreover, the FPGA-based implementation and the modified control structure has been proven to be feasible from an industrial perspective by the experimental validation. This topic of research is probably one of more debated and that raises more interest in academia for the extremum number of features and non-linear control objects that can be inserted in the decisional structure. The integration of modern FPGA-based platform in the new drive generations will be frequently considered a valid alternative, and this surely will lead to merging new control architecture, as the HDPC, in the future generations of AC electric drives.
The second part of the thesis (i. e. the work presented in Chap.5) was related to a novel self-commissioning algorithm for induction motors at standstill.
Recent developments in the field of controls for asynchronous induction motors require a precise knowledge of the non linear parameters of the machine, and one of the main contributions made by this research is in the complete mathematical description of each step of the identification procedure, as well as the possibility to estimate without limitations, and in real-time, the flux linkage components in different reference frames. The identification algorithm has the ability to return all the non-linear parameters of the inverse-Γ circuit of the motor with high accuracy, as demonstrated by the numerous experimental tests and finite element simulations. The effects related to the presence of the squirrel cage rotor on the flux linkage estimation technique have been clarified, and an off-line compensation routine was proposed.
Several experimental evidences proved the effectiveness and the practical feasibility of each control architecture in combination with a detailed theoretical insight. It has been highlighted that many problems reside in the voltage measurement, which is normally

replaced by a compensated version of the voltage references. As previously mentioned, the definitive solution is surely the measurement of the actual voltage applied to the motor, which should be included in every advanced AC drive as conventional standard.

AUTHOR'S PUBLICATIONS

Several ideas, concepts and figures within this dissertation have been presented by the author during his Ph.D. course in international conferences or journals. They are hereafter listed:

- M. Carraro, A. Costabeber, and M. Zigliotto, "Convergence analysis and tuning of ripple correlation based MPPT: A sliding mode approach," in Proc. of EPE'13, pp. 1-10, 2013.

- M. Carraro and M. Zigliotto, "Automatic parameter identification of inverter-fed induction motors at standstill," IEEE Transactions on Industrial Electronics, 2013.

- R. Antonello, M. Carraro, and M. Zigliotto, "Maximum torque per ampere operation of anisotropic synchronous PM motors based on extremum seeking control," IEEE Transactions on Industrial Electronics, 2013.

- M. Carraro, F. Tinazzi, and M. Zigliotto, "Estimation of the direct-axis inductance in PM synchronous motor drives at standstill," in Proc. of ICIT'13, pp. 313-318, 2013.

- M. Zigliotto, M. Carraro, and F. Tinazzi, "The influence of the squirrel cage rotor in the estimation of the IM flux linkage at standstill," in Proc. of ICIT'13, pp. 410-415, 2013.

- R. Antonello, M. Carraro, F. Tinazzi, and M. Zigliotto, "Parametric identification of PM synchronous motors: A Hammerstein-model approach" in Proc. of ICM'13, pp. 174-179, 2013.

- R. Antonello, M. Carraro, and M. Zigliotto, "Towards the automatic tuning of MTPA algorithms for IPM motor drives," in Proc. of ICEM'12, pp. 1121 -1127, 2012.

- R. Antonello, M. Carraro, and M. Zigliotto, "Theory and implementation of a MTPA tracking controller for anisotropic PM motor drives," in Proc. of IECON'12, pp. 2061 -2066, 2012.

- M. Carraro, F. Tinazzi, and M. Zigliotto, "A novel approach to torque estimation in IPM synchronous motor drives," in Proc. of IECON'12, pp. 4637 -4641, 2012.

- M. Carraro and M. Zigliotto, "Hierarchical direct predictive control of PMSM drives," in Proc. of PRECEDE'11, pp. 3 -9, 2011.

- E. Tedeschi, M. Carraro, M. Molinas, and P. Mattavelli, "Effect of control strategies and power take-off efficiency on the power capture from sea waves," IEEE Transactions on Energy Conversion, vol. 26, pp. 1088 -1098, 12 2011.

- E. Tedeschi, M. Molinas, M. Carraro, and P. Mattavelli, "Analysis of power extraction from irregular waves by all-electric power take off," in Proc. of ECCE'10, pp. 2370-2377, 9 2010

BIBLIOGRAPHY

[1] K. Rahman, N. Patel, T. Ward, J. Nagashima, F. Caricchi, and F. Crescimbini, "Application of direct-drive wheel motor for fuel cell electric and hybrid electric vehicle propulsion system," *IEEE Trans. Ind. Appl.*, vol. 42, no. 5, pp. 1185–1192, 2006. (Cited on page 3.)

[2] M. Carraro, A. Costabeber, and M. Zigliotto, "Convergence analysis and tuning of ripple correlation based mppt: A sliding mode approach," in *Proc. of EPE'13*, 2013, pp. 1–10. (Cited on page 3.)

[3] V. Honsinger, "The fields and parameters of interior type AC permanent magnet machines," *IEEE Trans. Power App. Syst. (through 1985)*, vol. PAS-101, no. 4, pp. 867–876, 1982. (Cited on page 5.)

[4] M. Zigliotto, *Dispense del corso di Azionamenti Elettrici Industriali. A.A. 2010-2011*. Vicenza: -, 2010. (Cited on pages 6, 15, 98, 99, 102, 119, and 131.)

[5] D. Meeker. (2003) Finite element method magnetics. [Online]. Available: http://femm.berlios.de (Cited on pages 13 and 138.)

[6] N. Bianchi, S. Bolognani, and G. Comelato, "Finite element analysis of three-phase induction motors: comparison of two different approaches," *IEEE Trans. Energy Convers.*, vol. 14, no. 4, pp. 1523–1528, 1999. (Cited on page 13.)

[7] N. Bianchi, *Calcolo delle macchine elettriche col metodo degli elementi finiti*. CLEUP, 2001. (Cited on pages 14 and 138.)

[8] R. Antonello, M. Carraro, F. Tinazzi, and M. Zigliotto, "Parametric identification of PM synchronous motors: a hammerstein-model approach," in *Proc. of ICM'13*, Feb. 2013. (Cited on page 17.)

[9] M. Carraro, F. Tinazzi, and M. Zigliotto, "A novel approach to torque estimation in IPM synchronous motor drives," in *Proc. of IECON'12*, oct. 2012, pp. 4637 –4641. (Cited on pages 17, 58, and 157.)

[10] R. Dutta and M. Rahman, "A comparative analysis of two test methods of measuring d - and q -axes inductances of interior permanent-magnet machine," *IEEE Trans. Magn.*, vol. 42, no. 11, pp. 3712 –3718, nov. 2006. (Cited on page 17.)

[11] S. Yamamoto, T. Ara, S. Oda, and K. Matsuse, "Prediction of starting performance of PM motors by dc decay testing method," *IEEE Trans. Ind. Appl.*, vol. 36, no. 4, pp. 1053 –1060, jul/aug 2000. (Cited on pages 17 and 136.)

[12] M. Zigliotto, M. Carraro, and F. Tinazzi, "The influence of the squirrel cage rotor in the estimation of the IM flux linkage at standstill," in *Proc. of ICIT'13*, 2013, pp. 410–415. (Cited on pages 17 and 107.)

[13] M. Barcaro, N. Bianchi, and F. Magnussen, "Permanent-magnet optimization in permanent-magnet-assisted synchronous reluctance motor for a wide constant-power speed range," *IEEE Trans. Ind. Electron.*, vol. 59, no. 6, pp. 2495–2502, 2012. (Cited on page 19.)

[14] S. Kim, Y.-D. Yoon, S.-K. Sul, and K. Ide, "Maximum torque per ampere (MTPA) control of an IPM machine based on signal injection considering inductance saturation," *IEEE Trans. Power Electron.*, vol. 28, no. 1, pp. 488–497, 2013. (Cited on page 19.)

[15] I. Boldea, M. Paicu, and G. Andreescu, "Active flux concept for motion-sensorless unified ac drives," *IEEE Trans. Power Electron.*, vol. 23, no. 5, pp. 2612–2618, 2008. (Cited on page 19.)

[16] M. Paicu, I. Boldea, G. Andreescu, and F. Blaabjerg, "Very low speed performance of active flux based sensorless control: interior permanent magnet synchronous motor vector control versus direct torque and flux control," *Electric Power Applications, IET*, vol. 3, no. 6, pp. 551–561, 2009. (Cited on page 19.)

[17] A. Kusko and D. Galler, "Control Means for Minimization of Losses in AC and DC Motor Drives," *IEEE Trans. Ind. Appl.*, vol. IA-19, no. 4, pp. 561–570, 1983. (Cited on page 19.)

[18] S. Morimoto, Y. Tong, Y. Takeda, and T. Hirasa, "Loss minimization control of permanent magnet synchronous motor drives," *IEEE Trans. Ind. Electron.*, vol. 41, no. 5, pp. 511–517, 1994. (Cited on page 19.)

[19] R. Moncada, J. Tapia, and T. Jahns, "Analysis of negative-saliency permanent-magnet machines," *IEEE Trans. Ind. Electron.*, vol. 57, no. 1, pp. 122 –127, Jan. 2010. (Cited on page 19.)

[20] P. Vas, *Sensorless vector and direct torque control*, ser. Monographs in electrical and electronic engineering. Oxford University Press, 1998. (Cited on pages 19, 22, 97, and 98.)

[21] T. Jahns, G. Kliman, and T. W. Neumann, "Interior Permanent-Magnet Synchronous Motors for Adjustable-Speed Drives," *IEEE Trans. Ind. Appl.*, vol. IA-22, no. 4, pp. 738–747, 1986. (Cited on page 19.)

[22] P. Niazi, H. Toliyat, and A. Goodarzi, "Robust maximum torque per ampere (MTPA) control of PM-assisted synrm for traction applications," *IEEE Trans. Veh. Technol.*, vol. 56, no. 4, pp. 1538 –1545, Jul. 2007. (Cited on page 19.)

[23] M. Chy and M. Uddin, "Development of a nonlinear speed controller of IPMSM drive incorporating MTPA with mechanical parameter estimation," in *Proc. of IEMDC'07*, vol. 1, 2007, pp. 322–327. (Cited on page 19.)

[24] G. Foo and M. Rahman, "Sensorless sliding-mode MTPA control of an IPM synchronous motor drive using a sliding-mode observer and hf signal injection," *IEEE Trans. Ind. Electron.*, vol. 57, no. 4, pp. 1270–1278, 2010. (Cited on page 19.)

[25] S. Fazeli, H. Ping, H. Zarchi, and J. Soltani, "Robust maximum torque per ampere (MTPA) control of interior permanent magnet synchronous motor drives using adaptive input-output feedback linearization approach," in *Proc. of TECHPOS'09*, 2009, pp. 1–6. (Cited on page 19.)

[26] Y. Mohamed and T. Lee, "Adaptive self-tuning MTPA vector controller for IPMSM drive system," *IEEE Trans. Energy Convers.*, vol. 21, no. 3, pp. 636–644, 2006. (Cited on page 19.)

[27] Y. Tan, W. Moase, C. Manzie, D. Nesic, and I. M. Y. Mareels, "Extremum seeking from 1922 to 2010," in *Proc. of CCC'10*, 2010, pp. 14–26. (Cited on pages 19 and 20.)

[28] S. Bolognani, L. Sgarbossa, and M. Zordan, "Self-tuning of MTPA current vector generation scheme in IPM synchronous motor drives," in *Proc. of EPE'07*, 2007, pp. 1–10. (Cited on pages 19, 20, and 23.)

[29] K.-W. Lee and S.-B. Lee, "MTPA operating point tracking control scheme for vector controlled PMSM drives," in *Proc. of SPEEDAM'10*, 2010, pp. 24–28. (Cited on page 19.)

[30] S. Kim, Y.-D. Yoon, S.-K. Sul, K. Ide, and K. Tomita, "Parameter independent maximum torque per ampere (MTPA) control of IPM machine based on signal injection," in *Proc. of APEC'10*, Palm Springs, California, 2010, pp. 103–108. (Cited on page 19.)

[31] S. Bolognani, L. Peretti, and M. Zigliotto, "Online MTPA control strategy for DTC synchronous-reluctance-motor drives," *IEEE Trans. Power Electron.*, vol. 26, no. 1, pp. 20–28, 2011. (Cited on page 19.)

[32] A. Dianov, K. Young-Kwan, L. Sang-Joon, and L. Sang-Taek, "Robust self-tuning MTPA algorithm for IPMSM drives," in *Proc. of IECON'08*, 2008, pp. 1355–1360. (Cited on page 20.)

[33] S. Bolognani, R. Petrella, A. Prearo, and L. Sgarbossa, "On-line tracking of the MTPA trajectory in IPM motors via active power measurement," in *Proc. of ICEM'10*, 2010, pp. 1–7. (Cited on page 20.)

[34] ——, "Automatic tracking of MTPA trajectory in IPM motor drives based on AC current injection," *IEEE Trans. Ind. Appl.*, vol. 47, no. 1, pp. 105–114, 2011. (Cited on pages 20, 22, and 26.)

[35] Y. Xia, K. Ahmed, and B. Williams, "A new maximum power point tracking technique for permanent magnet synchronous generator based wind energy conversion system," *IEEE Trans. Power Electron.*, vol. 26, no. 12, pp. 3609–3620, 2011. (Cited on page 20.)

[36] M. Krstic and H.-H. Wang, "Stability of extremum seeking feedback for general nonlinear dynamic systems," *Automatica*, vol. 36, no. 4, pp. 595 – 601, 2000. (Cited on pages 20, 26, and 27.)

[37] K. B. Ariyur and M. Krstic, *Real-Time Optimization by Extremum-Seeking Control*. Wiley Interscience, 2003. (Cited on page 20.)

[38] Y. Tan, D. Nešić, and I. Mareels, "On Non-local Stability Properties of Extremum Seeking Control," *Automatica*, vol. 42, no. 6, pp. 889–903, 2006. (Cited on page 27.)

[39] H. Khalil, *Nonlinear systems*. Prentice Hall PTR, 2002. (Cited on pages 31 and 112.)

[40] I. Boldea, V. Coroban-Schramel, G. Andreescu, S. Scridon, and F. Blaabjerg, "Bega starter/alternator - vector control implementation and performance for wide speed range at unity power factor operation," in *Proc. of IAS '08*, 2008, pp. 1–8. (Cited on page 50.)

[41] I. Boldea, M. Paicu, G.-D. Andreescu, and F. Blaabjerg, "Active flux orientation vector sensorless control of ipmsm," in *Proc. of OPTIM '08*, 2008, pp. 161–168. (Cited on page 50.)

[42] J. Rodriguez, J. Pontt, C. Silva, P. Correa, P. Lezana, P. Cortes, and U. Ammann, "Predictive current control of a voltage source inverter," *IEEE Trans. Ind. Electron.*, vol. 54, no. 1, pp. 495–503, 2007. (Cited on page 51.)

[43] P. Cortes, M. Kazmierkowski, R. Kennel, D. Quevedo, and J. Rodriguez, "Predictive control in power electronics and drives," *IEEE Trans. Ind. Electron.*, vol. 55, pp. 4312–4324, 2008. (Cited on page 51.)

[44] M. Kazmierkowski and L. Malesani, "Current control techniques for three-phase voltage-source PWM converters: A survey," *IEEE Trans. Ind. Electron.*, vol. 45, no. 5, pp. 691–703, Oct. 1998. (Cited on pages 51 and 64.)

[45] J. Holtz and S. Stadtfeld, "A predictive controller for the stator current vector of AC machines fed from a switched voltage source," in *Proc. of IPEC'83*, 1983, pp. 1665–1675. (Cited on page 51.)

[46] I. Takahashi and T. Noguchi, "A new quick response and high efficiency control strategy of an IM," in *Conf. Rec. of IAS annual meeting*, 1985, pp. 1665–1675. (Cited on page 51.)

[47] P. Mercorelli, "A switching model predictive control for overcoming a hysteresis effect in a hybrid actuator for camless internal combustion engines," in *Proc. of PRECEDE*, 2011, pp. 10–16. (Cited on page 51.)

[48] S. Qin and T. A. Badgwell, "A survey of industrial model predictive control technology," *Control Engineering Practice*, vol. 11, no. 7, pp. 733 – 764, 2003. (Cited on page 51.)

[49] H. Le-Huy, K. Slimani, and P. Viarouge, "Analysis and implementation of a real-time predictive current controller for permanent-magnet synchronous servo drives," *IEEE Trans. Ind. Electron.*, vol. 41, no. 1, pp. 110–117, 1994. (Cited on pages 51 and 58.)

[50] F. Morel, X. Lin-Shi, J.-M. Retif, B. Allard, and C. Buttay, "A comparative study of predictive current control schemes for a permanent-magnet synchronous machine drive," *IEEE Trans. Ind. Electron.*, vol. 56(7), pp. 2715–2728, 2009. (Cited on page 51.)

[51] J. Rodriguez, M. Kazmierkowski, J. Espinoza, P. Zanchetta, H. Abu-Rub, H. Young, and C. Rojas, "State of the art of finite control set model predictive control in power electronics," *IEEE Trans. Ind. Informat.*, vol. 9, no. 2, pp. 1003–1016, 2013. (Cited on pages 51 and 52.)

[52] R. Errouissi, M. Ouhrouche, W.-H. Chen, and A. Trzynadlowski, "Robust nonlinear predictive controller for permanent-magnet synchronous motors with an optimized cost function," *IEEE Trans. Ind. Electron.*, vol. 59, no. 7, pp. 2849 –2858, july 2012. (Cited on pages 51 and 59.)

[53] M. Kvasnica, P. Grieder, and M. Baotić, "Multi-parametric toolbox MPT," 2004. [Online]. Available: http://control.ee.ethz.ch/~mpt/ (Cited on page 51.)

[54] A. Bemporad, M. Morari, V. Dua, and E. N. Pistikopoulos, "The explicit solution of model predictive control via multiparametric quadratic programming," in *Proc. of American Control Conference (ACC)*, 2000. (Cited on page 51.)

[55] S. Mariethoz, A. Domahidi, and M. Morari, "Sensorless explicit model predictive control of permanent magnet synchronous motors," in *Proc. of IEMDC '09*, 2009, pp. 1250–1257. (Cited on page 51.)

[56] S. Bolognani, S. Bolognani, L. Peretti, and M. Zigliotto, "Combined speed and current model predictive control with inherent field-weakening features for PMSM drives," in *Proc. of MELECON 2008*, 2008, pp. 472–478. (Cited on page 51.)

[57] A. Linder and R. Kennel, "Model predictive control for electrical drives," in *Proc. of PESC'05*, 2005, pp. 1793–1799. (Cited on page 52.)

[58] S. Bolognani, S. Bolognani, L. Peretti, and M. Zigliotto, "Design and implementation of model predictive control for electrical motor drives," *IEEE Trans. Ind. Electron.*, vol. 36, pp. 1925–1936, 2009. (Cited on page 52.)

[59] X. Lin-Shi, F. Morel, A. Llor, B. Allard, and J.-M. Retif, "Implementation of hybrid control for motor drives," *IEEE Trans. Ind. Electron.*, vol. 54, no. 4, pp. 1946–1952, 2007. (Cited on page 52.)

[60] Y. Inoue, Y. Kawaguchi, S. Morimoto, and M. Sanada, "Performance improvement of sensorless IPMSM drives in low-speed region using online parameter identification," in *Proc. of ECCE'09*, 2009, pp. 1933–1938. (Cited on page 58.)

[61] A. Akrad, M. Hilairet, and D. Diallo, "Performance enhancement of a sensorless PMSM drive with load torque estimation," in *Proc. of IECON'10*, 2010, pp. 945–950. (Cited on page 58.)

[62] M. Carraro, F. Tinazzi, and M. Zigliotto, "Estimation of the direct-axis inductance in PM synchronous motor drives at standstill," in *Proc. of ICIT'13*, 2013, pp. 313–318. (Cited on page 58.)

[63] P. Wipasuramonton, Z. Zhu, and D. Howe, "Predictive current control with current-error correction for PM brushless AC drives," *IEEE Trans. Ind. Appl.*, vol. 42, no. 4, pp. 1071–1079, 2006. (Cited on page 58.)

[64] E. Schrijver and J. D. van, "Disturbance observers for rigid mechanical systems: equivalence, stability, and design," *Journal of Dynamic Systems, Measurement, and Control*, vol. 124, no. 4, pp. 539–548, 2002. (Cited on pages 58 and 59.)

[65] P. Cortes, S. Kouro, B. La Rocca, R. Vargas, J. Rodriguez, J. Leon, S. Vazquez, and L. Franquelo, "Guidelines for weighting factors design in model predictive control of power converters and drives," in *Proc. of ICIT'09*, 2009, pp. 1–7. (Cited on page 59.)

[66] F. Morel, J.-M. Retif, X. Lin-Shi, and C. Valentin, "Permanent magnet synchronous machine hybrid torque control," *IEEE Trans. Ind. Electron.*, vol. 55, no. 2, pp. 501–511, 2008. (Cited on page 64.)

[67] S. Vazquez, J. Leon, L. Franquelo, J. Carrasco, O. Martinez, J. Rodriguez, P. Cortes, and S. Kouro, "Model predictive control with constant switching frequency using a discrete space vector modulation with virtual state vectors," in *Proc. of ICIT'09*, 2009, pp. 1–6. (Cited on page 64.)

[68] S. Chai and L. Wang, "Finite control set model predictive control of 2LVSI-PMSM using interpolated switching states," in *Proc. of IECON 2012*, 2012, pp. 1799–1804. (Cited on page 65.)

[69] M. Carraro and M. Zigliotto, "Hierarchical direct predictive control of PMSM drives," in *Proc. of PRECEDE'11*, oct. 2011, pp. 3 –9. (Cited on pages 81 and 82.)

[70] A. Munoz and T. Lipo, "On-line dead-time compensation technique for open-loop PWM-VSI drives," *IEEE Trans. Power Electron.*, vol. 14, no. 4, pp. 683 –689, jul 1999. (Cited on pages 85 and 117.)

[71] J. Jeong and L. Jun-Young, "Parameter identification of an induction motor drive with magnetic saturation for electric vehicle," *Journal of Power Electronics*, vol. 11, pp. 418–423, 2011. (Cited on page 93.)

[72] K. B. Nordin, D. W. Novotny, and D. S. Zinger, "The influence of motor parameter deviations in feedforward field orientation drive systems," *IEEE Trans. Ind. Appl.*, vol. IA-21, no. 4, pp. 1009 –1015, july 1985. (Cited on pages 93 and 94.)

[73] A. Khambadkone and J. Holtz, "Vector-controlled induction motor drive with a self-commissioning scheme," *IEEE Trans. Ind. Electron.*, vol. 38, no. 5, pp. 322 –327, oct 1991. (Cited on pages 93 and 94.)

[74] J.-K. Seok, S.-I. Moon, and S.-K. Sul, "Induction machine parameter identification using PWM inverter at standstill," *IEEE Trans. Ind. Electron.*, vol. 12(2), pp. 127–132, 1997. (Cited on page 93.)

[75] M. Ranta, M. Hinkkanen, and J. Luomi, "Inductance identification of an induction machine taking load-dependent saturation into account," in *Proc. of ICEM'o8*, 2008, pp. 1–6. (Cited on page 93.)

[76] J. Guzinski and H. Abu-Rub, "Speed sensorless induction motor drive with predictive current controller," *IEEE Trans. Ind. Electron.*, vol. 60, no. 2, pp. 699–709, 2013. (Cited on page 94.)

[77] M. Sonnaillon, G. Bisheimer, C. De Angelo, and G. Garcia, "Automatic induction machine parameters measurement using standstill frequency-domain tests," *Electric Power Applications, IET*, vol. 1, no. 5, pp. 833 –838, sept. 2007. (Cited on page 94.)

[78] J. Maes and J. Melkebeek, "Speed sensorless direct torque control of induction motors using an adaptive flux observer," in *Conf. Rec. of IAS Annual Meeting*, vol. 4, 1999, pp. 2305 –2312 vol.4. (Cited on page 94.)

[79] K. Akatsu and A. Kawamura, "Sensorless very low-speed and zero-speed estimations with online rotor resistance estimation of induction motor without signal injection," *IEEE Trans. Ind. Appl.*, vol. 36, no. 3, pp. 764 –771, may/jun 2000. (Cited on page 94.)

[80] J. Holtz and J. Quan, "Sensorless vector control of induction motors at very low speed using a nonlinear inverter model and parameter identification," *IEEE Trans. Ind. Appl.*, vol. 38, no. 4, pp. 1087 – 1095, jul/aug 2002. (Cited on pages 94 and 117.)

[81] K. Wang, J. Chiasson, M. Bodson, and L. Tolbert, "A nonlinear least-squares approach for identification of the induction motor parameters," *IEEE Trans. Autom. Control*, vol. 50, no. 10, pp. 1622–1628, 2005. (Cited on page 94.)

[82] J. Stephan, M. Bodson, and J. Chiasson, "Real-time estimation of the parameters and fluxes of induction motors," *IEEE Trans. Ind. Appl.*, vol. 30, no. 3, pp. 746–759, 1994. (Cited on page 94.)

[83] R. Babau, I. Boldea, T. Miller, and N. Muntean, "Complete parameter identification of large induction machines from no load acceleration deceleration tests," *IEEE Trans. Ind. Electron.*, no. 4, pp. 1962–1972, 2007. (Cited on page 94.)

[84] M. Bertoluzzo, G. Buja, and R. Menis, "Self-commissioning of RFO IM drives: one-test identification of the magnetization characteristic of the motor," *IEEE Trans. Ind. Appl.*, vol. 37, no. 6, pp. 1801 –1806, nov/dec 2001. (Cited on page 94.)

[85] A. Proca and A. Keyhani, "Identification of variable frequency induction motor models from operating data," *IEEE Trans. Energy Convers.*, vol. 17, no. 1, pp. 24 –31, mar 2002. (Cited on page 94.)

[86] A. Boglietti, A. Cavagnino, and M. Lazzari, "Computational algorithms for induction-motor equivalent circuit parameter determination - part I: Resistances and leakage reactances," *IEEE Trans. Ind. Electron.*, vol. 58, 9, pp. 3723–3733, 2011. (Cited on page 94.)

[87] ——, "Computational algorithms for induction motor equivalent circuit parameter determination - part II: Skin effect and magnetizing characteristics," *IEEE Trans. Ind. Electron.*, vol. 58, 9, pp. 3734–3740, 2011. (Cited on page 94.)

[88] L. Peretti and M. Zigliotto, "Automatic procedure for induction motor parameter estimation at standstill," *Electric Power Applications, IET*, vol. 6, no. 4, pp. 214 –224, april 2012. (Cited on pages 95, 101, 117, 118, 128, and 136.)

[89] M. Ruff, A. Bunte, and H. Grotstollen, "A new self-commissioning scheme for an asynchronous motor drive system," in *Conf. Rec. of IAS annual meeting*, oct 1994, pp. 616 –623 vol.1. (Cited on pages 95 and 117.)

[90] J. Godbersen, "Stand-still method for estimating the rotor resistance of induction motors," in *Conf. Rec. of IAS Annual Meeting)*, vol. 2, 1999, pp. 900–905. (Cited on page 95.)

[91] J. Beraldin and W. Steenaart, "Overflow analysis of a fixed-point implementation of the goertzel algorithm," *IEEE Trans. Circuits Syst.*, vol. 36, no. 2, pp. 322 –324, feb 1989. (Cited on page 95.)

[92] A. V. Oppenheim and R. W. Schafer, *Discrete-time signal processing*. Upper Saddle River, NJ: Prentice-Hall, Inc., 2009. (Cited on pages 95, 122, and 125.)

[93] P. L. Alger and R. Arnold, "The history of induction motors in america," *Proc. of the IEEE*, vol. 64, no. 9, pp. 1380–1383, 1976. (Cited on page 97.)

[94] W. Theodore, *Electrical Machines , Drives And Power Systems, 5/E*. Pearson Education, 2002. (Cited on page 97.)

[95] A. Fitzgerald, C. Kingsley, and S. Umans, *Electric Machinery*, ser. McGraw-Hill Series in Electrical Engineering. McGraw-Hill, 2003. (Cited on page 97.)

[96] S. Bolognani and M. Zigliotto, "Essentials of IM parameters measurement for FOC drives tuning," in *Proc. of ICEM'02*, Mar. 2002. (Cited on page 106.)

[97] M. Sumner and G. Asher, "Autocommissioning for voltage-referenced voltage-fed vector-controlled induction motor drives," *Electric Power Applications, IEE Proceedings B*, vol. 140, no. 3, pp. 187–200, 1993. (Cited on page 106.)

[98] S. Williamson and M. Begg, "Calculation of the bar resistance and leakage reactance of cage rotors with closed slots," *Electric Power Applications, IEE Proceedings B*, vol. 132, no. 3, pp. 125 –132, 1985. (Cited on pages 107 and 127.)

[99] S. Bittanti, *Teoria della predizione e del filtraggio*. Pitagora, 2000. (Cited on page 118.)

[100] K. Nassiri-Toussi and W. Ren, "On the convergence of least-squares estimates," in *Proc. of Decision and Control*, 1992, pp. 2233–2238 vol.2. (Cited on page 118.)

[101] M. Arkan, D. Kostic-Perovic, and P. Unsworth, "Closed rotor slot effect on negative sequence impedance in induction motors," in *Proc. of IEEE IAS Conf.*, vol. 2, 2001, pp. 751–753. (Cited on page 127.)

[102] J. Hu and B. Wu, "New integration algorithms for estimating motor flux over a wide speed range," in *Proc. of PESC'97*, vol. 2, jun 1997, pp. 1075 –1081 vol.2. (Cited on page 129.)

[103] R. Bojoi, P. Guglielmi, and G.-M. Pellegrino, "Sensorless direct field-oriented control of three-phase induction motor drives for low-cost applications," *IEEE Trans. Ind. Appl.*, vol. 44, no. 2, pp. 475 –481, march-april 2008. (Cited on page 129.)

[104] L. Alberti, N. Bianchi, and S. Bolognani, "Variable-speed induction machine performance computed using finite-element," *IEEE Trans. Ind. Appl.*, vol. 47, no. 2, pp. 789 –797, march-april 2011. (Cited on page 138.)

[105] D. Dolinar, R. De Weerdt, R. Belmans, and E. Freeman, "Calculation of two-axis induction motor model parameters using finite elements," *IEEE Trans. Energy Convers.*, vol. 12, no. 2, pp. 133 –142, jun 1997. (Cited on page 138.)

[106] L. Peretti and M. Zigliotto, "Fpga-based voltage measurements in AC drives," in *Proc. of ICEM'10*, sept. 2010, pp. 1 –6. (Cited on pages 142 and 153.)

[107] K. Wang, J. Chiasson, M. Bodson, and L. Tolbert, "An online rotor time constant estimator for induction machine," in *Proc. of IEMDC'05*, 2005, pp. 608–614. (Cited on page 146.)